UNIVERSITY OF SOUTHAMPTON

FACULTY OF ENGINEERING AND THE ENVIRONMENT
Aerodynamics and Flight Mechanics

Unsteady Aerodynamic Loads on Aircraft Landing Gear

by

Stefano Spagnolo

Thesis for the degree of Doctor of Philosophy

June 8, 2016

UNIVERSITY OF SOUTHAMPTON

ABSTRACT

FACULTY OF ENGINEERING AND THE ENVIRONMENT
Aerodynamics and Flight Mechanics

UNSTEADY AERODYNAMIC LOADS ON AIRCRAFT LANDING GEAR

by Stefano Spagnolo

The aim of the current work is to improve the accuracy and efficiency of aerodynamic load predictions on landing gear in flight conditions, as part of the UK TSB ALGAAP (Advanced Landing Gear Aero-loads and Aero-noise Prediction) project. To this purpose, both experiments and simulations are performed on simplified landing-gear components. The new geometry presented in this work is a configuration composed of two simplified wheels in tandem. Experimental and numerical results from a single-wheel geometry are used as a baseline for comparison. The models are tested in the University of Southampton wind-tunnel complex, where forces, surface pressures and velocity fields are measured to gain a better understanding of both mean and unsteady flow features. Also, a vibration test is employed for the first time in a wind tunnel to validate the unsteady load measurements. The results of the experiments are presented in this thesis, showing the wake structure of the flow past the tandem wheels and the configurations that provide minimum values of mean drag and unsteady fluctuations. On the same single-wheel and tandem-wheel geometries, advanced numerical simulations such as Delayed Detached-Eddy Simulations (DDES) with the Spalart-Allmaras equation are used to predict the flow. The methodology is based on the use of techniques to improve the efficiency of the process, thus unstructured grids with a semi-structured boundary-layer mesh are employed to achieve the desired results. The results of the simulations are compared with the experiments, showing the importance of modifying the standard turbulence model in order to consider the laminar-turbulent transition for improved accuracy. Proper Orthogonal Decomposition (POD) is also employed to analyse the data of both experiments and simulation, in order to obtain a better insight of the flow features. Finally, additional simulations are performed on a simplified four-wheel landing gear to understand the effects of additional components, such as axles and bogie beam. The results show the high importance of the axles on the flow past the wheels and the effect of the modifications of the turbulence model on the full landing gear.

Contents

List of Figures

List of Tables

Declaration of Authorship

I, Stefano Spagnolo, declare that the thesis entitled *Unsteady Aerodynamic Loads on Aircraft Landing Gear* and the work presented in the thesis are both my own, and have been generated by me as the result of my own original research. I confirm that:

- this work was done wholly or mainly while in candidature for a research degree at this University;
- where any part of this thesis has previously been submitted for a degree or any other qualification at this University or any other institution, this has been clearly stated;
- where I have consulted the published work of others, this is always clearly attributed;
- where I have quoted from the work of others, the source is always given. With the exception of such quotations, this thesis is entirely my own work;
- I have acknowledged all main sources of help;
- where the thesis is based on work done by myself jointly with others, I have made clear exactly what was done by others and what I have contributed myself;
- parts of this work have been published as: conference paper Spagnolo et al. [75] (January 2015), conference paper Spagnolo et al. [74] (June 2015), journal paper Spagnolo et al. [76] (under review, 2016) and conference paper Spagnolo et al. [73] (to be presented in June 2016).

Signed:...

Date:...

Acknowledgements

The author is thankful to the UK Technology Strategy Board and to Airbus (Centre of Competence Landing Gear) for the support to this project. The author acknowledges the ANTC/AFM staff and the Dynamics Laboratory staff, for the scientific advice. The author also acknowledges the IRIDIS High Performance Computing Facility and the associated support services at the University of Southampton, fundamental in the completion of this work.

Nomenclature

$\overline{C}_D$	Mean drag coefficient
C_D	Drag coefficient (x-direction)
C_{DES}	Constant of the Spalart-Allmaras DES model
c_f	Local friction coefficient
$\overline{C}_L$	Mean lift coefficient
C_L	Lift coefficient (y-direction)
$\overline{C}_p$	Mean pressure coefficient
C_p	Pressure coefficient
$C_{p\ \mathrm{RMS}}$	Pressure coefficient RMS
C_S	Smagorinsky coefficient
C_x, C_y, C_z	Generic force component coefficients
D	Diameter, m
D_w	Wheel diameter, m
$\tilde{d}$	Corrected distance from the wall, m
d	Distance from the wall, m
E	Young's modulus, Pa
F_x, F_y, F_z	Force components, N
f_0	Natural frequency, Hz
ℓ	Smagorinsky length scale, m
G	Filter
i_t	Turbulent index
k	Kinetic energy, m^2/s^2
k_f	Stiffness, N/m
L	Inter-axis distance (generic)
L_w	Inter-axis distance (wheels)
ℓ_S	Smagorinsky length scale

m_w	Wheel mass, kg
N	Number of samples
n	Wall-normal direction
p, P, p'	Pressure, mean pressure and pressure fluctuation, Pa
p_∞	Free-stream static pressure, Pa
R	Wheel-shoulder radius, m
Re	Reynolds number (generic) $Re = U_\infty L/\nu$
Re_D	Reynolds number based on wheel/cylinder diameter
S	Frontal projected wheel area ($S = 0.012\,85\,\mathrm{m}^2$), m^2
s_{ij}, S_{ij}	Strain-rate tensor and mean strain-rate tensor, s^{-1}
$\overline{\mathcal{S}}$	Characteristic filtered rate of strain, s^{-1}
u_i, U_i, u_i'	Velocity, mean velocity and velocity fluctuation i-th component, m/s
u_τ	Friction velocity, m/s
U_∞	Free-stream velocity magnitude, m/s
$\overline{u}_i$	Filtered velocity, m/s
x, y, z	Global coordinate system, m
x_p, y_p, z_p	PIV coordinate system, m
y^+	Dimensionless wall distance
z_c	Confidence coefficient

Greek letters

α	Angle of attack (or installation angle), deg
Δ	Characteristic length in LES (or DES) models, m
δ_{ij}	Kronecker's delta
ϵ_μ	Relative error on the mean
ϵ_σ	Relative error on the standard deviation
Θ	Limiting streamlines angle, deg
θ	Azimuthal angle, deg
κ	Von Karman constant
μ	Dynamic viscosity, kg/(m s)
μ_t	Turbulent (dynamic) viscosity, kg/(m s)
ν	Kinematic viscosity, m^2/s
ν_{eff}	Effective viscosity, m^2/s

ν_t	Turbulent (kinematic) viscosity, $\mathrm{m^2/s}$
ν_{SGS}	Sub-grid scale viscosity, $\mathrm{m^2/s}$
$\tilde{\nu}$	RANS (or DES) variable in Spalart-Allmaras model, $\mathrm{m^2/s}$
ρ	Density, $\mathrm{kg/m^3}$
τ_{ij}^t	Reynolds stress tensor, $\mathrm{kg/(m\,s^2)}$
Ω_{ij}	Skew-symmetric part of velocity gradient, $\mathrm{s^{-1}}$
Ω	Vorticity magnitude, $\mathrm{s^{-1}}$
ω	Specific turbulent dissipation rate, $\mathrm{s^{-1}}$
ω_0	First natural angular frequency, $\mathrm{s^{-1}}$

Abbreviations

ALGAAP	Advanced Landing Gear Aero-loads and Aero-noise Prediction
ANTC	Airbus Noise Technology Centre
BGK	Bhatnagar-Gross-Krook method
CAA	Computational Aero-Acoustics
CADWIE	Control of Approach Drag Without Impact on the Environment
CFD	Computational Fluid Dynamics
EASA	European Aviation Safety Agency
ESDU	Engineering Sciences Data Unit
DDES	Delayed Detached-Eddy Simulation
DES	Detached-Eddy Simulation
DNS	Direct Numerical Simulation
FEA	Finite Element Analysis
FEM	Finite Element Method
FW-H	Ffowcs-Williams Hawkings (equations)
ICAO	International Civil Aviation Organization
IDDES	Improved DDES
LAGOON	LAnding Gear nOise database for CAA validatiON
LBM	Lattice Boltzmann methods
LDV	Laser Doppler Velocimetry
LES	Large-Eddy Simulation
MSD	Modelled-stress depletion
PIV	Particle Image Velocimetry

RANS	Reynolds-Averaged Navier-Stokes
RMS	Root mean square value (or standard deviation)
RNG	Re-Normalisation Group method
S-A	Spalart-Allmaras turbulence model
SGS	Subgrid scale
SST	Shear stress transport
URANS	Unsteady RANS
ZDES	Zonal DES

Subscripts

RMS	Root Mean Square
∞	Free-stream value
P	Relative to photopolymer LS600 material
C	Relative to composite material
lam	Laminar flow
turb	Turbulent flow
w	Wheel

Superscripts

f	Front wheel
r	Rear wheel
t	Total

Chapter 1

Introduction

1.1 Research problem and objectives

Landing gear sustains the aircraft on the ground, allowing them to take off, land and taxi without damage. The undercarriage is deployed during the final descent for the landing on a runway and they are retracted after the take-off, when a positive climb rate has been verified by the pilot. It has a significant contribution to the aircraft total drag in low-speed phases and they are considered one of the main sources of noise on modern aircraft.

Until a few years ago, most of the design activities that concern landing gear were based on the use of tables and charts that incorporate the main parameters in a generic undercarriage. For instance, one could refer to the data sheet ESDU 79015 [62]: using the formulas that are in the manual, it is possible to provide a rough estimate of the drag for the landing gear in the design stage. A problem with the database approach is that it considers some important parameters, such as the wheel diameter and width, the number of wheels and their configuration, the presence of struts and cavities, but the accuracy is low because the number of parameters is still limited and the aerodynamic interactions are difficult to analyse. Above all, nothing can be said on the unsteady fluctuations around the mean drag values. The lack of tools for unsteady load prediction lead to the lack of means for landing-gear noise prediction. In fact, accurate noise predictions rely upon reliable unsteady flow predictions. Thus, gaining a good understanding of the unsteady flow features past landing gear is an essential part of the path toward landing-gear noise prediction.

An example of landing gear is given in Figure 1.1, where the A340 main-landing-gear assembly is illustrated. The geometry is mainly comprised of bluff bodies, either with wheel shape or cylindrical shape, in addition to a number of structural features (e.g., torque links, articulating links, downlock actuator, etc.). A high level of interaction between the components can be expected because there are elements partially or totally in the wake of upstream elements. The components are mostly bluff with wake separation lines not clearly identifiable.

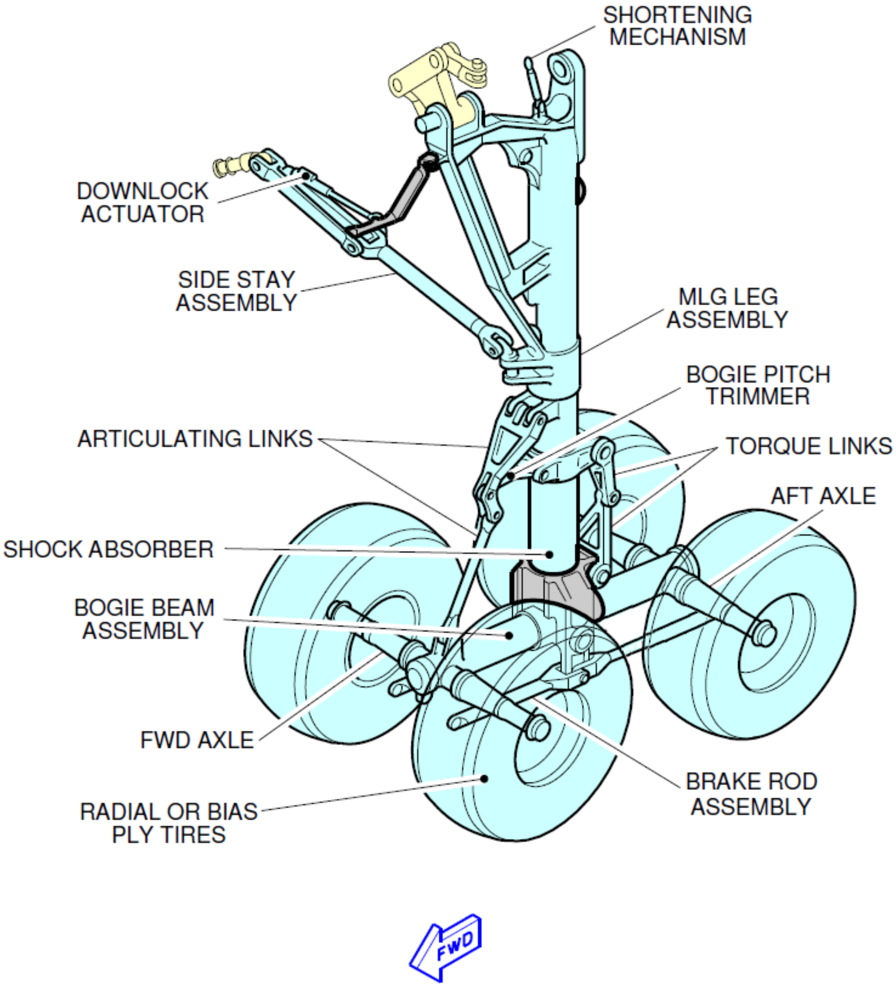

Figure 1.1: Airbus A340 main landing gear (picture simplified from the original picture in the A340 manual [4]).

Predicting the unsteady loads on landing gear with a reasonable accuracy is a challenging task due to the flow conditions: unsteady and detached flow past multiple bluff bodies. Reynolds-Averaged Navier-Stokes Simulations (RANS) and Unsteady RANS (URANS) can provide some information on the flow past landing gear, but this method relies on the model used, and the results are dependent on the chosen turbulence model. At the same time, Large-Eddy Simulations (LES) are too demanding in terms of computational cost, which means a long time-to-solution.

A new hybrid branch of prediction methodologies has been recently developed, for instance Detached-Eddy Simulations (DES) that proved to be more suitable than URANS in unsteady load estimations due to its higher computational efficiency. The technique switches to the RANS models to simulate the most demanding part of the LES simulations, i.e. the boundary layers, while the most relevant eddies are actually simulated as in a LES.

Lattice-Boltzmann Method (LBM) is also used to discretise the equations with a particle collision model. This approach, as described in the literature review (Section 2.1.3), has the advantage of working on a structured-block mesh with minimum computational time dedicated to the meshing process. However, given the absence of a boundary layer mesh, the boundary layer is usually not resolved up to the viscous sublayer, thus it often needs a wall function.

1.2 Motivations for the PhD project

The overall aim of this project is to improve the unsteady aerodynamic loads prediction. This general aim has been developed in the following list of objectives.

1. **Measurements of unsteady aerodynamic forces on landing-gear wheels.** In the literature (Section 2.1.2), large data sets are available for unsteady pressure measurements on landing gear surfaces, as well as flow visualizations by means of Particle Image Velocimetry (PIV). However, there is a general lack of direct unsteady force measurements on landing-gear components. In addition, the mean values provided are often measured on the whole bogie assembly, instead of providing the aerodynamic forces for each landing-gear component. The data provided in this way normally involve the use of high-frequency pressure sensors applied directly on the model surface, with high costs and long manufacturing time-scales. Consequently, the need for more cost-effective solutions for unsteady aerodynamic load measurements signifies the first motivation of the PhD project.

2. **Efficient numerical simulations of landing-gear components.** From the literature review of landing-gear simulations (Section 2.1.3), hybrid advanced numerical simulations appear promising in predicting the flow past bluff bodies like landing gear. But the reliability of the models is still low with errors as high as 30-40% on the mean drag coefficients. The solutions proposed are often oriented toward finer meshes, with increasing computational cost. Against the trend to increasing computational cost, feasible models have to be proposed in order to reduce the time-to-solution, while keeping the accuracy high. The efficiency of the simulations is defined as the accuracy of the predicted results compared with the overall time required. The overall time includes the whole process, from mesh generation to post-processing. To this purpose, the flow features recognition (both from experiments and simulations) is considered a fundamental part of the process that leads the development of the prediction methodology.

3. **Tandem-wheel geometry.** In addition, all the previous works can be divided in two categories: complex geometries (i.e. full landing gear) and basic components, which represent only a part of an undercarriage, for example a wheel or a strut. A new experimental geometry for the current PhD can fill the gap: it can be a model of landing-gear bogie with intermediate level of complexity, possibly with simplifications that reduce any risk of interference with secondary structures. The new geometry that is proposed here is the tandem-wheel geometry, which comprises two wheels in tandem configuration (one behind the other), in order to study the flow past the wheels. Only in this way, all the interactions with additional components can be neglected.

4. **Study of the interactions between landing-gear components.** The numerical procedure developed on tandem wheels is applied to a simplified landing-gear model with wheels having the same geometry as the tandem wheels. The data from the tandem-wheel experiments and simulations are compared with the numerical data from the tandem wheels in order to study the effects of the additional components, such as axles and strut, on the flow past the wheels.

The current PhD project is not only aimed at the extension of the previous knowledge on landing-gear unsteady aerodynamics but also at the improvement of the prediction methodologies. In fact, the work done during the project can be employed in the future for aeroacoustic studies that need reliable aerodynamic predictions in order to provide reliable noise predictions.

1.3 Thesis outline

The literature review elaborated in Chapter 2 covers the past works on the geometries of interest, which include not only full landing gear, but also rudimentary components. More specific works concerning turbulence modelling and experiments on dynamic loads are also reviewed and analysed.

The contribution of the current PhD project starts with the wind-tunnel model design in Chapter 3, where the design procedure is presented. The wind-tunnel test results on single and tandem-wheels results are reported with the testing procedure given in Chapter 6, which includes also a discussion of the main experimental findings.

The software, the equations, and the implementation of the numerical methods in OpenFOAM® (the CFD package used for the current simulations) are explained in Chapter 4 and tested on benchmarks in Chapter 5. The results of the main DDES simulations and the comparison with the experimental data collected in this PhD as reference are presented in Chapter 7. In Chapter 8, the effects of various landing-gear components on the flow past the wheels are evaluated.

The conclusions with the most relevant findings of the thesis and the future works are detailed in Chapter 9.

Chapter 2

Literature Review

2.1 Landing gear

2.1.1 Background on landing-gear noise

Unsteady flow on landing gear is mainly studied for aeroacoustics, because the major airframe noise sources for modern commercial aircraft is the landing gear, followed by slotted flaps, side edges and tracks of flaps/slats, spoilers and components-interaction noise sources [19]. The landing-gear noise is more relevant for wide-body aircraft than for single-aisle or regional aircraft, where the high-lift devices noise is as important as the landing-gear noise. Thus, noise reduction is the most common reason why the flow past landing gear is studied, under the pressure of the certification requirements for aircraft noise control.

Airframes became an important source of noise in the early 1970s, when the old noisy engines were replaced by the new quieter high-bypass ratio turbofans. The problem was more and more evident with the increasing bypass ratios of the aircraft engines during the following decades. Since then, the effort in noise abatement was not constant, mainly because of two fuel crises in the 1980s. The current requirement enforced by the European Aviation Safety Agency (EASA) [20] is based on the ICAO Annex 16 [31].

From early studies on airframe noise, a large amount of data was acquired with flyover tests of different aircraft models. It is possible to find a series of charts and formulas that can be used for a first estimation of the noise (e.g., Fink [23]). At the same time, Heller and Dobrzynski [28] proposed aeroacoustics experiments on jet or landing-gear models. Some of these experiments led to noise reduction systems that are still used nowadays, for example the porous edge extensions in the work by Bohn [9] for trailing edge noise reduction. Similar technologies are still the object of studies by researchers, for instance in the work by Khorrami et al. [36] on the evaluation of concepts for landing gear noise reduction. Nowadays, researchers use large aeroacoustics wind tunnels with microphone arrays and PIV. It is also possible to use computational fluid dynamics (CFD) and computational aeroacoustics (CAA) to simulate real-life conditions or experimental conditions [19].

Various studies on aircraft landing gear can be found in the literature, with different degrees of complexity (Figure 2.1): the simplified landing gear [40, 27], the rudimentary landing gear [90, 82, 91, 93], the Boeing 777 main landing gear [30], the Gulfstream G550 nose landing gear [95, 89], and the Airbus LAGOON (LAnding Gear nOise database for CAA validatiON) nose landing gear [46, 16]. The most relevant publications are described in the following two sections (Section 2.1.2 and Section 2.1.3), respectively subdivided in experiments and simulations on landing gear.

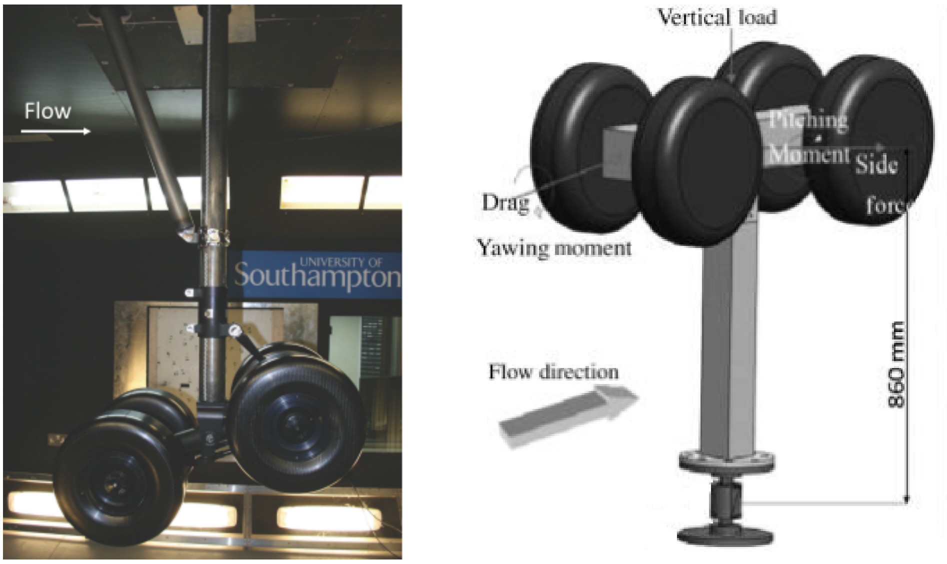

(a) Realistic model [83]

(b) Rudimentary landing gear [91]

Figure 2.1: Examples of four-wheel landing-gear models, different degrees of complexity.

2.1.2 Experiments on landing gear

In this section, the most relevant experiments for the current work are described. Other experiments are briefly listed in the previous Section 2.1.1.

The first simplified landing gear was experimentally tested by Lazos [40], who provided experimental data of the mean flow around a four-wheel landing gear by means of PIV in a streamwise plane surrounding the wheels. The flow appears asymmetric because of the strut on the wing side. In the part between the two in-line wheels two different mean flow states were found, one with a late separation and one with a massive separation. The change between the two states was approximately every 6 s or less for 74% of the occurrences. In addition, an unstable vortex was found in the flow between wheels: the vortex position changes in time at low frequency from the back of the front wheel to the rear wheel. The experiment *highlighted* the difficulties of predicting the flow on these geometries that are presumably sensitive to small variation of free-stream conditions, Reynolds number and surface roughness. This represents a major issue when comparing simulations with experimental results.

In order to reduce the Reynolds number dependency, a new four-wheel rudimentary landing gear was studied experimentally by Venkatakrishnan et al. [91] (also in [90]). The cross-section of the axles was rectangular to make the flow separation independent of the Reynolds number. The spacing between the front and the rear axles was equal to 1.165 wheel diameters. Since the blockage was approximately 9%, the surface pressures were monitored on the wind-tunnel top, bottom and side walls. Steady pressure data acquired on the wheel surface showed that the attachment lines were not located on the wheels centre-line because of the presence of the axles. The truck and the strut gave 43% of the total drag. There was also a significant asymmetry of the flow features between the ground-side and the wing-side halves of the model.

Stalnov et al. [83] experimentally studied a simplified $^1/_4$-scale model of a main landing gear. In addition to aeroacoustics measurements, mean aerodynamic loads were measured sequentially on sub-assemblies of the landing gear: from the main strut only to the full assembly (main strut, bogie and four wheels), mounting the components one at a time. In this way it was possible to analyse the effect on the various components on the landing gear, but it was not possible to exclude interactions between wheels and struts. The model was studied for horizontal (inclination angle $\alpha = 0\,\mathrm{deg}$), toe-up ($\alpha = 40\,\mathrm{deg}$) and toe-down ($\alpha = -20\,\mathrm{deg}$) bogie.

The LAGOON two-wheel landing gear study by Manoha et al. [46] is an example of an extensive database for CFD validation. Pressures (mean and RMS), PIV data, Laser Doppler Velocimetry (LDV) data, and hot-wire data were measured. Also other experiments on two-wheel landing gear (side by side) are present in the literature, but they are not particularly relevant for this thesis, which is mainly focused on four-wheel main landing gear.

2.1.3 Simulations on landing gear

In this section, some of the most relevant simulations on aircraft landing gear are detailed. The simulations that are validated against experiments are here discussed with reference to the experiments described in the previous Section 2.1.2. A few more cases are listed in Section 2.1.1.

An example of the use of RANS on landing gear was described by Li et al. [41], where the flow past a bogie was simulated by means of URANS. They found a strong influence of the diagonal struts and the door on the flow field, and the flow was asymmetric due to the asymmetric geometry. In spite of the large number of computational data, no direct comparison with experiments was considered for validation, except for the experiments by Lazos [40] on a different geometry.

There are also cases in which researchers find RANS more effective than LES. For instance in the work by Imamura et al. [32] the LES results for the mean pressure coefficient on their two-wheel landing gear were less accurate than RANS with respect to the experimental results. Presumably, the grid resolution in the LES case was not fine enough, thus the authors of the work suggested the use of hybrid LES/RANS to increase the accuracy without having to refine the mesh.

One of the first examples of simulations with hybrid models on a full landing gear is by Hedges et al. [27], where DES were employed on structured grids. The geometry was the Lazos' [40] simplified four-wheels landing-gear model. The simulations were performed on a 2.5-million-cells grid, which is shown in Figure 2.2, with the S-A DES. In spite of an underestimation of the mean drag coefficients on the wheels between 15% and 35% with respect to the experiments, the pressure contours on the wheels were closer to experiments than URANS. DES simulations show a higher level of unsteadiness than URANS: in the DES simulation the resolved turbulent kinetic energy was approximately doubled compared to the URANS simulation.

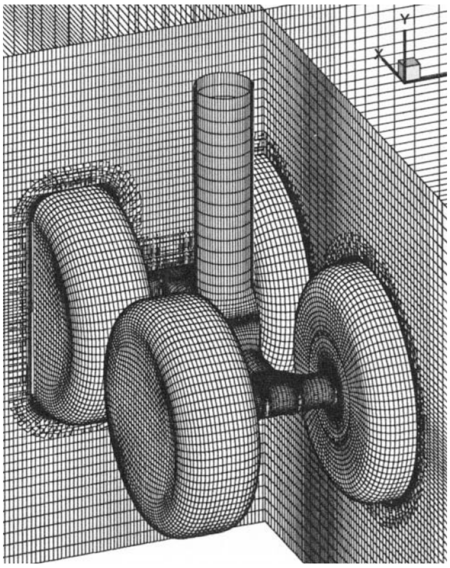

Figure 2.2: Grid used in Hedges et al. [27].

Soulinez et al. [72] performed landing-gear simulations with a compressible solver including a sub-grid scale turbulence model on unstructured grids. In order to predict the aeroacoustic far-field the Ffowcs-Williams Hawkings (FW-H) equations were integrated with the source terms on a permeable surface enclosing the landing gear. Recently Dahan et al. [15] used both RANS and DES to study the flow past a nose landing gear. The RANS captured most of the mean flow features but DES had to be used for the unsteady quantities, such as unsteady surface pressures. Despite the fact that steady

RANS provided information of the mean flow features with the coarsest grid they used (9.5 million mainly-hexahedral elements), there were issues with the grid convergence, probably because RANS was not capable of modelling a massively separated flow. The final DES simulations was performed on a finer mesh (22 million mainly-hexahedral elements) and an integral solution of FW-H equation was then sought to obtain far-field sound directivity.

Xiao et al. [93] performed DDES and IDDES (definitions in Section 2.3) simulations on the rudimentary landing gear by Venkatakrishnan et al. [91]. The work contained a sensitivity analysis on various grids, which did not show significant effects on the mean quantities, but influenced the unsteady quantities. Various flow features were thoroughly described for both DDES and IDDES, highlighting only a few differences between the two models. Both models were found to generate accurate results in comparison with the experimental data. The flow on the inner sides of the wheels was found to be significantly affected by the strut. There were strong interactions between the vortices and the edges of the strut, as well as between the in-line wheels, which increased the pressure fluctuations on the surface. Additional examples of simulations on the rudimentary landing gear is the work by Spalart and Mejia [82] and Larusson [39].

In addition to the cited papers, the current work also benefits from studies within the Airbus Noise Technology Centre (ANTC), at the University of Southampton. For instance, the flow past a typical element constituting landing gear can be found in the work by Peers [56] on the CADWIE (Control of Approach Drag Without Impact on the Environment) wheel. Another source of information is the nose landing gear examined by Peers [57]. Additional works on generic wheels are detailed in Section 2.2.2.

A completely different approach is based on LBM that employs a collision model such as Bhatnagar-Gross-Krook (BGK) with turbulence modelling activated. By means of this technique, with a RNG k-ε turbulence model, Keating et al. [33] obtained interesting results on a Gulfstream landing gear. The software used was PowerFLOW® (Exa [21]), which implements the LBM that discretise the equations on structured-blocks grids without boundary layer meshes.

A comparison for the same geometry between a traditional Navier-Stokes approach (with DES) and the collision model LBM was offered by the two conference papers respectively by Khorrami and Mineck [34] and Khorrami et al. [35]. The DES was performed using the code FUN3D with unstructured grids up to 151 million elements (mainly tetrahedrons), but with semi-structured boundary layer mesh to guarantee y^+ around unity for mesh efficiency. The Lattice-Boltzmann method was tested using PowerFLOW® with grids up to 2.6 billion hexahedral voxels (17 times larger than the DES mesh) and no boundary layer mesh. For this reason the surface size had to be refined up to approximately 0.1 mm, increasing the element count and resulting in a maximum y^+ around 150. A wall-function valid for favourable and adverse pressure gradient was used to correct the outer boundary-layer variables. Comparing the two works, the DES [34] is more complete and efficient compared to the LBM [35]. The semi-structured boundary layer is fundamental in providing low y^+ values at a low cost and the LBM mesh typically does not include this feature. Consequently, the simulation time-step had to be smaller in the LBM (respectively, 1.5×10^{-7} s against 2.5×10^{-6} s).

Another recent numerical work on two-wheel landing gear is the Zonal DES (ZDES) simulation on the LAGOON geometry [46] by de la Puente et al. [16] and the DES in combination with FW-H equations by Liu et al. [42] on the same geometry.

2.2 Rudimentary components

In contrast to the experiments and simulations described above, in which complex assemblies are considered, there are a number of studies on rudimentary geometries, representing isolated parts of landing gear. These studies are generally meant to provide a better understanding of the flow features.

2.2.1 Elementary three-dimensional geometries

The most basic example of a rudimentary component is the infinite circular cylinder. The geometry with non-fixed separation highlights the importance of the identification of the regime. In fact, Zdravkovich [96] included a large variety of experiments showing significantly different kinds of flow performed in different regimes. The regimes can be classified as follows, with increasing Reynolds number (refer to Figure 2.3): laminar (L), transition in wake (TrW), transition in shear layers (TrSL), transition in boundary layers (TrBL), and fully turbulent (T).

From the observation of Figure 2.3, it can be concluded that the transition location is the main factor in the determination of the flow regime. In a disturbance-free flow, three main regimes (TrW, TrSL and TrBL) can be identified based on the different position of the transition. From one regime to another, the force coefficients may change by one order of magnitude or more. Some of them show peculiar behaviours like a non-zero mean lift coefficient C_L due to the different transition position on the two sides of the cylinder. Conditions of asymmetric flow were also observed for other basic bluff bodies. For example, Sawanda and Suda [63] used a magnetic suspension system to support a sphere that showed non-zero mean lateral force coefficient in the transitional regime (up to Reynolds numbers higher than 4×10^5).

When the number of cylinders increases from one to two in interaction, the flow regimes become more complex. As reported in the review by Sumner [84], the flow past two circular cylinders is dependent both on Reynolds number and L/D ratio (the ratio

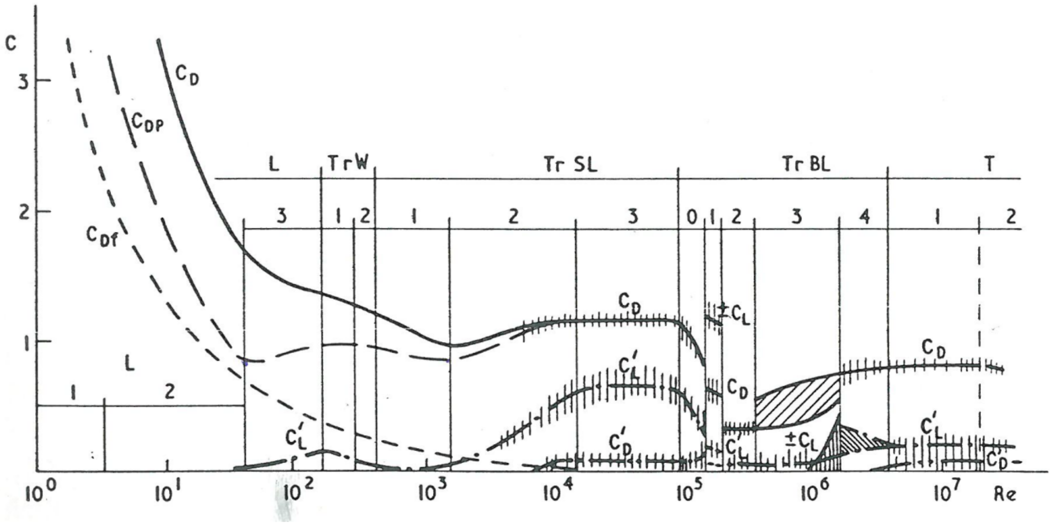

Figure 2.3: Force coefficients for a cylinder in disturbance-free flow (from Zdravkovich [96]).

between the inter-axis distance L and the cylinder diameter D). There are three types of interference behaviours (refer to Figure 2.4): extended body regime (approximately $1 < L/D < 2$), reattachment regime (approximately $2 < L/D < 5$) and co-shedding regime (approximately $L/D > 5$). Due to the Reynolds dependency, the L/D values given here are imprecise. In addition, the reattachment regime can be subdivided into two categories: in the range $2 < L/D < 3$, the reattachment happens mostly on the rear surface of the downstream cylinder, whilst in the range $3 < L/D < 5$, it occurs mainly on the front surface of the downstream cylinder. This leads to differences in the shedding Strouhal number and in the wake structures.

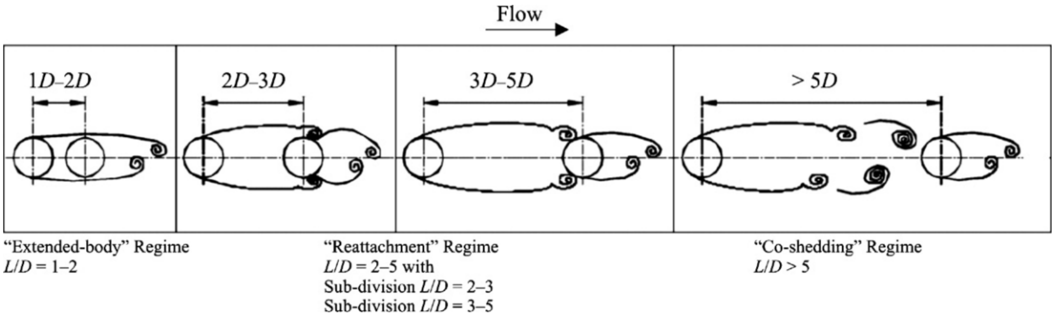

Figure 2.4: Qualitative classification of the regimes for tandem cylinders (from Zhou and Yiu [99]).

Khorrami et al. [37] provided experimental data on tandem cylinders, that were used by Xiao and Luo [94] to assess their IDDES, the latest version of DES by Shur et al. [68]. The results of their simulations were in good agreement with the experiments, in spite of some issues with the asymmetric flow. The issues were partly solved considering the effect of the transition in the boundary layer. In addition, other examples of numerical simulations on tandem cylinders that can be used as a benchmark can be found in the summary by Lockard [43].

2.2.2 Wheel-like geometries

Zdravkovich et al. [97] experimentally studied the flow past small aspect ratio cylinders (*coin-like*) cylinders with two free ends in the critical regime $2 \times 10^5 < Re < 6 \times 10^5$ (Re based on the diameter). Even studying rudimentary geometries simpler than wheels, the work still proves to be a valid source of information concerning the flow features. The cylinders are supported laterally from one of the flat sides. Also in this case the authors described the flow features around the coin-like cylinder, shown here in Figure 2.5. As in the previously mentioned papers, the wake is dominated by a vortex system that is clearly formed by four vortex filaments (opposite pairs) detaching on the rear part from each of the four areas located on the sharp edges (vortex filaments in dash-dot line). Other flow features that can be found on wheels are the separation bubbles (dashed line) on the flat sides after the front sharp edge where the adverse pressure gradient can be expected. The flow features are similar to those observed by Pattenden et al. [55] on a surface-mounted cylinder, with only one free end. Figure 2.6 shows the tip vortices, the recirculation area on the top face and the the separation line on the cylindrical surface.

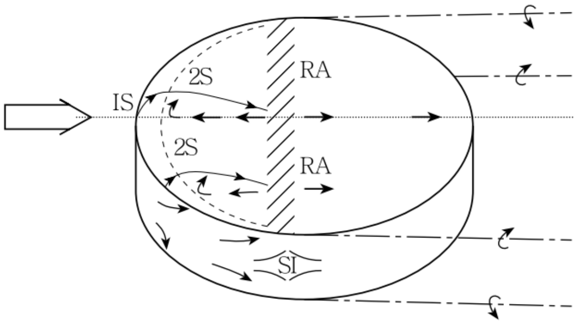

Figure 2.5: Sketch of flow features past coin-like gemetries (from Zdravkovich et al. [97]), where: IS - primary separation; 2S - secondary separation; SI - separation islet; RA - reattachment.

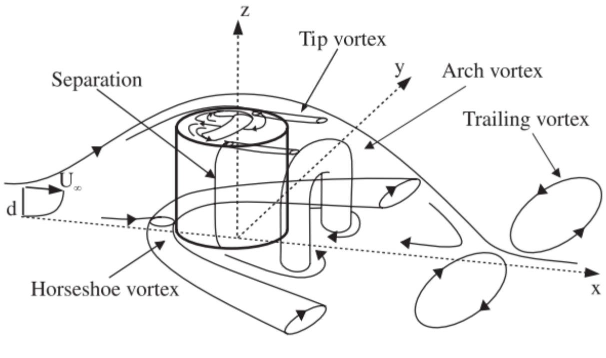

Figure 2.6: Flow features past a truncated cylinder (from Pattenden et al. [55])

The same types of features had been noticed on more realistic wheel shapes too. McManus and Zhang [47] performed simulations on the flow past an isolated wheel in contact with the ground, with both fixed and moving ground at the Reynolds number of 5.3×10^6. Among various observations, the two different separation typologies for the stationary and the rotating wheel appear of great interest. When the wheel is stationary on the ground, two opposite vortexes form on the top wheel shoulders while the flow in the middle part stays attached to the wheel for longer distances. On the contrary, when the wheel is rotating, the separated flow on the top part of the wheel form an arch vortex layer. Later, Zhang et al. [98] experimentally studied the flow past the 33%-scale CADWIE isolated wheel with two different hubs. It was found that the shape of the hubs did not have any significant effect on the flow.

The flow features reported by McManus and Zhang [47] are similar to those already observed for the simplified car body by Ahmed and Ramm [3]. For Ahmed's bodies, the rolled-up vortexes (similar to the vortices past the stationary wheel on the ground) are observed for the slanted rear surface in the 10–30 deg angle range. In detail, the 30 deg angle is the critical angle because of the bistable flow that can be associated with two different drag coefficients for the same angle. It is either possible to have two dominant vortices in the wake (associated with the higher drag coefficient $C_D = 0.38$) or a separated region (lower drag coefficient $C_D = 0.26$). As observed in Conan et al. [13], the bistable flow also depends on the Reynolds number at the critical angle: low-drag configurations predominantly occur at low Reynolds number. No previous publications on wheels in tandem configuration was found in the literature.

2.3 Turbulence simulation and modelling for industrial applications

In the literature, various simulations of high-Reynolds-number flows with massive separation regions can be found, but the focus of this section is to analyse the techniques related to turbulent flows of interest for industrial applications, where the aim is to produce reliable results at a reasonable computational cost. Here a brief description of the main techniques for turbulence simulation and modelling for industrial applications is presented.

2.3.1 RANS equations

The most common method to predict turbulent flows for practical applications solves the RANS equations. The equations for conservation of mass and momentum for incompressible flows are:

$$\frac{\partial u_i}{\partial x_i} = 0 \tag{2.1}$$

$$\rho\frac{\partial u_i}{\partial t}+\rho u_j\frac{\partial u_i}{\partial x_j}=-\frac{\partial p}{\partial x_i}+\frac{\partial}{\partial x_j}(2\mu s_{ij}) \tag{2.2}$$

where u_i $(i = 1, 2, 3)$ is the velocity, ρ the density, p the pressure, μ is the dynamic viscosity and s_{ij} is the strain-rate tensor, defined as follows:

$$s_{ij}=\frac{1}{2}\left(\frac{\partial u_i}{\partial x_j}+\frac{\partial u_j}{\partial x_i}\right) \tag{2.3}$$

The convective term can be rewritten in conservation form to simplify the time-averaging process,

$$\rho\frac{\partial u_i}{\partial t}+\rho\frac{\partial}{\partial x_j}(u_j u_i)=-\frac{\partial p}{\partial x_i}+\frac{\partial}{\partial x_j}(2\mu s_{ij}) \tag{2.4}$$

After the decomposition of every variable as a sum of a mean and its perturbation, and the application of the time-averaging process to Equation 2.1 and Equation 2.4, the *Reynolds-averaged equations* of motion in conservation form are:

$$\frac{\partial U_i}{\partial x_i}=0 \tag{2.5}$$

$$\rho\frac{\partial U_i}{\partial t}+\rho\frac{\partial}{\partial x_j}(U_j U_i)=-\frac{\partial P}{\partial x_i}+\frac{\partial}{\partial x_j}(2\mu S_{ij}-\rho\overline{u'_j u'_i}) \tag{2.6}$$

The averaging process introduces a new unknown, the Reynolds-stress tensor $\tau^t_{ij} = -\rho\overline{u'_j u'_i}$, which is a symmetric tensor with six independent components. Since during the averaging process no additional equation came out, it is necessary to find a *closure* for the system of ten unknowns in four equations. An additional strain tensor like the Reynolds-stress tensor is necessary in order to account for the macroscopic momentum transport due to the turbulence, in the same way the strain-rate tensor does for the microscopic (i.e., molecular) momentum transport.

Various models exist for this closure problem. The simplest models are the algebraic models, then there are models with only one ordinary differential equation added (1/2 equation models) and with one or more partial differential equations added (one equation, two equations, etc.). These models rely on the turbulent-viscosity hypothesis or Bousinnesq eddy-viscosity approximation:

$$\tau^t_{ij}+\frac{2}{3}\rho k\delta_{ij}=2\rho\nu_t\overline{S}_{ij} \tag{2.7}$$

which assumes a direct proportionality between the deviatoric Reynolds stress $(\tau^t_{ij} + \frac{2}{3}\rho k\delta_{ij})$ and the mean rate of strain $\overline{S}_{ij}$. The proportionality factor is the *turbulent viscosity* ν_t, a positive scalar. The assumption is given by the analogy with the relation between stress and rate of strain for a Newtonian fluid. The *effective viscosity* ν_{eff} is given by $\nu_{\text{eff}} = \nu+\nu_t$. Both one-equation and two-equation models retain the Bousinnesq eddy-viscosity approximation, but show a remarkable difference: early one-equation models are incomplete as they relate the turbulent length scale to some typical flow dimension, whilst later one-equation (e.g., Spalart and Allmaras [79], Baldwin and Barth [6]) and two-equation models are complete. In fact, the latter include in their equations all the information needed to estimate the turbulence scales, thus these models can be considered complete. A totally different branch of models is based on the Reynolds-stress tensor equation, but these models are not discussed in the thesis.

For all the RANS models, the governing equations are the result of time-averaging, thus the Reynolds-stress tensor τ^t_{ij} has the task of representing the effects of the turbulent fluctuations on the mean flow. This feature becomes a problem when the flows are massively separated at high Reynolds number and the unsteadiness in the wake affects the pressure on the body surface. In the RANS simulations all the turbulence is modelled, which usually gives a strong dependency of the results on the selected RANS model (from Wilcox [92]).

2.3.2 LES equations

To also consider strong unsteadiness of the flow, one can choose a model different from RANS, such as LES. Only the small turbulent scales are modelled, while the large eddies are resolved. To obtain the equations for this model, the velocity is decomposed into the sum of a spatially-filtered component $\overline{u}_i(\mathbf{x}, t)$ and a residual $u'_i(\mathbf{x}, t)$. In the filtered component (different from the averaged component of the RANS) there are the resolved large eddies, while the residual part, also called subgrid scale (SGS), is modelled.

The Navier-Stokes given by Equation 2.1 and Equation 2.4 are filtered with the following integration over the full domain,

$$\overline{u}_i(\mathbf{x}, t) = \int G(\mathbf{r}, \mathbf{x})\, u_i(\mathbf{x}, t)\, \mathrm{d}\mathbf{r} \tag{2.8}$$

where the filter $G(\mathbf{r}, \mathbf{x})$ satisfies the normalisation condition

$$\int G(\mathbf{r}, \mathbf{x})\, \mathrm{d}\mathbf{r} = 1 \tag{2.9}$$

but the filter could be homogeneous, i.e. independent of $\mathbf{x}$.

The residual field is defined as the difference between the velocity field and the filtered field:

$$u'_i(\mathbf{x}, t) = u_i(\mathbf{x}, t) - \overline{u}_i(\mathbf{x}, t). \tag{2.10}$$

The result of the application of the filtering to the Navier-Stokes equations is the *residual-stress tensor*, or SGS stress tensor, that must be modelled, for example by means of the Smagorinski model (Wilcox [92]). Within this model, the eddy-viscosity model links the residual stress to the filtered rate of strain:

$$\tau_{ij}^{t} = -2\nu_{\mathrm{SGS}}\overline{S}_{ij} \tag{2.11}$$

The SGS eddy viscosity ν_{SGS} is modelled according to the mixing-length hypothesis:

$$\nu_{\mathrm{SGS}} = \ell_S^2\overline{\mathcal{S}} = (C_S\Delta)^2\,\overline{\mathcal{S}} \tag{2.12}$$

where $\overline{\mathcal{S}} = (2\overline{S}_{ij}\overline{S}_{ij})^{1/2}$ is the characteristic filtered rate of strain, ℓ_S is the Smagorinsky length scale, which is proportional to the filter width Δ by means of the Smagorinsky coefficient C_S. With the Smagorinsky model, the transfer of energy is always from the resolved scales to the residual smaller scales in turbulence.

LES simulations are less sensitive to model errors because they mainly model only the SGS eddies that are isotropic and easier to model. But the main problem of this approach is the high number of elements required to resolve the flow in the boundary layers, where the characteristic length scales are typically small and need mainly homogeneous grid refinements close to the walls. In LES it is not sufficient to refine in the wall-normal direction only: it is necessary to have grids with elements small enough to resolve the small scales of turbulence close to the wall. Further information on turbulence modelling can be found in Wilcox [92] and Pope [59].

2.3.3 RANS/LES Hybrids

On the one hand RANS simulations generally have low computational cost, which is a major advantage for industrial applications, but on the other hand they cannot effectively predict large separation regions. This problem can be solved using LES simulations, that solve at least the main energy-containing turbulent scales and model only the smallest scales. But the actual grid size of a LES problem at high Reynolds number is high, due to the high resolution required for the boundary layers. In fact, near the wall a fine resolution is needed in order to simulate the turbulent scales that are required for a LES.

In 1997 Spalart et al. [80] proposed a hybrid model that behaves like RANS in the attached boundary layer and switches to LES in the separated zones: DES was the name given to this new kind of simulations. It is explained that the need for this hybrid comes from the belief that LES and RANS alone were not capable of efficiently solving the flow past bluff bodies (as explained in Section 2.1.3).

It is possible to create hybrid LES/RANS starting from different turbulence models, but here the original version based on the S-A turbulence model is used. Like other turbulence models, it is based on the Boussinesq's approximation that correlates the Reynolds stress tensor τ_{ij}^{t} with the product of the mean strain-rate tensor $\overline{S}_{ij}$ and the eddy viscosity μ_t:

$$\tau_{ij}^t = 2\mu_t \overline{S}_{ij} - \frac{2}{3}\rho k \delta_{ij}. \tag{2.13}$$

In the previous equation, δ_{ij} is the Kronecker's delta and k is the turbulent kinetic energy. The same Equation 2.13 can be rewritten dividing by the density ρ and getting $\nu_t = \mu_t/\rho$, which is the variable commonly used for incompressible flows. To close the model the solution of the partial differential equation of the variable $\tilde{\nu}$ has to be found,

$$\frac{\partial \tilde{\nu}}{\partial t} + U_j \frac{\partial \tilde{\nu}}{\partial x_j} = c_{b1} \tilde{S} \tilde{\nu} - c_{w1} f_w \left(\frac{\tilde{\nu}}{d} \right)^2 + \frac{1}{\sigma} \left\{ \frac{\partial}{\partial x_k} \left[(\nu + \tilde{\nu}) \frac{\partial \tilde{\nu}}{\partial x_k} \right] + c_{b2} \frac{\partial \tilde{\nu}}{\partial x_k} \frac{\partial \tilde{\nu}}{\partial x_k} \right\} \tag{2.14}$$

where

$$\nu_t = \tilde{\nu} f_{v1} \tag{2.15}$$

and

$$\tilde{S} = \omega + \frac{\tilde{\nu}}{\kappa^2 d^2} f_{v2} \tag{2.16}$$

with $\omega = \sqrt{2\Omega_{ij}\Omega_{ij}}$. For further information on the model and exact definition of the coefficients, refer to Chapter 4 of this thesis and to Wilcox [92].

On the left-hand side of Equation 2.14 there are the time-derivative and the convective term of the quantity $\tilde{\nu}$. The right-hand side of the equation is formed by the production term, the destruction term and the diffusive terms. The main parameter of interest for our purposes is the distance d from the closest surface. As a consequence, in the RANS version of the model, the destruction term is inversely proportional to the squared distance from the wall. The modification from this model to the DES model is based on the consideration that, in local equilibrium, the production term $\sim \tilde{S}_\nu \tilde{\nu}$ in Equation 2.14 is balanced by the destruction term $\sim (\tilde{\nu}/d)^2$, giving the relation:

$$\tilde{\nu} \sim \tilde{S}_\nu d^2 \tag{2.17}$$

that is similar to the Smagorinki's SGS model for LES if d represents the characteristic length Δ. Thus, substituting d with a convenient definition $\tilde{d}$ that can force RANS or LES depending on the wall distance:

$$\tilde{d} = \min(d, C_{\mathrm{DES}}\Delta) \tag{2.18}$$

with $\Delta = \max(\Delta x, \Delta y, \Delta z)$, which means the maximum edge size if the grids are structured, and $C_{\mathrm{DES}} = 0.65$. Another common definition of Δ, especially for unstructured grids, is the cubic root of the cell volume.

Consequently, if $d \gg \Delta$, the region is modelled as LES using Equation 2.14 as SGS model. On the contrary, if $d \ll \Delta$ the equation gives the S-A RANS model in the boundary layers, getting good results with meshes that are highly refined only in the wall-normal direction, as usual for RANS boundary layer meshes. There is normally a grey area between these two zones that may generate uncertainties in the results. The only geometries that do not present grey areas are the cases with abrupt separation, for example when it is fixed by sharp edges in the geometry.

The first application of a DES technique can be found in Shur et al. [67], where the DES was applied to the flow past a thin airfoil. Some grid types did not provide acceptable results. Figure 2.7 shows three different kinds of grid in the boundary layer region. The illustration at the top shows a traditional DES grid, with the wall-parallel grid spacing longer than the boundary layer height: this is the ideal situation to have a RANS region sufficiently thick. On the contrary, in the bottom right picture, the typical LES grid is illustrated, as the grid spacing in all directions is shorter than the boundary layer thickness. In the bottom-left of the picture, a grid that potentially creates problem with DES is shown. This type of grid affects the limiter definition, but it is still not sufficiently refined to fully support LES in the boundary layer. In this ambiguous case, with a mesh sufficiently fine to disable RANS modelling but too coarse for LES simulation, the DES limiter reduces the eddy viscosity, thus the Reynolds stress (i.e., the modeled stress) is lower than it should be. This problem is referred to as *modeled-stress depletion* (MSD), as stated by Spalart et al. [81].

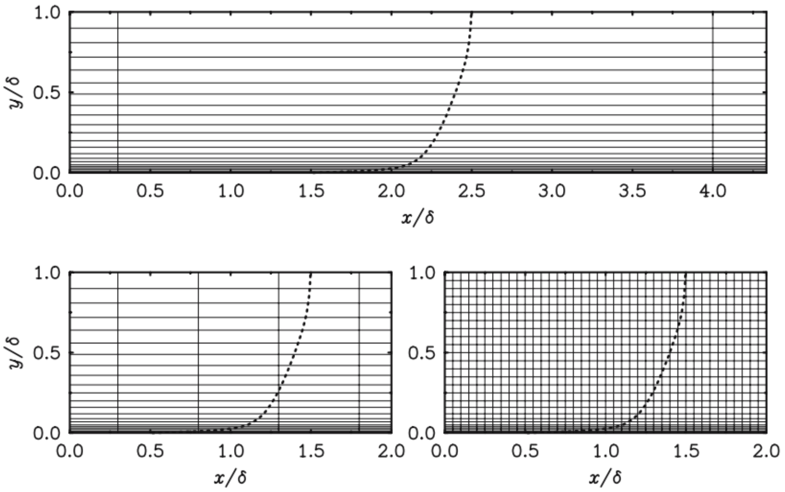

Figure 2.7: Boundary layer grid types: Type I natural DES (top), Type II ambiguous spacing (bottom left), Type III LES (bottom right), from Spalart et al. [81].

To avoid the MSD discussed above, a ZDES can be used as in the article by Deck [18], in which the characteristic grid size is set to an infinite value in the RANS regions. This approach is antithetical to the original idea of using exactly the same system of equations for both zones: with ZDES the flow is directly forced to behave according to one of the two models. Therefore, in spite of the apparent simplicity, this approach is potentially affected by errors: the user must decide where the flow is attached and where it is separated and, consequently, the resulting flow is dependent on the user decisions and experience. In addition, there are problems related to the continuity of the physical variables through the borders between RANS and LES regions.

In other previous papers the problem of grid-induced separation was discussed as a consequence of the MSD, for instance by Menter and Kuntz [48], where the MSD moved the separation forward in the DES on an airfoil. In contrast, RANS simulations do not suffer this problem. Thus, they proposed the *shielding*, valid for shear stress transport (SST) formulations: it acts as a switch that prevents the DES limiter from activating LES as long as the flow is still in a boundary layer, by means of the functions F_1 or F_2 of the SST two-equations RANS model. In the k-ω model, F_1 and F_2 are functions of the ratio between the internal length scale $\sqrt{k}/\omega$ and the distance from the wall y. For this reason, both F functions are equal to 1 in the boundary layer and then go quickly to 0.

The S-A DES model, on the contrary, does not have an internal length scale, but uses a slightly modified version r_d of the S-A RANS parameter r, which is the squared ratio between the model length scale and the wall distance:

$$r_d = \frac{\nu_t + \nu}{\sqrt{U_{i,j} U_{i,j}} \kappa^2 d^2} \tag{2.19}$$

with ν_t kinematic eddy viscosity, ν molecular viscosity, $U_{i,j}$ velocity gradients, κ von Kármán constant and d the distance from the closest wall. The subscript "d" means delayed. If the function r_d is used in the function f_d,

$$f_d = 1 - \tanh\left[(8r_d)^3\right] \tag{2.20}$$

the function is equal to 1 in the LES region (because $r_d \ll 1$) and 0 in the rest of the domain. After defining the f_d function, it is possible to modify the definition of $\tilde{d}$:

$$\tilde{d} = d - f_d \max\left(0, d - C_{DES}\Delta\right). \tag{2.21}$$

With this $\tilde{d}$, in spite of the grid size Δ much smaller then d, if the f_d function states that the flow is in a RANS region ($f_d = 0$), the length scale $\tilde{d}$ remains the same as the distance from the wall d. Otherwise, if $f_d = 1$ (in LES regions), the formula is again the original by Spalart et al. [80]:

$$\tilde{d} = \min\left(d, C_{DES}\Delta\right). \tag{2.22}$$

This improvement was proposed by Spalart et al. [81], and this new model is called *Delayed DES* (DDES). The DDES formula substantially improves the capability of the previous DES because the new $\tilde{d}$ depends not only on the grid but also on the eddy-viscosity field. This actually means that the length scale $\tilde{d}$ is time-dependent.

Breuer et al. [10] provided another confirmation of the high capability of LES and DES to capture the unsteady flow features on a flat plate at high incidence. DES provided higher unsteady content than LES simulations on the same grid. In addition, they suggested modifications of the base S-A DES model to reduce the eddy viscosity.

The latest progress in DES simulations is the *Improved Delayed DES* (IDDES) from the article by Shur et al. [68]. The aim of this new model is to resolve not only the MSD, but also the log-layer mismatch that is another major issue with DES simulations. In IDDES, the grid size Δ is defined as a function of the wall distance too. This modification makes Δ smaller near the wall with steep variations: this increases the resolved turbulent content. In addition, there are new empirical functions, which make the model behaviour more accurate and more complex.

Additionally, other techniques like Partially-Averaged Navier-Stokes (PANS) (e.g., Girimaji and Abdol-Hamid [24]) can reproduce the whole range of complexity from RANS to LES by changing the unresolved-to-total energy ratio. PANS require different computational effort depending the mentioned parameter: the smaller is the ratio, the higher is the computational effort and the accuracy.

2.3.4 Transition modelling

The role of flow transition is fundamental when predicting the flow past a bluff body, as it determines most of the flow features, even though some studies failed in selecting a laminar separation when needed, as stated by Spalart [78].

In the early DES tests on a cylinder, Travin et al. [87] predicted correctly both laminar separation and turbulent separation. Laminar separation was obtained specifying the turbulent variable $\tilde{\nu} = 0$ at the inflow boundary and $\tilde{\nu} \neq 0$ as an initial condition, so that the recirculation regions keep the turbulent viscosity and propagate it upstream to the separation region (trip-less approach by Shur et al. [69]). Turbulent separation was obtained using $\tilde{\nu} \neq 0$ at the inflow. The flow status (turbulent or laminar) can be monitored at the wall with the turbulent index i_t (e.g., from Spalart and Allmaras [79]), which is defined as:

$$i_t = \frac{1}{\kappa u_\tau} \frac{\partial \tilde{\nu}}{\partial n} \tag{2.23}$$

where κ is the Von Karman constant ($\kappa \approx 0.41$), u_τ is the friction velocity ($u_\tau \approx \sqrt{\nu\Omega}$ with Ω vorticity magnitude), and n is the wall-normal direction. If $i_t \approx 0$ the region is laminar, if $i_t \approx 1$ the region is turbulent. Similar applications can be found in Crivellini and D'Alessandro [14], where a modified S-A RANS was used in the trip-less approach to predict the flow with laminar separation bubbles over an airfoil.

More automatic methods can be developed since in theory a turbulence model with a transition model can be used as a skeleton model for a DES. Examples of results can be found in Sørensen [71], where a correlation-based transition model was employed together with DES to predict the cylinder drag crisis and the flow past a DU-96-W-351 airfoil.

It is difficult to find information about the boundary layer treatment in CFD simulations on the flow past landing gear, even when dealing with subcritical Reynolds numbers. Some attempts at acting on the boundary-layer separation on wheels were made by de la Puente et al. [16], who introduced numerical errors with an abrupt change of grid size on the wheel tyre at the 90 deg azimuthal angle from the point of highest stagnation, to fix the boundary-layer separation. To this purpose, different parameters in the boundary layer mesh were set up on the fore and the after body of the wheel (cells 5 times higher in the aft than in the fore): the jump in the boundary layer mesh forced the flow detachment.

2.4 Dynamic loads measurement

The measurement of the dynamic loads on a wind-tunnel model is here intended to obtain frequency spectra and a reliable quantification of the standard deviation of the loads around the mean values.

2.4.1 Balances

The most common approaches use a balance, which can be either a strain-gauge based sensor or a piezoelectric sensor (from Tropea et al. [88]). The strain-gauge based balances are the most used devices: the strain on the structure is measured and, after calibration, it is possible to estimate the forces. The piezoelectric sensors directly provide the forces, but they have poor low-frequency response and higher complexity.

In the literature, attempts with direct application of strain gauges to some relevant point of the models are present. For example, Schuster and Byrd [65] applied strain gauges but only the data from the pressure sensors were considered reliable: the structural dynamic modes affected the response of the strain gauges.

More common is the use of strain-gauge balances. For example, unsteady data for wind loads on wind-turbine models were obtained with a strain-gauge based balance by Hu et al. [29]. The balance was able to capture the unsteady loads at the blade rotation speed (17 Hz) and at the higher harmonic frequencies up to three times the rotation speed (i.e., 51 Hz). They completed the load data set with a characterisation of the wake by means of PIV.

For short-duration force measurements (e.g., Robinson and Hannemann [61]), models and special calibration rigs had to be prepared. This case is more complex than the previous ones because the model is designed on purpose for the dynamic calibration. A procedure used in dynamic analysis of vehicles suspensions consists in correcting the data from the force sensor with the inertial forces, with the method called *balance of forces*, described for example in the handbook by Cebon [12].

2.4.2 Surface-stress measurements

A totally different approach would be the use of pressure sensitive paint to obtain the loads after integration of the pressure, as reported in the work by De Lucca et al. [17]. The method proved to be effective with simple shapes, but more complex shapes can show a number of technical difficulties, such as the impossibility to have a uniform illumination on the model and the number of cameras needed to acquire pictures of some surfaces of the model.

Piezoelectric sensors can provide high frequency local information for both surface shear stress and surface pressure. For example, piezoelectric sensors were used for detecting wall transition and monitoring wall turbulence on wings in Nitsche and Mirow [52]. Twin configurations of piezoelectric foils allow a separation of the shear stress and the pressure. In that paper, the piezoelectric sensors allowed the identification of the flow instabilities (Tollmien-Schlichting waves) in the boundary layer at the frequency of 118 Hz.

Baban et al. [5] acquired unsteady forces on a circular cylinder with a piezoelectric sensors, which have very low sensitivity at low frequencies. In fact, as explained in the article, the mean forces were calculated by integration of the surface pressures.

The use of pressure sensors that give reliable response over a range of frequencies is often also employed for turbomachinery. For example, Capece and Fleeter [11] used Kulite sensors to measure aerodynamic pressures up to 20 kHz in a stator vane of an axial compressor. From the pressures, aerodynamic forces can then be integrated.

2.4.3 Case-specific force measurements

Mangalam and Davis [45] used a specific method to estimate loads on the wings. The procedure is based on the derivation of the unsteady loads by means of a state-space model that needs the position of the separation and the stagnation points. The positions are obtained analysing the data from the hot-film layer applied on the whole surface of the model.

The forces can theoretically be estimated using the momentum equations, like the forces on a square cylinder in Kurtulus et al. [38] who used PIV to obtain the velocity fields needed. In fact, for two dimensional flows, a time-resolved PIV can provide enough information to estimate all the terms of the momentum equation in a control surface that includes the body of interest. The time-derivative of the velocity can be estimated using the flows in subsequent frames, whilst the pressure can be estimated with the Bernoulli equation out of the wake and with an integration of Navier-Stokes in the wake.

A totally different technique of acquiring forces (mean and unsteady) consists of a magnetic support. The model is magnetised and a control system provides stability to the magnetic field in a given operating condition. Sawanda and Suda [63] used a magnetic suspension system to support a sphere around the critical regime and to measure the forces. The sampling frequency was 245 Hz, the sphere diameter 150 mm and the maximum reported Reynolds number was above 4×10^5. The method allowed not only to quantify the unsteady forces, but also to test the flow past a bluff body without any interference from the support.

2.5 Proper Orthogonal Decomposition

Concerning the analysis of the flow features, Proper Orthogonal Decomposition (POD) has been used to extract the modes of the flow field, both in experiments and simulations. POD allows the identification of systematic dynamic flow structures in turbulent flows. Such a technique needs to be used because the turbulent flow in the wake is chaotic, random, and has strong influence on the surface pressure distribution, and therefore also on the loads. POD allows the identification of the POD modes and their classification by energy content [7]. After the extraction of the POD modes, the modes can also be used to reconstruct the flow and the accuracy of the reconstruction is related to the number of modes employed in the process and their relative energy content. The higher the energy content, the more relevant the modes are for the dynamics of the flow. Various techniques to extract POD modes exist, but this section is mainly focused on the *snapshot POD* by Sirovich [70], which does not require time-resolved PIV.

Meyer et al. [49] used the snapshot POD [70] to compare PIV and LES data on a jet in cross flow. In the experiments, the three velocity components were acquired with two one-Megapixel cameras (stereoscopic PIV), acquiring 1000 frames for each plane. The velocity vector maps contained 33×37 vectors. Similarly the POD was applied on 1000 frames extracted from the LES results. Comparing the results (Figure 2.8), the POD modes of experiments and simulations showed the same features, even though the energy content showed a difference as high as $3\% - 4\%$ (relative to the total energy of all the modes), depending on the case. In the POD modes it was clearly possible to observe the formation and the movement of the vortices past the jet in cross flow.

Bernero and Fiedler [8] applied the POD technique on the PIV fields of a jet in counterflow. In this case, only 400 frames were used for the POD analysis. In this paper, detailed information about the cumulative energy of the POD modes were included:

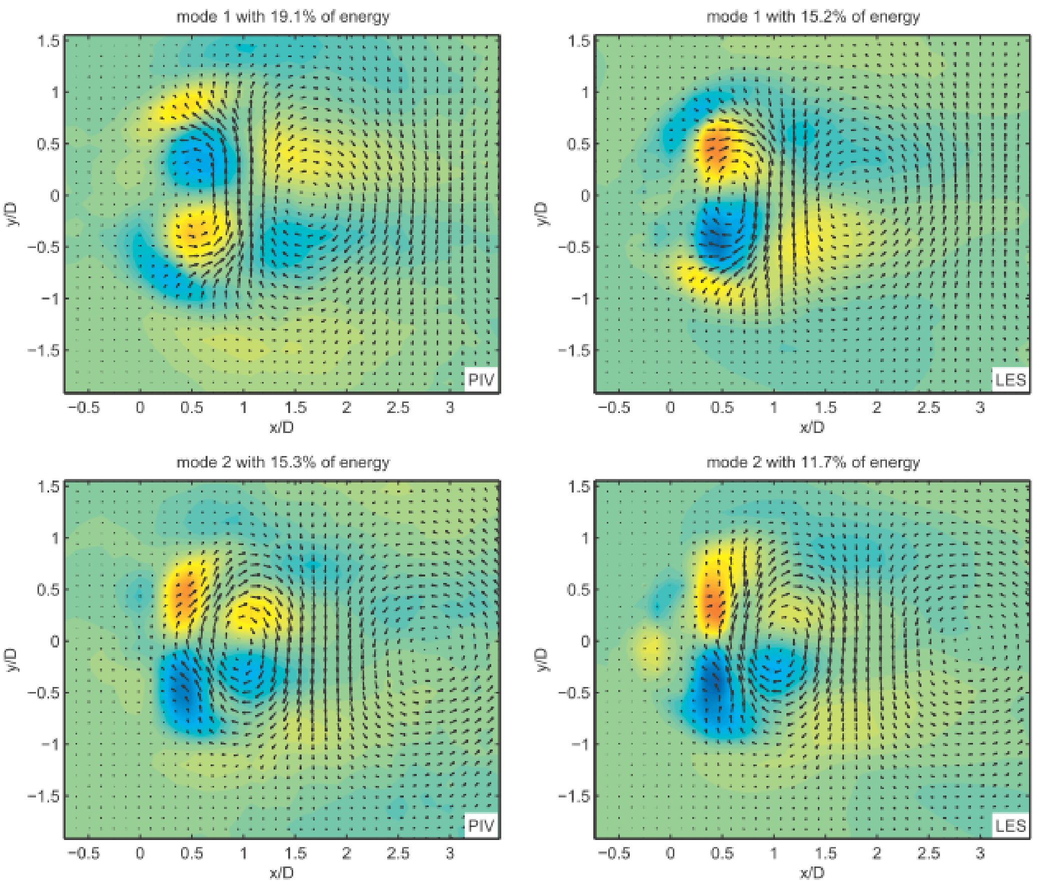
mode 1 with 19.1% of energy

mode 1 with 15.2% of energy

mode 2 with 15.3% of energy

mode 2 with 11.7% of energy

Figure 2.8: POD modes (first and second only) on crossflow jet from Meyer et al. [49]: PIV (left) and LES (right).

the first 10 modes contained about 60% of the total energy. The cases with low jet-to-counterflow velocity ratios were found to have higher cumulative energy content for the first 10 modes, proving that the presence of stable flow conditions reduced the disordered oscillations. The energy content in the first modes is still lower than in the flows with coherent vortical structures (e.g., cylinders). For each mode, frequency spectra were also provided, in order to quantify the various frequency contributions of each mode. This analysis was performed for the first 10 modes, i.e., those with the highest energy content.

Tirunagari et al. [85] applied POD on LES data of subsonic jets with three velocity components. The curves for the energy content in the modes are not given. Snapshot POD was also used by Rajaee et al. [60] to study the free-shear-flow coherent structures with hot-wire measurements for a total of 251 × 251 locations. In this case, a low-dimensional description of the flow was also provided, by projecting the Navier-Stokes equations on a basis set of principal eigenfunction modes. The simulations showed similar results as the experiment.

2.6 Oil-flow Visualisation

Surface oil-flow is used as well to help the identification of the flow structures on the body surfaces. A thorough description of the surface oil flow visualisation can be found in the paper by Lu [44]. As stated in the paper, oil-flow visualisation is mainly useful for initial indication about the flow and for qualitative information on the flow features. Normally, it is required to follow topological rules in order to understand the meaning of the patterns.

According to Lu [44], on two-dimensional flows, only two types of separation may occur: open separation, when the streamline emanating from the separation point (i.e., zero wall shear stress) does not reattach onto the surface, and closed separation, when the streamline reattaches in another point (reattachment point) on the surface because of a favourable pressure gradient. In case of three-dimensional flows, there is a larger variety of separation-reattachment features. Considering the flow depicted in Figure 2.9, with a transverse pressure gradient, the streamlines in the three-dimensional boundary layer show different curvature depending on their distance from the wall. In fact, the streamlines that are closer to the wall are more affected by the pressure gradient, having lower velocity.

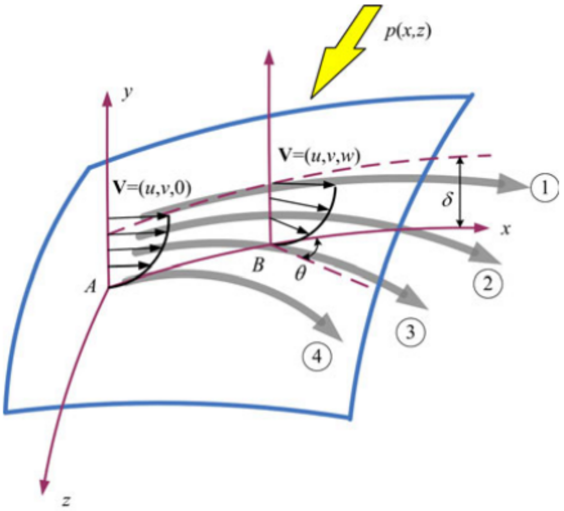

Figure 2.9: Streamlines in a three-dimensional boundary layer with cross flow, originated from a two-dimensional boundary layer (from Lu [44]).

In order to describe the flow features in three-dimensional boundary layers, Sears [66] defined the concept of *limiting streamlines* (or surface streamlines), which are given by the following direction with respect to the streamwise direction (x-axis):

$$\tan\Theta = \lim_{y\to 0}\frac{w}{u} \tag{2.24}$$

where u is the streamwise velocity component and w is the cross-flow component. For Newtonian fluids, limiting streamlines are coincident with *skin-friction lines* (i.e., lines such that each of their points is tangent to the local skin-friction vector). The limiting streamlines can only meet in the critical points. In the presence of cross flow, the limiting streamlines converge on the separation line, being the line from which the limiting streamlines diverge. According to Tobak and Peake [86], there are two types of critical points (in Figure 2.10): nodes and saddle points. In the nodes, the skin-friction lines converge either all inward (separation node) or all outward (attachment node). If all the skin-friction lines are tangential to the line BB, except one (line AA), they are called nodal points. If this is not the case, than the node is called focus. In the saddle points, only two skin friction lines (CC and DD) pass through the point, one inward and the other one outward. An example of the application of this technique on landing gear is shown in Xiao et al. [93]. Oil flow visualisation and numerical results are compared with the analysis of the surface flow features. The presence of critical points was found to be correlated with areas with higher pressure fluctuations.

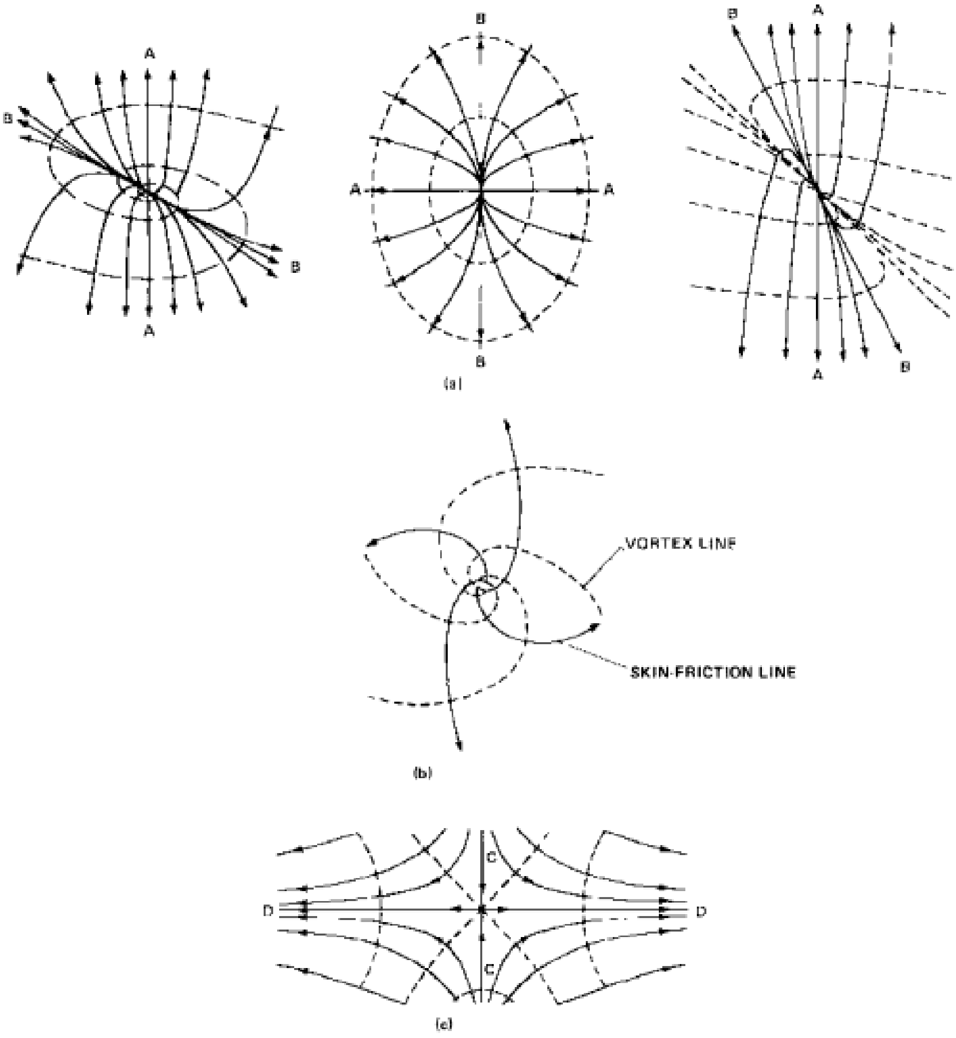

Figure 2.10: Critical points: (a) nodal points; (b) focus; and (c) saddle point (from Tobak and Peake [86])

2.7 Summary of the background research

In this chapter a thorough review of the previous works related to this thesis was given. From the analysis of the background research, a few major gaps emerged. No evidence exists for experiments and simulations of wheels in tandem configuration without the interference of axles and struts, which is the main reason for testing the new tandem-wheel model proposed in this thesis. In addition, in spite of examples of unsteady aerodynamic forces on simple geometries (often two-dimensional geometries), unsteady aerodynamic loads were never measured before on landing-gear components. Concerning the numerical techniques, the main flaw is the general trend toward larger and more complex simulations. The considerations on the flow features and the meshing process are often neglected. The mesh generation with automatic procedures could significantly improve the overall time-to-solution, as well as a deeper understanding of the flow features can significantly improve the accuracy of the predictions. In order to enhance the current understanding of the flow features, the new tandem-wheel configuration can be studied with the help of POD and oil-flow visualisation.

Chapter 3

Wind-Tunnel Model Design

The design of the wind-tunnel model is reported in this chapter, after a definition of the requirements. The design procedure is detailed from the concept definition to the modal analysis (for the definition of the frequency response) and a structural verification. At the end of the chapter, the test plan for the wind-tunnel experiment is detailed.

3.1 Requirements

In the literature two main branches of geometries have been analysed so far: full landing gear (Section 2.1) and rudimentary components (Section 2.2). And, as highlighted in the motivations given in Section 1.2, there is a gap left in the literature. Whilst there are works on full landing gear and on single wheels, wheels in tandem configurations have not yet been analysed in the literature. In addition, there is a general lack of unsteady aerodynamic load measurements on wind-tunnel models, as it has been clarified in Section 2.4. Thus, the experimental techniques and the numerical methods of this PhD project can be developed around a new geometry, *tandem wheels*, representing half of a four-wheel main landing gear, but without struts, doors, and any other sources of interaction.

A wind-tunnel model constituted of two wheels in tandem configuration was designed, manufactured and tested in the University of Southampton wind tunnel. The reference wind tunnel is the $7' \times 5'$ wind tunnel at the University of Southampton: it has a $2.1\,\mathrm{m} \times 1.5\,\mathrm{m}$ cross section and can operate at wind speeds up to 48m/s. For completeness, the model should include the possibility to test a single wheel (with the same shape). The experimental results have been used for better understanding of the flow features and for CFD validation.

A sketch of the concept model for the tandem-wheel case is illustrated in Figure 3.1, with the reference sizes (inter-axis distance L and angle of attack α). The model rig has to include structures to hold the wheels in the prescribed configurations, preferably with low level of interactions on the flow and enough mounting flexibility to allow several mounting configurations for the tandem wheels (at least three inter-axis distances and two angles of attack).

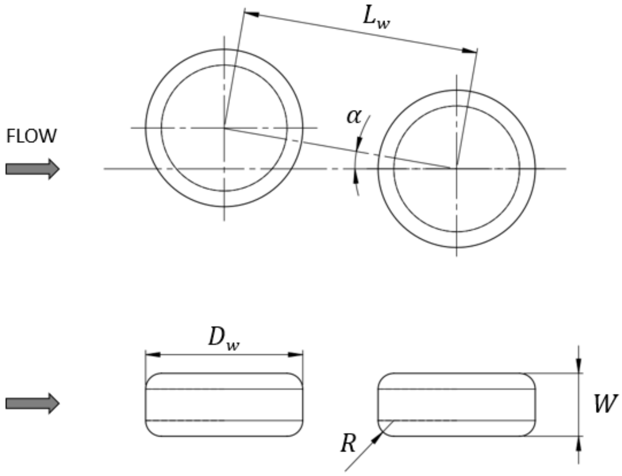

Figure 3.1: Tandem-wheel geometry with inter-axis distance L and angle of attack α.

The leading structural requirement for static loads are the wind-tunnel model stiffness and the force sensor stiffness. In design conditions ideally the model should not deform enough to affect the test more than the manufacturing tolerances, to prevent the introduction of new forms of error. At the same time, the requirements for the dynamic load is to design the model in such a way that the balance is in optimum conditions for dynamic loads measurement. This requirement is developed in more detail in the next sections.

3.2 Concept Design

At the first stage, a concept of the main parts and the assembly is outlined. Each of the two wheels is mounted on its own streamlined strut (i.e., a wing) and the struts are fixed on a plate aligned with the wind tunnel wall and fixed to the wind tunnel frame.

The early version of the model drawing is shown in Figure 3.2, with the three main parts of each wheel model:

- wheel: the object of the wind tunnel test;
- force sensor (or load sensor, or balance): the tool to measure the forces acting on the wheel;
- support: the streamlined strut that is needed to position the wheel inside the test section.

The wheel is sustained by the support to which it is linked by means of the force sensor that measures the aerodynamic forces acting on the wheel only. The model is a 12.5%-scale wheel from an Airbus A340 aircraft landing gear, which is not the final wheel shape sent to manufacturing. The support is a tapered wing with a NACA0024 profile and it hosts a cavity at the tip for the force sensor mounting. The reference sizes for the concept drawing of Figure 3.2 were: diameter $D_w = 181\,\mathrm{mm}$, wheel width $W = 81\,\mathrm{mm}$ and support length $b = 300\,\mathrm{mm}$. This is not the final version of the rig but only a concept design of the model to identify the main components.

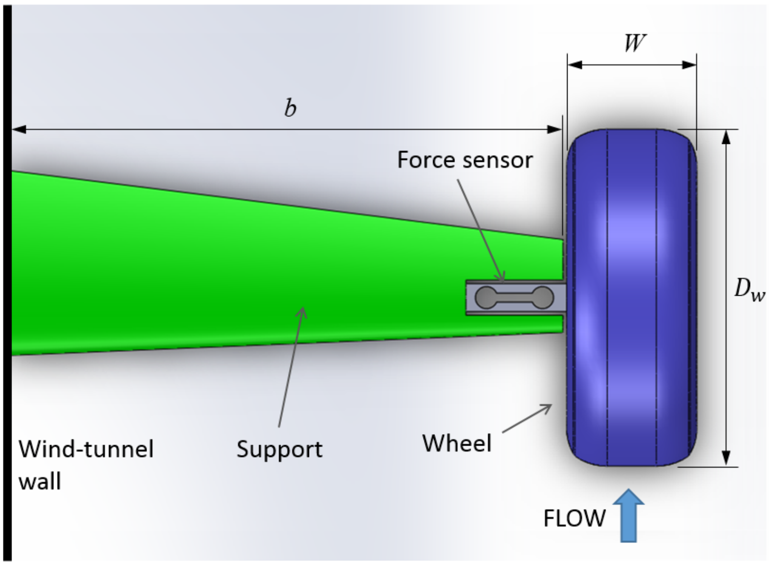

Figure 3.2: Concept drawing for the wind tunnel rig of a single wheel: the wheel shape is generic, the support is a tapered wing, and the load cell is mounted between the support and the wheel.

3.3 Preliminary Design

At this stage, the main options for each component are investigated with simple structural models (finite elements analysis, FEA) and small-scale experiments on components. The main aim is to understand feasibility and potentials of the main options for each components in addition to the cost.

3.3.1 Design options

Early structural simulations of the wheels and the supports were performed to understand the feasibility of the various parts. The early results are not shown here, but the main findings were the need for high-modulus materials to gain stiffness (both for static and dynamic load measurements) and the need for light materials on the wheel (for dynamics). Other aspects of the project, like time-scale and budget, encourage the use of rapid-prototyping techniques for the manufacturing. The support can either be machined completely in aluminium or prepared with composite materials (e.g., carbon fibre reinforced plastic to increase the stiffness). The wheel shape is unsuitable for machining, but with the 3D printing process in photo-polymer the wheel can be manufactured directly with most of the final features.

The most challenging part of the design at this stage is the definition of the force sensor. The main issue is to understand the effective capabilities of the strain-gauge balance to obtain dynamic loads. Before making any consideration on the options for the force sensor, the strain-gauge based force sensor in Figure 3.3 was tested for dynamic loads, to gain the understanding of the fundamental parameters for the decision of the force sensor.

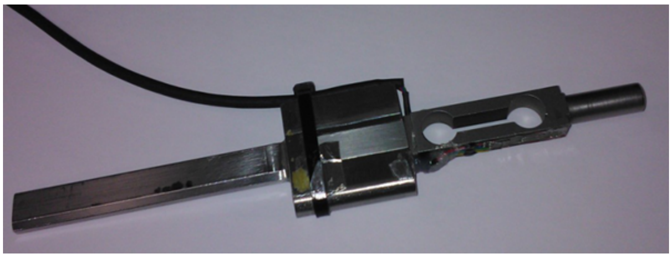

Figure 3.3: Picture of the wind-tunnel load gauge, previously used for mean drag measurments on racing cars.

3.3.2 Preliminary test on force sensor

An early test was performed on a standard one-axis force sensor, depicted in Figure 3.3 and previously adopted in the wind tunnel for mean-drag measurements on racing-car wheels. In fact, the tool is reliable in providing measurement of the mean load but it has never been tested previously for dynamic load measurements. The sensor measures the loads indirectly, by means of strain gauges that provide the strain of the material in particular areas.

The sensor was tested in the Dynamics Laboratory at the University of Southampton, using a LDS-V201 shaker to force the sensor with a known sinusoidal force $F(t)$, acquiring both loads from an external piezoelectric force sensor (PCB Model 208C01) and the strain from the wind-tunnel gauge. As illustrated in Figure 3.4, the sensor is clamped on the lab bench, and the shaker is linked to the free end of the gauge by an aluminium coupling. The cantilevered mass M in this test, given mainly by the coupling element, is 0.11 kg.

The test results show the first natural mode is at $f_0 = 180\,\mathrm{Hz}$ approximately. Assuming that the model behaves like the mass-spring-damper system described in the appendix

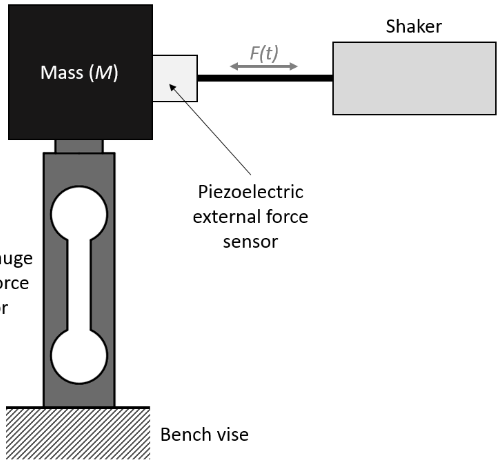

Figure 3.4: Sketch of the vibration test setup.

Section B.1, the formula to calculate the natural frequency ω_0 is:

$$\omega_0 = \sqrt{k/m} \tag{3.1}$$

with k the spring stiffness and m the mass. Thus, for the current setup, the stiffness k_f is:

$$k_f = m\omega_0^2 = m(2\pi f_0)^2 \tag{3.2}$$

that provides a stiffness approximately equal to $1.4 \times 10^5\,\mathrm{N/m}$. At this stage, a conservative estimation for the wheel model mass is $m_w = 0.4\,\mathrm{kg}$, which in terms of natural frequency f_{0w} means:

$$f_{0w} = \frac{\omega_{0w}}{2\pi} = \frac{1}{2\pi}\sqrt{k_f/m_w} \tag{3.3}$$

that is 94 Hz. The test performed at this stage did not include any component other than the force sensor, but in the final model rig the situation is more complex. The force sensor is only one of the elements that contribute to determine the structural dynamic behaviour of the wind-tunnel model, thus previously estimated frequency has to be set as an upper limit for the first natural frequency of the final model assembly. Thus, the reference stiffness $k_f = 1.4 \times 10^5\,\mathrm{N/m}$ just obtained from the preliminary test can be used either to improve the current design of the gauge to increase the natural frequency or to buy an already calibrated balance with higher stiffness.

3.3.3 Force sensor options

As shown in the previous section, the stiffness of the tested one-axis force sensor is considered too low for the wind-tunnel model, because the wind-tunnel model mass is higher than the mass previously tested. Thus, to adopt this type of force sensor, a new version of the current one-axis force sensor would need to be designed, manufactured and calibrated. Also, it would only measure the forces in one direction (the drag component). An alternative option would be to use a new strain-gauge balance, already calibrated and with capability to measure at least two components of the forces. A third option would be to use piezoelectric load sensors, which have the advantage of a direct measure of the loads (refer to Section 2.4) and which are normally more suitable for dynamic loads. But the low response of piezoelectric sensors at low frequencies (i.e., difficulties in mean loads measurement) makes this option less reliable.

In conclusion, since a one-axis force measurement was not considered enough and because of the additional time needed for the preparation of a new version, the second option was chosen: a new six-axis sensor (three forces and three moments) is employed in the current test. From the ATI catalogue, the *mini40* force sensor (shown in Figure 3.5) meets all the requirements and it is consequently introduced into the project. The stiffness of the mini40 force sensor is listed in Table 3.1 for the various components.

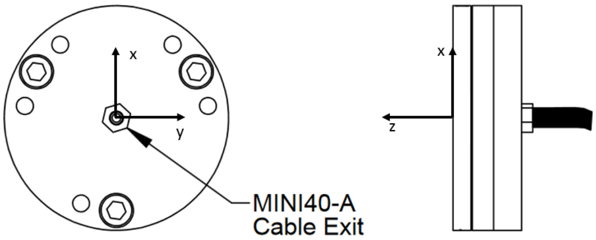

Figure 3.5: Drawing of the mini40 force sensor.

Table 3.1: Stiffness matrix for the ATI mini40 balance. Local axes are defined in Figure 3.5.

Component	**Stiffness**
X-axis and Y-axis force (Kx, Ky)	1.1×10^7 N/m
Z-axis force (Kz)	2.0×10^7 N/m
X-axis and Y-axis torque (Ktx, Kty)	2.8×10^3 Nm/rad
Z-axis torque (Ktz)	4.0×10^3 Nm/rad

3.4 Detailed design: computational procedure

3.4.1 Geometry simplification

The CAD drawings of the model have to be processed to remove the superfluous features that would only increase the computational time, but have little influence on the calculation. The simplification is as follows for the three main components of each wheel assembly. The wheel is modelled mainly as it appears in the manufacturing drawings (Figure 3.6 and Figure A.1), except for the fastening holes.

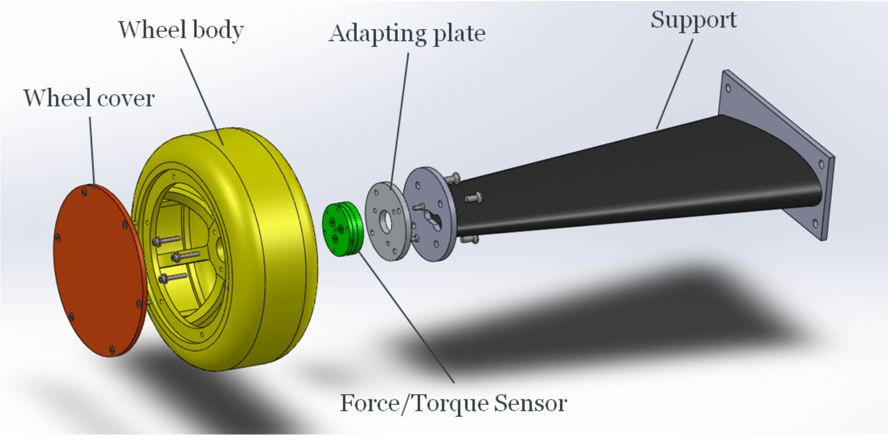

Figure 3.6: Exploded view of the model. The wheel is mounted on the support and the aerodynamic forces are measured with the force sensor inside the wheel model.

The force sensor is modelled as a link element with assigned stiffness and mass, which is introduced between the wheel and the support without considering the actual force sensor geometry. The link has a defined size and assigned stiffness, according to Table 3.1. The manufacturing drawings of the support include a combination of materials: aluminium and carbon-fibre reinforced plastic (CFRP). The model is reproduced by removing small features such as holes and chamfers.

3.4.2 Physical parameters

For the structural simulations, the two major parameters are density and elastic modulus. The material properties of the model are as follows.

Wheel. The 3D-printer material (LS600) can be assumed isotropic, with elastic modulus E from the specifications sheet: $E_P = 1800\,\mathrm{MPa}$. The density of this material is approximately $\rho_P = 1100\,\mathrm{kg/m^3}$.

Force sensor. The force sensor has sizes and stiffness fully characterised in the specifications sheet Table 3.1. The mass of the balance is 0.050 kg.

Support. The aluminium alloys have a constant elastic modulus $E \approx 70\,000\,\mathrm{MPa}$, while a big variability remained on the CFRP because it is a laminate with multidirectional fibers. If the data on the final layout of the plies are known, the elastic properties of the laminate can be deduced, but in this case the final layout depended on the manufacturer. Thus, an elastic modulus $E_C = 90\,000\,\mathrm{MPa}$ was assumed from the mean between the woven MTM28 T300 4×4 lamina ($E = 60\,000\,\mathrm{MPa}$) and the unidirectional MTM28 HS-T700 ($E = 121\,000\,\mathrm{MPa}$). The density of the support was approximated with a mean value $\rho_C = 2000\,\mathrm{kg/m^3}$.

3.4.3 Mesh generation

After the geometry simplification, a finite element grid was generated. In finite-element analysis, the two most common kinds of elements are hexahedrons and tetrahedrons. Figure 3.7 shows an example of the mesh for the wind-tunnel model. The mesh was generated using ANSYS® Workbench™. The maximum size of the mesh elements is 5 mm, that corresponds to a fine grid with 2×10^5 elements approximately.

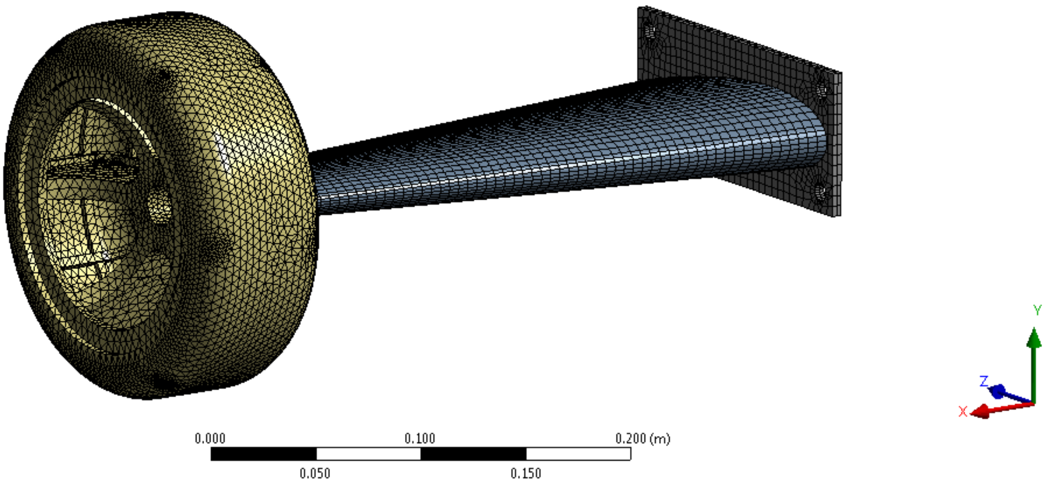

Figure 3.7: Example of the wind-tunnel model mesh for the structural calculations and the modal analysis, in (x, y, z) local coordinate system for FEA calculations).

3.4.4 FEA Modal analysis

Modal analysis with the finite elements method provides estimations of the natural frequencies of the model, which characterise the model dynamic behaviour (refer to appendix Section B.1).

After generating the mesh, the constraints must be assigned, in such a way that all six degrees of freedom of a body free to move in a three-dimensional space are constrained. Since it is a modal analysis, every unconstrained degree of freedom gives a null natural frequency.

A large number of approximations are present in the FEA model for the prediction of the unsteady loads, but a test of the validity of the model was firstly performed to check the reliability of the analysis on this kind of geometry. Converged results are obtained between the fine grid and the extra-fine grid.

A list of the first six natural frequencies for the final model is reported in Table 3.2, where the verification of the FEA model for different grids is reported. A result with the base plate uniformly fixed is in Figure 3.8.

Table 3.2: List of natural frequencies for different grids.

	Frequency [Hz]			
Mode	**Coarse grid** (131k nodes)	**Medium grid** (154k nodes)	**Fine grid** (200k nodes)	**Extra-fine grid** (266k nodes)
1	154	153	140	140
2	267	260	162	161
3	373	368	185	185
4	398	396	262	262
5	575	520	502	490
6	756	744	530	528

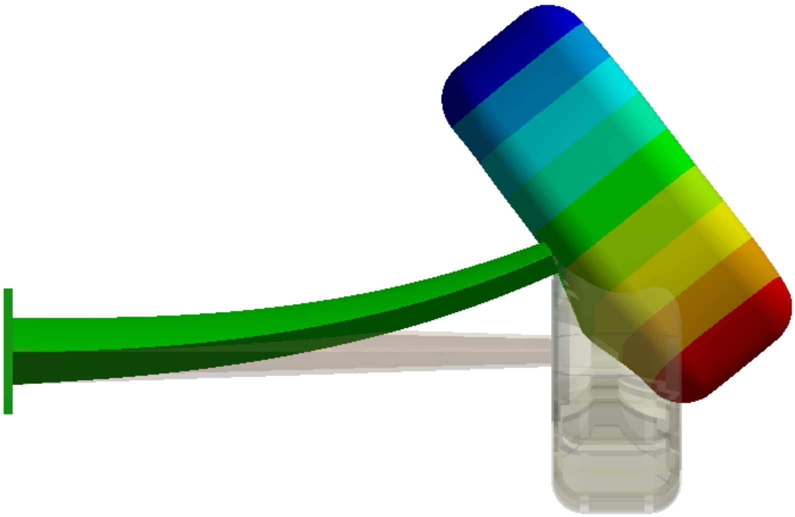

Figure 3.8: Example of the first natural mode for the structure uniformly fixed at the base plate (exaggerated deformation), at frequency $f = 140\,\mathrm{Hz}$.

3.4.5 FEA Static structural final verification

Beyond the dynamic characterisation of the wind-tunnel model for measurement purposes, the model has structural functions too that must be verified before manufacturing. For static verification, the quantities to be analysed are no longer related to the dynamic, but mainly to the static stress/strain field. For this purpose, the *Static structural* tool in ANSYS® Workbench™ is used. The geometry and the mesh is the same mesh that was used for the modal analysis, but in this case the loads need to be applied to the structure. The loads can be either estimated from CFD or from assumptions on the force coefficients given by experience.

After considering a few testing conditions, the values to verify are that the maximum stress is below the strength of the material, the maximum strain is below the maximum elongation of the material and the maximum displacement is sufficiently small to prevent interferences with the aerodynamic field. The results of the static simulation show that all the static requirements are satisfied by the model developed with the Modal Analysis in the previous stage.

3.4.6 Manufacturing

In Figure 3.9 the drawing of the final model is shown at a higher level of detail, in the configuration $L = 1.3D$, $\alpha = 20\,\text{deg}$. The plate in the background of the picture is mounted on an aluminium frame directly linked to the wind-tunnel frame, in such a way that the offset between the plate and the wind-tunnel side wall is negligible (less than 4 mm). The aluminium plates allow the user to perform tests on the tandem-wheel case in different configurations, and also the single-wheel case. The wheel is supported from the hub by means of three screws that are the interface with the balance, as illustrated in Figure 3.6.

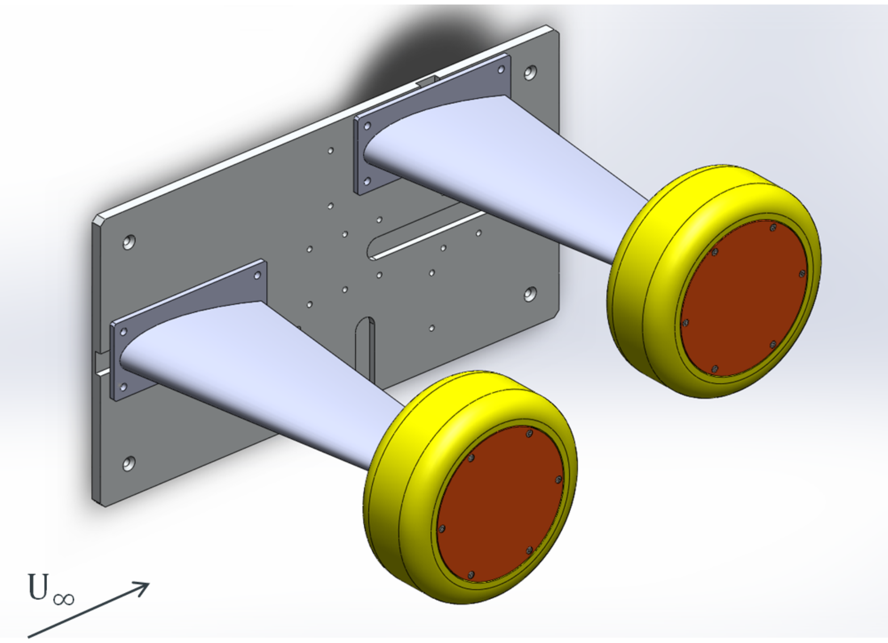

Figure 3.9: View of the wheel model and its support. The plate on which the wheels are mounted is directly fixed to the wind-tunnel frame. The holes on the plate allow to test various positions of the wheels (changing inter-axis distance and installation angle.

In the final version, the relevant sizes of the model are: wheel diameter $D_w = 181\,\text{mm}$, wheel width $W = 72\,\text{mm}$ and support length $b = 300\,\text{mm}$ (refer to Figure 3.2). Three different versions of the cover are prepared for the single-wheel case, as illustrated in Figure 3.10.

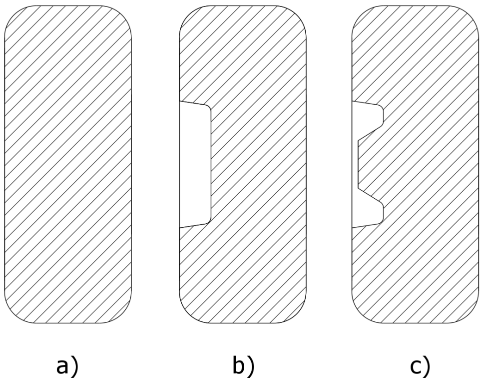

Figure 3.10: Wheel frontal cross-section for the three different covers: a) flat cover; b) cavity only; c) cavity with hub.

In addition to the previously described components, one version of the wheel was manufactured to host the pressure sensor, a Scanivalve ZOC33. This version of the wheel has the same external shape as the previously described version. This additional wheel is compatible with the covers of the other wheels, but due to limited space inside, when the pressure sensor is fitted inside the wheel, only the flat cover can be used. A drawing for manufacturing purposes of the assembly (wheel and support) is given in Figure A.1.

3.5 Experimental transfer function

Experimentally, it is possible to determine the resonance frequencies of the model. Before the wind-tunnel session, the model was tested in the Dynamics Laboratory.

The wheel-model was mounted on a support fixed on the ground, attempting to reproduce the wind tunnel mountings. During the dynamic test the wheel was forced with *Data Physics* shaker type 4. The natural frequencies of the model were estimated by applying a random force input, then the transfer function between acceleration and the applied force along two axes was calculated.

If comparing the two transfer functions in Figure 3.11, the first predicted mode as shown in Table 3.2 at 140 Hz is found at exactly 140 Hz on the y-axis transfer function. This result is consistent with the first deformation mode, which is mainly a bending mode in the y direction (compare again with Figure 3.8). Also the second mode, which is not illustrated but is a bending mode in the x direction, can be found at the frequency 164 Hz on the x-axis plot, whilst the predicted frequency was 161 Hz, confirming that the first two modes are well-predicted by the FEA model.

The third and the fourth modes are bending modes of the wheel around the hub, thus with the current position of the shaker (that is almost coaxial with the rotation centre of this modes) it is not expected to be found on the transfer function. The fifth and the sixth modes predicted by FEA are modes that involve an out-of-plane deformation of the wheel cover, not present in the current setup. It is hard to find such complex modes with this elementary experimental setup.

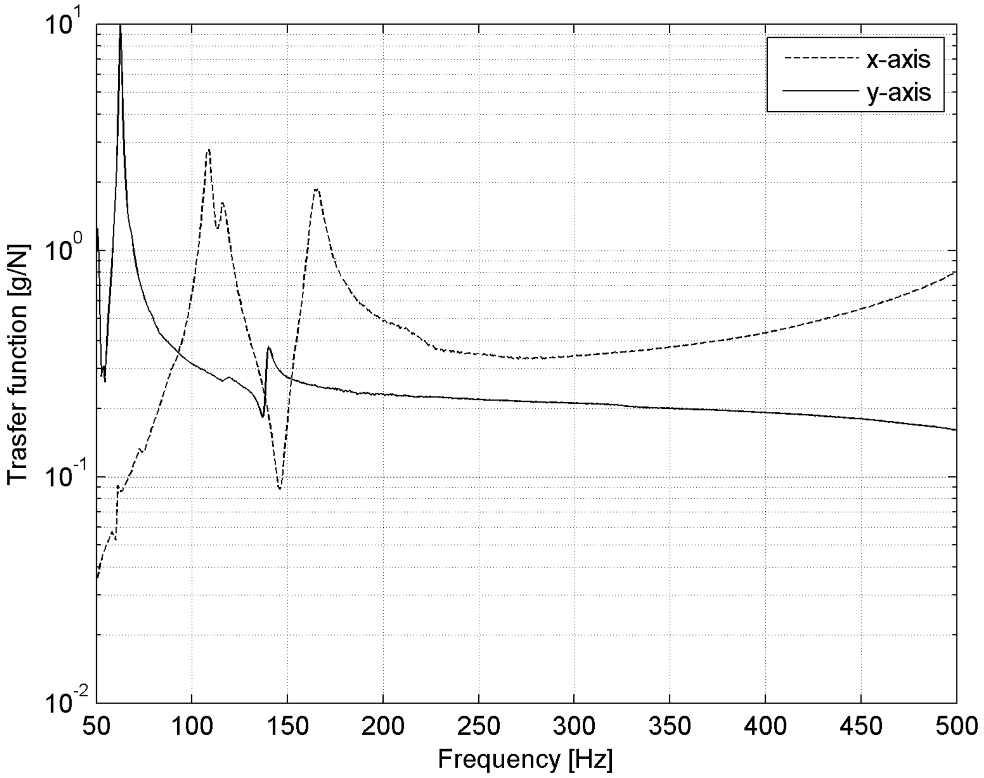

Figure 3.11: Transfer functions between acceleration and applied force both for x-axis shaking and y-axis shaking.

On the contrary, in the transfer function there are low-frequency modes that were not found in the first attempt of FEA analysis. A reconsideration of the approach and the relative approximations is advised for the future work, in order to setup a second iteration of FEA that includes the lower modes.

3.6 Test plan

The experimental plan is divided in two main parts: single wheel and tandem wheels. Both parts include enough configurations and measurements to provide physical insight on the new geometry and a database for CFD validation. The test plan is listed in Table 3.3, where the measured quantities are reported on the right-hand-side column for each configuration.

Each configuration is determined by a setup number followed by the hash symbol in the table and by the tripping (in Table 3.3). The setup numbering system includes a jump in the current version of the table because the table shown in this document is a subset of a larger experimental table generated in earlier stages. Loads, surface pressures and PIV data are acquired for the various configurations. These three techniques bring different levels of difficulty and have different costs: only some of the configurations are analysed with all the three techniques, as indicated in the table.

The experiments are tested at the maximum Reynolds number Re_D (based on wheel diameter) of 6×10^5, which presumably involves transition phenomena in the boundary layer. To extrapolate the current results at high-Reynolds numbers that are not achievable within the experiment, tripping devices are used to force a turbulent flow on the wheels surface. The tripping techniques in Table 3.3 can be classified as follows:

- UT: untripped, no tripping applied, smooth wheel surface;
- T zigzag: tripped with zigzag tape;
- T Grit60: tripped with Grit60 tape.

More details on the tripping are given in Chapter 6, where the experimental procedure of the wind-tunnel test is detailed.

Table 3.3: List of the wind-tunnel measurements for each configuration.

Configuration			
Geometry	**Setup**	**Tripping**	**Measurements**
One Wheel	#0A (flat cover)	UT	Loads, Pressure, PIV, Oil-flow
		T zigzag	Loads, Pressure, PIV, Oil-flow
		T Grit60	Loads
	#0B (cavity only)	UT	Loads
	#0C (cavity+hub)	UT	Loads
		T zigzag	Loads
		T Grit60	Loads
Tandem Wheels	#1 ($L_w = 1.1D_w$, $\alpha = 0\,\text{deg}$)	UT	Loads, PIV
		T zigzag	PIV
	#2 ($L_w = 1.3D$, $\alpha = 0\,\text{deg}$)	UT	Loads, Pressure, PIV
		T zigzag	Loads, Pressure, PIV
	#3 ($L_w = 1.5D$, $\alpha = 0\,\text{deg}$)	UT	Loads, Pressure, PIV, Oil-flow
		T zigzag	Loads, Pressure, PIV, Oil-flow
	#18 ($L_w = 1.3D_w$, $\alpha = 20\,\text{deg}$)	UT	Loads, Pressure, PIV
		T zigzag	Loads, Pressure, PIV
	#11 ($L_w = 1.5D_w$, $\alpha = 10\,\text{deg}$)	UT	Loads, Pressure
		T zigzag	Loads, Pressure, PIV
	#19 ($L_w = 1.5D_w$, $\alpha = 20\,\text{deg}$)	UT	Loads, Pressure, Oil-flow
		T zigzag	Loads, Pressure

Chapter 4

CFD Numerical Tools

In this chapter, the software packages used in this work and their interfaces are described, with reference to the diagram in Figure 4.1. The main blocks *CAD simplification*, *mesh generation*, *solver* and *post-processing* are described in the following sections, whilst the simulation inputs and the geometry are described in the text every time that a new geometry is introduced. Also, if some minor changes are needed in the method, the differences and the motivations are explained for each case.

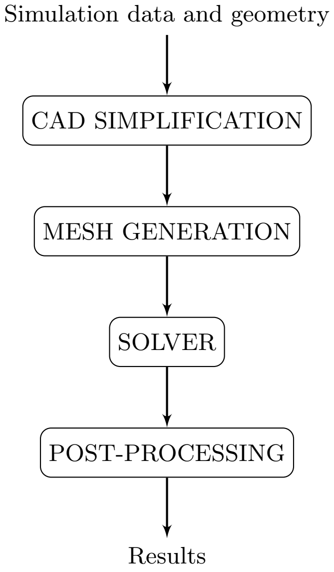

Figure 4.1: General diagram of a CFD simulation.

Most of the software employed in this thesis is freely or commercially available software. In terms of development of numerical tools, the original contribution of this work is the creation of a procedure that combines multiple pre-existing CFD tools and the implementation of additional functionalities and turbulence models in OpenFOAM®.

4.1 CAD simplification: Solidworks

Firstly, the manufacturing geometries undergo a defeaturing process to obtain the simulation geometry. It is a preparatory process needed before starting the meshing process: the geometry is simplified to remove the small features that would increase the mesh element count without changing the results. The defeaturing could be automatically performed by specific software packages, setting for instance the minimum fillet and hole radii to be kept in the geometry. An automatic process in normally necessary when dealing with complex geometries.

Within the PhD thesis research, both for benchmark cases and for the final simulations on tandem wheels, the level of complexity of the geometries would be relatively low, thus a manual defeaturing process is used. Within this project, the software used to generate and consequently edit the CADs is Solidworks. Thus, for the geometries designed within the project, it is possible to directly deactivate the features of the CAD model prepared for manufacturing. Further details on the defeaturing process are given for each simulation, either on the benchmark cases or the final geometry.

4.2 Mesh generation: Icem CFD™, snappyHexMesh, and HEXPRESS/Hybrid

The choice of the kind of mesh and of the mesh parameters affects the computational efficiency, i.e. the accuracy for a given simulation wall time.

For the various simulations performed in the PhD, different kinds of meshes are used. These can be summarised as follows.

Block-structured mesh. It is used here only for basic geometries, otherwise not convenient in terms of pre-processing time. This mesh is generated here both with `blockMesh` (the structured-mesh generator in OpenFOAM®) and with ANSYS® ICEM CFD™.

Unstructured tetrahedrons with semi-structured boundary layer mesh. The most versatile mesh, suitable for complex geometries, indicated for vertex-centred solvers. Here, it is generated with ANSYS® ICEM CFD™.

Unstructured hexa-dominant with semi-structured boundary layer mesh. The default mesh for OpenFOAM®, suitable for most of the complex geometries. In the PhD project, three different mesh generators are used to generate this mesh: snappyHexMesh (the unstructured-mesh generator in OpenFOAM®), ANSYS® ICEM CFD™ and HEXPRESS™/Hybrid.

The details of the mesh generation are given later for each simulation, but generally, the mesh sizes are defined with reference to the criteria given by Spalart [77]), especially for DES. The domain can be divided into the following regions:

- the *near-body* region that contains the body and part of the wake associated with it;
- the *wake* region, which is leeward with respect to the bodies and in which most of the wake is contained;
- the *potential* part of the flow in which the flow is mainly uniform and unaffected by the presence of the bodies and their wake.

Concerning the near-body region, there is the need for a flexible grid (e.g., ideally unstructured tetrahedral elements) with the possibility to have a semi-structured grid in the boundary layer areas (typically, triangular prisms). In the wake region it is important to have a good degree of refinement, especially with DES (Spalart [77]). In the potential region the mesh can be much coarser than in the other two but it is good to reach the coarse size with a progressive transition from the near-body region to the mainly uniform flow.

4.3 Solver: OpenFOAM®

OpenFOAM®, an open-source toolbox developed by OpenCFD Ltd, implements a large number of different solvers and methods. It relies on the finite volume discretisation with a cell-centred approach. The scalability with the number of cores is proved [53], and the software comes with open-source license, i.e., open code and possibility to use as many cores as available on the cluster.

4.3.1 Governing equations

The steady simulations here are based on the incompressible RANS equations as reported in Section 2.3. For clarity, the equations are rewritten here:

$$\frac{\partial U_i}{\partial x_i} = 0 \tag{4.1}$$

$$\rho\frac{\partial U_i}{\partial t} + \rho\frac{\partial}{\partial x_j}(U_j U_i) = -\frac{\partial P}{\partial x_i} + \frac{\partial}{\partial x_j}(2\mu S_{ij} - \rho\overline{u'_j u'_i}) \tag{4.2}$$

The quantity $-\rho\overline{u'_j u'_i}$ is the Reynolds-stress tensor that is approximated with the Boussinesq equation (Equation 2.7), i.e. $\tau^t_{ij} = 2\rho\nu_t\overline{S}_{ij} - \frac{2}{3}\rho k\delta_{ij}$.

This project employs the one-equation S-A turbulence model that is described here in two different versions. The S-A model is based on the working variable $\tilde{\nu}$ that appears in Equation 2.14 (from NASA [50]):

$$\frac{\partial \tilde{\nu}}{\partial t} + U_j \frac{\partial \tilde{\nu}}{\partial x_j} = c_{b1} \tilde{S} \tilde{\nu} - c_{w1} f_w \left(\frac{\tilde{\nu}}{d} \right)^2 + \frac{1}{\sigma} \left\{ \frac{\partial}{\partial x_k} \left[(\nu + \tilde{\nu}) \frac{\partial \tilde{\nu}}{\partial x_k} \right] + c_{b2} \frac{\partial \tilde{\nu}}{\partial x_k} \frac{\partial \tilde{\nu}}{\partial x_k} \right\} \tag{4.3}$$

from which the turbulent viscosity ν_t is calculated by means of f_{v1}:

$$\nu_t = \tilde{\nu} f_{v1} \tag{4.4}$$

and f_{v1} is defined as follows:

$$f_{v1} = \frac{\chi^3}{\chi^3 + c_{v1}^3} \tag{4.5}$$

with χ equal to the ratio between the working variable $\tilde{\nu}$ and the fluid viscosity ν:

$$\chi = \frac{\tilde{\nu}}{\nu} \tag{4.6}$$

The production term $c_{b1} \tilde{S} \tilde{\nu}$ in the model is proportional to the quantity $\tilde{S}$:

$$\tilde{S} = \Omega + \frac{\tilde{\nu}}{\kappa^2 d^2} f_{v2} \tag{4.7}$$

where S is the vorticity magnitude $\Omega = \sqrt{2 \Omega_{ij} \Omega_{ij}}$, with $\Omega_{ij} = (\partial U_i / \partial x_j - \partial U_j / \partial x_i)/2$ the skew-symmetric part of mean velocity gradient tensor ∇U.

Additional definitions of the model (same notation as in NASA [50]) are:

$$\begin{aligned} f_{v2} &= 1 - \frac{\chi}{1 + \chi f_{v1}} & g &= r + c_{w2}(r^6 - r) \\ f_w &= g \left[\frac{1 + c_{w3}^6}{g^6 + c_{w3}^6} \right]^{1/6} & r &= \min \left[\frac{\tilde{\nu}}{\tilde{S} \kappa^2 d^2}, 10 \right] \end{aligned} \tag{4.8}$$

With the following constants:

$$\begin{aligned} c_{b1} &= 0.1355 & c_{w3} &= 2 \\ \sigma &= 2/3 & c_{v1} &= 7.1 \\ c_{b2} &= 0.622 & c_{t3} &= 1.2 \\ \kappa &= 0.41 & c_{t4} &= 0.5 \\ c_{w2} &= 0.3 & c_{w1} &= \frac{c_{b1}}{\kappa^2} + \frac{1 + c_{b2}}{\sigma} \end{aligned} \tag{4.9}$$

Further information of the model can be found in Wilcox [92]. The boundary conditions normally used are $\tilde{\nu} = 0$ at the wall and $3\nu < \tilde{\nu} < 5\nu$ at the inflow.

The version described so far is referred to as the *standard* version without f_{t2} term. This version is called “SA-std-noft2”, here simply referred to as “SA-std” or standard model, because the SA-std-noft2 is not implemented at any stage of the current project. The SA-std-noft2 was firstly introduced in order to make zero a stable solution of the equation in case of use of the trip term. Since here the trip term is not used, the SA-std-noft2 is not needed (refer again to NASA [50]). The SA-std-noft2 was implemented in OpenFOAM® during the current PhD project and used as reference version instead of the previously available SA-fv3-noft2, which is the default SA model in OpenFOAM®.

However, the SA-fv3-noft2 (here also referred to as SA-fv3) is often used as a second term of comparison. The difference with the standard version is a different definition of $\tilde{S}$, as follows (NASA [50]):

$$\tilde{S} = f_{v3}\Omega + \frac{\tilde{\nu}}{\kappa^2 d^2} f_{v2} \tag{4.10}$$

and of f_{v2} and f_{v3}:

$$f_{v2} = \frac{1}{(1 + \chi/c_{v2})^3} \tag{4.11}$$

$$f_{v3} = \frac{(1 + \chi f_{v1})(1 - f_{v2})}{\chi} \tag{4.12}$$

with $C_{v2} = 5$ as before. This version is not an official version of the model, and it is not advisable to use it because of its pseudo-transitional behaviour (NASA [50]). This is the main reason why in the current project, it appears only as a secondary version, while the leading role is left to the standard version (widely used and tested, with a more defined transitional behaviour).

Following the definitions given in Section 2.3, in the case of DDES, the only change is the substitution of the distance d in the $\tilde{S}$ definition with the value $\tilde{d}$:

$$\tilde{d} = \min(d, C_{\mathrm{DES}}\Delta) \tag{4.13}$$

with $C_{\mathrm{DES}} = 0.65$. The cell size Δ is defined as the cubic root of the cell volume:

$$\Delta = V^{1/3} \tag{4.14}$$

where V is the cell volume. But there is also the possibility to define it as the maximum cell size:

$$\Delta = 2 \max_i h_i \tag{4.15}$$

where h_i is the distance of the i-th face from the cell centre for each cell ($i = 1, ..., m$, where m is the number of faces for each element). This definition can be used for unstructured cells and, in case of structured grids, it is equivalent to the definition $\Delta = \max(\Delta x, \Delta y, \Delta z)$ in Spalart et al. [80].

In IDDES, the adopted criterion for the characteristic size is more complex (as can be found in Shur et al. [68]):

$$\Delta = \min\{\max[C_w d_w, C_w h_{\max}, h_{wn}],\, h_{\max}\} \tag{4.16}$$

where h_{wn} is the grid step in the wall-normal direction, $h_{\max}$ is the maximum local grid spacing, d_w is the distance from the wall and C_w is 0.15.

4.3.2 Algorithms

The `simpleFoam` solver is used for steady simulations (also useful to initialise the unsteady simulations) and `pimpleFoam` for the unsteady simulations. Both solve the incompressible Navier-Stokes equations, with the selected turbulence models. The choice of the incompressible equations is because the velocities that are tested in this project are sufficiently low to fully justify the incompressibility approximation: in this way, the set of equations is simpler and consequently faster to solve. In the present work, the hybrid LES/RANS is largely used, for instance S-A DES (in the versions DDES and IDDES). In order to presolve the unsteady flows a more traditional RANS model is used for steady simulations, for example k-ω SST and S-A.

The SIMPLE (Semi-Implicit Method for Pressure-Linked Equations) algorithm solves the Navier-Stokes equations iteratively. The algorithm is based on the repetition of a loop that separately solves the momentum equations and the pressure correction equation derived from the continuity equation. The equations are under-relaxed to increase the stability of the solution. In detail, each iteration starts with the setup of the boundary conditions, then the algorithm solves the discretised momentum equation to compute an intermediate velocity field and then to compute the mass fluxes at the cell faces. It solves the pressure correction equation (and applies the under-relaxation) to correct the mass fluxes at the cell faces. Finally it corrects the velocities on the basis of the new pressure field and updates the values to satisfy the boundary conditions. The process is repeated until convergence (Ferziger and Peric [22]).

In the PIMPLE (PIso-siMPLE) algorithm, there are three levels of loops that describe the solution process. The most external level is the time-step advancement loop (one cycle per time step), the second level is the PIMPLE outer loop for velocity-pressure coupling and the third level is the inner pressure corrector loop. This process allows a larger time step because the momentum equation can be relaxed (like in the SIMPLE algorithm) for increased convergence. Only the last cycle of the outer loop is calculated without relaxation on the velocity equation. PIMPLE algorithm can be operated in PISO mode setting only one outer loop, so that pressure and velocity are coupled only once per time step. When this algorithm is run in PISO mode, no under-relaxation is applied on the momentum equation.

4.3.3 Numerical schemes

The numerical schemes used for the DES in PIMPLE are second-order schemes. In the momentum equations, the convective term (`div(phi,U)` in the code) is calculated with a combination of linear and upwind schemes, to improve the stability. Examples of such schemes are the `LUST` method (Linear Upwind Stabilised Transport) or the TVD (total variation diminishing) scheme `limitedLinearV`. The Laplacian scheme is a Gauss linear integration with a 0.33 non-orthogonal correction, the gradient scheme is a Gauss linear, and the surface normal gradient scheme is calculated with a non-orthogonal correction (0.33 of orthogonal part). During the flow initialisation with the steady RANS solver SIMPLE, the schemes employed are fully corrected for the non-orthogonality and the convective term is calculated with a `linearUpwindV` method.

4.3.4 Implementation of the turbulence models

Either with pure RANS simulations or with DES, the turbulence model plays an important role, which is more obvious with RANS (or URANS) simulations where all the turbulence is modeled by the turbulence model. On the contrary, in DES turbulence modelling keeps playing its fundamental role only in the RANS regions where the turbulence model is activated (i.e., boundary layers). In fact, in the LES regions the scope is usually to minimise the sub-grid-scale viscosity in such a way that the resulting flow has a minimal dependency on the turbulence model employed.

The turbulence model that is the base of the used DES model is the S-A model [80] and it is described in Section 4.3.1. In the following subsections, the differences between the two versions of the SA model are described, together with the approach used for the manual setup of the laminar-turbulent transition in the simulations within the project.

The default S-A version included in OpenFOAM® according to the NASA nomenclature is the SA-fv3-noft2 version (refer to NASA website [50]). As a consequence, starting from the OpenFOAM® default SA-fv3-noft2 version, the following parts were modified. In the `SpalartAllmaras.C` source file, the function returning f_{v2}

```
tmp<volScalarField> SpalartAllmarasStd::fv2
(
    const volScalarField& chi,
     const volScalarField& fv1
) const
{
   return 1.0/pow3(scalar(1) + chi/Cv2_);
}
```

had been replaced with the following

```
   tmp<volScalarField> SpalartAllmarasStd::fv2
(
```

```
     const volScalarField& chi,
     const volScalarField& fv1
) const
{
   return 1.0 - chi/(1.0 + chi*fv1);
}
```

and the function returning the f_{v3} were removed, together with all the references to f_{v3}.

The final step was to include a version that considers the possibility to be able to model laminar regions in the domain. This numerical transition feature is already implemented in some commercial CFD codes such as Fluent[1]. The procedure is taken from the report by Abedi [2] and it implies the addition of a switch coefficient α_1 to the $\tilde{\nu}$ equation. Instead of using the default equation:

```
    tmp<fvScalarMatrix> nuTildaEqn
    (
        fvm::ddt(nuTilda_)
      + fvm::div(phi_, nuTilda_)
      - fvm::laplacian(DnuTildaEff(), nuTilda_)
      - Cb2_/sigmaNut_*magSqr(fvc::grad(nuTilda_))
     ==
        Cb1_*Stilda*nuTilda_
      - fvm::Sp(Cw1_*fw(Stilda)*nuTilda_/sqr(d_), nuTilda_)
    );
```

The production term `Cb1_*Stilda*nuTilda_` is multiplied by the `alpha1_` field, as follows:

```
    tmp<fvScalarMatrix> nuTildaEqn
    (
        fvm::ddt(nuTilda_)
      + fvm::div(phi_, nuTilda_)
      - fvm::laplacian(DnuTildaEff(), nuTilda_)
      - Cb2_/sigmaNut_*magSqr(fvc::grad(nuTilda_))
     ==
        alpha1_*Cb1_*Stilda*nuTilda_
      - fvm::Sp(Cw1_*fw(Stilda)*nuTilda_/sqr(d_), nuTilda_)
    );
```

Setting the α_1 field equal to 1 in the initial conditions, the domain is fully turbulent and the standard S-A equations apply. On the contrary, setting α_1 locally equal to 0, the region is laminar because the production term is cancelled: the viscosity is still a transported quantity, but it becomes negligible in the laminar areas.

4.3.5 Implementation of the wall boundary conditions

The S-A model can be used as a low-Reynolds model, i.e. resolving the boundary layer up to the viscous sublayer (within $y^+ < 5$) and imposing $\tilde{\nu} = \nu_t = 0$ at the wall. For this use of the turbulence model, a first cell centre height located in the viscous sublayer is generally needed (ideally $y^+ \approx 1$). Since industrial problems generally have complex geometries, which make it hard to generate a uniform boundary layer mesh, this condition can hardly be respected. But, if this is the case, the error on the wall shear stress becomes larger with results that do not show consistency.

To restore a solution that is physically correct, wall functions are normally used as boundary conditions instead of applying $\nu_t = 0$ directly at the wall. The `nutUWallFunction` sets a corrected value of the turbulent viscosity ν_t at the wall, so that the wall shear stress keeps being physically valid when the first cell centre is also in the log layer (i.e., outside the laminar viscous sublayer). Firstly, the code calculates with a self-iterating loop the y^+_{lam} value, which is the limit between the linear laminar part and the log-layer:

$$(y^+_{lam})^{i+1} = \frac{\ln\left(E(y^+_{lam})^i\right)}{\kappa}. \tag{4.17}$$

where $(y^+_{lam})^i$ is the value of y^+_{lam} at the i-th iteration. The loop is started with a $y^+_{lam} = 11$. For example, with $E = 9.8$ and $\kappa = 0.41$, the result is $y^+_{lam} = 11.5$.

The fundamental step is the calculation of the local y^+, for each wall face in the mesh. It is not possible to use the log-law

$$u^+ = \frac{\ln(Ey^+)}{\kappa} \tag{4.18}$$

as it is, because of the missing information on u^+. But, rewriting $u^+ = u/u_\tau$ and multiplying both sides for $y^+ = yu_\tau/\nu$, the following formula includes only known variables and the requested y^+:

$$\frac{yu}{\nu} = \frac{y^+ \ln(Ey^+)}{\kappa} \tag{4.19}$$

To solve the previous non-linear equation in y^+, the OpenFOAM® developers implemented an iterative solution using Newton's method that leads to:

$$(y^+)^{i+1} = \frac{\kappa yu/\nu + (y^+)^i}{\ln\left(E(y^+)^i\right) + 1} \tag{4.20}$$

where $(y^+)^i$ is the value of y^+ at the i-th iteration.

Eventually, assuming that the wall shear stress of the current mesh has to be the same as the τ_w estimated with the log-law for $y^+ > y^+_{lam}$, the starting equation to calculate the equivalent ν_t at the wall is:

$$\rho(\nu_t + \nu)\frac{u}{y} = \tau_w = \rho u_\tau^2 \tag{4.21}$$

which can be resolved for ν_t:

$$\nu_t = \nu\left(\frac{y^+\kappa}{\ln\left(Ey^+\right)} - 1\right). \tag{4.22}$$

If $y^+ < y^+_{lam}$, the default $\nu_t = 0$ keeps being used, even if the wall function is enabled. Whilst ν_t is calculated with the wall function, the boundary value of the other variables are not touched by this implementation.

The effect of a physically-meaningful wall shear stress is felt by the whole equation system though. In fact, the ν_t calculated by means of the wall function directly affects the momentum equations (being part of it) and indirectly this changes the continuity equation and the turbulent variable equation. It is an effective approach that involves only the minor changes in the code described above.

Alternatively, a wall function with the Spalding's blended law is available:

$$y^+ = u^+ + \frac{1}{E}\left[\exp\left(\kappa u^+\right) - 1 - \kappa u^+ - \frac{1}{2}\left(\kappa u^+\right)^2 - \frac{1}{6}\left(\kappa u^+\right)^3\right] \tag{4.23}$$

which has the same behaviour as the two-layer wall functions, but the slope of the function is always continuous, also in the buffer layer ($5 < y^+ < 30$). In OpenFOAM®, also for the Spalding's wall function, an iterative Newton's method is applied in each cell in order to solve the following equation:

$$-\frac{yu_\tau}{\nu} + \frac{u}{u_\tau} + \frac{1}{E}\left[\exp\left(\kappa\frac{u}{u_\tau}\right) - 1 - \kappa\frac{u}{u_\tau} - \frac{1}{2}\left(\kappa\frac{u}{u_\tau}\right)^2 - \frac{1}{6}\left(\kappa\frac{u}{u_\tau}\right)^3\right] = 0 \tag{4.24}$$

which is the same as Equation 4.23, substituting $y^+ = yu_\tau/\nu$ and $u^+ = u/u_\tau$.

All the wall functions described so far are available in in OpenFOAM®, thus no additional work was required on the implementation of the wall functions.

4.4 Post-Processing

4.4.1 Software

The post-processing is performed with various software packages.

OpenFOAM. The solver is capable of processing data during run-time, which is fundamental when dealing with large computations. Most of the mean and RMS quantities are calculated during run-time (typically pressure and velocity), whilst the flow field is stored only for few reference times. Some additional features allow also the calculation of vorticity and Q-criterion in post/processing.

Paraview. It is an open-source visualisation software, used with various kinds of simulations. It can be used either to open an OpenFOAM simulation directly or to open a `vtk` file with fields information.

Tecplot. Commercial code to be used as an alternative to Paraview for larger data sets.

Matlab. It is used for coherent line data plot preparation throughout the project, especially when comparing with experimental results.

4.4.2 Further post-processing

According to Haller [26], there are multiple ways to identify vortical structures in a complex three-dimensional CFD simulation. One of the most common methods consists in showing contours (or iso-surfaces) of vorticity ω, which is simply defined as:

$$\boldsymbol{\omega} = \nabla \times \mathbf{u} \tag{4.25}$$

where $\mathbf{u}$ is the velocity. The definition of vortex can be given in a more complex way, for instance with regard to the *Q criterion*:

$$Q = \frac{1}{2}\left(|\boldsymbol{\Omega}|^2 - |\mathbf{S}|^2\right) > 0 \tag{4.26}$$

where $\boldsymbol{\Omega} = \frac{1}{2}\left(\nabla\mathbf{u} - (\nabla\mathbf{u})^T\right)$ and $\mathbf{S} = \frac{1}{2}\left(\nabla\mathbf{u} + (\nabla\mathbf{u})^T\right)$, respectively the skew-symmetric and the symmetric part of the velocity gradient tensor. The vortices are defined in the regions with Q greater than zero. Other criteria also exist, e.g., the λ_2 criterion, but in this thesis Q is used for the vortex identification.

In OpenFOAM® the default implementation of the Q-criterion is the equivalent form:

```
0.5*(sqr(tr(gradU)) - tr(((gradU)&(gradU))))
```

where `tr` is the trace and `gradU` is the velocity gradient tensor $\nabla\mathbf{u}$.

4.5 Simulations plan

The previous sections of this chapter are a comprehensive description of the various software packages and implementations used throughout the PhD project for the CFD simulations.

Various aspects of the simulation procedure are analysed in Chapter 5 with two benchmark cases performed in the early stages of the PhD project on previously-available experimental/theoretical data.

Later, in Chapter 7 and 8, the main simulations of the PhD project are detailed. The CFD numerical procedure is applied to the single-wheel and tandem-wheel geometry, of which experimental data were obtained during the PhD, and on the four-wheel bogie.

Chapter 5

CFD Benchmark Cases

In this chapter, the CFD numerical procedure outlined in Chapter 4 is applied to two test cases and the results are compared with available databases (from the literature or specific benchmark cases). The first case is a turbulent boundary layer on a flat plate, which is used to validate the turbulence models implemented in OpenFOAM®against the default versions and the theoretical/experimental results from Schlichting and Gersten [64]. The second test is a DES performed on the tandem-cylinder geometry compared with experiments by Khorrami et al. [37].

5.1 Turbulent flow on 2D flat plate with zero pressure gradient

This section is a benchmark of the turbulence models implemented in OpenFOAM and used in the current work. A generic introduction to the turbulence models is given in Section 2.3, and a description of the turbulence models used in the current work is detailed in Section 4.3. A fundamental benchmark case to verify the implementation of the turbulence model is a turbulent flat plate.

5.1.1 Geometry and mesh

The geometry is a flat plate aligned with the free-stream velocity and immersed in a rectangular domain. Since here the only purpose is to validate the turbulence model, the domain can be two-dimensional.

The length of the flat plate is based on the maximum Reynolds number of interest (approximately 2×10^6), while the domain height and the length of the upstream domain (before the leading edge of the plate) is based on analogous validation cases present in the literature (e.g., the NASA 2D zero-pressure-gradient flat plate validation case [51]).

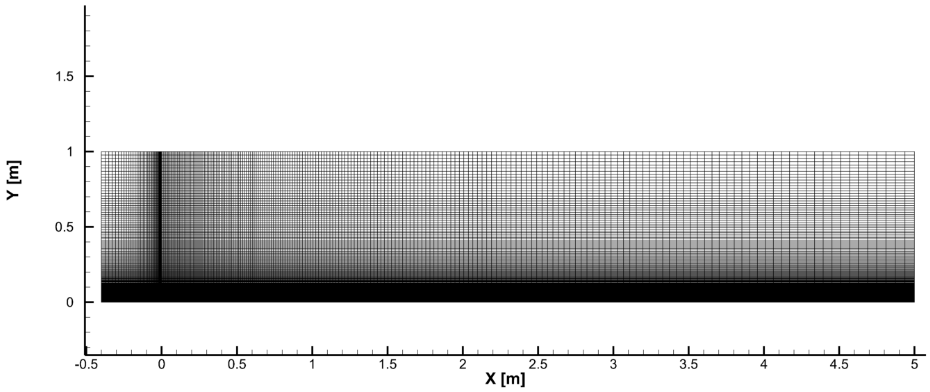

Figure 5.1: Flat-plate mesh.

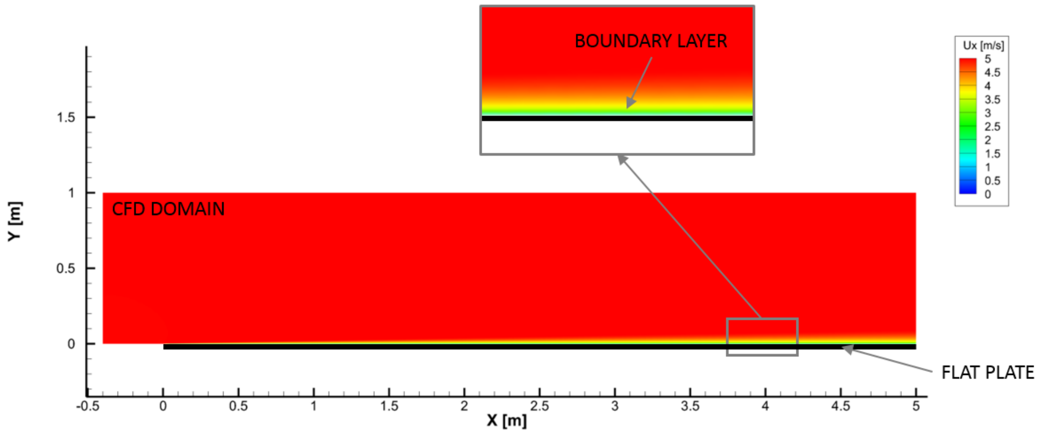

Figure 5.2: Flat-plate boundary streamwise velocity component.

The rectangular domain is automatically meshed with snappyHexMesh. Meshes with assigned number of elements in each direction can be generated. The growth rate between two consecutive elements is indirectly defined in snappyHexMesh: it is the result of the number of divisions of each geometric edge and the growth rate between the first and the last division.

5.1.2 Turbulence models and result comparison

The results of the test are illustrated according to the three aims of this benchmark: proving that a convergence exists with an increasing number of elements, showing the difference between the turbulence models (or versions), and illustrating the effectiveness of the wall functions with coarser boundary layer meshes. The analysed results are briefly shown on two plots: a skin friction coefficient C_f chart and the boundary layer profile at $Re_x = 1.5 \times 10^6$.

The skin friction coefficient C_f is always plotted including the reference to the fully-laminar plate and the fully-turbulent plate. The laminar skin friction coefficient (from Schlichting and Gersten [64]) is:

$$C_{f\mathrm{lam}} = \frac{0.664}{\sqrt{Re_x}}, \tag{5.1}$$

whilst the fully turbulent skin friction (from Schlichting and Gersten [64]) is:

$$C_{f\mathrm{turb}} = \left[2\log(Re_x) - 0.65\right]^{-2.3}. \tag{5.2}$$

In Figure 5.3 the convergence analysis for the two versions of the S-A model and for the $k-\omega$ SST model is shown. To prove the convergence, the 2D RANS were solved on three different grids.

The differences between the three turbulence models can be seen in Figure 5.4. As mentioned in this thesis, the SA-fv3 version of the S-A model shows a transitional behaviour that none of the the other two models (SA-std and $k-\omega$ SST) show. For low values of Re_x, the skin friction is lower with the fv3 version than with the standard version, confirming the two different behaviours. The fv3 versions shows a pseudo-transitional behaviour, whilst the standard version is fully turbulent.

Further tests on the three turbulence models were performed to understand the effectiveness of the wall function. In Figure 5.5, the S-A standard model with unresolved viscous sublayer is compared with the resolved viscous sublayer. Even with zero-pressure-gradient, the cases with the wall function are not as good as the resolved viscous sub-layer case.

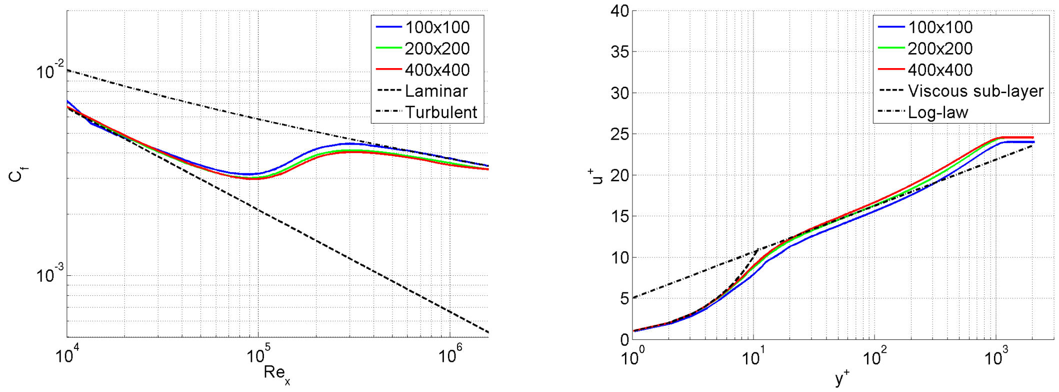

(a) S-A fv3, $C_f - Re$ (b) S-A fv3, $u^+ - y^+$

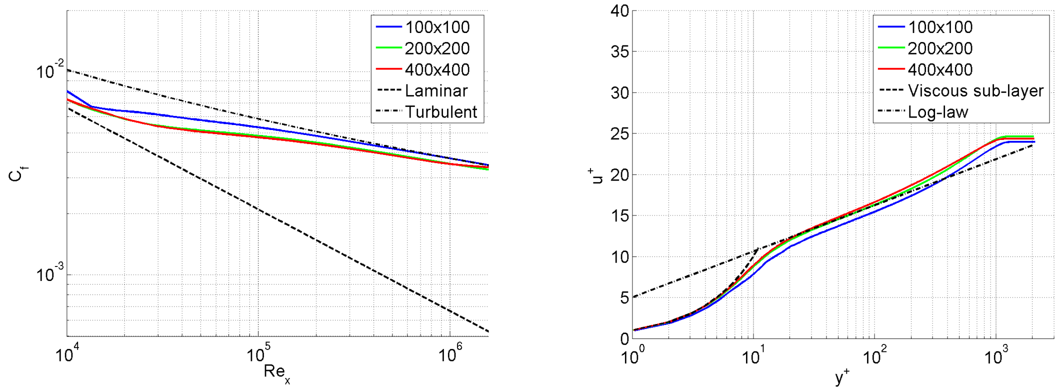

(c) S-A std, $C_f - Re$ (d) S-A std, $u^+ - y^+$

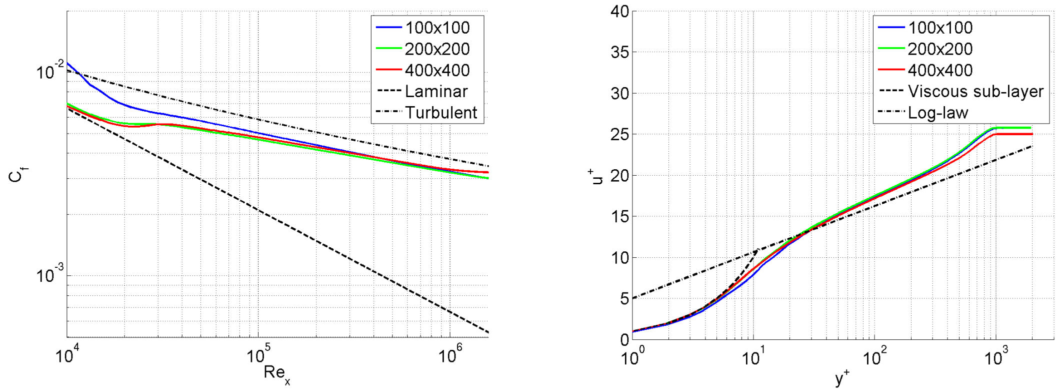

(e) $k - \omega SST$, $C_f - Re$ (f) $k - \omega SST$, $u^+ - y^+$

Figure 5.3: Convergence analysis: skin friction coefficient C_f and boundary layer profile u^+ at $Re_x = 1.5 \times 10^6$.

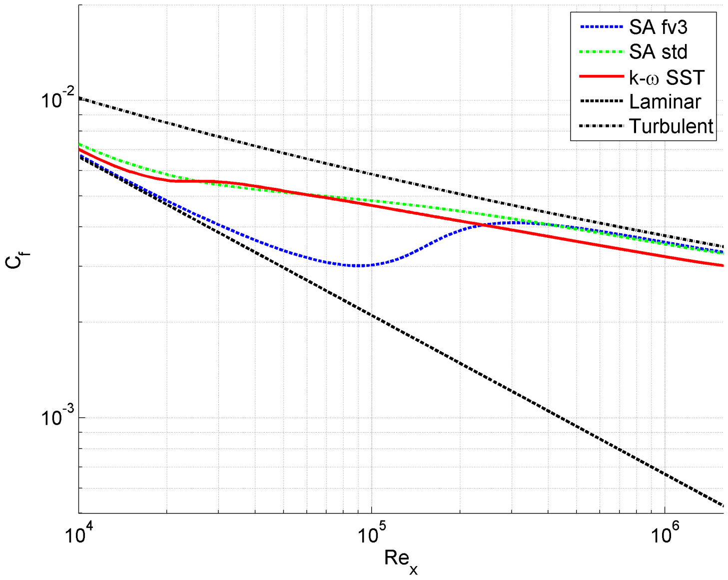

(a) $C_f - Re$

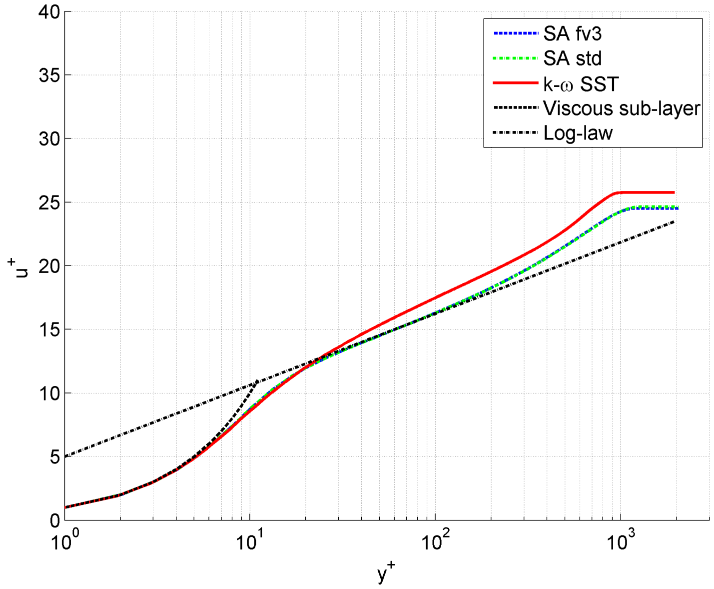

(b) $u^+ - y^+$

Figure 5.4: Comparison of the different models: skin friction coefficient C_f and boundary layer profile u^+ at $Re_x = 1.5 \times 10^6$.

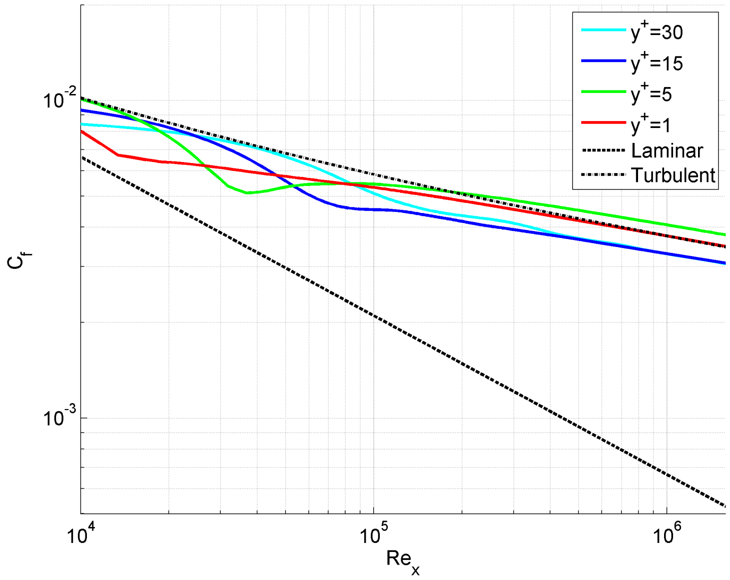

(a) $C_f - Re$

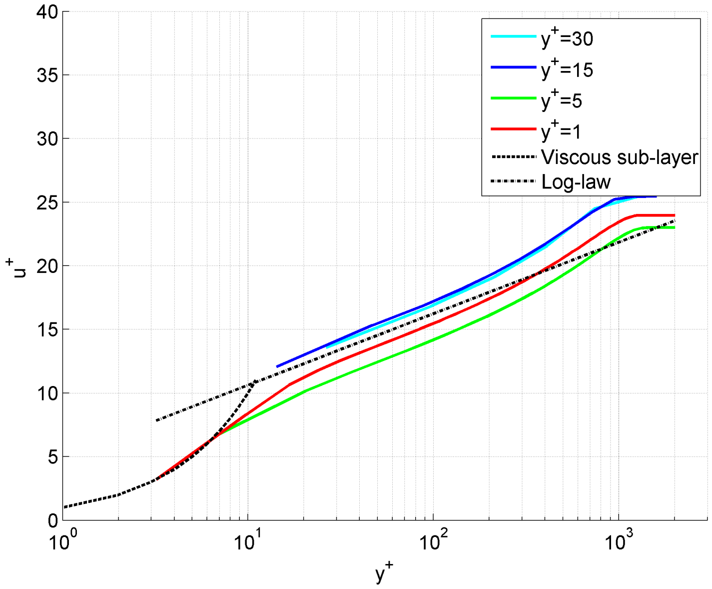

(b) $u^+ - y^+$

Figure 5.5: Test with the wall function: skin friction coefficient C_f and boundary layer profile u^+ at $Re_x = 1.5 \times 10^6$.

5.2 Tandem cylinders in subcritical spacing

In order to understand the most important parameters influencing the DES results, it is interesting to set up and run DES on a benchmark case: the flow past two tandem infinite circular cylinders. In fact, in the literature, a large number of experiments and simulations can be found on this topic. For instance, Sumner [84] showed useful charts and correlation distances for a range of cylinder separations at various Reynolds numbers. In spite of the number of published papers, most of these works concern flows at low Reynolds numbers, which are not suitable as a benchmark for the simulations at high Reynolds number past tandem wheels. Thus, the paper by Khorrami et al. [37] is here used as a benchmark case, in which a comparison between experimental data and unsteady RANS in 2D for tandem cylinders at a Reynolds number of 1.66×10^5 is presented. In the article, two different configurations are reported, at two different distances between the axes of the cylinders: only $L = 1.435D$ is selected (with D the cylinder diameter and L the inter-axis distance).

Since Khorrami et al. [37] did not perform any three-dimensional simulations, the work by Travin et al. [87] on the DES of the flow past a single cylinder is chosen as a guide for the DES mesh generation. The technical report by Spalart [77] is also considered. Further information on the DES simulation for this benchmark case can be found in the recent conference paper [94].

5.2.1 Geometry and mesh

The geometry comprises two infinite cylinders in tandem configuration, i.e. one behind the other in cross flow. A sketch of the reference axes and dimensions that are predominantly used in the literature is in Figure 5.6.

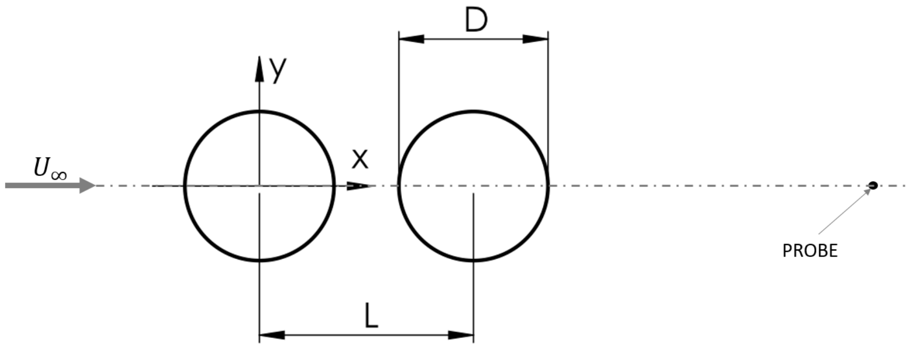

Figure 5.6: Cylinders geometry showing the flow direction (from left to right) and the probe location.

As illustrated in Figure 5.7, the domain in the longitudinal plane extends 15 diameters upstream and 16.4 diameters downstream of the front cylinder axis. The height of the domain in the cross-flow y direction is 30 diameters. The domain is split into two zones: an external region with a coarse mesh and an inner region with a refined mesh. Figure 5.8 shows a detailed view of the refined region. The mesh interface between the two regions is not conformal. In fact for this interface, the AMI (Arbitrary Mesh Interface) was used. The maximum element size in the coarse mesh region is 0.2 D, while it is 0.05 D in the finest mesh region. It is a size coherent with Travin et al. [87], with 15–32 elements per diameter in the spanwise direction. The finest mesh region is 6 diameters high in y direction over the line $x = 0$.

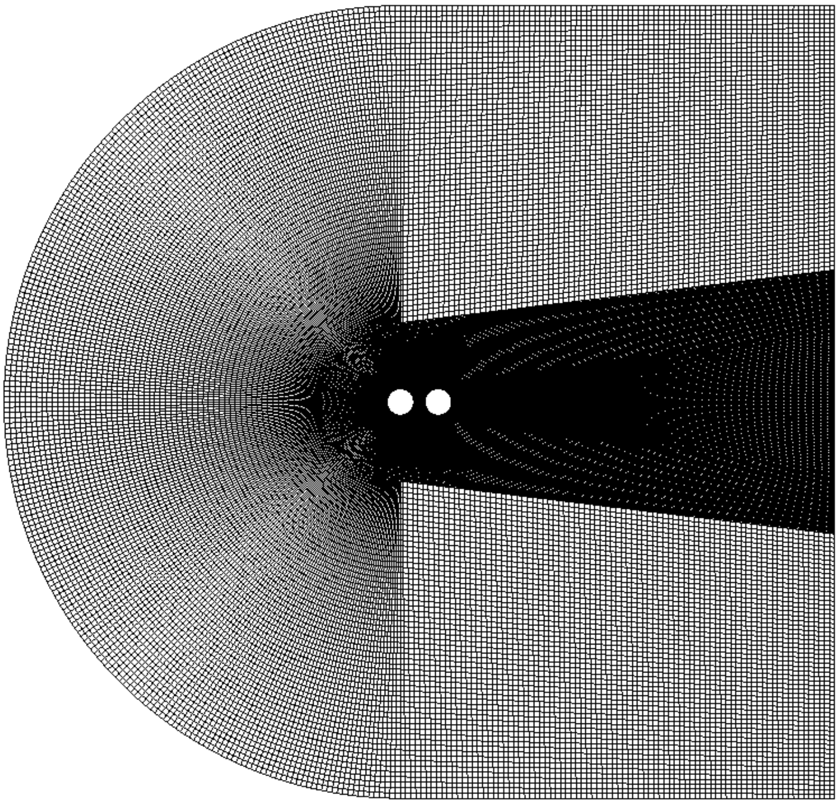

Figure 5.7: View of the global mesh in the longitudinal plane.

First, the mesh is generated in the top half of the domain: the meshes in the two regions are created separately with two-dimensional mapped blocks, using ANSYS Icem CFD (see the gray blocks scheme in Figure 5.9). Then the two meshes are merged and extruded in the spanwise direction. Finally, the mesh is mirrored around the symmetry plane (keeping both halves) directly in OpenFOAM, before running the simulations. The only difference between the URANS2D mesh and the DES mesh is the number of extruded elements, since OpenFOAM$^{\circledR}$needs a three-dimensional mesh with only one element in the spanwise direction for two-dimensional simulations. On the contrary, in the DES the mesh was extruded with 60 elements along 3 diameters in the spanwise direction.

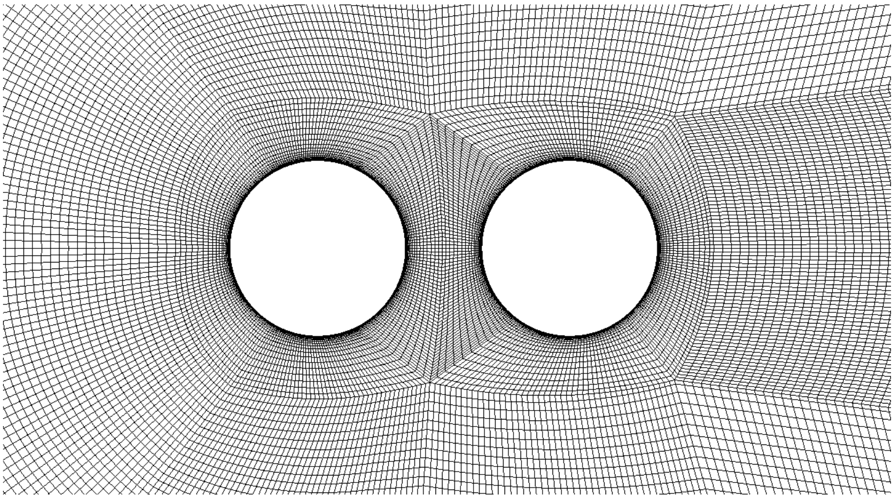

Figure 5.8: View of the mesh in the refined region (longitudinal plane).

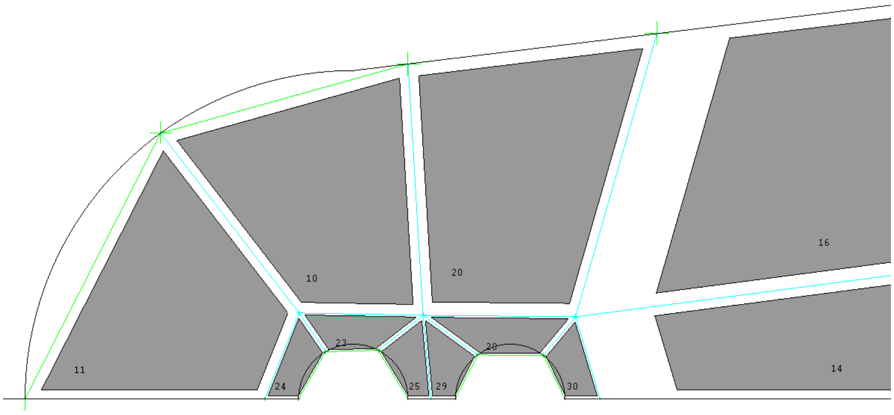

Figure 5.9: Detail view of the blocking scheme in the inner mesh region (11 mapped blocks for half domain).

The boundary layer mesh on both cylinders grows from an initial height of 1×10^{-4} D on the surface with a rate 1.2, until reaching a height of 0.05 D. The surface element size is 0.01 D. In order to assess the convergence of the results with increasing number of elements, the simulations were repeated on a set of three different meshes, which are detailed in Table 5.1.

Table 5.1: Reference sizes for the three meshes used in tandem-cylinder case.

Grid name	**N. spanwise cells**	**Total n. cells**
Coarse	60	3.5 M
Medium	60	5.7 M
Fine	60	8.8 M

The coarse mesh can be considered a first attempt of DES simulation. The reason is that the aim is not to reproduce the experimental results with the highest possible accuracy, but to find the best compromise in terms of accuracy and computational cost. The y^+ number is always kept below 1.

5.2.2 Simulations setup

The required Reynolds number for the simulation is $Re = 1.66 \times 10^5$. In order to run the non-dimensional simulation in OpenFOAM, the viscosity associated with a unitary free-stream velocity and diameter (the mesh was created using $D = 1$) has to be calculated. The viscosity for the simulation is thus the inverse of the Reynolds number $\nu = 1/Re$, equal to 6.024×10^{-6}. Consequently, the free-stream velocity that is needed as a boundary condition is $U_\infty = 1$.

The boundary conditions are reported in Table 5.2 and Table 5.3 separately for the two simulations. The inlet includes the arc and the two straight boundaries parallel to the streamwise flow direction, the outlet is the vertical straight boundary at the end of the domain. The surface of the cylinders are treated as a wall with a no-slip condition, and the spanwise boundaries of the domain (that are distant three diameters in spanwise direction) are treated as periodic faces in the DES case.

Table 5.2: Boundary conditions for the URANS2D simulation.

Field	**Inlet**	**Outlet**	**Cyl. surface**
U	fixedValue = 1	inletOutlet	fixedValue
p	zeroGradient	fixedValue = 0	zeroGradient
ν_t	fixedValue = 6×10^{-5}	inletOutlet	fixedValue = 0
$\tilde{\nu}$	fixedValue = 6×10^{-5}	inletOutlet	fixedValue = 0

Table 5.3: Boundary conditions for the DES simulation.

Field	**Inlet**	**Outlet**	**Cyl. surface**	**Front/back planes**
U	fixedValue = 1	inletOutlet	fixedValue	periodic
p	zeroGradient	fixedValue = 0	zeroGradient	periodic
ν_{SGS}	fixedValue = 6×10^{-5}	inletOutlet	fixedValue = 0	periodic
$\tilde{\nu}$	fixedValue = 6×10^{-5}	inletOutlet	fixedValue = 0	periodic

The periodic boundary conditions are imposed with the new Arbitrary Mesh Interface (AMI) *periodic* boundary conditions in OpenFOAM®. This makes it possible to have periodic boundary conditions without renumbering the nodes on the surfaces, or even with meshes that are totally different on the two periodic surfaces. Since the DES mesh is extruded in the spanwise direction, the interpolation error given by the AMI interface is negligible: the two periodic planes have exactly the same mesh but with a different numbering order of the nodes.

The URANS2D simulations started from the RANS steady solution, using the same turbulence model. In contrast DES was initialised with the velocity and the pressure of the RANS steady solution, with the numerical viscosities $\tilde{\nu}$ and ν_{SGS} at a value 100 times higher than the free-stream value to speed-up the convergence. In comparison to the URANS2D case, in DES the sub-grid-scale viscosity ν_{SGS} is effectively different from the turbulent viscosity ν_t.

5.2.3 Results comparison

The simulations were run for a sufficient number of time-steps to obtain flow independence from the starting condition and then the data were acquired for more than 100 convective dimensionless time units (based on the diameter and the free-stream velocity). For DES the acquisition time required for the statistics is normally not less than 200 non-dimensional time units. For example, the URANS2D was run starting from the RANS steady solution for 245 dimensionless time units and post-processed using additional 250 dimensionless time units.

The simulations reported in this section are all with characteristic length taken as the cubed-root of the element volume, though a sensitivity analysis to both criteria were carried out for different grids. The results with the two criteria are slightly different, but at convergence they are less important than the comparisons proposed in these pages, for example with different turbulence models.

The convergence analysis presented in Figure 5.10 shows that results from different meshes are in good agreement in spite of the significantly different number of elements of the grids. The residuals for a sample simulation on tandem cylinders are shown in Figure 5.11, where it can be seen that for each timestep the final residuals are are below 10^{-6} for the pressure and below 10^{-8} for the three velocity components.

The resulting mean pressure coefficient for the middle cross section is illustrated in Figure 5.12 for the two-dimensional simulations and in Figure 5.13 for our DES. In both figures, our results are compared with previous results by Khorrami et al. [37].

It can be noted that the pressure coefficients in Figure 5.12 of the two-dimensional URANS2D case are in good agreement with the two-dimensional CFD case at $AOA = 0\,\text{deg}$ (zero angle of attack) by Khorrami et al. [37]. The front cylinder pressures for the two compared 2D cases are exactly the same: the negative peak of C_p is at about 70 deg with a value -1.6; the aft part pressure coefficient is at about -0.6 excepting the hump in the 180 deg area, where it goes beyond -0.5. On the rear cylinder, there is a small discrepancy in the pressure coefficient value (-0.1 instead of -0.2 approximately)

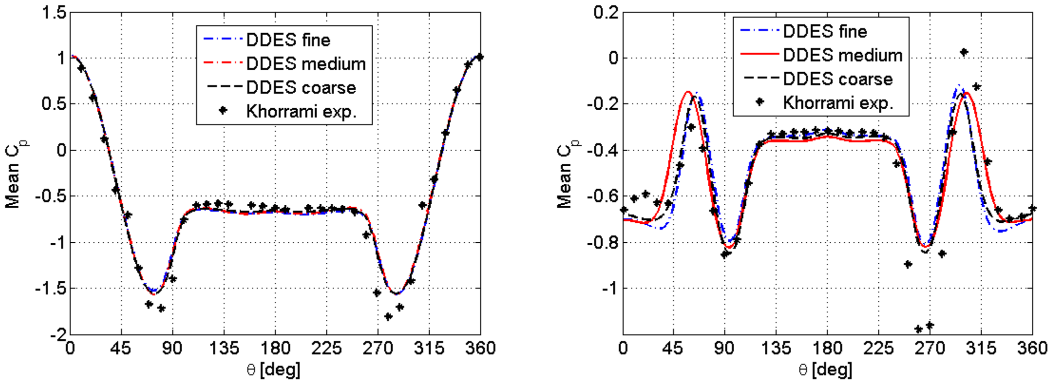

(a) Front cylinder (b) Rear cylinder

Figure 5.10: Mean pressure coefficient on the cylinders cross section: results for the DDES case with three different meshes (coarse, medium, fine) compared with experiments by Khorrami [37].

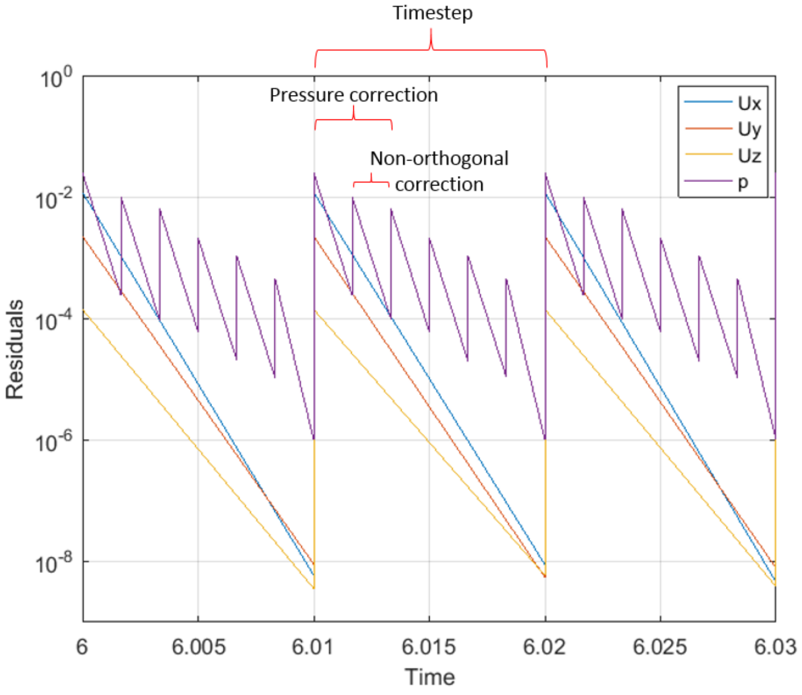

Figure 5.11: Residuals for the PIMPLE algorithm operated in PISO mode (1 outer loop) for a sample tandem-cylinder case. The three velocity components are solved once per timestep, while the pressure is corrected 3 times per time-step with an additional non-orthogonal corrector for each pressure correction. The final residuals for each timestep are below 10^{-6} for the pressure and below 10^{-8} for the three velocity components.

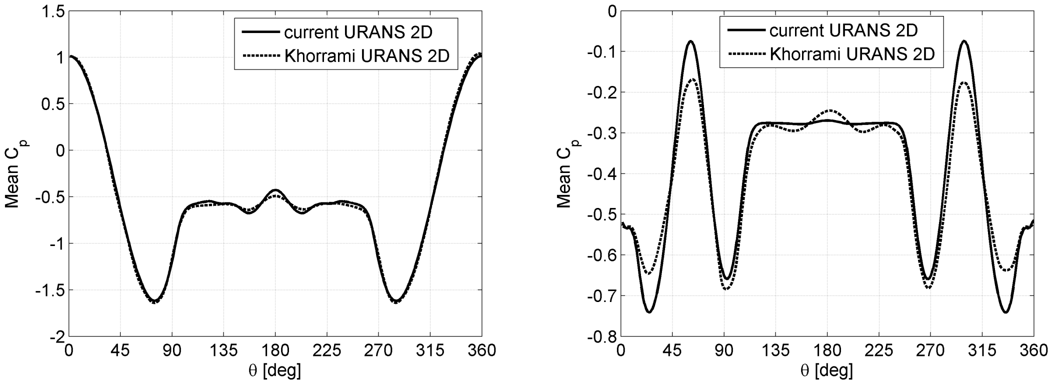

(a) Front cylinder (b) Rear cylinder

Figure 5.12: Mean pressure coefficient on the cylinders cross section: results for the URANS2D case compared with 2D unsteady RANS by Khorrami [37].

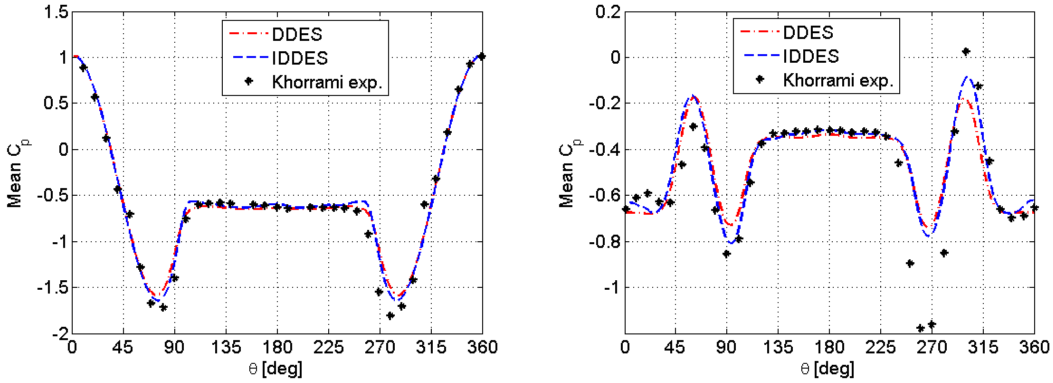

(a) Front cylinder (b) Rear cylinder

Figure 5.13: Mean pressure coefficient on the cylinders cross section: results for the DDES and IDDES cases compared with experiments by Khorrami et al. [37].

between the URANS2D and the experiments. The two suction zones at are found properly, but the pressure value on the second suction zone at about 90 deg is closer to the simulation by Khorrami et al. [37] than the first suction at 30 deg. This difference is due to the fact that the flow is massively separated before the first suction area: the RANS method is well known to behave incorrectly in this kind of region and the grid is less refined than the grid used in Khorrami et al. [37]. The aft pressure on the rear cylinder is the same for the two compared 2D simulations.

The two current DDES and IDDES simulations and the experimental data from Khorrami et al. [37] are compared in Figure 5.12. In fact both should be able to represent the three-dimensional effects of the flow past two tandem cylinders. The front cylinder shows the same behaviour for both, including the area at 180 deg that changes from the hump of the two-dimensional cases to a flat profile. The mean flow is slightly asymmetric in the IDDES simulation; a possible explanation is that the time of acquisition for the post-processing was not sufficient, though the flow was averaged in the spanwise direction z for each angle θ. Another possible reason is that the three-dimensional flow is effectively bi-stable for zero angle of attack.

Better agreements are found substituting the S-A f_{v3} formulation, which is the default S-A in OpenFOAM®. The results are shown in Figure 5.14: the standard formulation is a better approximation than that obtained using the fv3 formulation.

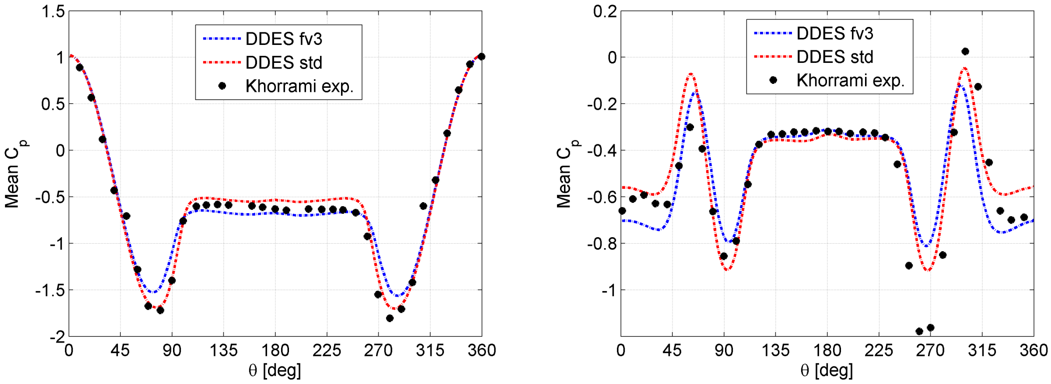

(a) Front cylinder (b) Rear cylinder

Figure 5.14: Mean pressure coefficient on the cylinders cross section: results for the DDES cases with S-A f_{v3} formulation and standard formulation, both compared with experiments by Khorrami et al. [37].

A final verification is performed with three different time-steps using the fine mesh and the standard DDES formulation. The results are shown in Figure 5.15. No differences can be observed for the mean pressures on the front wheel, whilst minor differences on the suction peaks can be observed for the mean pressures on the rear wheel in the high-pressure regions on the front and the suction regions. In spite of doubling the time-step for each simulation, the differences are of the order of $\Delta C_p \approx 0.01$. All the chosen time-steps produce results that are reasonably close to the experimental data, but the solution time per unit of simulated time is approximately double when halving the time-step.

In the two-dimensional simulation, a strong damping can be observed, as shown in Figure 5.16 for the lift coefficient on the front cylinder: even if the flow starts with a strong unsteady component, it is damped in less than one hundred convective times based on the diameter. This behaviour was also found by Khorrami et al. [37], for the case $L/D = 1.435$. On the contrary, looking at the lift coefficient for the DES simulation (in Figure 5.17), the flow is much more chaotic and there is no evidence of such a damping. The time axis in Figure 5.16 and Figure 5.17 cannot be compared directly because effectively the two simulations started with different initial conditions.

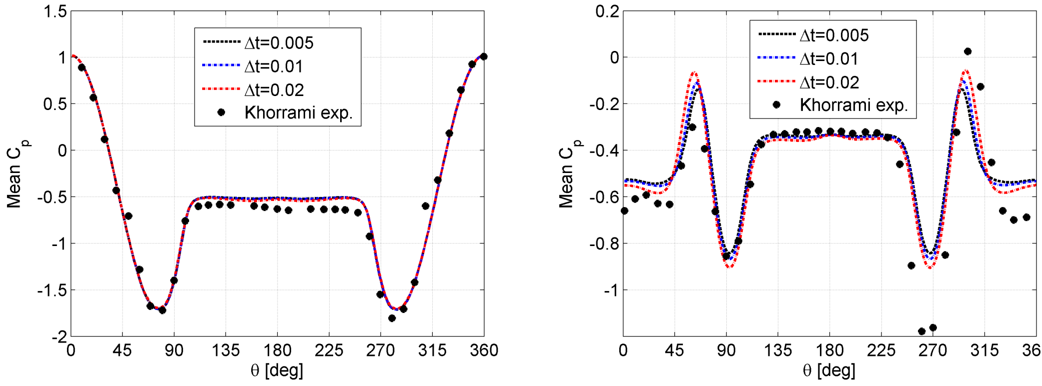

(a) Front cylinder (b) Rear cylinder

Figure 5.15: Mean pressure coefficient on the cylinders cross section: results for the DDES cases with S-A standard formulation with three different time-steps, in comparison with the experiments by Khorrami et al. [37].

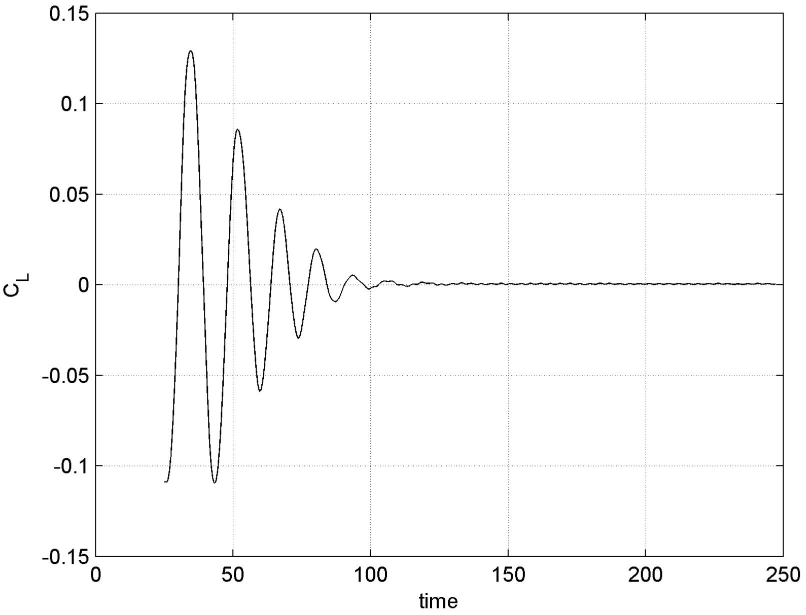

Figure 5.16: Lift coefficient for the front cylinder in the URANS2D simulation.

For DES cases, the unsteady velocity field is analysed using a probe at a streamwise distance $x = 2.7D$ from the axis of the rear cylinder and at a vertical location $y = -0.69D$, as in the paper by Khorrami et al. [37] (shown in Figure 5.6). The probe is in the mid-span plane for the DES case. The power spectral density (PSD) for the DDES cases is reported in figures 5.18: in the experiments considered as reference for this case, only one peak is found in the PSD of the velocity perturbation, at the frequency $St = 0.28$. The peak at $St = 0.27$ could be due to the sampling time that is smaller than in the experiments.

An image of the DES, by means of the Q-criterion, is reported in Figure 5.19, in which the

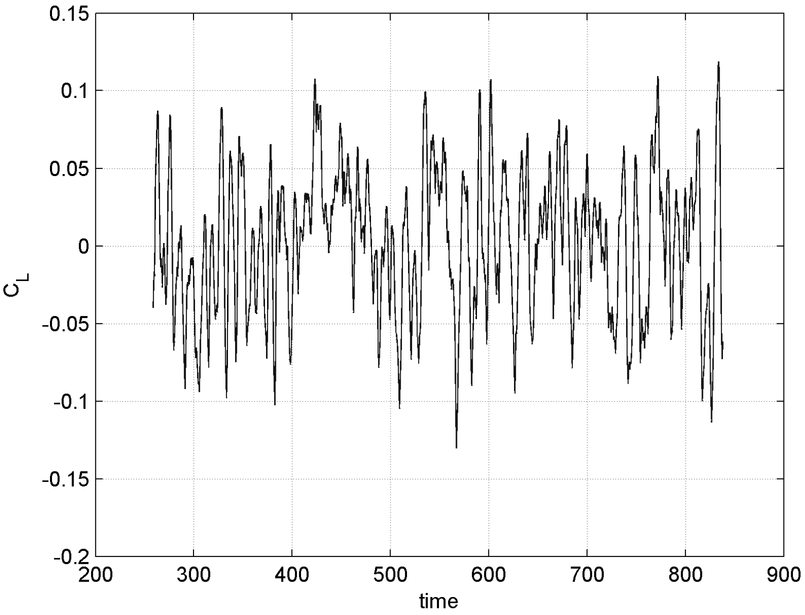

Figure 5.17: Lift coefficient for the front cylinder in the IDDES simulation.

visual confirmation of the vortex shedding phenomenon and of the presence of spanwise fluctuations is clear.

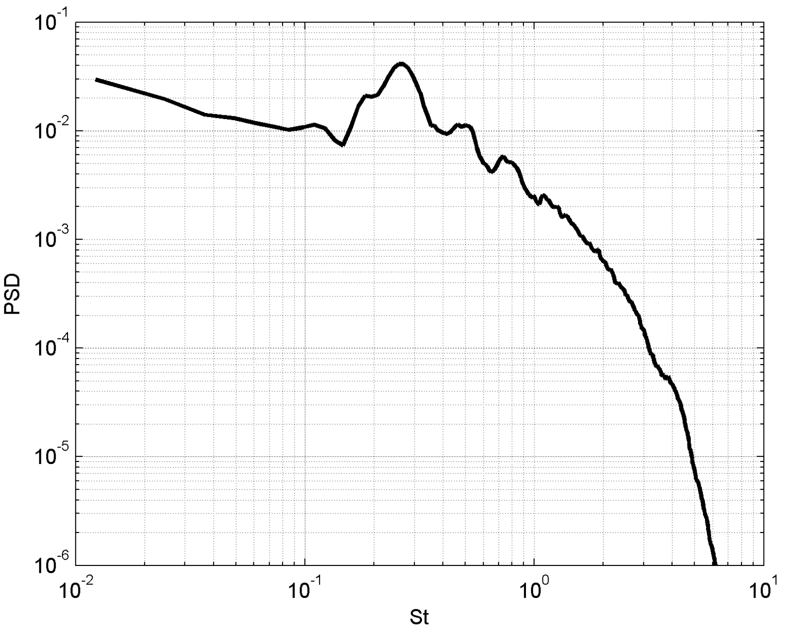

Figure 5.18: Power spectral density of the DDES case: streamwise velocity component at probe location $(4.135, -0.69, 1)D$, see Figure 5.6.

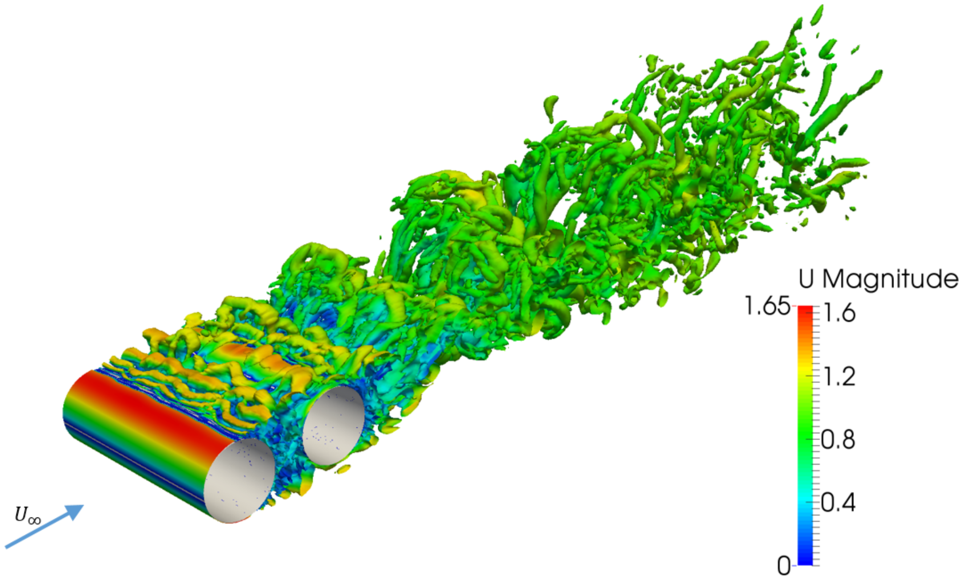

Figure 5.19: Flow visualisation of IDDES case by means of Q-criterion contours ($Q = 0.5$). The flow comes from bottom left.

5.3 Summary of the used methodologies

Steady RANS solutions can be used to initialise DES in OpenFOAM®. This means that less computational time is required for the DES simulations. The simulations, which usually need to be run for at least 400 dimension-less time units (based on free-stream velocity and diameter) to provide reliable frequency spectra. If one is interested in unsteady values more than in mean values, in spite of the finer mesh needed, it is recommended to use advanced simulations like DES. Unsteady RANS tend to have a high damping that does not allow the generation of a reliable frequency spectrum, as shown here for the tandem cylinders.

Nevertheless, even though DES meshes are computationally demanding both in terms of grid size and required simulation time needed, it is necessary to prove the mesh convergence with grid refinements. The major issues would be in the case of *no-eddy* simulation, which could be the case if the grid size is too coarse: differently from RANS, DES could give data with a significant discrepancy in this case.

Finally, advanced simulations are also available in a variety of models and versions. Different versions of the DES turbulence model can be tried to gain a better understanding of its importance, as proved here with IDDES and DDES, or with SA-fv3 and SA-std versions of the S-A model. The turbulence model on which the DES model is built is not a secondary consideration: between the SA-fv3 and the SA-std version of the S-A model, significant differences can be observed, even with the mean values.

Chapter 6

Experiments on Single and Tandem Wheels

In this chapter the experiments on the single and tandem wheels are described. It is the key chapter in terms of experimental results on the new tandem-wheel geometry and the new application of the vibration test in wind tunnels. The details on the wind-tunnel model are given in Chapter 3. The contents of this chapter are also published in the conference paper [75] and, more extensively, in the journal paper [76] (currently under review).

6.1 Experimental Setup and Procedures

6.1.1 Test facility and model geometry

The experiments were conducted at the University of Southampton, in a closed-circuit closed-test-section wind tunnel with a cross-section of $2.1\,\mathrm{m} \times 1.5\,\mathrm{m}$. The wind tunnel can be operated at free-stream velocities U_∞ between $10\,\mathrm{m/s}$ and $48\,\mathrm{m/s}$ corresponding to a Reynolds number $Re_D = U_\infty D_w/\nu$ range between 1.2×10^5 and 5.8×10^5 for the current model (where D_w is the wheel diameter and ν is the kinematic viscosity of air).

The current model consists of two wheels in tandem. The wheel is a generic model of a landing-gear wheel, as shown in Figure 6.1(a). The geometric parameters are defined as follows: the wheel diameter D_w is $0.181\,\mathrm{m}$, the width W is $0.4D_w$, and the fillet radius R is $0.1D_w$ (uniform). Measurements are performed in different configurations for three inter-axis distances L_w ($1.1D_w$, $1.3D_w$ and $1.5D_w$) and three installation angles α (0 deg, 10 deg and 20 deg). The wheels are supported by streamlined struts to minimise the interference. A picture of the tandem-wheel model (mounted in the wind tunnel) is shown in Figure 6.1(b) and a drawing with additional views and cross sections is given in Figure A.1. The two supports are tapered zero-sweep half wings with a NACA-0024 cross section. The length of the support is 300 mm and its taper ratio (tip/root chord ratio) is 0.46. The supports are mounted to have zero installation angle for all the tested configurations. The blockage ratio is between 0.5% and 1%, depending on the specific configuration. The blockage is not expected to affect the flow and the measured data if compared to a free-stream case.

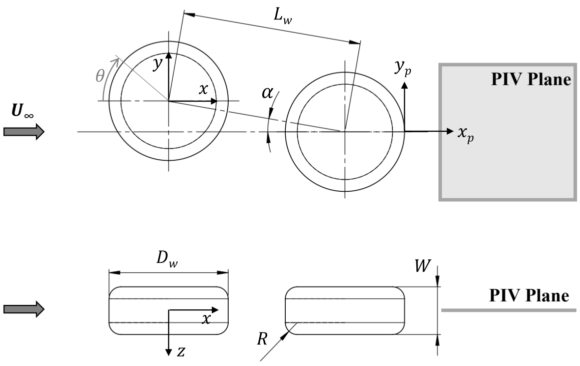

(a) Schematic drawing of a generic tandem-wheel configuration.

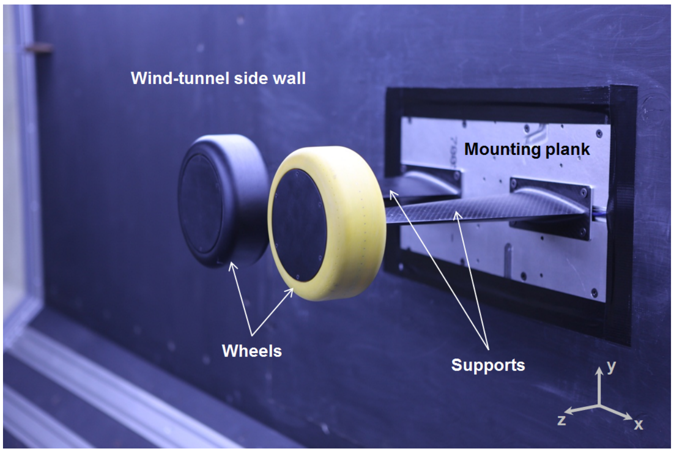

(b) Picture of the wind-tunnel model assembly.

Figure 6.1: Tandem-wheels experimental assembly with the main geometric parameters and the global reference system (x the streamwise, y the vertical, and z the spanwise direction).

The model is manufactured by means of rapid prototyping techniques. In detail, the wheels are made by 3D printing with a LS600 photopolymer machine, while the supports are made of carbon-fibre reinforced plastic (CFRP) and aluminium alloy. The interfaces with the wind-tunnel frame are standard aluminium profiles plus a machined aluminium plate. The manufacturing tolerances for the external wheel surface can be estimated to be ±0.1 mm with respect to the axis system of the 3D-printing machine. The maximum error on the wheels position is ±1 mm.

In this chapter the discussion is focused on the untripped configurations with flat hub cover (Figure 6.1(b)), and all presented results data are from this configuration unless otherwise specified. In Spagnolo et al. [75], a detailed description of the tests with various tripping devices and with wheel covers other than the flat cover is given.

6.1.2 Loads and pressure acquisition systems

In the current work, the forces acting on the two wheels are measured separately. Aerodynamic forces are described in terms of both mean and unsteady values (i.e., the root mean square of the force signal).

A wind-tunnel balance would measure the combined force acting on the wheels and the supports. In order to isolate the force acting on the wheel, an internal force sensor (which measures only the loads acting on the wheels) is fitted inside one of the wheels. The force sensor is an ATI mini40, a 6-axis strain-gauge based transducer. The sampling time is approximately 60 seconds at a frequency of 1000 Hz. The repeatability of the mean force coefficients is within 0.001 at a speed of 40 m/s.

An additional wheel model with identical external shape was manufactured for on-surface data collection. This additional model was designed to host a miniature pressure scanner with multiple channels (instead of the balance) inside the wheel. The pressure scanner is the miniature 64-channels Scanivalve ZOC33. The model is manufactured with 21 equally-spaced holes for pressure taps along a 120-deg sector along the centre-line circumference. Rotating the wheel four times (with each rotation being through 90 deg) allows for acquiring the full circumferential pressure data with a 30 deg overlap for each rotation position. Overall, surface pressure data are available for 60 points equally spaced in the azimuthal angle θ on the full centre-line circumference, with $\theta = 0\,\text{deg}$ representing the most windward point on the circumference. The static reference pressure p_∞ and the reference dynamic pressure $\rho U_\infty^2/2$ are directly provided by a Pitot tube positioned in the test section. Two different sampling frequencies were tested, 113.6 Hz and 568.2 Hz for each channel, and no difference was found in the results. The results are shown for the 113.6 Hz sampling frequency.

In total, there are three available wheel models: one wheel is equipped with the pressure sensor, one wheel is equipped with force sensors and one wheel is not instrumented. Pressure measurements and force measurements are not performed simultaneously because of the slightly different procedures. Normally, when testing the wheels in a tandem configuration, one wheel is instrumented and the other wheel is not instrumented, then the two wheels are swapped to acquire the data for the other wheel.

6.1.3 Vibration test and unsteady loads

The strain-gauge based balance inside the wheel model quantifies the forces by means of the strain of the balance itself. For dynamic load measurements, at high frequencies the sensor measures the dynamic response of the model assembly [58]. In addition, the dynamic response is generally different in each direction, and the modes are coupled: this means that even forcing the model in one direction only, the balance measures non-zero dynamic values in the other components. Here, the aerodynamic unsteady loads are validated by a preliminary vibration test to identify the model dynamic response. The vibration test must be performed *in situ*: the model is mounted in the wind tunnel and an electro-magnetic shaker is used to force the model in different spots. The vibration-test equipment consists of a Data Physics Signal-Force GW-V4/PA30E shaker and a Dytran 1053V piezoelectric force sensor. The shaker can provide both a random and a sinusoidal force, which is transmitted to the model through the piezoelectric force sensor.

The force measured by the force sensor inside the model and the excitation force are simultaneously acquired. To understand the accuracy of the measured dynamic values, the transfer function between the external forces and the measured values from the balance can be calculated. The transfer functions T for excitation forces along each of the two axes x and y are given in Figure 6.2, which shows that the unsteady load data measured by the balance are consistent with the externally applied loads up to approximately 30 Hz. The transfer functions were obtained in the wind-tunnel for one configuration only, but similar transfer functions can be assumed for the other configurations since the only difference is the position of the supports on the mounting plate, which has minimal effects on the dynamic response of the structure.

The transverse sensitivity can be attributed to the mode coupling phenomena, positioning or alignment errors in the shaking system, and additional modes relative to the wind tunnel mountings or to minor features of the model. The transverse sensitivity (not shown) is within 15% of the external load. The transfer functions of the moments show analogous results, with less accuracy, due to the lower intensity of the moments applied. In the following sections of the current work, only the F_x and F_y forces are considered, both in terms of mean loads and unsteady loads.

The vibration test allows the calculation of the cut-off frequency on the basis of the model response with a clear identification of the ratios between the external forces and the measured forces, for each axis.

6.1.4 PIV setup

The current PIV setup uses a single 4 Megapixel camera equipped with a Sigma lens of 105 mm focal length to acquire the two in-plane components within a square frame

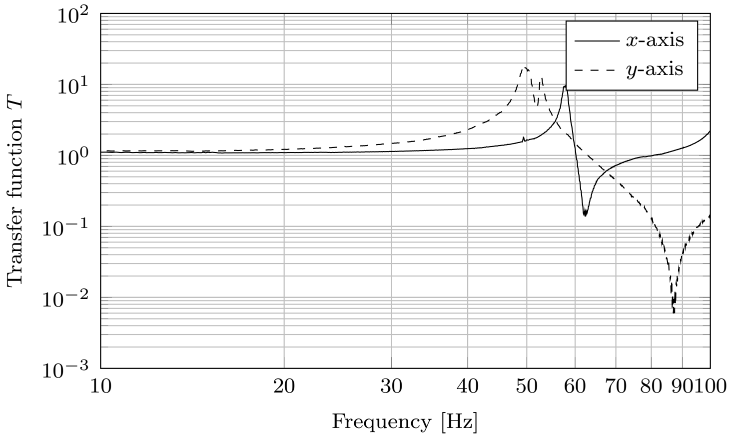

Figure 6.2: Transfer function from the vibration test with external force applied along the x-axis and along the y-axis.

behind the rear wheel. The reference axes x_p-y_p for the PIV frames are positioned at the most downwind point of the rear wheel, as illustrated in Figure 6.1(a). For single-wheel configurations the front wheel is removed. The fields are measured only at a free-stream velocity $U_\infty = 40\,\mathrm{m/s}$ on the wheel centre-line plane ($z = 0$), in Figure 6.1(a).

The camera is mounted at a distance of approximately 1.8 m from the target plane, outside the wind tunnel. The laser, a Quantel Twins BSL 200, is configured to fire two consecutive shots with a 20 μs delay. The frame acquisition is repeated at a frequency of 3.63 Hz for 500 frames. The results reported in Section 6.2 are shown for a frame of 200 mm × 200 mm. Each frame is dived into 32 × 32 windows with 50% overlap to extract the velocities.

To estimate the maximum relative errors, ϵ_μ and ϵ_σ, on the resulting mean velocity component $\overline{U}_i$ and its standard deviation $U_{\mathrm{RMS},i}$, the following formulas (Grant and Owens [25]) are applied:

$$\epsilon_\mu = \frac{z_c U_{\mathrm{RMS},i}}{\overline{U}_i \sqrt{N}} \tag{6.1}$$

$$\epsilon_\sigma = \frac{z_c}{\sqrt{2N}} \tag{6.2}$$

where N is the number of samples and z_c is the confidence coefficient (here assumed equal to 1.96, which corresponds to a 95% confidence level for a normal distribution).

For the current tests, the error on the mean fields is lower than 1.6 m/s and the error on the standard deviation is within 1 m/s (both with a confidence level of 95%). The errors are higher in the region close to the wheel, and become smaller further away. This is because the turbulence level is high, affecting the statistical estimation of the error in Equation 6.1 and Equation 6.2.

6.1.5 Proper Orthogonal Decomposition (POD)

The POD is applied to the velocity fields from PIV to recognise the most energetic patterns in the wake. The POD methodology used is the snapshot POD by Sirovich [70]. The analysis is performed on the fluctuating part of the two velocity components (u_j^n, v_j^n) components captured in the PIV, where j is the index of the point and n is the index of the frame number. The velocity components are ordered in a matrix $\mathbf{U}$ of size $2M \times N$, where M is the number of velocity components for each snapshot and N is the number of acquired snapshots.

$$\mathbf{U} = \left[\mathbf{u}^1 \mathbf{u}^2 \dots \mathbf{u}^N\right] = \begin{bmatrix} u_1^1 & u_1^2 & \dots & u_1^N \\ \vdots & \vdots & \vdots & \vdots \\ u_M^1 & u_M^2 & \dots & u_M^N \\ v_1^1 & v_1^2 & \dots & v_1^N \\ \vdots & \vdots & \vdots & \vdots \\ v_M^1 & v_M^2 & \dots & v_M^N \end{bmatrix} \tag{6.3}$$

The eigenvalue problem

$$\tilde{\mathbf{C}}\mathbf{A}^i = \lambda^i \mathbf{A}^i \tag{6.4}$$

has to be solved. $\tilde{\mathbf{C}}$ is the autocovariance matrix that is defined as $\tilde{\mathbf{C}} = \mathbf{U}^t\mathbf{U}$. After reordering the eigenvalues in decreasing order, the eigenvectors can be used to generate the POD modes:

$$\phi^i = \frac{\sum\limits_{n=1}^{N} A_n^i \mathbf{u}^n}{\left\| \sum\limits_{n=1}^{N} A_n^i \mathbf{u}^n \right\|} \tag{6.5}$$

with $i = 1, \dots, N$, and A_n^i the n-th component of the eigenvector corresponding to λ_i. The discrete 2-norm is defined as:

$$\|y\| = \sqrt{y_1^2 + y_2^2 + \dots + y_M^2} \tag{6.6}$$

The POD modes ϕ^i can be grouped in a matrix $\mathbf{\Phi} = \left[\phi^1 \phi^2 \cdots \phi^N\right]$. The POD coefficient a_i for the i-th mode can be obtained by projecting the fluctuating velocity components onto the POD modes:

$$\mathbf{a}^n = \mathbf{\Phi}^t \mathbf{u}^n \tag{6.7}$$

The outcome of the POD analysis is presented in 6.2.3. This includes the energy contents associated with the modes and the cumulative energy content for both the single wheel and the tandem wheels.

6.1.6 Surface oil-flow visualisation

The use of the oil flow visualisation technique provides insight to the flow features on the surface of the wheels. The visualisation liquid is applied on the surface of the wheels and the wind tunnel is run for approximately 10–15 minutes at $Re_D = 4.8 \times 10^5$. At the end of each run, most of the liquid is dried and only the pigments are left on the surfaces.

6.2 Results and Discussion

6.2.1 Effects of Reynolds number

The model was tested up to a Reynolds number of 5.7×10^5, which is approximately one order of magnitude lower than a full-scale landing-gear. In this section, the effect of Reynolds number on the flow past a single wheel and tandem wheels is analysed. The mean drag coefficient $\overline{C}_D$ of the single wheel and one reference configuration of tandem wheels ($L_w = 1.5D_w$ and $\alpha = 0\,\mathrm{deg}$) are shown as functions of Reynolds number Re_D in Figure 6.3. The force coefficients are calculated with the frontal projected area $S = 0.012\,85\,\mathrm{m}^2$. Both for the single wheel and the tandem wheels, the mean drag coefficient generally decreases with Reynolds number. For Reynolds numbers in the range $3.6 \times 10^5 < Re_D < 5.7 \times 10^5$, the mean drag coefficient is approximately constant for the rear wheel in the tandem configuration, whilst it retains a slightly negative slope on the single wheel and the front wheel in the tandem setup. The RMS of the force coefficients show similar dependency on Reynolds number.

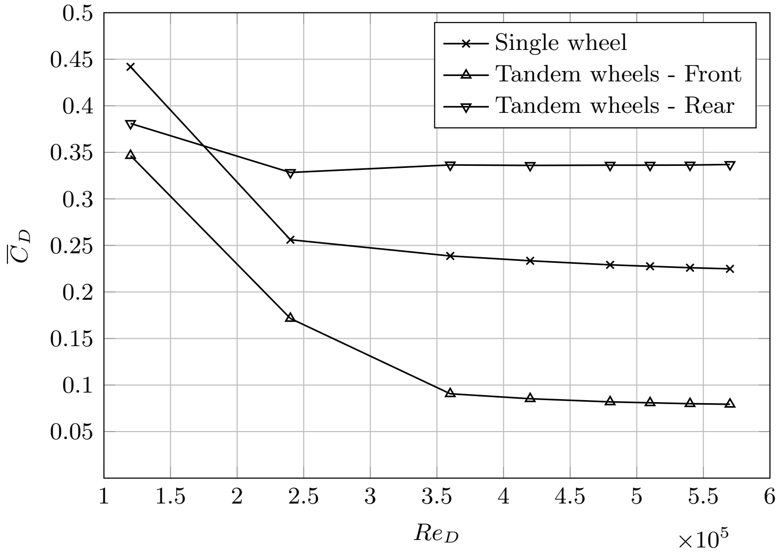

Figure 6.3: Mean drag coefficient $\overline{C}_D$ as a function of Reynolds number Re_D for single and tandem wheels ($L_w = 1.5D_w$ and $\alpha = 0\,\mathrm{deg}$), untripped.

The flow is dependent on Reynolds number because of the laminar flow features that are present on the wheel surface in this flow regime. The evolution of the pressure coefficients on the wheel centreline with increasing Reynolds numbers is given in Figure 6.4 for the single wheel. Similarly to what happens on a circular cylinder, the position of the suction peaks moves towards the rear of the wheel with more pronounced peaks for increasing Reynolds numbers until the value stabilises at $\overline{C}_p = -0.9$ above $Re_D = 3.6 \times 10^5$, which is the same Reynolds number that marks the beginning of the low-slope part of the curve in Figure 6.3. The two blips on the curves of $\overline{C}_p$ (located at approximately 120 deg and 240 deg) and the corresponding peaks of $C_{p,\mathrm{RMS}}$ indicate the presence of two recirculation bubbles. The plateau in the pressure coefficient is a typical feature of separation bubbles.

In order to understand the extent to which this feature affects the flow, pressure coefficients C_p for the untripped and the tripped configurations (Spagnolo et al. [75]) of the single wheel are compared in Figure 6.5 at $Re_D \approx 4.8 \times 10^5$. The tripping technique used is zig-zag tape on the front part of the wheel. The blips are present in the untripped configuration only, at approximately 120 deg and 240 deg, as it has been previously shown. Instead, in the tripped configuration, these features are not identifiable in the $\overline{C}_p$ plot, whilst it is still possible to observe the corresponding peaks in the $C_{p,\mathrm{RMS}}$ plots. In Figure 6.6, the recirculation bubble on the untripped configuration is shown with the oil-flow visualisation. The top bubble is located on the wheel surface at approximately $100\,\mathrm{deg} < \theta < 120\,\mathrm{deg}$ on the wheel surface. This feature is related with the laminar-turbulent transition and it becomes less important with increasing Reynolds number. The change of the surface flow features between the untripped and the tripped configurations can also be seen in Figure 6.7, where the picture at the top for the untripped single wheel reveals the presence of the separation bubble at $100\,\mathrm{deg} < \theta < 120\,\mathrm{deg}$ followed by a reattachment. The flow does not show the same feature for the tripped case (bottom picture). Instead a similar recirculation area is present but it is in the separation region for $\theta > 130\,\mathrm{deg}$. The added tripping promotes the flow transition and keeps it attached for longer.

Additional separation bubbles are located in the proximity of the wheel side, as indicated in Figure 6.8. With the experimental apparatus for pressure measurements, the lateral separation bubble cannot be captured. It can only be seen in the oil-flow visualisations. Thus, the laminar separation bubbles are expected to be the main cause of the Reynolds number dependency. On the tandem wheels, only the top separation bubble is visible on the rear wheel at high installation angles, as in Figure 6.9. This is because the top part of the wheel is not contained in the wake of the front wheel. As it was found in Figure 6.3, at low angles of attack, the variation of the force coefficients on Reynolds number is low because the flow impinging on the rear wheel is turbulent and no Reynolds-dependent features are present. On the contrary, the separation bubbles are always present on the front wheel, which shows a curve similar to that of the single wheel. Also in this

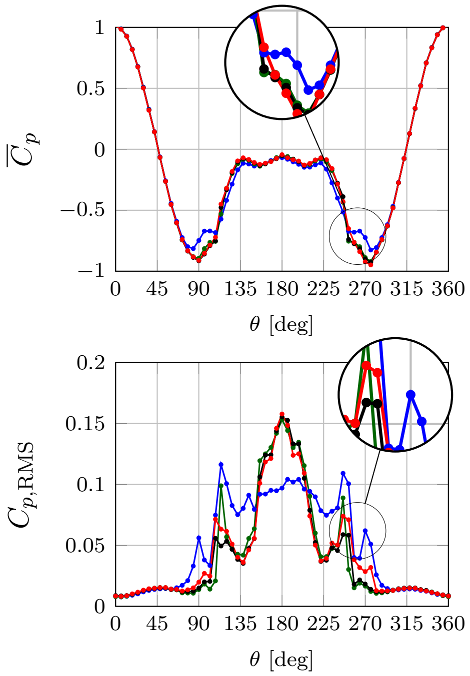

Figure 6.4: Single wheel, untripped case: mean and RMS values of C_p along the wheel centreline, comparing various Reynolds numbers Re_D: 2.7×10^5 (—•—), 3.6×10^5 (—•—), 4.8×10^5 (—•—), and 5.6×10^5 (—•—).

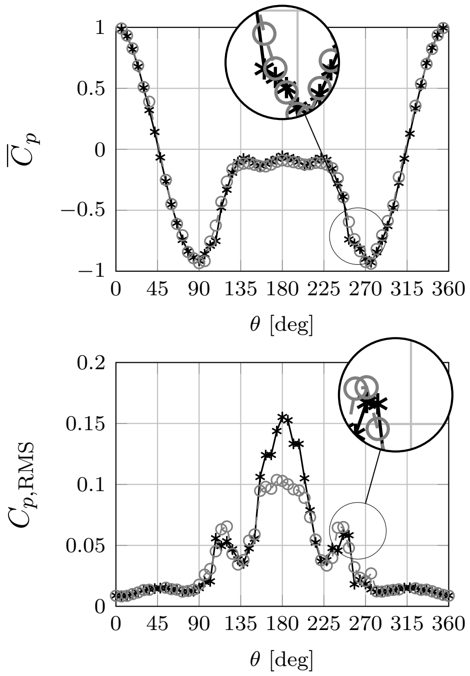

Figure 6.5: Single wheel ($Re_D \approx 4.8 \times 10^5$): mean and RMS values of the pressure coefficient C_p along the wheel centreline, comparing the untripped (—✱—) and the tripped (- ⊖ -) case.

case, the bubbles can be observed on the plots of the pressure coefficients shown later in Section 6.2.4. The laminar separation bubbles are not visible in the configurations with tripping devices (not shown), similarly to what happens in the single wheel case.

As mentioned in Section 6.1, the single wheel was tested also with two additional versions of the cover. The mean drag coefficient for the single wheel at 40 m/s was 0.238 with the cavity-only cover, while it was 0.241 with the cover including the simplified hub. Generally, the effect of the two additional covers is small, since an increase in drag coefficient within 5% from the baseline geometry with flat cover is observed. This is also confirmed by previous tests on the CADWIE wheel [98]. For this reason, no further tests were performed.

Overall, the analysis of the flow features reveals that the flow on the single wheel and on the front wheel of the tandem wheels is affected by laminar-turbulent transitional features, but the dependency on Reynolds number in the range $3.6 \times 10^5 < Re_D < 5.7 \times 10^5$ is generally low if considering the force coefficients. The rear wheel at low angles of attack does not show Reynolds dependency for $Re_D > 3.6 \times 10^5$. All the rest of the data shown in this chapter are given for the untripped configurations.

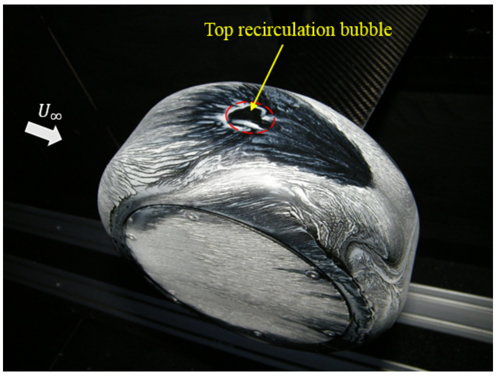

Figure 6.6: Oil flow visualisation on single wheel, top recirculation bubble, untripped configuration at $Re_D \approx 4.8 \times 10^5$.

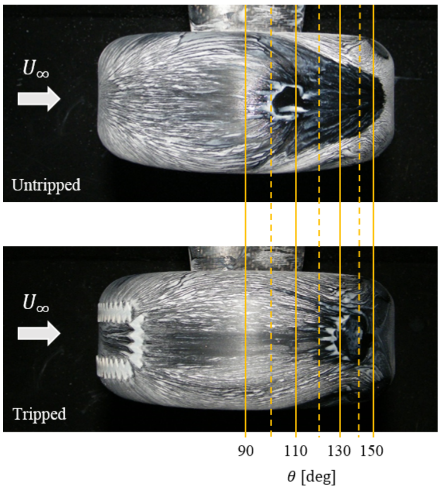

Figure 6.7: Oil flow visualisation on single wheel for both untripped and tripped configurations at $Re_D \approx 4.8 \times 10^5$.

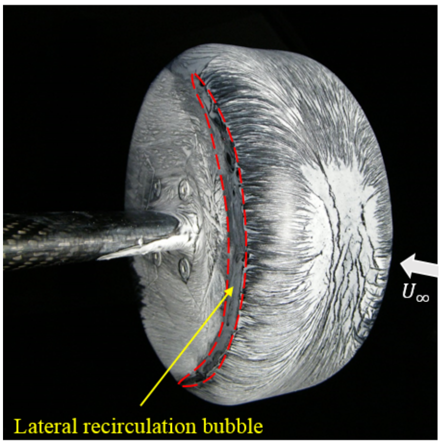

Figure 6.8: Oil flow visualisation on single wheel, lateral separation bubble, untripped configuration at $Re_D \approx 4.8 \times 10^5$.

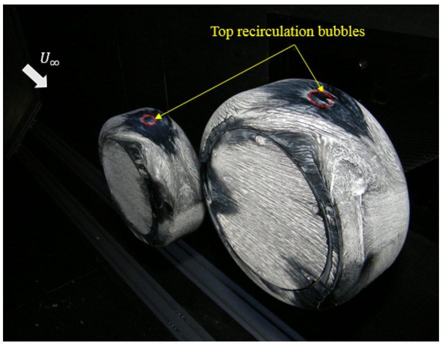

Figure 6.9: Oil flow visualisation on tandem wheels, installation angle $\alpha = 20\,\text{deg}$, at $Re_D \approx 4.8 \times 10^5$.

6.2.2 Flow topology

This section presents a detailed description of the wake structures. As it can be noted from Figure 6.10, the mean flow past the single wheel is made of four distinct vortices, like those found by Zdravkovich et al. [97] on short-aspect-ratio cylinders. The vortices are such that adjacent pairs have opposite streamwise vorticity. Similarly, the flow past tandem wheels is made of four vortices. In Figure 6.10 (left), the pattern left by the vortices on the single wheel can be clearly seen, whilst the pattern left by the vortices behind the rear wheel of the tandem-wheel case in Figure 6.10 (right) is less clear and the size of the vortices appear to be different. It can also be seen that the separation line on the bottom part of the rear wheel has a different shape from that of the single wheel case, which in this case can be associated with the slight asymmetry of the flow. In Figure 6.11, the mean flow past tandem wheels is schematically illustrated. The illustrated flow features were generated with additional information from CFD data (Chapter 7). In general, for tandem wheels, the behaviour of the vortices is different depending on the installation angle.

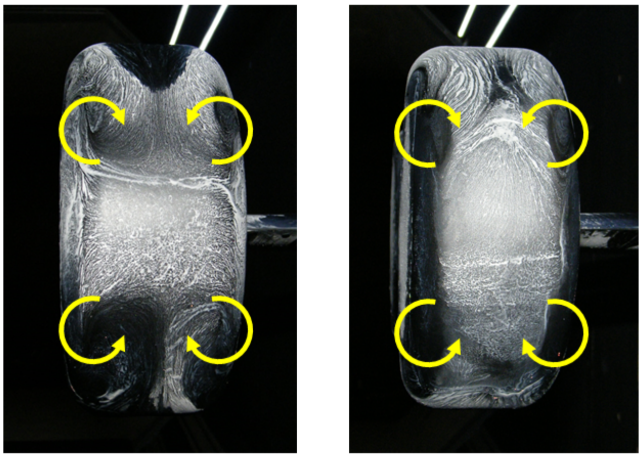

Figure 6.10: Oil flow visualisation on single wheel (left) and tandem-wheel rear wheel (right), rear view with wake vortical system in yellow.

If the installation angle α is zero, as in Figure 6.11(a), the flow shows a system of four vortices that detach from the front wheel and impinge on the rear wheel mixing with the boundary layer on the surface. Two adjacent vortices always contain streamwise vorticity of opposite sign. At low installation angles, a system of four vortices also detaches from the rear wheel. The vortices from the front wheel interact with the boundary layer of the rear wheel, making the flow on the rear wheel substantially different from the flow on an isolated wheel. If no tripping devices are applied on the wheel surface, a laminar separation bubble is present on each side of the front wheel, and two additional laminar separation bubbles are present on the top and the bottom part of the wheel. In contrast, the flow on the rear wheel is fully turbulent because it is fully immersed in the turbulent wake generated by the front wheel.

If the rear wheel is mounted with a high installation angle, such as in Figure 6.11(b) where $\alpha = 20\,\text{deg}$, the vortices detaching from the front wheel do not impinge on the rear wheel. The pair of vortices that detach from the top part of the front wheel are stronger in intensity and size than the pair of vortices detaching from the bottom part because the detachment area is located further downstream. In this case an additional system of four vortices is generated on the rear wheel. In the cases where the rear wheel is not mounted at $\alpha = 0\,\text{deg}$, the flow features on the front wheel are not symmetrical. Also, the rear wheel is partly immersed in the wake of the front wheel, thus laminar features are expected in the areas where clean flow is impinging on the rear wheel. For instance in Figure 6.11(b) only the top recirculation bubble is present on the rear wheel because the bottom part is partly immersed in the wake of the front wheel.

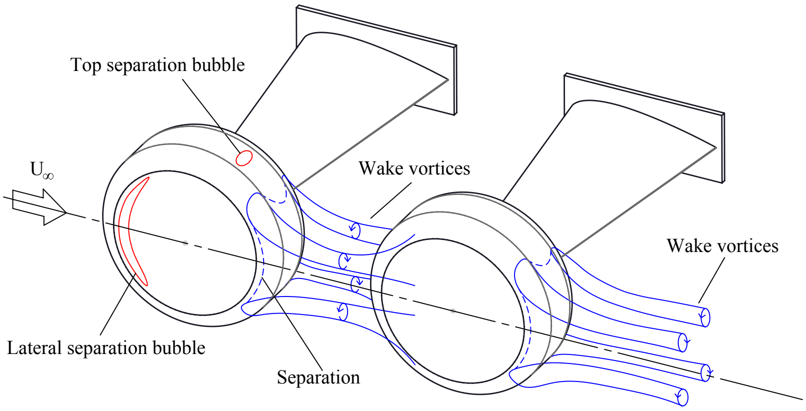

(a) $\alpha = 0\,\mathrm{deg}$

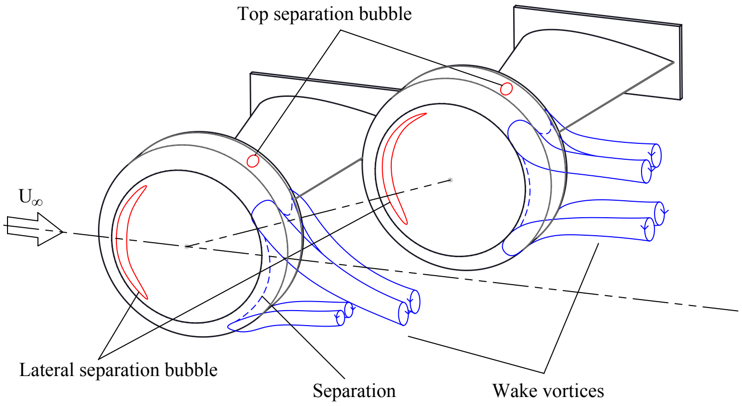

(b) $\alpha = 20\,\mathrm{deg}$

Figure 6.11: Schematic drawing of mean flow features on tandem wheels at $L_w/D_w = 1.5$ and two different installation angles.

A longitudinal plane of the velocity field was acquired in various configurations at constant-z planes. The resulting mean velocity magnitude past the single wheel is shown in Figure 6.12(a) and for one of the tandem-wheel cases ($L_w = 1.5D_w$, $\alpha = 0\,\mathrm{deg}$) in Figure 6.12(b). The mean field past the single wheel is similar to that past the tandem wheels (in the chosen configuration). Both wakes have same shape, but the width of the wake past the tandem wheels is higher. The difference in the size of the wake past the two cases is more evident looking at the 2D turbulent kinetic energy.

Thus, the features in the flow past the tandem wheels can be considered as a combination of flow features past the single wheel. The wake of the flow past tandem wheels is larger and shows stronger fluctuations than in the case with only one wheel.

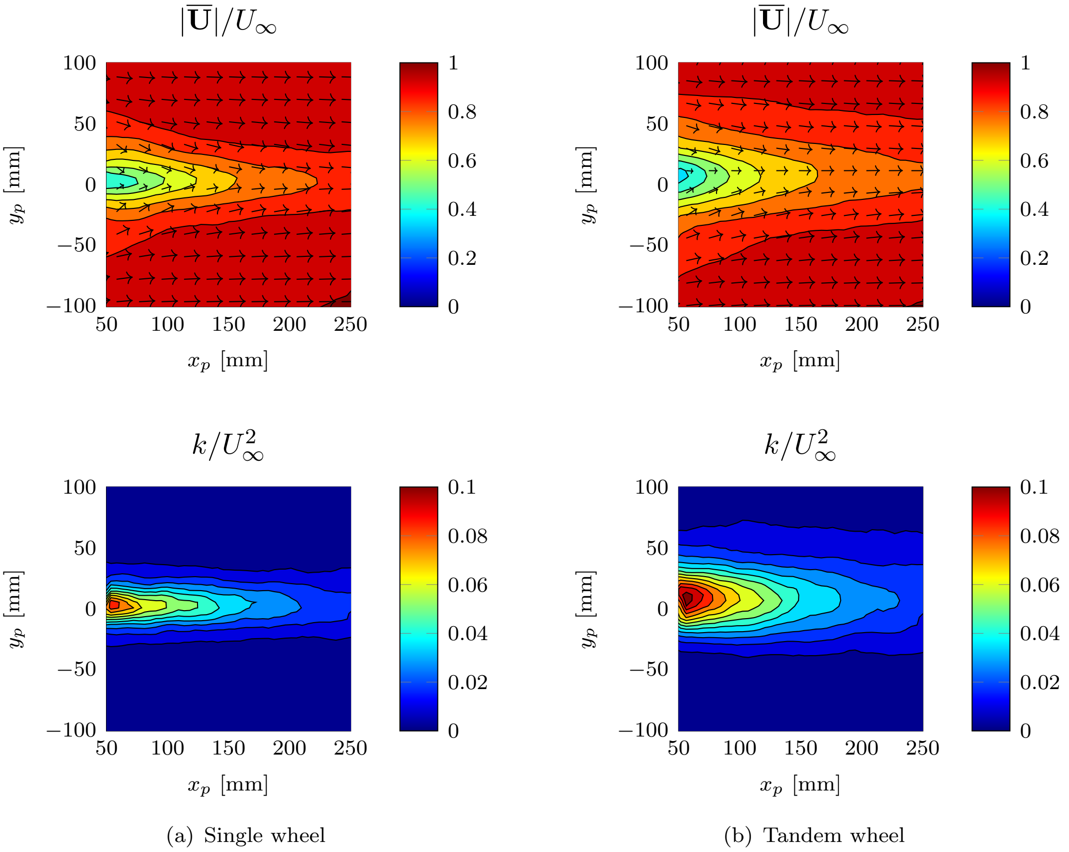

(a) Single wheel (b) Tandem wheel

Figure 6.12: Mean velocity magnitude $|\mathbf{U}|$ and 2D turbulent kinetic energy k fields in non-dimensional form (Plane A) for single wheel and tandem wheels ($L_w = 1.5D_w$, $\alpha = 0\,\mathrm{deg}$, $Re_D \approx 4.8 \times 10^5$).

6.2.3 POD modes

To enhance the analysis of the unsteady wake, POD modes were extracted from the PIV images. The first three POD modes are illustrated in Figure 6.13 for the single wheel and the tandem wheels at $\alpha = 0$ and $L_w = 1.5D_w$.

The first mode (Figure 6.13(a) and Figure 6.13(b)) is similar in both cases, it involves a coherent vertical displacement (y-direction) on a large portion of the frame. It is the most energetic mode containing 40% and 25% of the total energy content of the single wheel and the tandem wheels, respectively. It is a flapping mode that can be identified from the time series of the velocity field in the wake. The first mode, being the most energetic mode involving vertical displacements in the wake, can be considered responsible for generating most of the fluctuations of the lift coefficient.

The second (Figure 6.13(c)) and third mode (Figure 6.13(e)) of the single wheel can also be identified in the tandem wheels, but their shapes appear in an inverted order (third and second, respectively in Figure 6.13(f) and Figure 6.13(c)). The second mode for the single wheel consists of two areas of opposite vertical velocity located in two different streamwise positions. This is the mode that mainly contributes to the sinusoidal shape of the wake that can be seen in some frames of the PIV. This mode is associated with the downstream motion of the wake structures. The third mode for the single wheel is a symmetric pulsating mode of flow that alternately converges and diverges toward the wake centreline ($y_p = 0$ in the pictures).

The inverted position of the modes in the tandem wheels and the higher energy content of the first mode are indicative of the lower importance of the coherent structures of Figure 6.13(c) or Figure 6.13(f) in the tandem-wheel case. In fact, the lower relative energy of the other modes is indicative of the lower importance of these structures in the tandem-wheel case with respect to the single-wheel case.

The other modes (not shown) present multiple areas with non-zero vertical velocities, representing the downstream motion of the structures observed in the second mode for the single wheel and in the third mode for the tandem wheels. The wake of the tandem wheels shows a certain level of asymmetry, which is due to the asymmetry of the wake that deforms the POD modes too.

The modes energy content is given in Figure 6.14(a) and Figure 6.14(b), for the single wheel and the tandem wheels respectively. The figures show the relative importance of the modes, in decreasing order. The energy of the first mode is higher for the tandem wheels than for the single wheel because the unsteadiness of the flapping movement in the wake is more relevant in the tandem-wheel case. In Figure 6.15, the convergence plot of the two cases shows a faster convergence of the tandem wheels, mainly because of the higher energy content of the first mode.

In summary, the POD technique provides a description of the most energetic mode in the wake (the flapping mode), showing that its relative importance is higher in the tandem-wheel case.

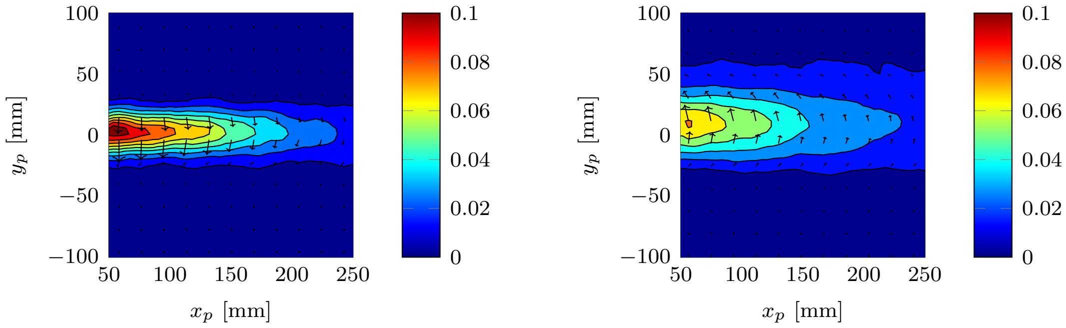

(a) Single-wheel POD Mode 1, 25.4% energy

(b) Tandem-wheel POD Mode 1, 41.6% energy

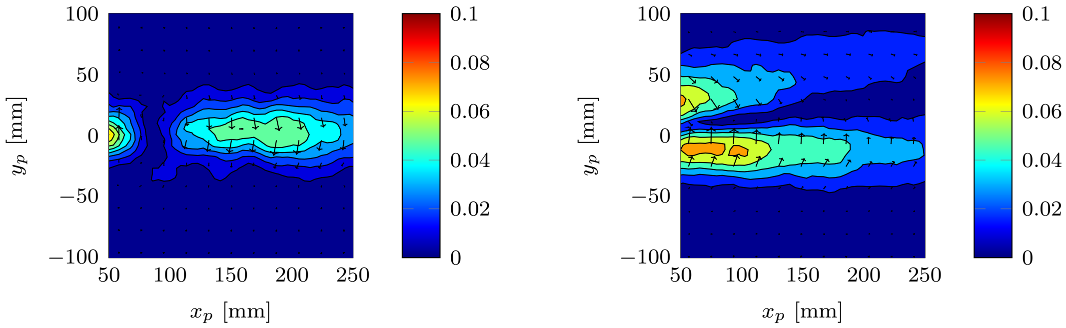

(c) Single-wheel POD Mode 2, 8.2% energy

(d) Tandem-wheel POD Mode 2, 8.2% energy

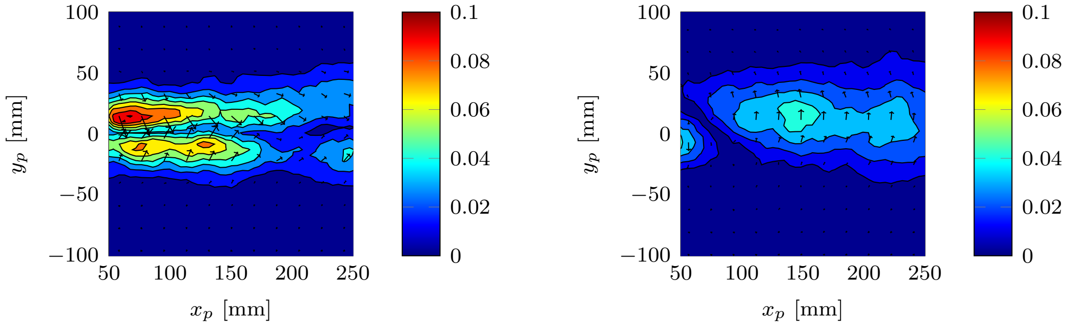

(e) Single-wheel POD Mode 3, 4.8% energy

(f) Tandem-wheel POD Mode 3, 4.9% energy

Figure 6.13: Comparison of the first three POD modes for single (left) and tandem wheels (right), contours of dimensionless velocity magnitude (refer to Equation 6.5).

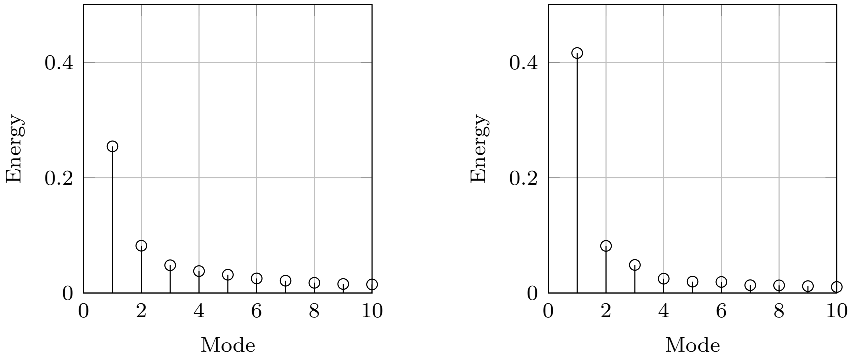

(a) Single wheel

(b) Tandem wheels

Figure 6.14: POD energy content.

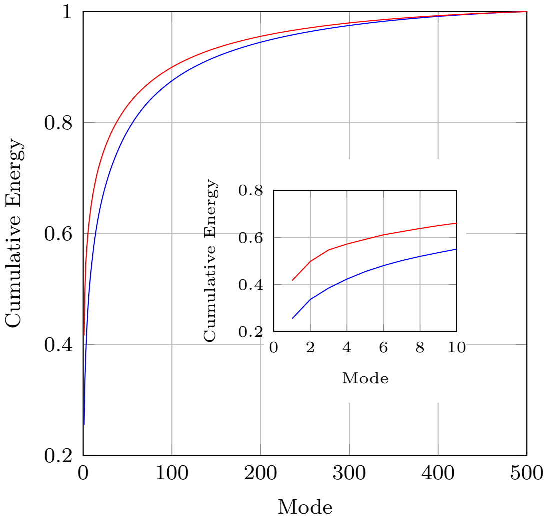

Figure 6.15: POD cumulative energy content for single wheel (——) and tandem wheels (——).

6.2.4 Effects of inter-axis distance and installation angle on tandem wheels

In order to understand the effect of the configurations on the mean forces and the unsteady fluctuations, various tests were repeated in a range of L_w/D_w ratio and α. The vibration test allowed a reliable assessment of the unsteady forces for the first time in the wind tunnel. The front-wheel drag coefficient $\overline{C}_D^f$ and rear-wheel drag coefficient $\overline{C}_D^r$ are summarised in Table 6.1, together with the total drag coefficient $\overline{C}_D^t$ from both wheels ($Re_D = 4.8 \times 10^5$). The results are also shown in Figure 6.16.

For the tandem-wheel case, the front wheel has a smaller mean drag coefficient than the rear wheel. The mean drag of the tandem-wheel configuration is slightly lower than twice the isolated single wheel. The rear wheel alone shows an increase of drag with respect to an isolated wheel, while the front wheel has a lower mean drag coefficient (see also 6.3). The reason for the lower mean drag on the front wheel is the high pressure region on the fore part of the rear wheel, which also affects the pressure on the downstream part of the front wheel, leading to a lower mean drag coefficient. The higher mean drag coefficient of the rear wheel is explained by the higher intensity of the four vortices detaching from the rear wheel compared to the single wheel case. The vortices are stronger because they are the combination of the vortices formed on the front wheel and the vortices formed on the rear wheel. The vortices form suction areas on the wheel shoulders that contribute to the increase of drag.

A change in the inter-axis distance has the main effect of redistributing the drag coefficient between the two wheels, without dramatically affecting the total drag coefficient (differences within 5%). The flow is asymmetric for small inter-axis distances, which is

Table 6.1: Effect of the geometric parameters on mean loads ($Re_D = 4.8 \times 10^5$).

Configuration			$\overline{C}_D^f$	$\lvert\overline{C}_L^f\rvert$	$\overline{C}_D^r$	$\lvert\overline{C}_L^r\rvert$	$\overline{C}_D^t$
Name	α [deg]	L_w/D_w					
Single wheel			0.229	0.004			0.229
Tandem wheels	0	1.1	0.093	0.137	0.305	0.004	0.398
	0	1.3	0.060	−0.048	0.337	0.003	0.397
	0	1.5	0.082	0.002	0.336	−0.024	0.418
	10	1.5	0.124	−0.022	0.313	−0.035	0.437
	20	1.3	0.181	0.005	0.384	−0.032	0.565
	20	1.5	0.190	−0.010	0.320	−0.021	0.510

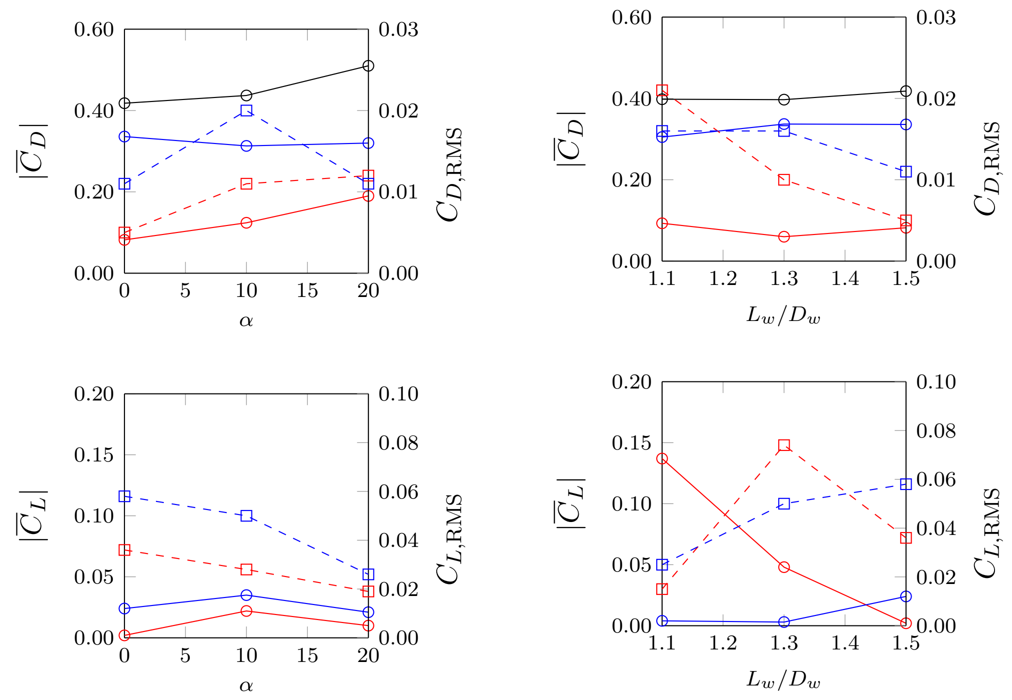

Figure 6.16: Mean and RMS force coefficients $\overline{C}_D$ and $|\overline{C}_L|$ as a function of the geometric parameters L_w/D_w and α): front wheel (−○−), rear wheel (−○−), and total (−○−). Solid lines are mean values, dashed lines are RMS values ($Re_D = 4.8 \times 10^5$).

revealed by the non-zero mean lift coefficients. This is due to a higher sensitivity of the flow itself to perturbations.

At $\alpha = 0\,\text{deg}$, $\overline{C}_L^f$ decreases with increasing L_w/D_w ratio within the tested range, whilst the rear lift coefficient increases. The front-wheel mean lift coefficient $\overline{C}_L^f$ is not zero in the lowest and in the medium distances ($L_w/D_w = 1.1$ and 1.3) in spite of a zero installation angle. Similar asymmetric flows were previously reported by Khorrami et al. [37] on tandem cylinders in similar Reynolds number ranges. On the contrary, with the highest $L_w/D_w = 1.5$ the flow is symmetric, i.e. the mean lift is small for both wheels. The maximum rear lift coefficient is never as high as the front lift coefficient in the inter-axis distance of $L_w = 1.1D_w$. Increasing the installation angle from 0 deg to 20 deg, the total drag coefficient increases by 22% with $L_w = 1.5D_w$ and by 42% with $L_w = 1.3D_w$. In fact, a global drag increase is expected due to the larger projected frontal area, but also the drag distribution on the two wheels changes with a marked increase of drag on the front wheel.

For the tandem-wheel case, the standard deviations are given in Table 6.2. The standard deviations are globally higher for the tandem-wheel case than for the single-wheel case. The lift coefficient RMS is generally higher than the respective drag coefficient RMS. The configurations that provide the lowest levels of RMS overall are the cases with high installation angle, in spite of the higher mean drag coefficient. When comparing configurations at $\alpha = 0$ deg, a higher inter-axis distance generally corresponds to lower RMS, especially on the front wheel.

Table 6.2: Effect of the geometric parameters on loads standard deviations ($Re_D = 4.8 \times 10^5$).

Configuration			$C^f_{D,\mathrm{RMS}}$	$C^f_{L,\mathrm{RMS}}$	$C^r_{D,\mathrm{RMS}}$	$C^f_{L,\mathrm{RMS}}$
Name	α [deg]	L_w/D_w				
Single wheel			0.005	0.032		
Tandem wheels	0	1.1	0.021	0.015	0.016	0.025
	0	1.3	0.010	0.074	0.016	0.050
	0	1.5	0.005	0.036	0.011	0.058
	10	1.5	0.011	0.028	0.020	0.050
	20	1.3	0.013	0.017	0.012	0.031
	20	1.5	0.012	0.019	0.011	0.026

A peak was observed in the PSD of the lift coefficient, in the range that was used for the calculation of the filtered RMS. The peak is not considered structural, since it did not result from the vibration test and it changes frequency with velocity. The peak occurs at the Strouhal number $St \approx 0.07$ in the range $3.6 \times 10^5 < Re_D < 5.7 \times 10^5$. A smaller peak at $St \approx 0.07$ and a secondary peak at a Strouhal number $St \approx 0.14$ can be observed in the drag coefficient too. The phenomenon is expected to be related with the transitional flow, because the tripped configurations do not show the same feature. [75]

In Figure 6.17, the pressure coefficients C_p of three tandem-wheel configurations are compared to analyse the effect of inter-axis distance and installation angle. The two cases with $\alpha = 0\,\text{deg}$ show differences of mean values only in the fore part of the rear wheel. The case with the shorter inter-axis distance ($L_w/D_w = 1.3$) has a lower pressure at $\theta = 0\,\text{deg}$ because the flow velocity between the two wheels remains lower, generating lower dynamic pressure. Except for the region in the proximity of $\theta = 0\,\text{deg}$, the two considered cases at $\alpha = 0\,\text{deg}$ ($L_w/D_w = 1.3$ and $L_w/D_w = 1.5$) are similar, showing symmetric high-pressure areas ($C_p \approx 0.8$) at 30 deg and 330 deg on the rear wheel, where flow that has separated from the front wheel impinges on the rear wheel. The short distance increases the unsteady interactions between the front and the rear wheels, as can be seen from the RMS. Most of the difference is concentrated in the areas between the two wheels, not only on the rear wheel where the wake from the front wheel impinges on it, but also on the aft part of the front wheel. The presence of the rear wheel affects the unsteady flow on the front wheel.

The pressure coefficients C_p for the same inter-axis distance $L_w/D_w = 1.5$ and two angles of attack ($\alpha = 0\,\text{deg}$ and $\alpha = 20\,\text{deg}$) are also compared in Figure 6.17. The mean flow past the rear wheel at $\alpha = 20\,\text{deg}$ is substantially different from the flow past the rear wheel at $\alpha = 0\,\text{deg}$. At such a high installation angle, the flow past the rear wheel shows a trend similar to the flow past a single wheel: only one stagnation point in the front and recirculation bubbles at approximately $\theta = 120\,\text{deg}$ (only on one side). The flow on the wheels is clearly not symmetrical due to the wake past the front wheel. The maximum suction peak at $\theta = 270\,\text{deg}$ has a lower $\overline{C_p}$ than the suction peak at $\theta = 90\,\text{deg}$. Most of the unsteady content is concentrated around $\theta = 180\,\text{deg}$, similarly to the trend observed on the single wheel, but with slightly higher values. Overall, in the case with $\alpha = 20\,\text{deg}$ the curve of the RMS on the rear wheel shows lower RMS than that in the configuration at $\alpha = 0\,\text{deg}$.

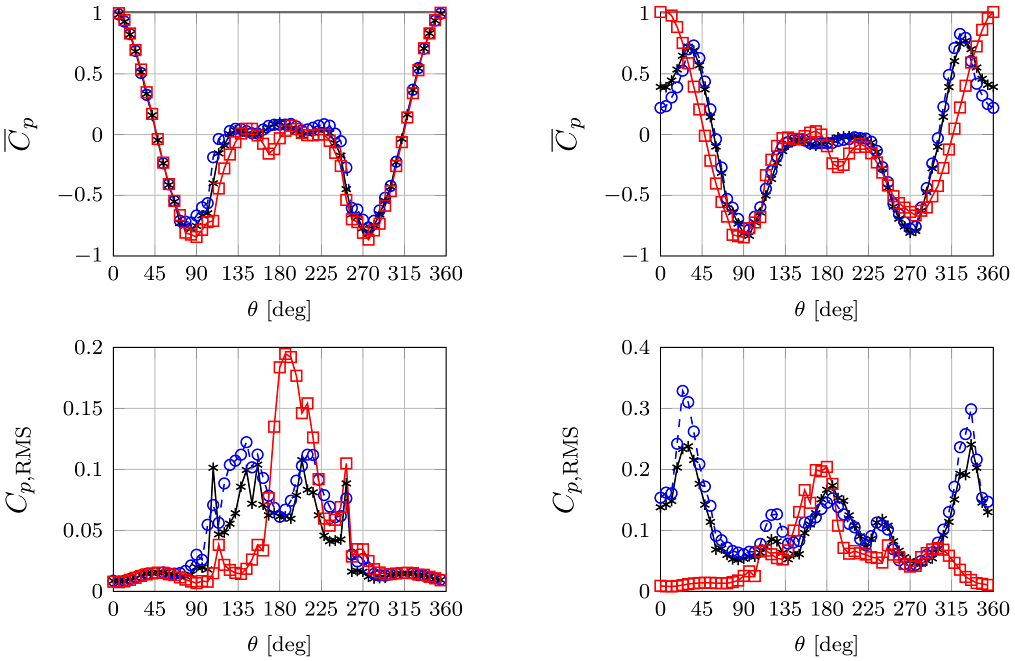

(a) Front wheel (b) Rear wheel

Figure 6.17: Mean and RMS values of the pressure coefficients C_p along the wheel centreline, comparing the tandem-wheel configurations $L_w/D_w = 1.3$ (- ○ -), $L_w/D_w = 1.5$ (—∗—), both at $\alpha = 0\,\mathrm{deg}$, and $L_w/D_w = 1.5$ at $\alpha = 20\,\mathrm{deg}$ (—□—).

6.3 Summary

Aerodynamic loads, pressures and velocity fields were experimentally measured for the flow past single and tandem wheels. The tandem-wheel model represents half of a simplified four-wheel landing gear. The aerodynamic forces were validated with a preliminary vibration test on the model structure, to estimate the dynamic response of the balance. The wind-tunnel tests were performed in the $2.1\,\mathrm{m} \times 1.5\,\mathrm{m}$ wind tunnel at the University of Southampton, and were repeated for the listed configurations (various inter-axis distances and various installation angles). One of the main findings of this experiment is the limited effect of the inter-axis distance on the global mean drag coefficient in the tested range of L_w/D_w (inter-axis distance over diameter ratio) between 1.1 and 1.5, while the effect on the standard deviations is more relevant. The general trend is toward a higher mean drag coefficient and a lower RMS of force coefficients with increasing inter-axis distance. In spite of zero installation angle, a non-symmetric mean flow was found for small L_w/D_w ratios. Similar asymmetric flows are also observed when applying tripping devices. The effect of the installation angle is relevant both for mean and RMS values. Higher installation angles lead to higher mean drag coefficients but to lower RMS of the force coefficients. For this reason, both mean and unsteady values should be analysed. PIV and oil-flow images allowed the identification of the four vortices in the wake, along with the identification of the POD modes that are responsible for the generation of the force fluctuations. A transverse plane of the flow field (not measured here) would allow the identification of the exact position of the vortices. Overall, the tested model shows evidence of a low sensitivity to Reynolds number in this transitional regime, which is characterised by the presence of both laminar and turbulent flow features.

Chapter 7

DDES Simulations on Single and Tandem Wheels

DDES simulations on the single and tandem wheels geometries are here reported. The procedure adopted for the simulations is detailed in Chapter 4, while the geometry and other minor details on the specific meshes are described in this chapter. Some of the contents of this chapter are also published in the conference paper Spagnolo et al. [74].

7.1 Computational geometry of the experimental setup

The validation data for the simulations reported in the following sections were generated during the experiments reported in Chapter 6 and in Spagnolo et al. [75], conducted at the University of Southampton.

The aim of these simulations is to validate the numerical method against the experiments (Figure 7.1(a)). Thus, the current simulations are performed on the geometry in Figure 7.1(b) that resembles the experimental setup. To prove the reliability of the method, the simulation methodologies are tested on both the single wheel and the tandem wheels (in various configurations of the geometric parameters L and α).

In the simulations, the test section is approximated with a rectangular box with the same cross-section as the wind tunnel and it is extended up to approximately $5D_w$ upstream and $10D_w$ downstream of the rear wheel. The inlet has a fixed velocity $U_\infty = 40\,\mathrm{m/s}$, normal to the inflow face, and the outlet boundary has a fixed zero gauge pressure. The wind-tunnel boundary layer is neglected (assuming slip conditions for the walls) as well as the test-section divergence in the spanwise direction, i.e. assuming the wind-tunnel walls are normal to the inlet boundary. These two assumptions are reasonable because, if the wind tunnel is operated in design conditions, the boundary layer and the divergence compensate each other. The effect of the boundary layer on the model is considered negligible because the closest lateral wall (with slip condition) is 300 mm from the wheels (approximately $1.7D_w$) and the boundary layer thickness is 90 mm. Thus, even if in the experiment the root part of the support is immersed in the shear flow, the balance acquires only the aerodynamic forces on the wheel. The effect of the supports is also quantified by running two sets of simulations with and without supports. The Reynolds number calculated with the wheel diameter is $Re_D = 5 \times 10^5$.

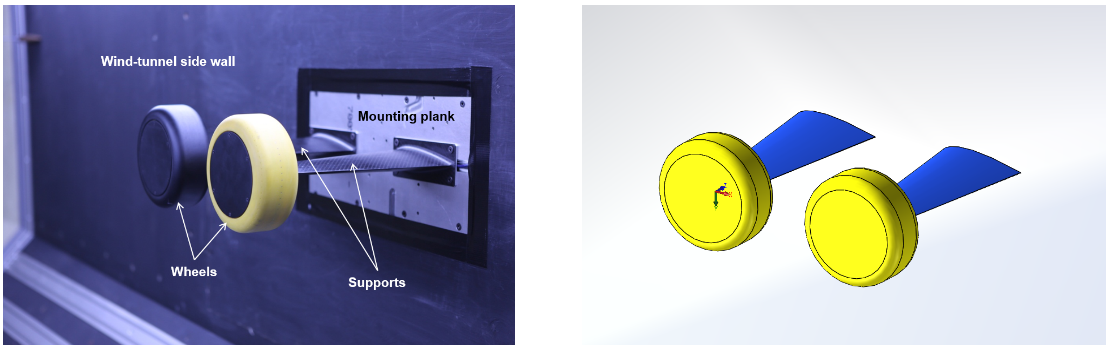

(a) Wind-tunnel model. (b) Simulations CAD.

Figure 7.1: Tandem-wheels experimental assembly.

7.2 Computational setup

7.2.1 Turbulence models

All cases are run in OpenFOAM® 2.3.0 using the incompressible Navier-Stokes equations with S-A DDES [81]. Different approaches to turbulence modelling are adopted to reproduce the experimental results. The production term of the $\tilde{\nu}$ equation is deactivated in the regions that are assumed to be laminar in the experiment, for the three cases in Figure 7.2. The standard S-A DDES is used in case A with fully-turbulent inflow, whilst the transition is fixed on the front wheel for cases B and C at 120 deg azimuthal angle (the angle is chosen from the experimental data in Chapter 6). The difference between cases B and C is the flow on the lateral flat surface of the wheel, which is set to laminar in B and turbulent in C.

Various versions of the S-A model exist. The versions used in this work are the *standard* version without the f_{t2} term (briefly "SA-std-noft2") and the fv3 model without the f_{t2} term ("SA-fv3-noft2"). These two models are here referred to as "SA-std" or "SA-fv3". The difference between the two versions is the definition of the $\tilde{S}$ term, as described in Chapter 4.

Different approaches to the turbulence modelling are adopted to reproduce the experimental results: by means of a multiplying factor α_T, the production term of the $\tilde{\nu}$

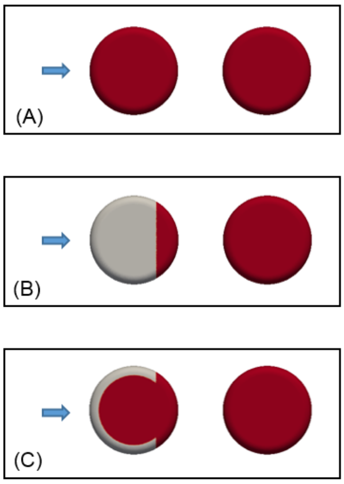

Figure 7.2: Surface visualisation of the laminar (grey) and turbulent (red) parts for: (A) DDES standard model; (B) DDES with fixed transition at constant-x plane; and (C) DDES with fixed transition at constant-x plane and wheel flat side.

equation is deactivated in the regions that are assumed to be laminar in the experiment. The factor α_T is equal to 1 in the turbulent regions while it is 0 in the laminar part. This is a convenient way to deactivate the turbulence model without defining two different zones in the mesh. The turbulent variable $\tilde{\nu}$ equation is also resolved in the laminar regions, but without production the turbulent viscosity values are not allowed to increase.

7.2.2 Solver

The OpenFOAM® library is used for the simulations to solve the incompressible Navier-Stokes equations. In detail, the flow is initialised with `simpleFoam`, which implements the SIMPLE algorithm for steady simulations (Ferziger and Peric [22]), and the DDES is performed with `pimpleFoam`, which uses the PIMPLE algorithm, a combination of SIMPLE and PISO algorithms (Ferziger and Peric [22], OpenFOAM® solvers [54], and Section 4.3.2).

7.2.3 Meshes

Since the aim of the project is to develop efficient aerodynamic load prediction methods through simulations, only automatic mesh generation strategies are considered for this work in order to reduce the meshing time. The final simulation setup includes two different kinds of hybrid meshes: Mesh I, hexa-dominant mesh generated in ANSYS® ICEM CFD™ starting from the Octree tetrahedral decomposition; and Mesh II, hexa-dominant mesh with volume mesh generated in HEXPRESS™/Hybrid or in OpenFOAM® snappyHexMesh and boundary-layer semi-structured mesh extruded in OpenFOAM® snappyHexMesh. The reason for generating Mesh II in two steps is to better control the mesh quality and the smallest cell size (for stability and performance). In Figure 7.3, a section corresponding to the plane $z = 0\,\mathrm{m}$ is given for a sample grid that was entirely generated in OpenFOAM® snappyHexMesh. Mesh I is generally a high-quality mesh that adapts better to complex features, while the generation of Mesh II is more suitable for multiple mesh generations on similar geometries.

The two grids are generated with similar criteria, employing both refinement zones and a semi-structured boundary-layer mesh. The grids have coarse cells $(0.1D_w - 0.2D_w)$ in the regions far from the bodies and one or more refinement blocks (with cells about $0.01D_w - 0.04D_w$). The surface mesh is $0.005D_w - 0.01D_w$ in order to correctly describe the surface of the bodies and capture the surface flow features. All of the meshes include a boundary-layer semi-structured mesh extruded from the wall surface mesh of the bodies of interest, while the wind-tunnel walls do not have prismatic boundary-layer extrusions. The semi-structured grid on the bodies' surface is extruded with first-cell centre height approximately 10^{-5}m in order to obtain the target maximum $y^+ \approx 1$. Mesh I includes a high-quality boundary-layer prismatic mesh with constant first-cell height in order to have low y^+ (around unity and rigorously below 5), whilst Mesh II may have a non-uniform first-cell centre height on the wheel surface that locally activates the wall function in the proximity of complex features. Mesh II may also need further refinement on the wall surface, which in this case limits the maximum extrusion height of the boundary-layer prismatic cells. For this reason, a high number of refined isotropic hexahedral cells is often needed in the proximity of the walls in order to correctly capture the flow boundary layer. If Mesh II is generated on simple geometries, it usually provides the same quality and similar mesh sizes as Mesh I.

7.2.3.1 Mesh I

The first procedure, which implies the use of ANSYS IcemCFD, generates the mesh starting from the surfaces (imported directly from Solidworks in `sldprt` format). The surface mesh is generated with the specific target and minimum size indicated in the software. First, a triangular mesh is created on the surface. Then, the volume mesh is created with the Octree procedure: the tetrahedrons are oriented with the wind-tunnel axes. In this way, after mesh generation, there is a conversion process from 12 tetrahedron to 1 hexahedron. Semi-structured boundary-layer cells are inserted on the surface (the wall normal direction is structured to better calculate the boundary layer). The boundary layer mesh has a first row small enough to have the first cell at $y^+ < 1$ on the whole surface. Finally, a conversion from the resulting mesh to the dual mesh is performed in OpenFOAM. The reason for this last process is the need to improve the mesh quality for OpenFOAM. A sample mesh is shown in Figure 7.4.

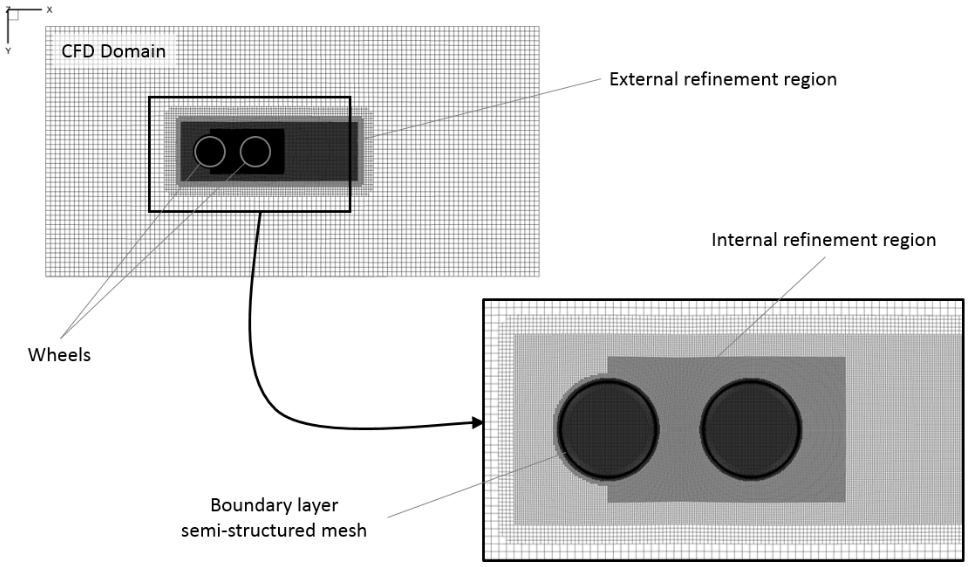

Figure 7.3: Slice of the computational grid for tandem wheels at $z = 0$.

The procedure relies on the efficient Octree mesh generation, that allows the creation of hexahedral meshes with about 10 million cells in approximately 1 hour on 16 cores. The intermediate conversion process is the bottle-neck of the procedure since the tetrahedral mesh has about 12 times the number of cells of the final mesh. This bottle-neck is not particularly demanding for the meshes that are used in this project. However, the main reason why the next procedure was here adopted is the technical difficulty in automatically converting the boundary layer mesh to its dual if there are complex features. The thin cells that are necessary to have $y^+ < 1$ generate errors during the conversion.

7.2.3.2 Mesh II

This three-stage procedure starts from a structured volume mesh, which is usually coarse with respect to the final cell size in the proximity of the bodies. In the first stage, the cells that fall inside the volume delimited by the surface of the body (defined by means of `stl` files) are removed: the mesh is now a *castellated* mesh. In the second stage, the mesh is snapped onto the surface, so that the surface mesh adheres to the solid bodies. And in the third stage the boundary layer mesh is extruded from the surface. A sample mesh is shown in Figure 7.5.

This mesh can be generated with HEXPRESS™/Hybrid or in OpenFOAM® snappyHexMesh. This procedure can be run on multiple cores, without limit of licenses. The software used is part of OpenFOAM, so there are no intermediate conversions and the resulting mesh can be directly employed in OpenFOAM.

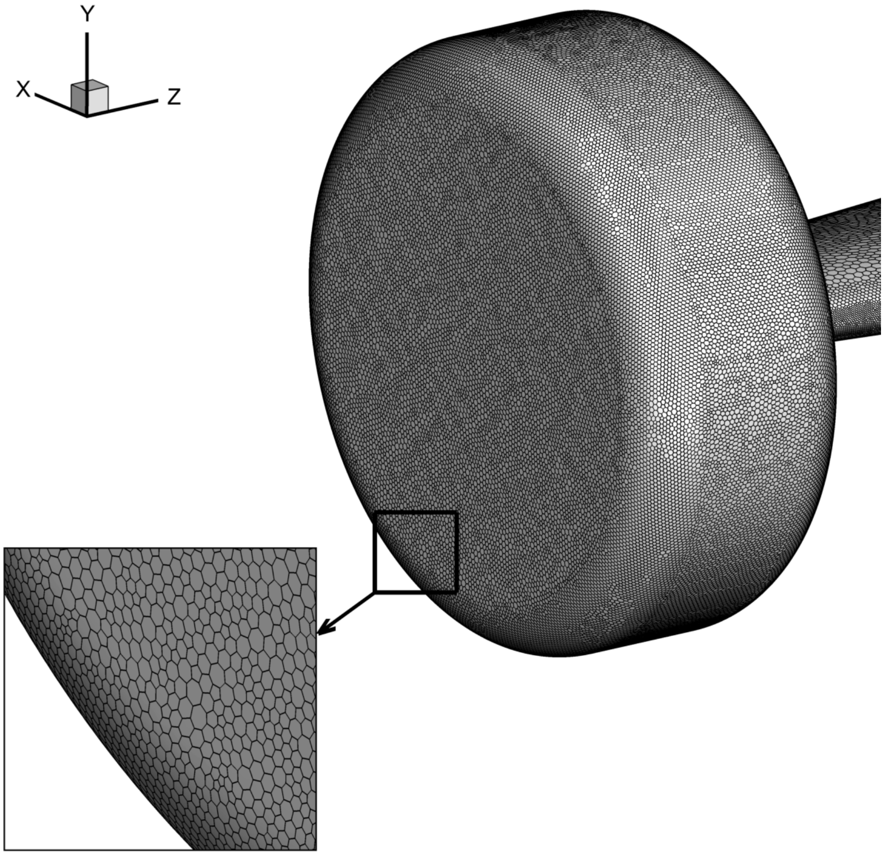

Figure 7.4: Surface mesh created with IcemCFD, after conversion to polyhedrons.

The main problem with this procedure is that, given the lower quality of the surface mesh with respect to Mesh I, the boundary layer cells have to be higher in order to give a good-quality mesh. This means y^+ values approximately 5 times higher than with IcemCFD.

7.2.4 Computational Procedure

The solution procedure is composed of three parts: mesh generation, a steady RANS simulation to initialise the flow and DDES. The statistics are considered converged when the average drag coefficients are within 1% with respect to the value averaged over half of the simulated time. The standard deviations show time-convergence errors within 10%. The data sampling used for post-processing starts from $t = 0.2\,\mathrm{s}$ (more than 40 diameter-based convective times) and lasts until convergence, thus some simulations are based on larger data sets. The minimum sampling time is approximately $0.5\,\mathrm{s}$ (corresponding to 5 domain flow-through times or about 100 diameter convective times). For each meshing strategy, a minimum of two grids with progressively refined number of cells are tested on at least one representative case in order to confirm the convergence of the results with the grid size.

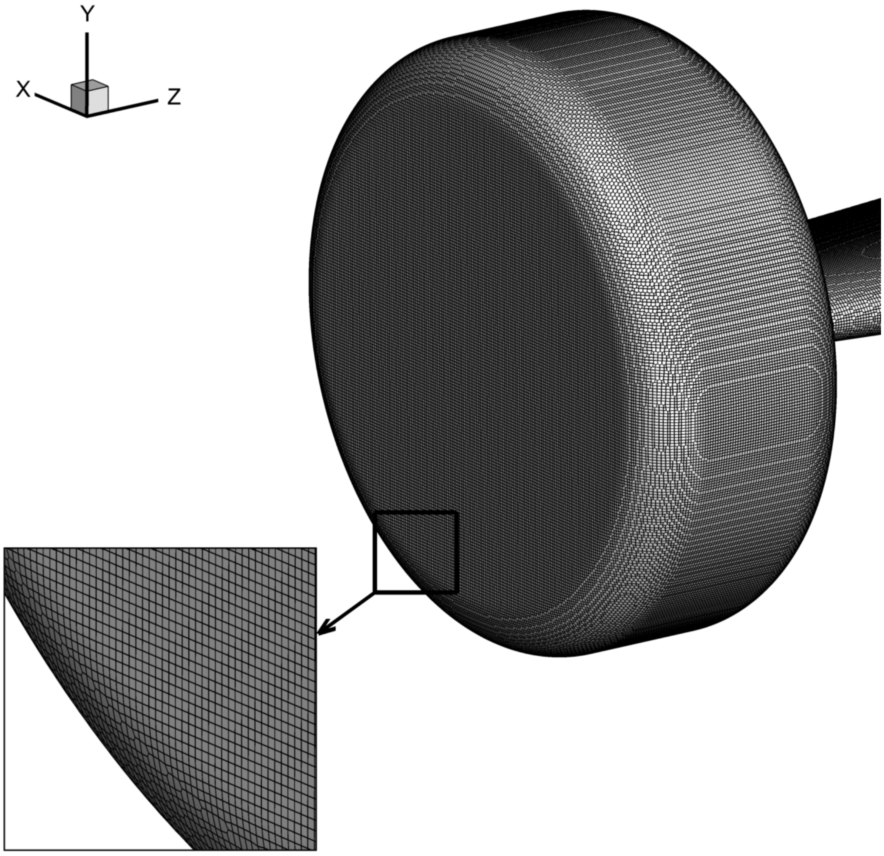

Figure 7.5: Surface mesh created with snappyHexMesh.

The surface pressures are monitored at 60 points on each wheel, corresponding to the points measured in the experiments. An example of flow visualisation on one of the tandem-wheel DDES simulations is given in Figure 7.6. As a reference, on a 14-million-cell grid for the tandem wheels, the computational wall-time is approximately 100 hours on 128 cores for 0.5 s of simulation time on the Iridis 4 cluster (University of Southampton).

7.3 Results

7.3.1 Convergence test

The first test consists of a proof of mesh convergence with three progressively refined grids on the single-wheel case without the support generated with ANSYS® ICEM CFD™ and one supplementary test grid generated with snappyHexMesh. The test showed the grid convergence of the turbulence model implemented during the current work, i.e. DDES-SA-std.

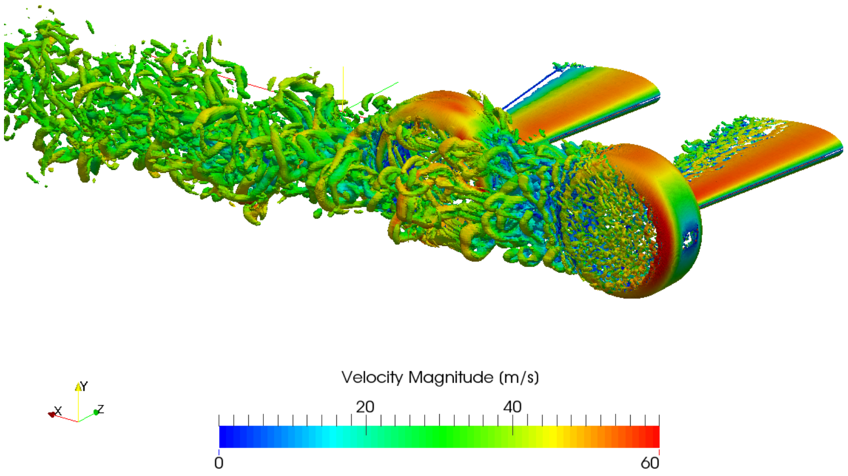

Figure 7.6: Isosurface of $Q = 5 \times 10^5\,\mathrm{s}^{-2}$ coloured with velocity magnitude.

In Table 7.1, two consecutive ANSYS® ICEM CFD™ grids have a refinement factor of $\sqrt{2}$ in the volume mesh and a refinement factor of 2 in the surface mesh. The drag coefficient progressively converges toward 0.171 with mesh refinement, which is also confirmed by the snappyHexMesh grid. Minor differences in the mesh sizes and in the cell count between the meshes generated with the two methodologies are due to the different procedures. In addition, the grids generated with ANSYS® ICEM CFD™ have a maximum y^+ value approximately 1 while the grids generated with snappyHexMesh have a maximum y^+ around 5.

Table 7.1: Mesh convergence results for single-wheel case without supports, DDES-SA-std.

Mesh generator	**Grid name**	**Mesh Sizes**			**Cells total**	$\overline{C}_D$
		Max cell	**Min cell**	**Surface**		
ANSYS® ICEM CFD™	Coarse	0.200 D	0.040 D	0.020 D	3.9 M	0.206
	Medium	0.141 D	0.028 D	0.010 D	6.7 M	0.179
	Fine	0.100 D	0.020 D	0.005 D	9.5 M	0.171
snappyHexMesh	Fine	0.160 D	0.010 D	0.005 D	5.5 M	0.177

A sample plot of residuals for the PIMPLE algorithm is shown in Figure 7.7. The three velocity components are solved three times per timestep (once per outer loop), while the pressure is corrected 3 times per outer loop with an additional non-orthogonal corrector for each pressure correction. The final residuals for each timestep are below 10^{-6} for the pressure and below 10^{-8} for the three velocity components.

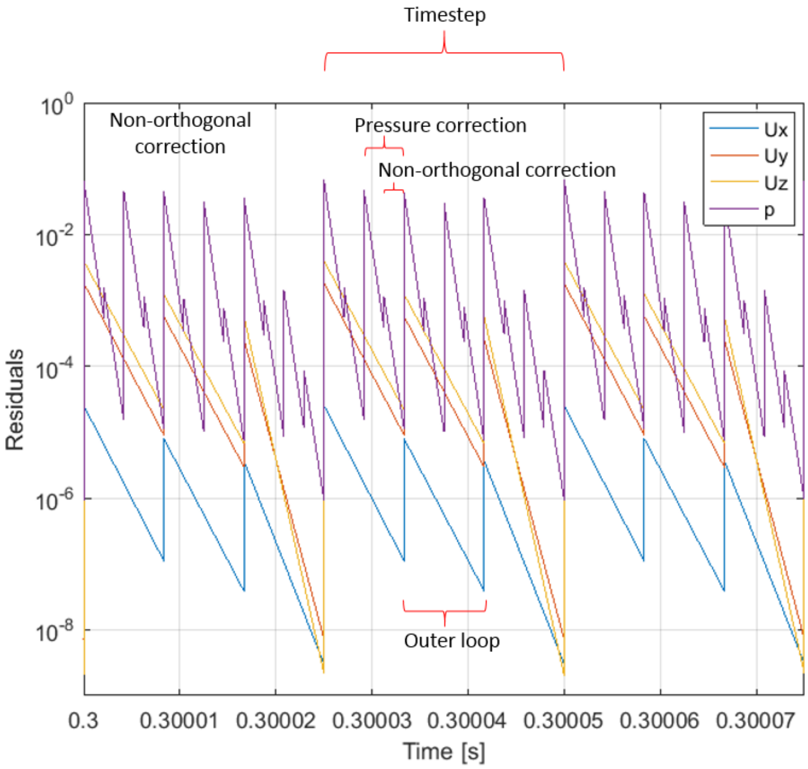

Figure 7.7: Residuals for the PIMPLE algorithm for a sample single-wheel case. The final residuals for each timestep are below 10^{-6} for the pressure and below 10^{-8} for the three velocity components.

In Table 7.2, the simulation on the single-wheel fine grid (SA standard DDES) is repeated for both the PISO and PIMPLE algorithm, showing the discrepancy on the results and the gain in simulation wall time. For the most accurate results, PISO algorithm with small time-step (approximately 2.5×10^{-6} s) is needed. Doubling the time-step (up to 5.0×10^{-6} s) corresponds to approximately half the computational time required for the solution and a 1.6% error on the results. The implemented version of PISO did not allow the increase of time-step beyond Courant numbers above one (here approximatley 5.0×10^{-6} s) for stability reasons. However, PIMPLE employs multiple PISO iterations within the same time-step for increased stability. Thus, if wall time is considered as a priority, the PIMPLE algorithm with time-step below 2.50×10^{-5} s can be used, with a slight reduction of accuracy. The PIMPLE case considered in Table 7.2 shows discrepancy up to 7.1% with respect to the original PISO case, but the time to solution is only 34.8%. In the PIMPLE case considered, only three outer loops are required for stability.

7.3.2 Test with wall functions

An additional test on the maximum y^+ value was performed. Starting from the finest ANSYS® ICEM CFD™ grid given in Table 7.1, the convergence test was repeated

Table 7.2: Convergence results for PISO and PIMPLE algorithms on the single-wheel case without supports (DDES-SA-std, fine mesh, 256 cores). Unit wall time is given in hours (on 256 cores) needed to perform one second of simulation. The relative discrepancy and relative unit wall time is referred to the first PISO case in the table.

Algorithm	**Time-step** (s)	$\overline{\mathrm{C}}_{\mathrm{D}}$	**Rel. discrepancy**	**Unit wall time** (h/s)	**Rel. unit wall time**
PISO	2.50×10^{-6}	0.184	0.0%	161.48	100.0%
PISO	5.00×10^{-6}	0.181	1.6%	85.692	53.1%
PIMPLE	2.50×10^{-5}	0.171	7.1%	56.147	34.8%

for three different first-cell centre heights: a range of maximum y^+ between 1 and 30 was tried, enabling the wall function. With $y^+ \approx 5$, the results show that the drag coefficient is 6% underestimated with respect to the baseline case test $y^+ \approx 1$. With this mesh the wall function is automatically deactivated because the first layer still falls in the viscous sub-layer, but the grid is not capable of predicting the boundary layer as well as for $y^+ \approx 1$. On the contrary, the wall function behaviour is tested on a mesh with a maximum $y^+ \approx 30$, in which a part of the first layer is located outside of the viscous sublayer. The discrepancy is approximately 15% (overestimated). Some differences in this case are expected, and the quantification of the discrepancy is useful for future trade-off analysis when both computational time and accuracy are considered for practical application.

7.3.3 Effect of the wheel support

The numerical simulations have the advantage of being able to perform virtual experiments that are not feasible for experiments. Simulations can be used to understand the importance of the supports in the data experimentally obtained. The mean drag coefficient in the simulation with the support is 0.238, whilst the drag coefficient in the simulation without the support (wheel only) is 0.246. The effect of the support on the single wheel case is then approximately 3% on the drag coefficient.

7.3.4 Forces

7.3.4.1 Mean Forces

In this section, the force coefficients for the single-wheel and tandem-wheel cases are analysed. The experimental mean drag coefficient $\overline{C}_D$ on the single wheel at $Re_D = 5 \times 10^5$ is 0.229 (untripped case Chapter 6). The force coefficients are calculated with the frontal projected area $S = 0.012\,85\,\mathrm{m}^2$. The fully-turbulent DDES model on the fine grids with a maximum $y^+ \approx 1$ predicts a drag coefficient of 0.176, which underestimates the drag coefficient by approximately 23%.

The reasons for this discrepancy is due to the turbulent inflow condition which results in a fully-turbulent boundary layer on the wheel surface. The experiments are performed at a transitional Reynolds number, thus the boundary layer on the wheel surface is laminar up to the separation-induced transition area, at approximately 120 deg azimuthal angle on the wheel tyre (Chapter 6). In fact, the simulations with fixed-transition case C predict a mean drag coefficient of 0.222 (i.e., 3% difference compared with the experiment). This case was run with two grids, generated with the Mesh II strategy, and with 5.8 million cells and 19.7 million cells. The results show a difference on the mean drag coefficient of approximately 1% between the two grids. On the contrary, case B shows higher variability with different meshing strategies and sizes because of the separation bubbles on the lateral flat surfaces of the wheel with unresolved eddies, as described in Section 7.3.6.

Similar behaviours are observed for the tandem wheels, as shown in Table 7.3. The reference mean drag coefficients for the case $L = 1.5D$ and $\alpha = 0\,\mathrm{deg}$ are 0.082 for the front wheel and 0.336 for the rear wheel (Chapter 6). The standard DDES model applied in case A is not capable of predicting the untripped experimental results, with differences on the total drag coefficient as high as 20%. They also tend to generate non-symmetric flows at zero angle of attack. On the contrary, the DDES model with the fixed transition of case C provides the correct mean drag and lift coefficients. Also in this case, the key element in obtaining accurate predictions is the correct simulation of the laminar part of boundary layer on the front wheel, and the prediction of the flow transition. The two different meshing strategies are compared in Table 7.3. On the full geometry, Mesh I is more accurate than Mesh II, in spite of the lower cell count and the higher maximum y^+ (see Section 7.2.3), arguably because of the boundary-layer mesh in the proximity of the bodies. The replacement of the outer boundary-layer mesh with highly-refined isotropic cells in Mesh II does not provide the same over-all efficiency as the boundary-layer prismatic mesh of Mesh I in spite of a faster mesh generation. Also, Mesh I has a uniform first cell-centre height that is always in the viscous sub-layer, whilst Mesh II does not guarantee the first cell-centre height close to complex geometric features. The local non-uniformities of the boundary-layer mesh can remarkably increase the error.

The effect of the angle of attack is analysed in two additional simulations at $\alpha = 10\,\mathrm{deg}$ and $\alpha = 20\,\mathrm{deg}$, on grids of Mesh II type because this strategy generally requires minimal effort when generating similar grids. The grid size is between 14.1 and 15.1 million cells. As in the previously discussed simulations, the transition is fixed on the front wheel (case C). The results for these comparisons are given in Figure 7.8. The experimental trend of the mean drag coefficient that increases with increasing angles of attack is correctly reproduced in the simulations, but the discrepancy of the total drag coefficient raises from 7% to 15% on similar grids. The lower accuracy at high angle of attack is due to the

Table 7.3: Comparison of mean force coefficients from DDES simulations on the tandem-wheel case at $L_w/D_w = 1.5$ and $\alpha = 0$ deg. The two adopeted meshing strategies are compared on a Mesh I of 8.4 million cells and on a Mesh II of 14.1 million cells.

Model	**Mesh type**	$\overline{C}_{Df}$	$\lvert\overline{C}_{Lf}\rvert$	$\overline{C}_{Dr}$	$\lvert\overline{C}_{Lr}\rvert$	$\overline{C}_{Dt}$	$\overline{C}_{Dt}$ error
Standard A	Mesh I	0.109	0.163	0.352	0.151	0.461	10.3%
	Mesh II	0.128	0.176	0.375	0.216	0.503	20.4%
Fixed transition B	Mesh I	0.095	0.001	0.337	0.025	0.432	3.4%
Fixed transition C	Mesh I	0.081	0.000	0.341	0.014	0.422	1.0%
	Mesh II	0.085	0.007	0.364	0.098	0.449	7.4%
Experiment		0.082	0.002	0.336	0.024	0.418	

missing separation bubble on the rear wheel because the flow on the rear wheel is fully-turbulent in the simulations, but in the experiment at high angles of attack a laminar separation bubble can be also observed on the rear wheel. The laminar separation bubble is only observed on the part of the rear wheel that is not immersed in the wake of the front wheel and it is the major cause of discrepancies between the experiments and the simulations at high angles of attack. The high accuracy of the mean drag coefficient on the front wheel also at high angle of attack confirms that most of the error comes from the flow on the rear wheel.

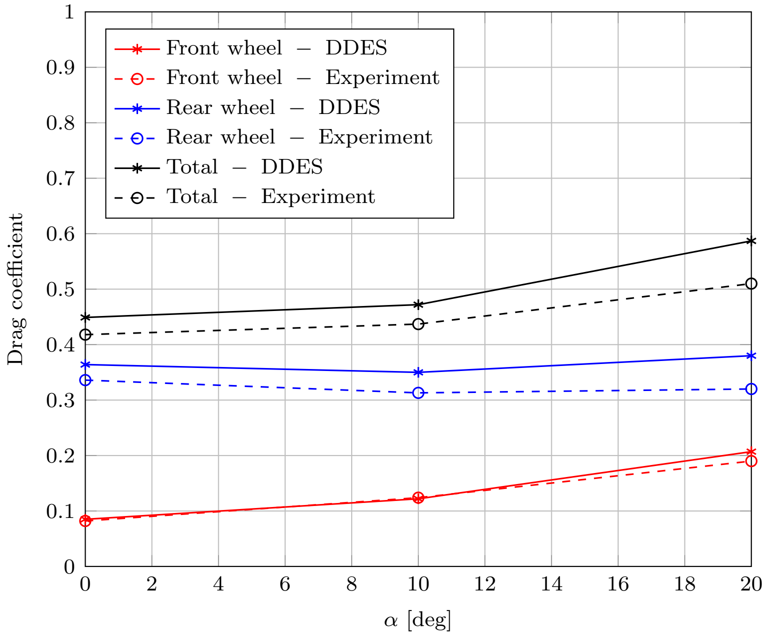

Figure 7.8: Comparison of experiments and simulations at various angles of attack on tandem wheels, results of simulations on Mesh II, transtition case C.

7.3.4.2 Unsteady Forces

On the single wheel case, the RMS values from the experiments are $C_{D,\mathrm{RMS}} = 0.005$ and $C_{L,\mathrm{RMS}} = 0.033$ and the simulations give $C_{D,\mathrm{RMS}} = 0.004$ and $C_{L,\mathrm{RMS}} = 0.019$, both filtered as in the experiments (i.e., low-pass filtering at 30 Hz). Thus the RMS of the drag coefficient matches better with the experiments (errors around 20%) than the lift coefficient (more than 50% difference). The RMS of the drag coefficient are generally better predicted for the tandem-wheel case using Mesh I on case C, as seen in Table 7.4, whilst the RMS of the lift coefficients show higher discrepancies. The accuracy of the RMS is lower than the accuracy of the mean values arguably because generally the time-convergence errors are higher on the RMS values than the mean values and because of the uncertainty of the experimental procedure (Chapter 6).

The time-convergence error on the RMS is up to 10%, estimated from the changes with respect to half sampling time (for simulations between 0.5 s and 1 s), which indicates the need of much higher computational resources to estimate the unsteady aerodynamic loads with accuracy comparable to the mean loads. If the same simulations are run for a time longer than 2 s, the convergence of the unsteady data with respect to half sampling time is in the range $1\% - 5\%$. For instance, on Mesh I with fixed transition case C, the values for the simulation with the extended sampling time are reported in Table 7.4 alongside the data based on the shorter sampling time of 1 s. As expected, there is a change in the unsteady data but the change of the mean values for the extended-sampling simulation is within 1%, thus confirming that such a sampling time is needed to increase the accuracy of the unsteady data.

Table 7.4: Comparison of RMS force coefficients (filtered at 30 Hz) from DDES simulations on the tandem-wheel case at $L_w/D_w = 1.5$ and $\alpha = 0$ deg. The two adopted meshing strategies are compared on a Mesh I of 8.4 million cells and on a Mesh II of 14.1 million cells.

Model	**Mesh type**	$C_{Df,\mathrm{RMS}}$	$C_{Lf,\mathrm{RMS}}$	$C_{Dr,\mathrm{RMS}}$	$C_{Lr,\mathrm{RMS}}$
Standard A	Mesh I	0.014	0.019	0.024	0.037
	Mesh II	0.018	0.031	0.016	0.027
Fixed transition B	Mesh I	0.005	0.030	0.012	0.071
Fixed transition C	Mesh I	0.005	0.022	0.011	0.080
	Mesh I (extended sampling)	0.005	0.024	0.013	0.083
	Mesh II	0.006	0.021	0.020	0.083
Experiment		0.005	0.036	0.012	0.058

The power spectral density (PSD) of the lift and drag coefficients are given in Figure 7.9 for the single wheel. No peak is present, but the highest contribution to the unsteady aerodynamic forces is in the region $10\,\mathrm{Hz} < f < 40\,\mathrm{Hz}$. The drag coefficient contains energy at higher frequencies than the lift coefficient, but the overall spectral energy of the drag coefficient is one order of magnitude lower than the energy of the lift coefficient.

In Figure 7.10 the cumulative energy integrated from the PSD plot over the frequency range shows the part of the energy that is lost in the experimental filtering of the data for CFD comparison. Cutting off the frequencies above 30 Hz, the difference on the RMS (because of the square root in the standard deviation equation) is 45% on the drag coefficient, whilst only 30% on the lift coefficient. The comparison with the experiments is therefore valid, in spite of some limitations on the highest sampling frequency.

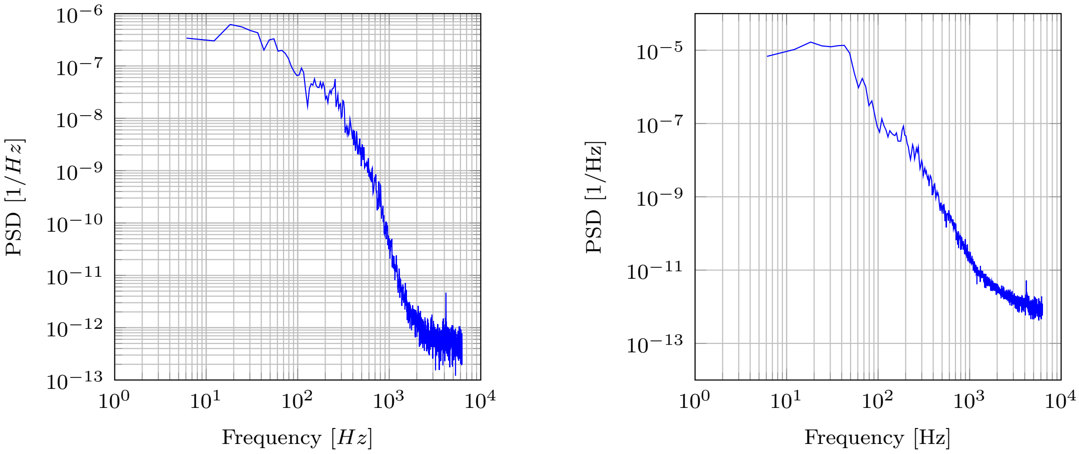

(a) Drag coefficient

(b) Lift coefficient

Figure 7.9: PSD of drag and lift coefficient for the single wheel.

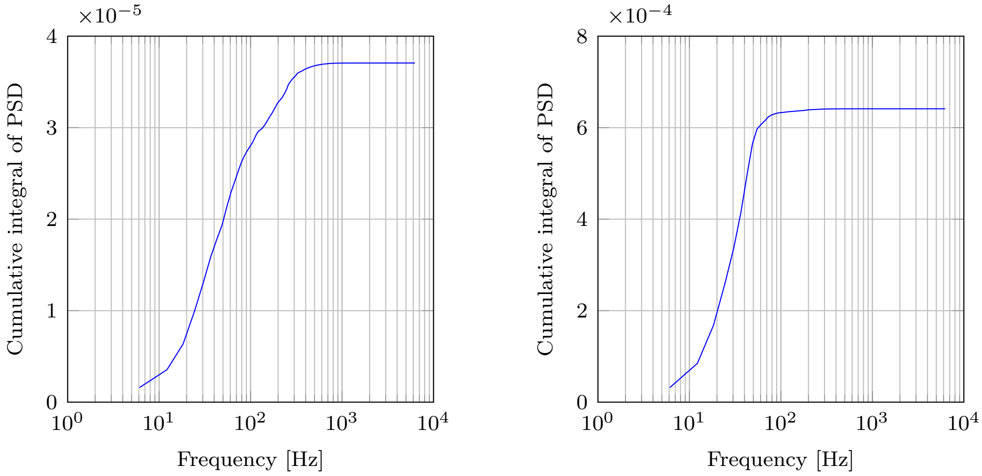

(a) Drag coefficient

(b) Lift coefficient

Figure 7.10: Cumulative integration of the PSD of drag and lift coefficients for the single wheel.

7.3.5 Surface Pressures

The pressure coefficients C_p can be compared with the experiments considering both the mean values and the standard deviations. The simulations with fixed transition are compared with the untripped experiments, whilst the fully-turbulent simulations are compared with the tripped experiment.

In Figure 7.11, both the simulation with fixed transition case B and the untripped experiment show two separation bubbles that are absent in the fully-turbulent simulations case A and in the tripped experiment. The separation bubble is identified by the small blip in $\overline{C}_p$ profiles, as indicated in Figure 7.11. The RMS are also in good agreement, except for the spikes at the bubble location (at 120 deg and 240 deg). The PSD for two representative probes at $\theta = 114\,\text{deg}$ and at $\theta = 180\,\text{deg}$ on the wheel surface along the center-line plane in the simulations are shown in Figure 7.13. The probe at $\theta = 114\,\text{deg}$ shows mainly high frequencies, whilst the probe at $\theta = 180\,\text{deg}$ shows mainly low frequencies. In the experiments, the high-frequency contributions could not be measured, due to the low-pass filtering effect of the tubes of the pressure measurement system. In order to compare the experimental data with the simulations, the simulations have to be filtered.

Various cut-off filtering frequencies were tested in the range $400\,\text{Hz} - 1000\,\text{Hz}$, showing minor differences (not shown here). In Figure 7.11 only the standard deviations filtered at 600 Hz are illustrated. The filtered standard deviations overlap the experimental data with less discrepancies than the unfiltered data. In Figure 7.12 the comparison between experiments with tripped wheels and fully turbulent simulations is illustrated. Mean profiles are in good agreement but the standard deviations are mispredicted in the downwind part of the wheel. In this case, filtering does not improve the results.

The tandem wheels at $L = 1.5D_w$ and $\alpha = 0\,\text{deg}$ is analysed in Figure 7.14(a) (front wheel) and Figure 7.14(b) (rear wheel), on a grid of type Mesh I, in case C. The results of the simulations are close to the experiments, both on the front wheel and on the rear wheel. On the front wheel, the blips in the $\overline{C}_p$ profiles highlight two separation bubbles, while on the rear wheel these features are absent. Also in this case, the filtered RMS are in better agreement than the unfiltered in the proximity of the separation bubbles on the front wheel. The RMS do not show improvements on the results of the rear wheel.

In Figure 7.15 the mean pressure coefficients are shown for three angles of attack at constant $L = 1.5D_w$ (Mesh II, case C) and compared with the experiments. Figure 7.15(a), Figure 7.15(c) and Figure 7.15(e) show good agreement between simulations and experiments on the front wheel. The same behaviour was observed in the analysis of the drag coefficients on the wheels at the same angles of attack (Figure 7.8). On the other hand, the mean pressure coefficients on the rear wheel in Figure 7.15(b), Figure 7.15(d) and Figure 7.15(f) show higher discrepancy, mainly in the downstream region and at angles of attack other than zero, on the side where the rear wheel is not immersed in the front wheel wake.

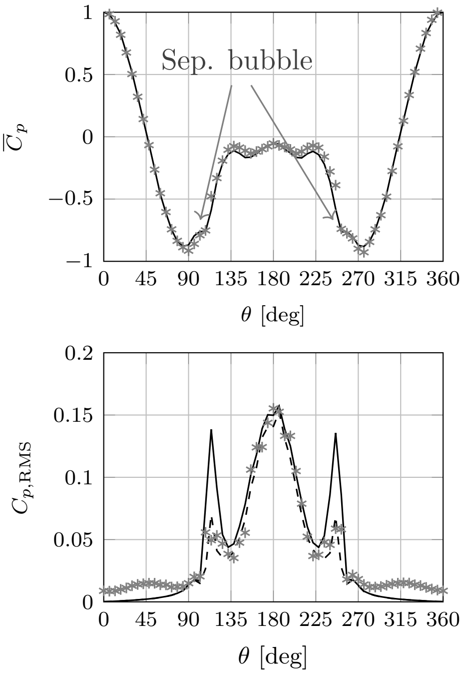

Figure 7.11: Pressure coefficients along the wheel centreline on single wheel: DDES results from case B with fixed transition (——) compared with untripped experiments (∗). Also the filtered RMS are reported (- - -).

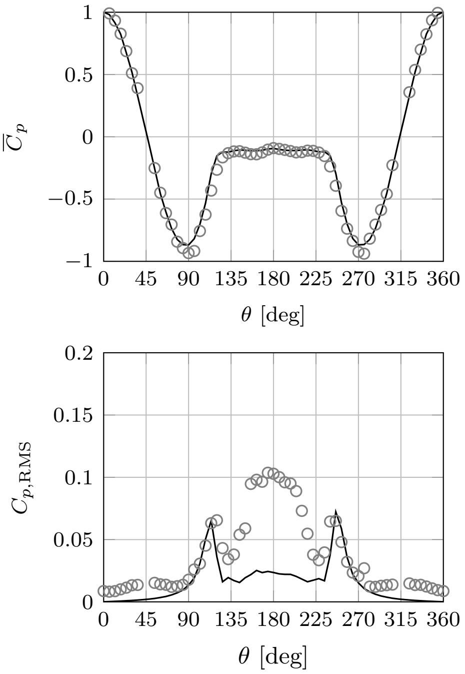

Figure 7.12: Pressure coefficients along the wheel centreline on single wheel: DDES results from the standard case A (——) compared with tripped experiments (○).

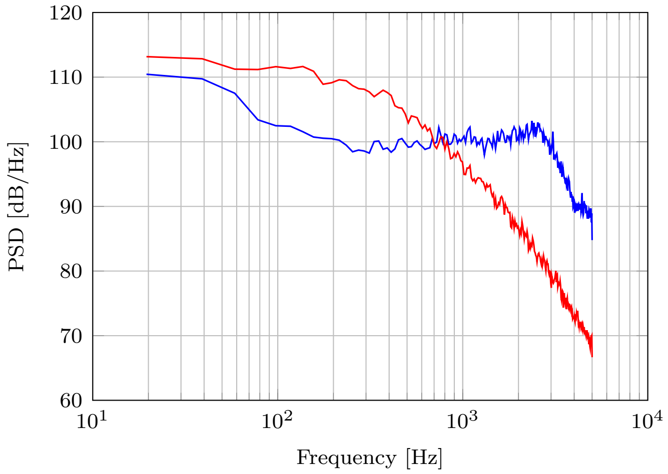

Figure 7.13: PSD of two probes at 114 deg (——) and 180 deg (——) on the wheel centreline, single wheel with fixed transition B.

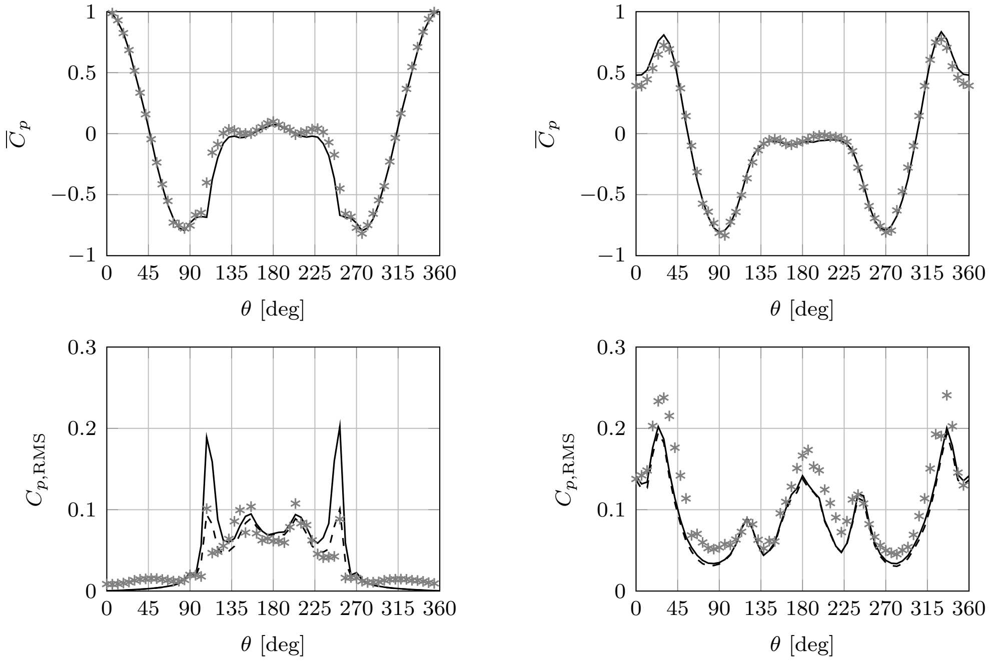

(a) Front wheel

(b) Rear wheel

Figure 7.14: Pressure coefficients C_p along the wheel centreline on tandem wheels at $L = 1.5D_w$ and $\alpha = 0\,\mathrm{deg}$: DDES with fixed transition C (——) is compared with untripped experiments ($*$). Also the filtered RMS are reported (- - -).

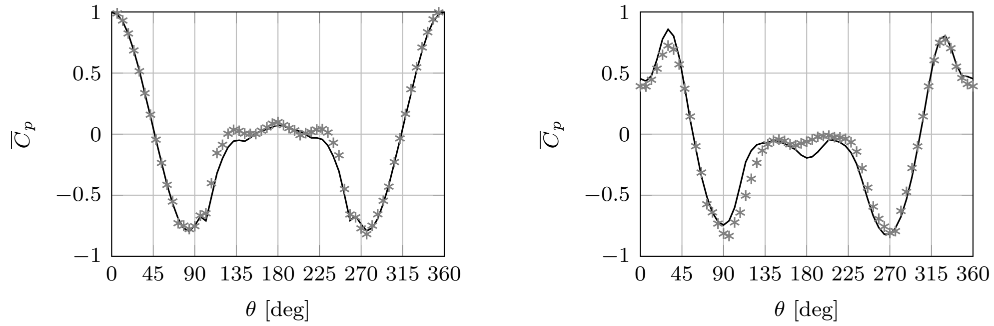

(a) Front wheel: $\alpha = 0\,\mathrm{deg}$

(b) Rear wheel: $\alpha = 0\,\mathrm{deg}$

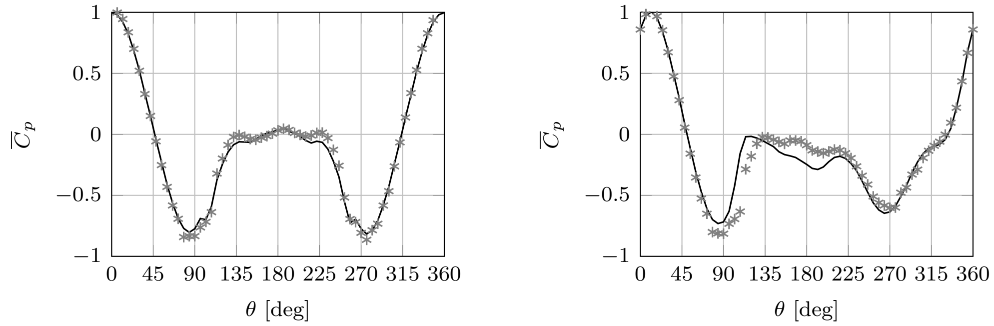

(c) Front wheel: $\alpha = 10\,\mathrm{deg}$

(d) Rear wheel: $\alpha = 10\,\mathrm{deg}$

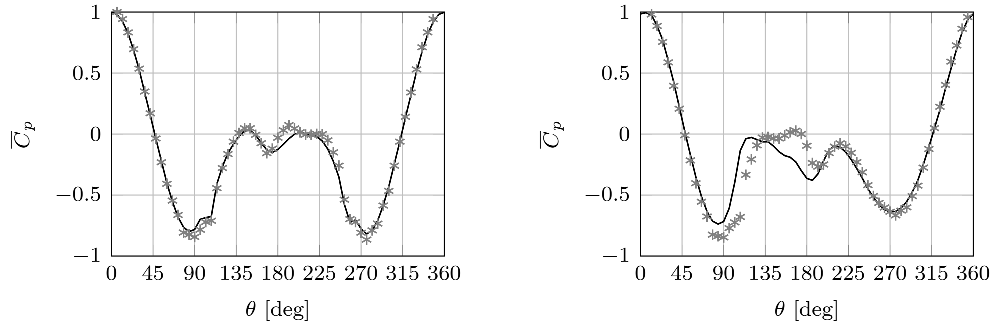

(e) Front wheel: $\alpha = 20\,\mathrm{deg}$

(f) Rear wheel: $\alpha = 20\,\mathrm{deg}$

Figure 7.15: Mean pressure coefficients along the wheel centreline on tandem wheels at $L = 1.5D_w$ and α equal to 0 deg, 10 deg and 20 deg: DDES with fixed transition C (——) is compared with untripped experiments ($*$).

7.3.6 Surface Flow Features

The surface features are illustrated in Figure 7.16 for the single wheel with the mean skin friction coefficient in the streamwise direction (along the x-axis). The laminar boundary layer generates a separation bubble with a crescent-like shape on the wheel side surface. The crescent-like separation bubble (visible only in case B and C) is located in the front part of the flat lateral surface of the wheel.

The flow is attached on the wheel surface and is laminar up to the separation bubble at approximately 120 deg. In the simulations with fixed transition B and C, the flow reattaches on the wheel surface after the separation bubble. In the standard case A, the flow is attached for a longer distance and then separates. A small area with negative skin friction can be observed in case A too, but it is located at higher azimuthal angle and almost coincides with the final flow separation area.

The flow separates on the rear part of the wheel in approximately the same position for the three cases, but the stream-line patterns in the separated area are different. Similar features are seen for the surface streamlines of the tandem-wheel case (not shown), even though the flow is more complex to analyse because of the interactions between the wheels.

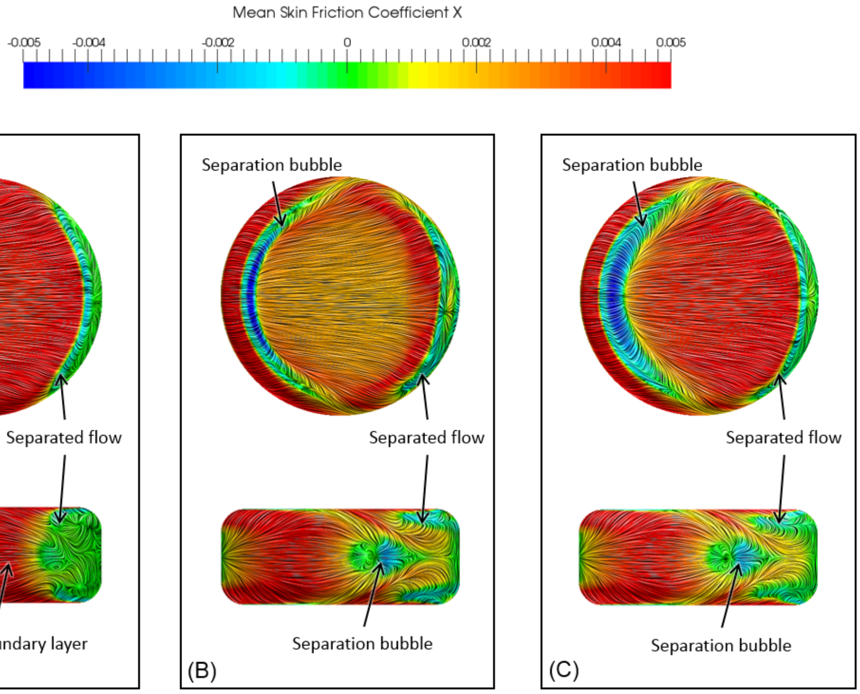

Figure 7.16: Surface streamlines on single wheel coloured by mean skin friction coefficient in streamwise direction: standard DDES model A, DDES with fixed transition at constant streamwise plane B, and DDES with transition at constant streamwise plane and wheel lateral surface C.

7.3.7 Velocity Field

A comparison of the mean velocity field on a plane in the wake of the single wheel and the PIV data is illustrated in Figure 7.17, where the mean streamwise velocity from PIV is used to validate the DDES simulations. The 2D turbulent kinetic energy is shown in Figure 7.18 for both experiments and simulations. The two-dimensional contour plot provides some qualitative information on the wake. The wake in the single wheel case is symmetric, in all the tested DDES, as in the case illustrated in Figure 7.17. On the contrary, in the case of the tandem wheels at $\alpha = 0\,\text{deg}$ (not shown here), asymmetric wakes are generated with the DDES case A, as in the tripped experiment. PIV data are available only for two components of velocity, thus a comparison of three-dimensional turbulent kinetic energy is not possible. In Figure 7.19 the difference between the three-dimensional and the two-dimensional turbulent kinetic energy is shown. The difference is mainly in intensity rather than in shape.

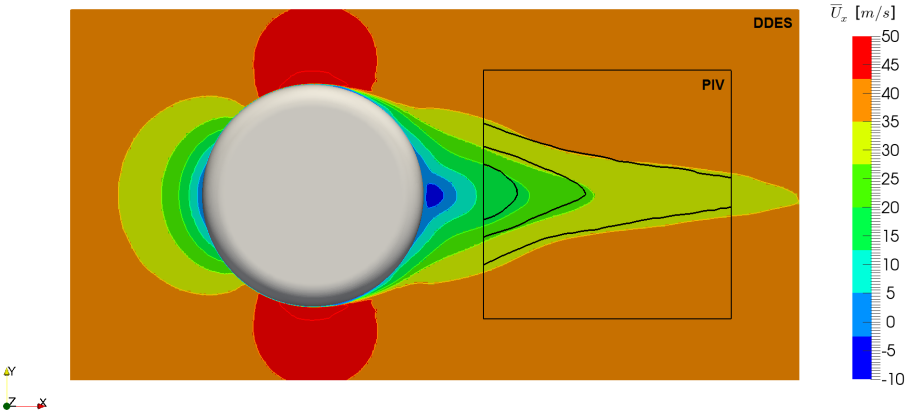

Figure 7.17: Mean streamwise velocity field for single wheel at the centreline plane: DDES with fixed transition case C (coloured contours) and PIV from experiment (black contours with same level values).

A velocity profile on a vertical line can be extracted from the PIV plane. In Figure 7.20, the vertical line is at the streamwise position corresponding to a distance D_w downstream of the wheel axle for the single-wheel case (or the rear-wheel axle for the tandem wheels). The agreement between CFD and experiments for both models on the single wheel case is satisfactory (Figure 7.20(a)) with maximum discrepancies of less than 8% on the minimum velocity values. The mesh used in this specific plot is the Mesh II type, and the results for the single wheel case are not sensitive to the type of meshing strategy as described earlier in this chapter.

Concerning the tandem wheels $L = 1.5D$ and $\alpha = 0\,\text{deg}$ in Figure 7.20(b), the standard model A shows discrepancies in the wake prediction for the tandem wheels. Only the

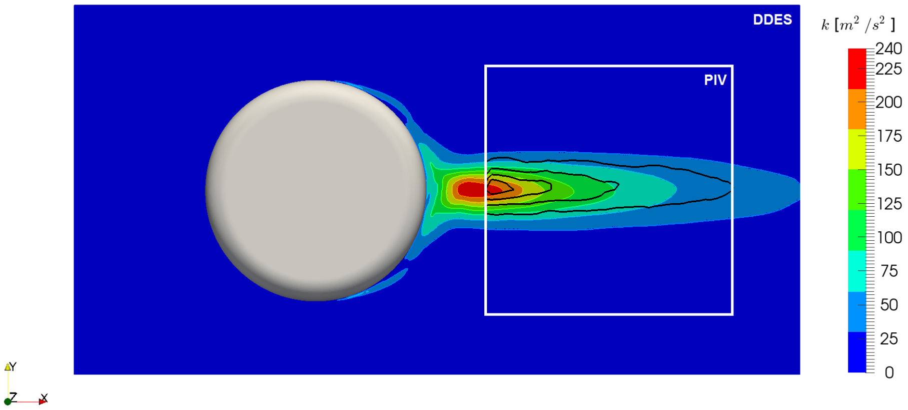

Figure 7.18: Two-dimensional turbulent kinetic energy velocity field for single wheel at the centreline plane: DDES with fixed transition case C (coloured contours) and PIV from experiment (black contours with same level values).

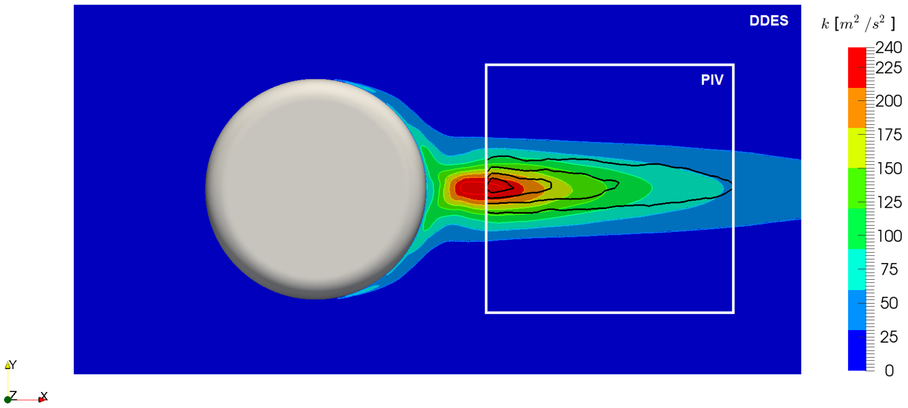

Figure 7.19: Three-dimensional turbulent kinetic energy of DDES is compared to two-dimensional turbulent kinetic energy of PIV, for single wheel at the centreline plane: DDES with fixed transition case C (coloured contours) and PIV from experiment (black contours with same level values). A comparison between three-dimensional turbulent kinetic energy of experiments and simulations is not possible because only two velocity components were acquired during the experiment.

models with fixed transition used in case B (not shown) and case C are capable of reproducing the experimental PIV data. In detail, Figure 7.20(b) shows the development of an asymmetric wake (in the y direction) for the tandem wheels at zero angle of attack, as confirmed by non-zero lift coefficients from CFD for this configuration. Similar phenomena happened with tripped experiments. For both cases, negligible differences are found between the fixed-transition cases B and C. As noted previously, Mesh I shows higher prediction accuracy over Mesh II, thus the results given here are for Mesh I only.

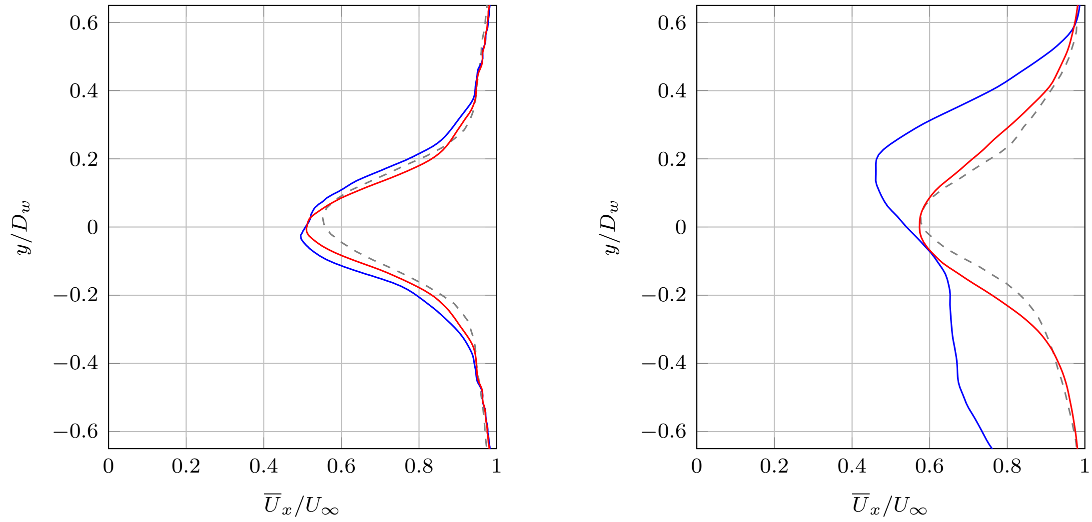

(a) Single wheel

(b) Tandem wheels: $L = 1.5D$, $\alpha = 0\,\mathrm{deg}$

Figure 7.20: Mean velocity field for single and tandem wheels at distance D_w downstream of the rear wheel centreline (or from the single wheel centreline, depending on the case): experiment (- - -), standard DDES case A (——), and DDES with fixed-transition case C (——).

The vortical structures described in Chapter 6 can be observed in Figure 7.21, where the four vortices are illustrated with the mean vorticity in the wake of the single wheel. In Figure 7.22, the same features are shown between the front and the rear wheel for the tandem wheels and in Figure 7.23 after the rear wheels.

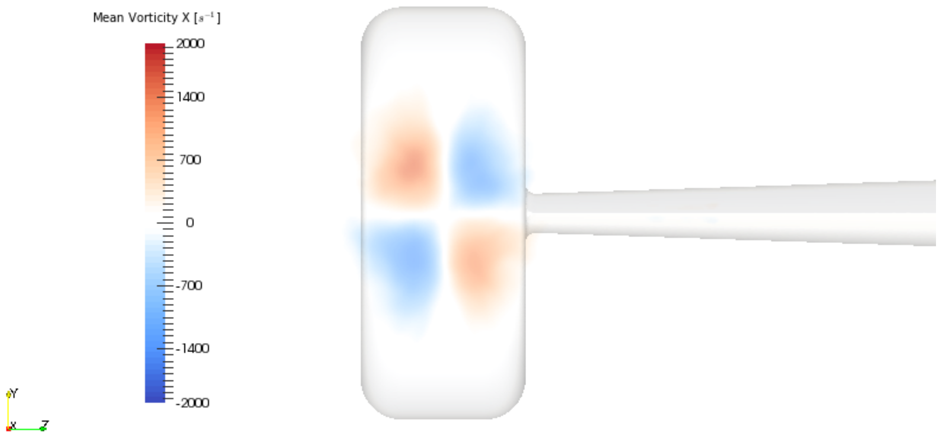

Figure 7.21: Mean vorticity (x-component) past the single wheel in the yz-plane at the location $x = D_w$.

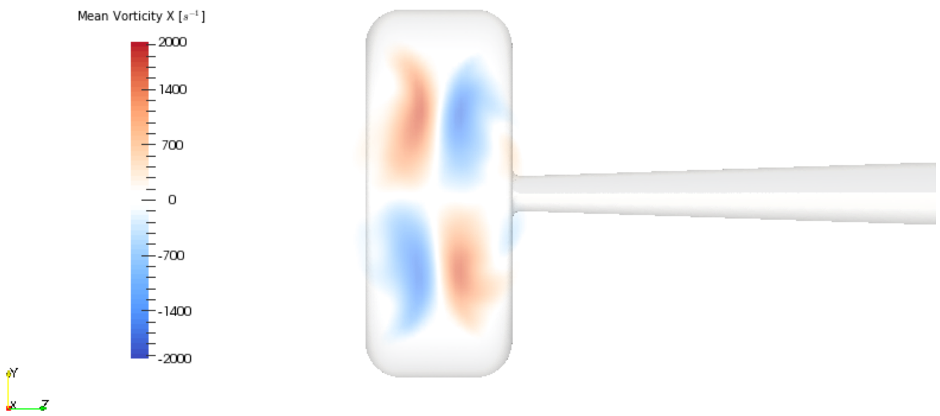

Figure 7.22: Mean vorticity (x-component) past the tandem wheels in the yz-plane at the location $x = 0.75D_w$. The plane is located in the midplane between the front and the rear wheels.

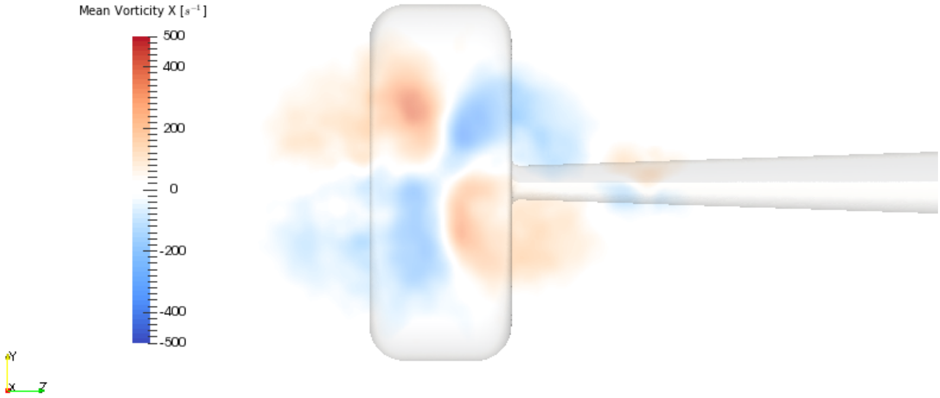

Figure 7.23: Mean vorticity (x-component) past the tandem wheels in the yz-plane at the location $x = 2.5D_w$. The plane is located in the midplane between the front and the rear wheels.

7.3.8 POD analysis

POD analysis was used in order to compare the POD modes between experiments and simulations. In the single wheel case, the energy content for the first ten modes is given in Figure 7.24, and the POD modes extracted from the CFD are compared with the experimental POD modes in Figure 7.25 and Figure 7.26. The energy content and the shape of the first two modes and their respective energy content is in good agreement with the experiments, whilst the third mode is different. This is due to a slightly different energy content of the modes, which are sorted by energy content.

The energy content of the tandem-wheel simulation is given in Figure 7.27, whilst the POD modes from CFD are compared with the experimental modes in Figure 7.28 and Figure 7.29. This case, like the single wheel, shows the same modes for the first and the second position, but the third mode is not the same due to a different order of the modes. In fact, the modes are ordered by energy content, but modes with comparable energy contents may appear swapped between experiments and simulations for small differences in energy content.

The comparison of the POD modes between CFD and experiments allows the identification of the cells that are correctly modeled in the CFD. In this case, the result is satisfactory also in terms of POD modes.

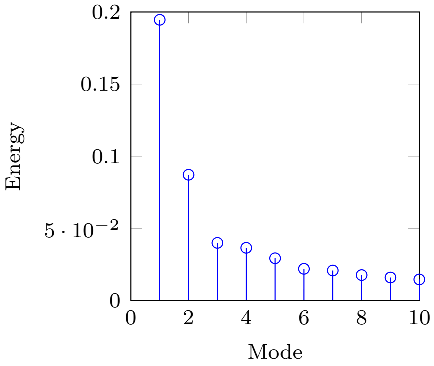

Figure 7.24: POD energy content for the single-wheel simulations.

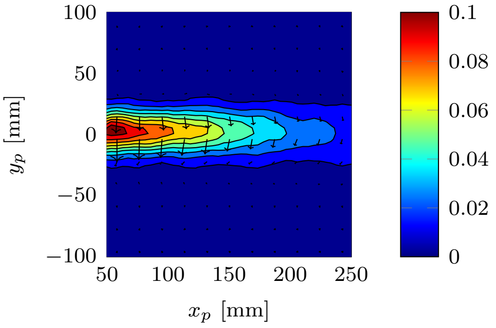

(a) POD Mode 1, 25.4% energy

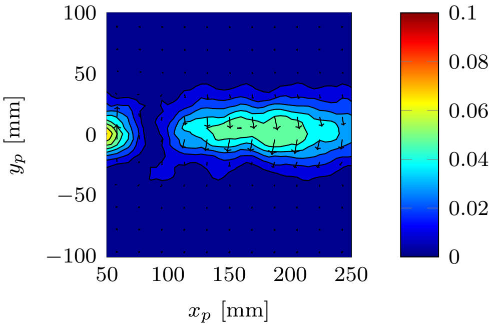

(b) POD Mode 2, 8.2% energy

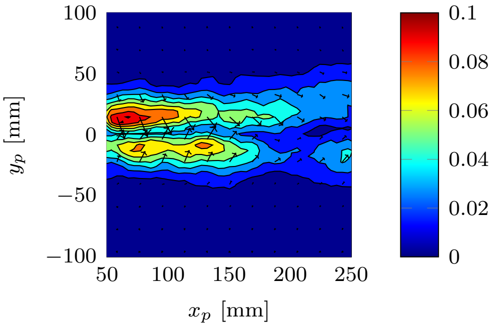

(c) POD Mode 3, 4.8% energy

Figure 7.25: Dimensionless velocity of POD modes (refer to Equation 6.5), single-wheel experiment

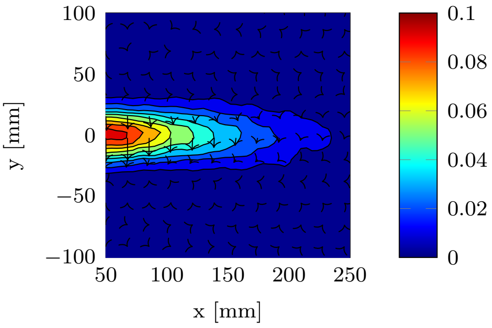

(a) POD Mode 1, 19.5% energy

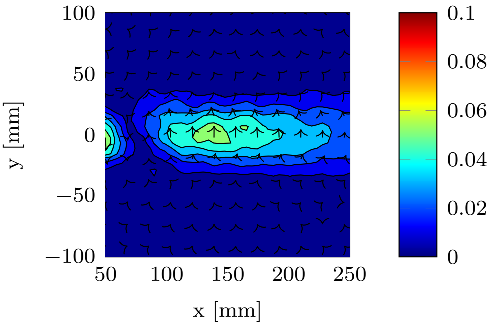

(b) POD Mode 2, 8.7% energy

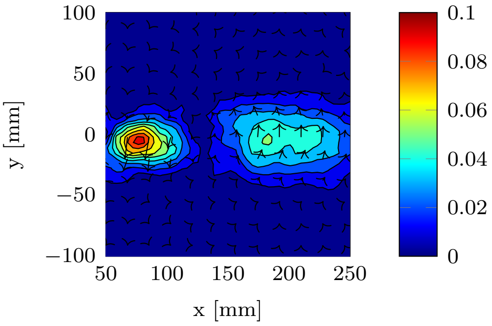

(c) POD Mode 3, 4.0% energy

Figure 7.26: Dimensionless velocity of POD modes (refer to Equation 6.5), single-wheel simulations.

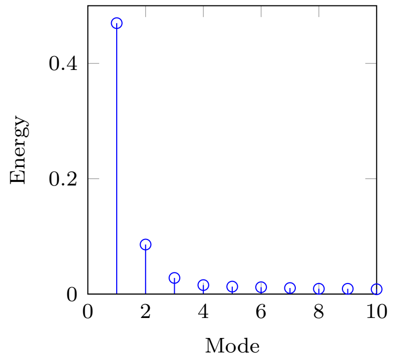

Figure 7.27: POD energy content for the tandem-wheel simulations.

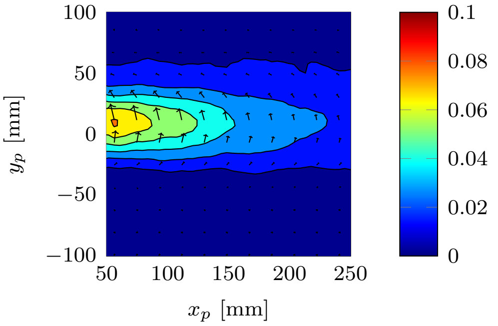

(a) POD Mode 1, 41.6% energy

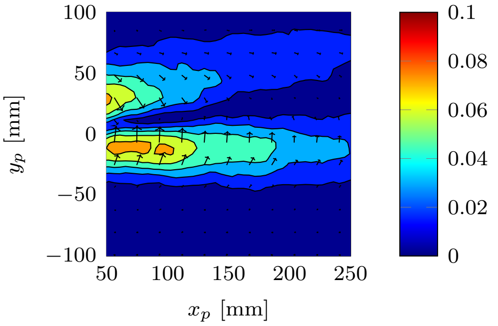

(b) POD Mode 2, 8.2% energy

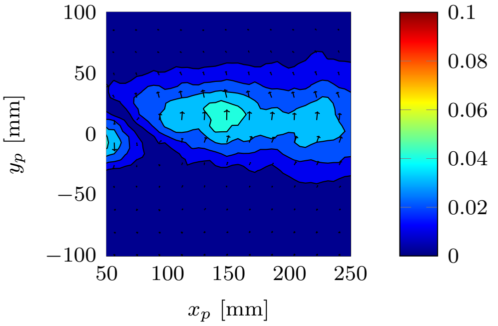

(c) POD Mode 3, 4.9% energy

Figure 7.28: Dimensionless velocity of POD modes (refer to Equation 6.5), tandem-wheel experiments.

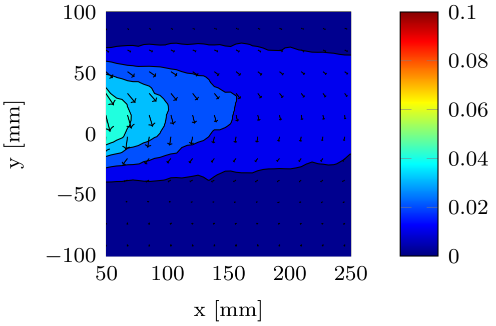

(a) POD Mode 1, 47.0% energy

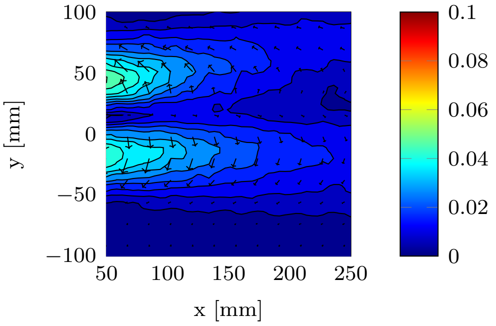

(b) POD Mode 2, 8.6% energy

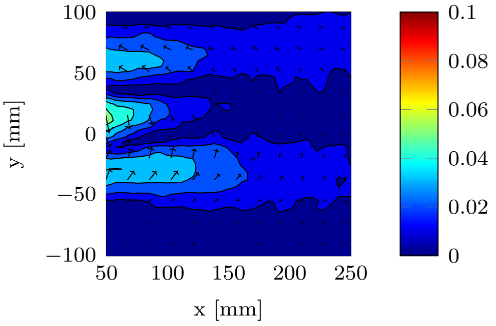

(c) POD Mode 3, 2.8% energy

Figure 7.29: Dimensionless velocity of POD modes (refer to Equation 6.5), tandem-wheel simulations.

7.4 Summary

DDES simulations were performed on a scaled model of generic landing-gear wheels in single and tandem configurations. The aim was to develop more accurate and efficient prediction methodologies for landing-gear aerodynamic loads. The results highlight the need for correctly modelling the flow physics in the boundary layer in order to reproduce the experimental data. For this reason, the use of semi-structured boundary-layer meshes is needed throughout the boundary-layer height in order to ensure the maximum efficiency, without loss of accuracy. The main source of discrepancy is the fully-turbulent boundary layer while simulating flows in the transitional regimes (in this case, Reynolds number $Re_D \approx 5 \times 10^5$). This problem can be overcome by deactivating the turbulence model in the laminar part of the flow. The improved results obtained by fixing the transition are in good agreement with the experiments (within 1%) both for the single wheel and the tandem wheels at zero angle of attack. Higher errors (up to 15%) are found on the tandem wheels at high angles of attack, mainly because of the uncertainties in modelling the separation bubbles on the part of the rear wheel that is not contained in the wake of the front wheel. In the current setup, the transition location is determined using the experimental data. In order to exploit the simulation methodologies on transitional cases on which no experimental data are available, more advanced means to set the transition location should be developed. Further work on the transitional models in combination with DDES may be of interest for various applications.

Chapter 8

Landing-gear components interactions

In order to understand the effects of additional components on the tandem-wheel, a four-wheel simplified landing-gear bogie is analysed with a progressively increasing number of components: four wheels only, four wheels with axles and bogie beam, and the full simplified landing gear. The work in this chapter will be published in Spagnolo et al. [73].

8.1 Computational Model Geometry

In this study, three cases are numerically evaluated for the analysis of the interactions between landing-gear components (see Figure 8.1):

(a) four wheels (no linking elements), Figure 8.1(a);

(b) four-wheel assembly (axles and bogie beam), Figure 8.1(b);

(c) simplified four-wheel landing gear (axles, bogie beam and main strut), Figure 8.1(c).

The geometry of case (a) comprises four wheels with the same shape as the single and tandem wheels presented in Chapter 6 and Chapter 7. In case (b), two axles and one bogie beam are included, and in case (c) the landing-gear strut is also added to the model. As shown in Figure 8.2, the geometric parameters are defined as follows: the wheel diameter D_w is 0.181 m, the wheel width W is $0.4D_w$, the axle length S_w is $0.7D_w$, the axle and bogie-beam diameter is $0.17D_w$, the inter-axis distance L_w is $1.5D_w$ and the fillet radius R is $0.1D_w$. The landing-gear strut has a diameter $D_l = 0.25D_w$ and a length of $H_l = 2D_w$. The landing gear is placed in a domain $25D_w$ long, at $10D_w$ from

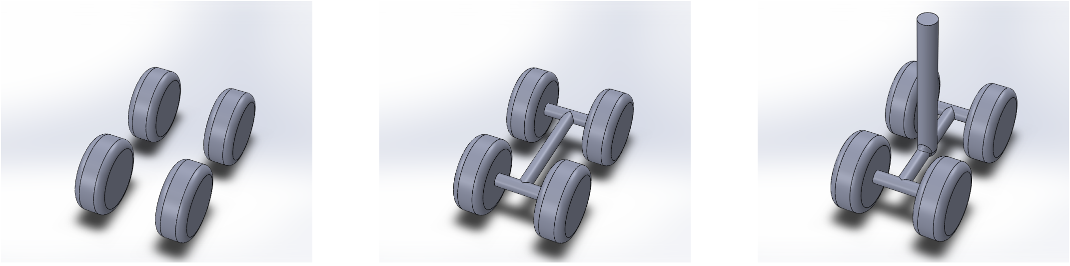

(a) Four wheels only

(b) Four wheels, axles and bogie beam

(c) Simplified four-wheel landing gear

Figure 8.1: Geometries of the three analysed cases.

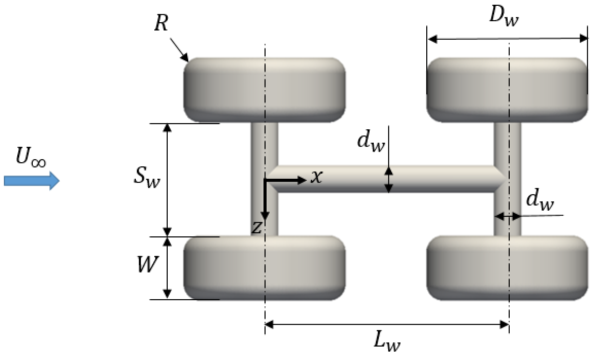

Figure 8.2: Geometry of four-wheel bogie with reference lenghts.

the inlet. The cross-section of the domain is $15D_w \times 15D_w$. The free-stream velocity U_∞ is 40 m/s, corresponding to a Reynolds number Re_D of 5×10^5.

8.2 Computational Setup

8.2.1 Governing Equations and Solver

The simulations were run in OpenFOAM® with the PISO algorithm. For all the simulations in this chapter, the turbulence is suppressed in the upstream part of the CFD domain as previously done on tandem wheels in Chapter 7, (see Figure 7.2(C)). The only exception is the study of the effects of the fixed transition on the four-wheel bogie, where a fully-turbulent simulation is also performed (as shown in Figure 7.2(A)). The flow on the axles and the bogie beam is fully turbulent in all the simulations of this chapter, in order to minimise the effect of the transition on the cylinder-like structures.

8.2.2 Meshes

The mesh used for the simulations is hexa-dominant and it is generated in HEXPRESS™/Hybrid. The grids are generated with criteria similar to those previously used in Chapter 7, employing both refinement zones and a semi-structured boundary-layer mesh. The grids have coarse cells ($0.1 - 0.2D_w$) in the regions far from the bodies and one or more refinement blocks (with cells about $0.01 - 0.04D_w$). The surface mesh is $0.005 - 0.01D_w$ in order to correctly describe the surface of the bodies and capture the surface flow features. All the meshes include a semi-structured boundary-layer mesh extruded from the wall surface mesh of the bodies of interest. The semi-structured grid on the bodies surface is extruded with first cell-centre height approximately 10^{-5}m in order to obtain the target maximum $y^+ \approx 1$. An example of mesh for case (b) is illustrated in Figure 8.3.

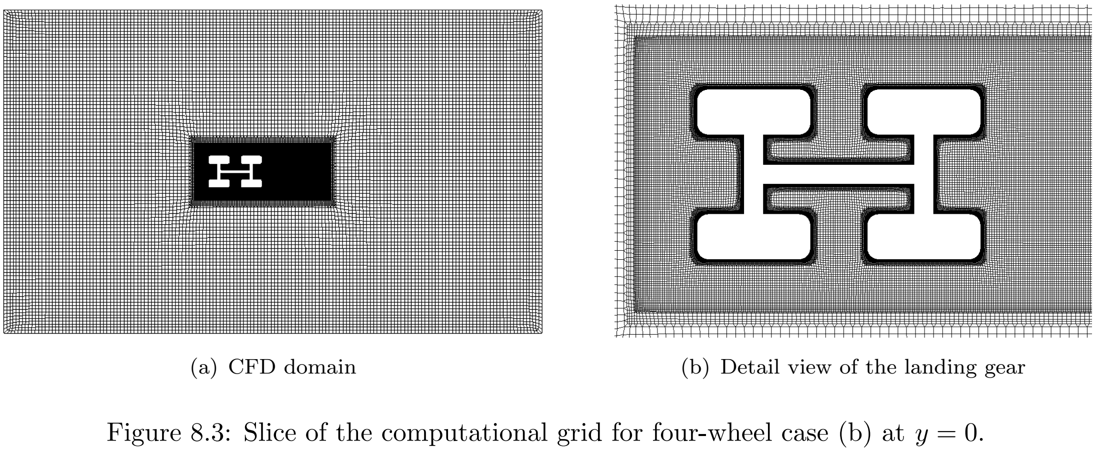

(a) CFD domain

(b) Detail view of the landing gear

Figure 8.3: Slice of the computational grid for four-wheel case (b) at $y = 0$.

8.2.3 Computational Procedure

After the mesh is generated, the case is initialised with a precursor steady RANS run, as previously explained. The flow is then simulated in DDES mode for 0.2 s (more than 40 diameter-based convective times) before starting the data sampling, which lasts until convergence of the statistical results. The statistics are considered converged when the average drag coefficients are within 1% with respect to the value averaged over half of the simulated time. This corresponds to approximately 0.5 s of simulation time. The surface pressures are monitored at 60 points on each wheel, corresponding to the points measured in the experiment on the tandem wheels (Chapter 6) . As a reference, on a 27-million-cell grid, the computational wall-time is approximately 300 hours on 384 cores for 0.5 s of simulation time on Iridis 4 (University of Southampton).

8.3 Results

8.3.1 Comparison of the three configurations

The resulting mean forces for the three configurations are given in Table 8.1 and in Table 8.2. The force coefficients are calculated with the frontal projected area $S = 0.012\,85\,\mathrm{m}^2$. As a reference, for tandem wheels (same geometric parameters) the front wheel mean drag coefficient is 0.082 in the experiments and 0.081 in the simulations, while the mean drag coefficient of the rear wheels is 0.336 in the experiments and 0.341 in the simulations. Mean pressure coefficients are given in Figure 8.4 for the three configurations, again using the tandem wheels as a reference case (both experiments and simulations).

In case (a), the mean drag coefficients of the front wheels are reasonably close to the tandem-wheel case, whilst the mean drag coefficients of the rear wheels are higher. The reasons for the higher mean drag coefficient on the rear wheels are the blockage effect induced locally by the presence of the wheels and interactions between the wakes past wheels of opposite sides.

The mean lift coefficient is not zero for the wheels on the right-hand side of the geometry (negative z in Figure 8.2), a behaviour similar to that previously observed for tandem wheels. The different behaviours of the wheels belonging to opposite sides (in case (a) only) is typical of this configuration. The additional elements like axles and struts have a strong impact on the stability of the symmetrical flow.

In Figure 8.5 it can be noted that the mean flow past the front left and right wheel generates vortices that interact with the flow around the rear wheels of the opposite side. The blockage given by the presence of the wheels side by side increases the velocity of the fluid impinging on the rear wheels. This increases the values of the pressure coefficients

Table 8.1: Mean drag coefficients for the three cases. Left and right are with positve and negative values of z in Figure 8.2, respectively.

Part	**Case (a)**	**Case (b)**	**Case (c)**
Front Left Wheel	0.087	0.361	0.381
Wheel Front Right	0.085	0.368	0.375
Wheel Rear Left	0.383	0.436	0.412
Wheel Rear Right	0.390	0.434	0.400
Axle Front		0.113	0.115
Axle Rear		0.113	0.113
Bogie Beam		0.001	0.001
Strut			0.671
TOTAL	0.945	1.826	2.468

Table 8.2: Mean lift coefficients for the three cases. Left and right are with positve and negative values of z in Figure 8.2, respectively.

Part	**Case (a)**	**Case (b)**	**Case (c)**
Front Left Wheel	0.002	0.000	-0.020
Front Right Wheel	-0.001	0.002	-0.025
Rear Left Wheel	-0.024	0.055	-0.098
Rear Right Wheel	-0.160	-0.058	-0.042
Front Axle		0.000	0.000
Rear Axle		0.003	0.006
Bogie Beam		-0.002	0.029
Strut			0.113
TOTAL	-0.183	0.000	-0.037

on the fore part of the rear wheel, as shown in Figure 8.4. In Figure 8.6 the vortical system between the front wheels and the rear wheels is shown. At that streamwise position, the vortices are still independent from each other. The mean vorticity shows the same pattern of vorticity that can be expected between the front wheel and the rear wheel in the tandem-wheel configuration. It is as the vortices move downstream that they start to interact with the vortices from the other pair.

When the axles and the bogie beam are added to the four-wheel configuration, i.e. in

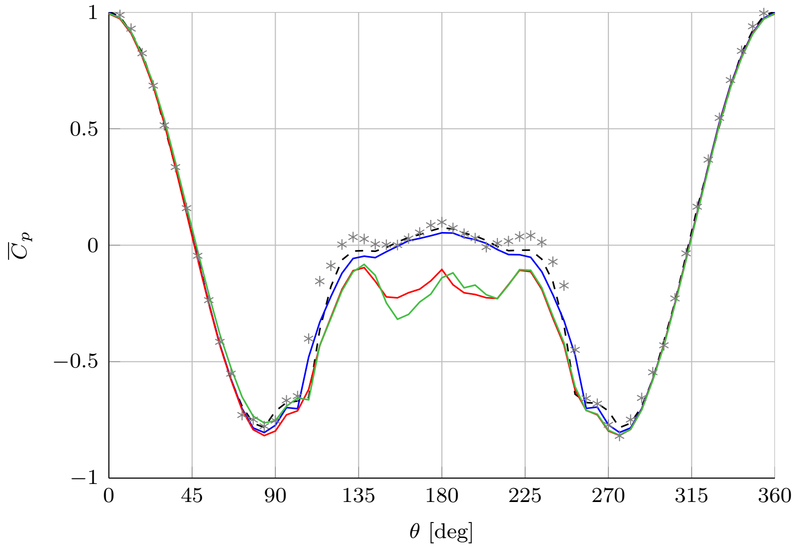

(a) Front wheel

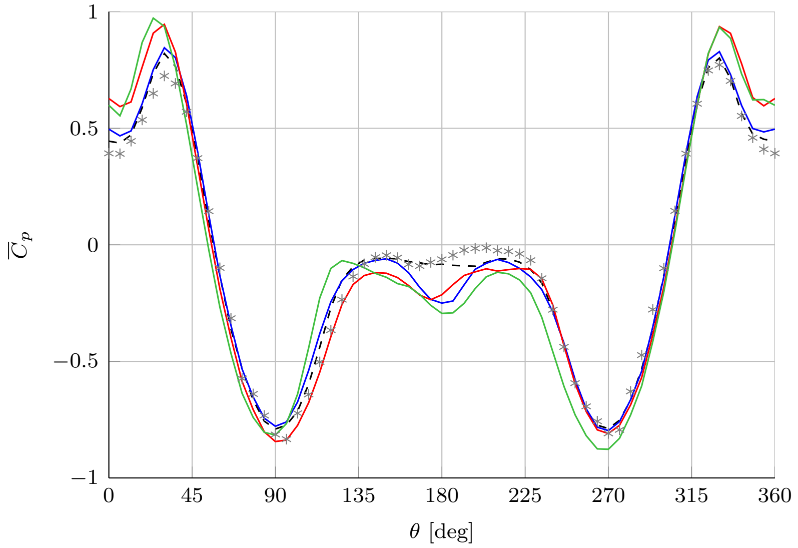

(b) Rear wheel

Figure 8.4: Mean pressure coefficient $\overline{C}_p$ along the wheel mid-plane circumference: four-wheel landing-gear simulations for the three cases (a) ——, (b) —— and (c) ——. Also the curves for the reference tandem-wheel simulations from Chapter 7 (- - -), and tandem-wheel experiments from Chapter 6 ($*$) are shown.

case (b), the mean drag coefficient of the front wheels is much larger than the tandem-wheel case and the forces on the rear wheels are slightly higher than in the previous case. As can be seen in Figure 8.4, the low-pressure area past the front axle changes the aft pressure on the front wheels with respect to the tandem wheels. This difference in pressure is one of the causes for a large difference in the values of the drag coefficients of the front wheels. Also, the two high-pressure areas on the fore part of the rear wheels have a higher $\overline{C}_p$ than in the tandem-wheel case, contributing to the increase of mean

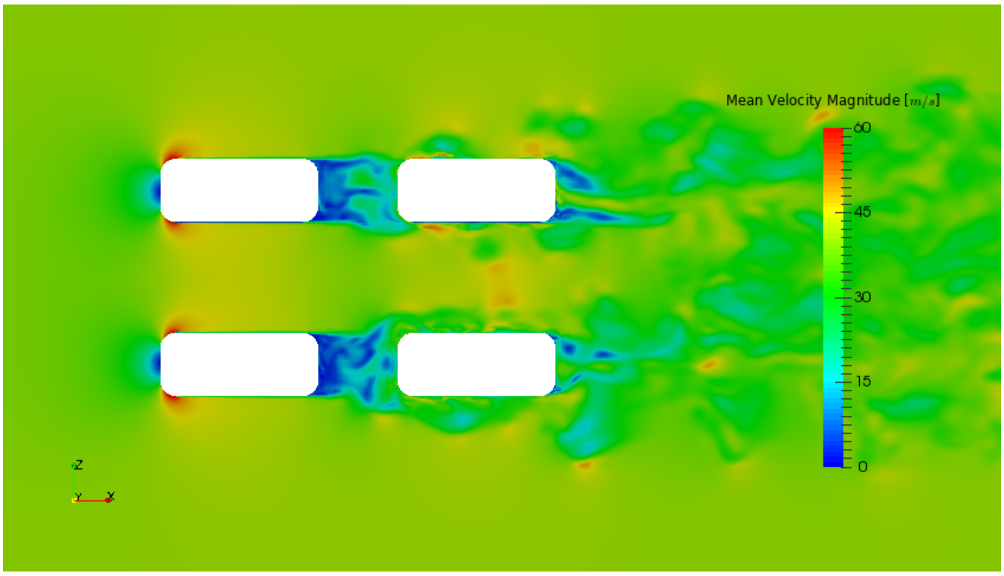

Figure 8.5: Case (a): instantaneous velocity magnitude in the xz-plane at the symmetry plane $y = 0$, four-wheel configuration.

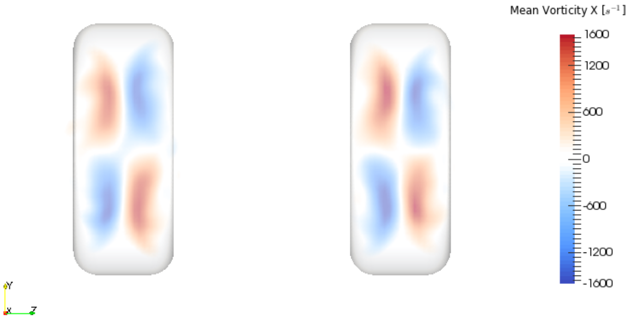

Figure 8.6: Case (a): mean vorticity (x-component) in the yz-plane at the location $x = 0.75D_w$. The plane is located in the midplane between the front and the rear wheels.

drag coefficient. The axles and the bogie beam create a blockage effect that is larger than in the case with four wheels only.

The wake impinging on the rear wheels in case (b) is formed by multiple vortical structures that combine the flow features detaching from the wheels and those detaching from the axles. The mean velocity magnitude contours are given in Figure 8.7. The flow past the front wheels interacts with the front axle and the bogie beam. An example of instantaneous streamwise vorticity is shown in Figure 8.8. The vortical structures between the front and the rear wheels are shown by means of mean streamwise vorticity in Figure 8.9. The vortical system past the wheels is linked with the wake past the cylindrical axle. The two internal pairs of vortices for each front wheel merge with the vorticity detaching from the axles forming a system of eight counter-rotating vortices, with the internal four vortices showing higher intensity and size. The two internal vortices for each wheel are enhanced by the presence of the axle. A secondary vortex system on the bogie beam can be observed in the picture. For each internal vortex past the wheels a secondary vortex is generated on the bogie beam surface, rotating in the opposite direction.

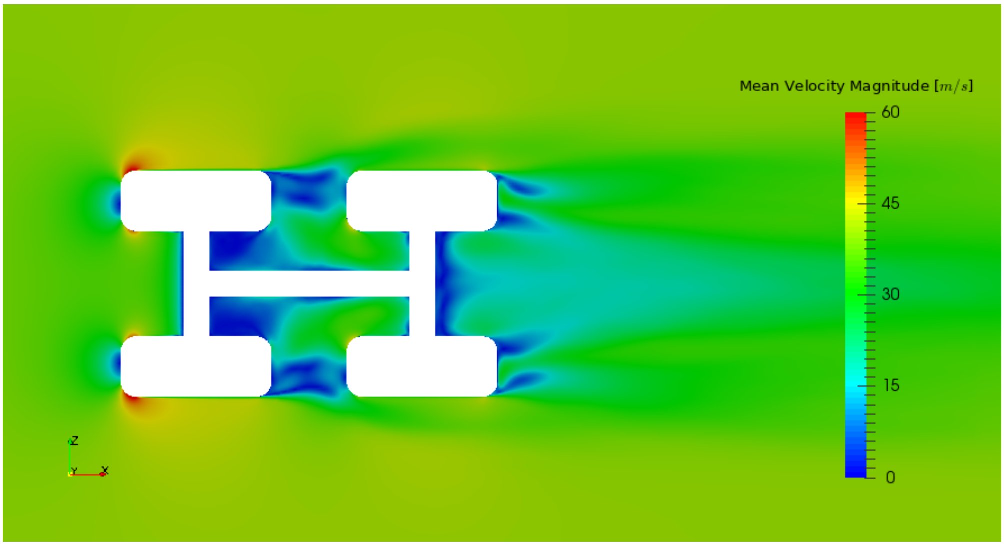

Figure 8.7: Case (b): mean velocity magnitude in the xz-plane at the symmetry plane $y = 0$.

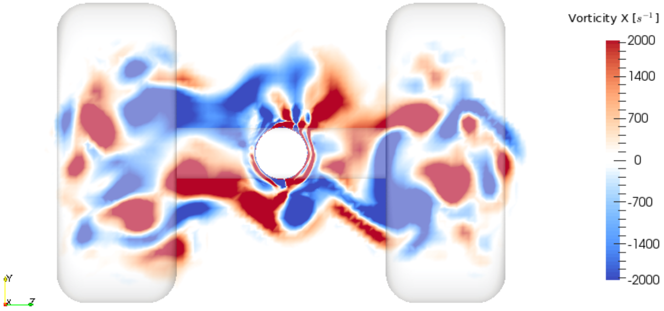

Figure 8.8: Case (b): instantaneous vorticity (x-component) in the yz-plane at the location $x = 0.75D_w$. The plane is located in the midplane between the front and the rear wheels.

The high degree of interaction present between the components of the geometry in case (b) is also confirmed by the shape of the horse-shoe vortex that is formed on the intersection between wheels and axles, in Figure 8.10. The zone that is affected by the wake of the axle has a size that is comparable with the wheel diameter. The flow in this part of the geometry significantly differs from the flow past the tandem wheels (Chapter 7) where the streamlined supports did not have such a strong effect on the flow past the wheels.

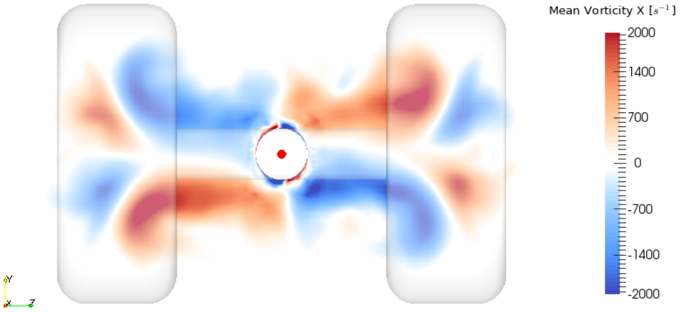

Figure 8.9: Case (b): mean vorticity (x-component) in the yz-plane at the location $x = 0.75D_w$. The plane is located in the midplane between the front and the rear wheels.

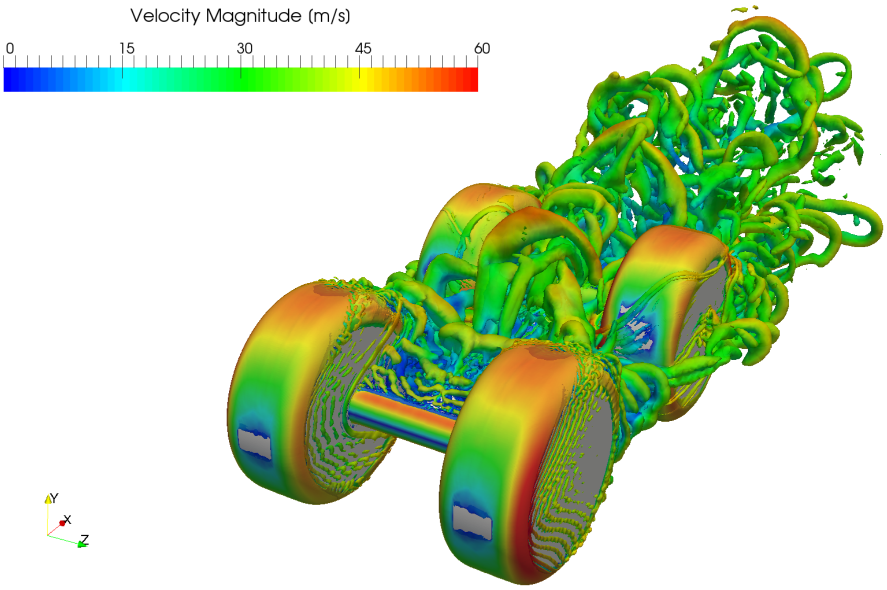

Figure 8.10: Case (b): isosurface of $Q = 5 \times 10^5\,\mathrm{s}^{-2}$ coloured with velocity magnitude.

Case (c) is the configuration with the highest total drag coefficient (Table 8.1), of which a large part is due to the additional vertical strut (the main strut). Instead, it can be seen that the mean drag coefficient on each component is only minimally different from case (b). The main strut has the effect of generating a slight increase in the flow velocity in the region between the front and the rear wheels, which lowers the pressure behind the front wheels and before the rear wheels (Figure 8.4). This increases the mean drag coefficient on the front wheels and reduces the mean drag coefficient on the rear wheels (differences between 3 and 8% with respect to case (b)).

The changes in terms of mean streamwise vorticity are shown in Figure 8.11. The structure of the upper central vortices is broken by the presence of the cylindrical strut, with the additional formation of two smaller vortices in the proximity of the node between the bogie beam and the main strut. An example of Q-criterion of case (C) is shown in Figure 8.12.

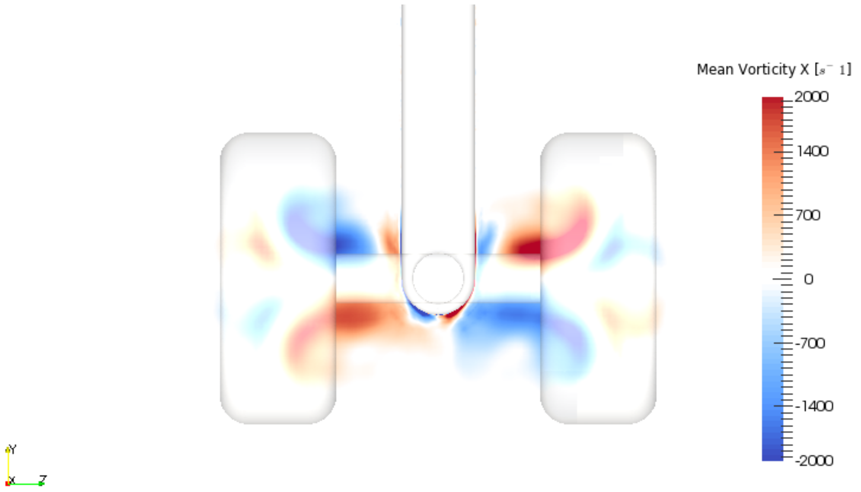

Figure 8.11: Case (c): mean vorticity (x-component) in the yz-plane at the location $x = 0.75D_w$. The plane is located in the midplane between the front and the rear wheels.

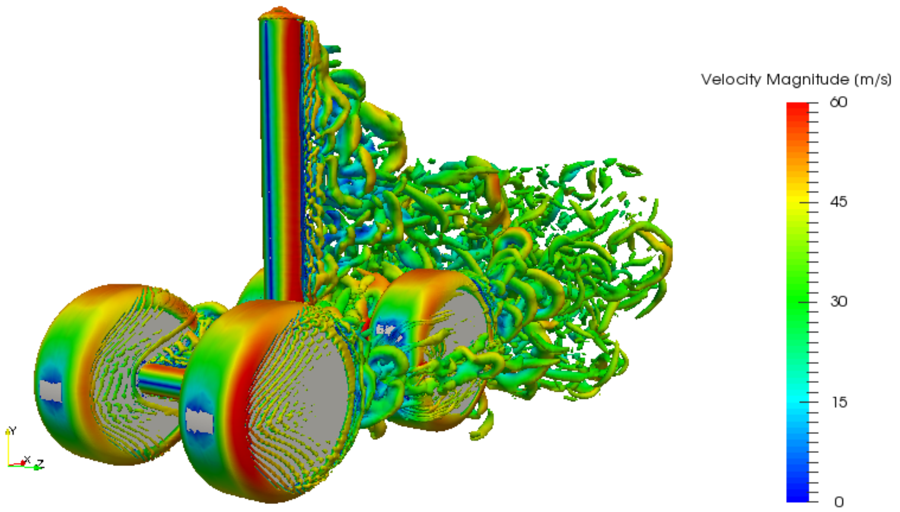

Figure 8.12: Case (c): Q-criterion isocontour coloured with velocity magnitude.

The RMS of the force coefficients are shown in Table 8.3 and Table 8.4. Overall, the rear wheels are more affected by fluctuations in the aerodynamic loads, together with the rear axle (which is immersed in the wake of the upstream bodies). Similarly to the flow past tandem wheels, drag coefficients generally show smaller RMS values than the respective lift coefficients for each component.

Most of the differences between case (a) and case (b) can be seen in the RMS values, especially on the aerodynamic loads on the rear wheels. The reason is again the influence of the wake past the axles and bogie beam, which acts on two separate levels: the wake past the additional components creates more perturbation and therefore higher unsteadiness on the aerodynamic loads; and the additional components modify the mean flow, which has as the change of RMS as a secondary effect. An example of the direct effect of the mean flow on the RMS is the difference of mean lift coefficient and RMS lift coefficient of the rear wheels in case (a). The non-zero mean lift coefficient of the rear right wheel makes the flow more stable around a non-symmetrical configuration with low levels of RMS, whilst the rear left wheel has zero lift coefficient with higher levels of RMS because the flow is less stable around that configuration.

Table 8.3: RMS drag coefficients for the three cases. Left and right are with positve and negative values of z in Figure 8.2, respectively.

Part	**Case (a)**	**Case (b)**	**Case (c)**
Front Left Wheel	0.0074	0.0229	0.0194
Front Right Wheel	0.0057	0.0235	0.0245
Rear Left Wheel	0.0253	0.0413	0.0353
Rear Right Wheel	0.0247	0.0401	0.0354
Front Axle		0.0025	0.0022
Rear Axle		0.0189	0.0192
Bogie Beam		0.0003	0.0004
Strut			0.0455

Table 8.4: RMS lift coefficients for the three cases. Left and right are with positve and negative values of z in Figure 8.2, respectively.

Part	**Case (a)**	**Case (b)**	**Case (c)**
Front Left Wheel	0.0165	0.0255	0.0249
Front Right Wheel	0.0277	0.0283	0.0296
Rear Left Wheel	0.1371	0.0798	0.0536
Rear Right Wheel	0.0362	0.0587	0.0673
Front Axle		0.0068	0.0067
Rear Axle		0.0485	0.0485
Bogie Beam		0.0643	0.0568
Strut			0.0152

8.3.2 Effect of fixed transition on the bogie

In order to understand the effects of fixed transition on a geometry like a full bogie, one simulation on the four-wheel bogie with axles and bogie beam was repeated with the standard DDES model (results in Table 8.5 and Table 8.6). The differences between the results on a geometry with more complex features are negligible in terms of mean forces, while in terms of RMS of the force coefficients the values show some differences (not shown). The reasons for the lower importance of this result in this configuration can be explained by the different sensitivity of the flow to the separation position.

In the case of tandem wheels or four wheels without axles, the mean flow can easily become asymmetric because of changes of separation position. This problem was observed both in experiments and simulations. Thus it can be considered a physical problem of the specific case. In the case of a four-wheel bogie (with axles and bogie beam) the wake past the wheels interacts with the wake past the other bluff bodies, the effect of which is to stabilise the wake around a symmetrical condition at the installation angle $\alpha = 0\,\mathrm{deg}$.

As can be seen in Figure 8.13, the application of the transition shows few differences on the wheels. The main difference is the presence of the laminar separation bubble in the case with fixed transition. So, the effect of the fixed transition applied to a full landing-gear is less important than it was for single wheels. The difference between the two models goes from approximately 9% of the tandem wheels to approximately 1% of the full landing gear. Therefore, for this more complex case a model with fixed transition is not necessary to estimate the forces, even though the flow features are not completely captured by the standard model.

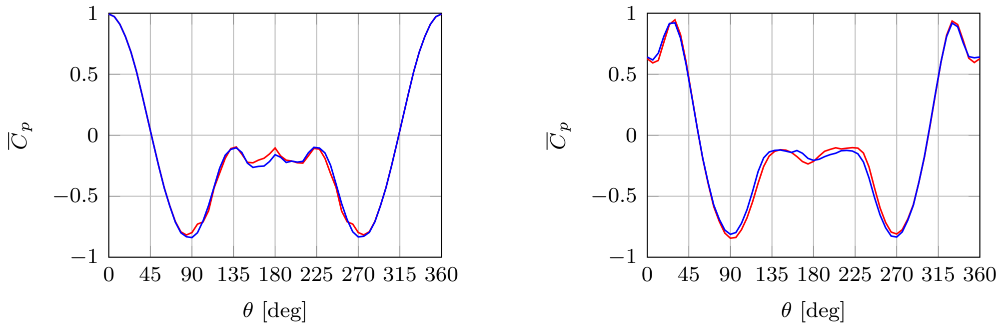

(a) Front wheel

(b) Rear wheel

Figure 8.13: Mean pressure coefficient $\overline{C}_p$ along the wheel mid-plane circumference: four-wheel landing-gear simulations for case (b) with standard model (——) and fixed transition (——).

Table 8.5: Case (b): mean drag coefficients with fixed transition and with the standard model.

Part	**Fixed transition**	**Standard**
Front Left Wheel	0.361	0.360
Front Right Wheel	0.368	0.355
Rear Left Wheel	0.436	0.428
Rear Right Wheel	0.434	0.426
Front Axle	0.113	0.114
Rear Axle	0.113	0.114
Bogie Beam	0.001	0.001
TOTAL	1.826	1.798

Table 8.6: Case (b): mean lift coefficients with fixed transition and with the standard model.

Part	**Fixed transition**	**Standard**
Front Left Wheel	0.000	0.010
Front Right Wheel	0.002	-0.001
Rear Left Wheel	0.055	-0.021
Rear Right Wheel	-0.058	0.010
Front Axle	0.000	0.000
Rear Axle	0.003	0.001
Bogie Beam	-0.002	0.007
TOTAL	0.000	0.006

8.4 Discussion

The main differences for the tested cases were identified on the front wheels, arguably because of the effect of the axle on the flow past the front wheels. The low-pressure of the wake generates a large difference in drag coefficient between the front wheels of the bogie and the front wheel of the tandem wheels. The effect of adding the axles and the bogie beam is a significant increase of mean drag on the front wheels and a slight increase on the rear wheels. Adding a main strut reduces the mean drag of the downstream wheels, but the mean drag of the front wheels slightly increases. The increase of drag on the front wheels is compatible with experiments from similar landing-gear studies previously available in the literature, such as the rudimentary landing gear [90, 91] or the simplified landing gear [27]. Both the rudimentary landing gear and the simplified landing gear have the drag coefficient of the front wheels higher than the drag coefficient of the rear wheels.

A similar trend is seen with the RMS values, which are of the same order of magnitude for the lift and drag coefficients only in the configurations with the additional components. This is in agreement with the results of simulations on full landing gear in the literature, such as the DES on the simplified kanding gear [27]. On the contrary, in the case with four wheels only, the RMS of the drag coefficient of the front wheels are one order of magnitude below the lift coefficient.

The pressure profiles and the flow structures are similar to those observed during the tandem-wheel experiments and simulations (from Chapters 6 and 7). This shows that, in general, the prediction methodology and some of the considerations on tandem wheels are valid for more complex geometries like a four-wheel landing gear, with or without additional components.

The application of the fixed transition in the simulations, which was needed in Chapter 7, is not particularly relevant for wheels with axles and additional components because in this case the wake is less sensitive to the separation position on the wheels.

8.5 Summary

The interactions between the landing-gear components as well as the differences between the four-wheel bogie and the tandem-wheel case were studied in this chapter. In order to study the interactions between landing-gear components, simulations on three different configurations were performed. The geometry with four wheels showed various analogies with the tandem-wheel case, compared to which the only difference is the interaction of wheels side by side. A few more differences (both on mean and unsteady forces) were found in the two configurations with the axles and the main strut. In detail, the mean drag coefficient of the front wheels is significantly higher. The change between a fully turbulent flow and a flow with fixed laminar-turbulent transition (firstly employed in 7) was less relevant on the full assembly than it was on the tandem wheels. This is because of the higher levels of perturbation induced by the presence of the axles and the strut.

Chapter 9

Conclusions

In this final chapter, the research questions and the main findings of the thesis are discussed, together with the implications, limitations and remarks for future works.

9.1 Reasons for Studying the Unsteady Flow past Tandem Wheels

Gaining a deeper insight into the unsteady aerodynamic flow past landing gear is important both for aeroacoustics and for unsteady aerodynamic loads on landing gear. Aeroacoustics often dictates design choices on modern aircraft Dobrzynski [19], as well as efficient tools for the prediction of aerodynamic loads on landing gear may improve the design of certain aircraft components. Various experiments and simulations were available in this field before the beginning of the PhD project, but there were a few major gaps: no experimental data of unsteady aerodynamic loads on landing-gear components, no experiments on wheels in tandem configurations, lack of efficiency consideration in the CFD methodologies. The research questions that were given in Section 1.2 can be summarised as follows.

1. Is it possible to measure the unsteady aerodynamic loads on landing-gear components? If yes, to what extent?
2. Is there any way to improve the current prediction methodologies for unsteady flows past bluff bodies such as landing-gear components?
3. Can the analysis of two wheels in tandem configuration enhance the current knowledge of the flow features of a four-wheel landing gear? Can it be used as a sample geometry for the answer to the previous two questions?
4. How is it possible to extend the work on the tandem wheel geometry to a full landing gear?

The answers to each of these four questions were given in the thesis and are respectively summarised in the next sections.

9.2 Main Findings, Implications, Limitations and Remarks for Future Works

9.2.1 Measurements of Unsteady Aerodynamic Loads

The measurements of the unsteady aerodynamic loads have been attempted a number of times on various geometries using different methods. The loads (or forces) are here intended as an integration of the aerodynamic pressure and shear stress on the body surface. As such, various methods based on the mathematical integration have been attempted, measuring the unsteady pressures in various locations and conveniently summing them. However, this did not suit our case due to the complexity of the landing-gear geometries. Typical examples of pressure integrations are circular cylinders. Thus, this work was immediately oriented toward a global measurement of the forces, such as strain-gauge based balances, and piezoelectric load sensors. Piezoelectric load sensors can be used for unsteady loads measurements, but they have the drawback of being unusable for mean forces and showing poor response at low frequencies. For these reasons, the piezoelectric sensors were discarded too, leaving the strain-gauge balances as the only option left. Other case-specific force measurements were described in the literature, but they were discarded for this specific case either because of cost or feasibility on complex geometries. The decision was then made to design a wind-tunnel model for optimal dynamic response. In practice, this means that the ratio between the aerodynamic loads and the measured loads is required to be approximately equal to one up to a frequency that has to be as high as possible, whilst also being compatible with the other requirements. After the design process, which utilised finite-elements modal analysis, the model was manufactured and tested for the resonances.

The novelty here was to introduce the vibration test as a validation tool for the accuracy of the unsteady loads. By means of the vibration test, it is possible to identify the upper limit of frequencies that are considered acceptable and that can be used to calculate RMS values of the unsteady aerodynamic loads. The power spectral densities of the acquired forces on tandem wheel geometries show that it was possible to acquire unsteady aerodynamic forces up to approximately 30 Hz, with errors of unsteady loads with respect to the higher frequencies that are estimated to be up to 30%. The errors on the RMS depend on the flow velocities, which affects both Strouhal number and Reynolds number. The errors increase with the velocity. The upper limit, as it has been made clear in some parts of the text, is mainly due to specific parts of the model, which reduce the upper limit to the stated value of 30 Hz. This means that redesigning some parts of the model the upper frequency limit may significantly increase.

The results are encouraging because the unsteady loads can be measured on simple but representative wind-tunnel models, and that a traditional strain-gauge based balance is sufficient for the unsteady measurements. The data were used as a validation database for the following CFD simulations with general good agreement. The strain-gauge balances proved to have great flexibility, providing both mean and unsteady loads (up to certain frequencies). The method can be implemented on more complex geometries using all the lessons learnt throughout the tests described so far. An important consideration is to allocate enough time and resources at the early stages to allow more than one design/manufacturing iteration.

The main limitation of this technique and this case is the maximum frequency up to which it is possible to measure the unsteady loads. But this problem is due to a well-known issue that could have been overcome by simply adding one more iteration of the design, manufacture and test process. Also, the specific technique used for the validation of the unsteady loads is the only technique attempted, but the idea of validating the aerodynamic unsteady loads *in situ* could be exploited with different approaches too. Other techniques may be used to asses the frequency response of the wind-tunnel model, such as a test with the hammer instead of a shaker. The analysis of other techniques would be beneficial, as long as the candidate techniques can be performed in the wind tunnel without dramatically affecting the wind-tunnel test matrix.

9.2.2 CFD Methodologies for Landing gear

Various CFD methodologies were available in the literature, such as URANS, LES, and hybrid RANS-LES. For this work, hybrid RANS-LES were chosen due to time constraints and the high expectations in terms of unsteady flow. The use of the hybrid turbulence modelling is not a novelty in the field of aerodynamic flows past landing gear. On the contrary, a number of studies highlight the feasibility and the accuracy of the methodologies, even though most of the publications cannot compare the unsteady forces with experimental data. Also, the simulations performed with only the aim of aeroacoustic prediction often do not show enough aerodynamic data or comparisons because it is considered secondary. The efficiency of the simulations is often not considered either, whereas here the efficiency is considered by relating the accuracy of the results to the time taken to complete the simulations.

Given the scale of the problem, and on the basis of previous works, a large number of cores were expected (in the range of 128 to 512 cores, depending on the case and mesh size). For this reason, an open-source code was advantageous to the successful accomplishment of the project. A secondary aspect that influenced the decision toward open-source software was the possibility to customise the code on the basis of what was needed. The results of the early simulations in OpenFOAM with the S-A DES versions (basic DES, DDES and IDDES) proved that the hybrid technique was the right choice in terms of compromise between the requirements: computational scale, time-to-solution, and accuracy. The early simulations were performed on benchmark cases with external data available (the work on tandem cylinders by Khorrami et al. [37]). The benchmark cases allowed the identification of some issues that needed to be fixed. After that, the final version of the model was chosen: S-A DDES.

The quality of the mesh was also found to be important. In general, the aspects that affect the performance of the simulations on a DDES case in OpenFOAM are: quality of cells, type of cells, smallest element in the domain and number of cells. The mesh globally needs to contain a high number of hexahedrons that were found to provide good efficiency in OpenFOAM, but at the same time it has to be suitable for complex geometries with automated mesh generation techniques. Also, in order to properly capture the boundary layer, the dimensionless height of the first cell center (y^+) has to be unity, and the cell size has to progressively grow from that size (typically of the order of microns), to the size of the cells in the proximity of the bodies (typically around 1% of the body reference length). The ratio between the two sizes may be up to three orders of magnitude, for which a semi-structured boundary-layer mesh is generally employed. Unstructured meshes were used (with a high number of hexahedrons) and a semi-structured mesh in the proximity of the bodies. Various software were tested for this purpose with the results described in the specific sections of the thesis.

The combination of the DDES turbulence model and the unstructured hexa-dominant meshes in OpenFOAM gave the expected results on the main simulations on tandem wheels in terms of efficiency, although a few questions remained. The accuracy can be increased from the 30–40% error of a URANS to the 5–10% of the DDES with reasonable computational time. The simulations on tandem wheels, after setting up the computational procedure, could be run with a schedule of one-week to two-week time, including meshing and post-processing. In the simulations, in order to respect the required schedule, the computational time of the simulation needed to be controlled. Thus, the simulations were performed with maximum Courant number higher than 1, since this was not a hard requirement given the implicit method used. This is not expected to affect the results because of previous tests performed, and because the main reason for the high maximum Courant is the smallest element size (order of microns), rather than the high time step (order of microseconds). In fact, the main limitations of the current simulations is the limited control on the smallest element size in the domain, which most of the tested meshing software do not rigorously respect. If solved, this technical problem could remove any doubt on the effect of the Courant number on the accuracy and it could substantially reduce the computational cost by increasing the time step.

Wall functions are a valid alternative to the boundary-layer semi-structured mesh, or they could be used in combination with a boundary-layer mesh that aims at the log layer, which would be coarser. The benefits in terms of performance are clear, but also the possible problems. In fact, the wall functions need to be valid for adverse and favourable pressure gradient. Also, the wall function would need to consider the effect of cross-flow in the boundary layers of the wheel-like geometries. The wall functions are often used by CFD methodologies that must use cartesian grids, and therefore cannot provide a boundary-layer mesh. Typical examples of this kind of technique are Lattice-Boltzmann Methods, which need a large number of voxels in proximity to the bodies in order to correctly model the boundary layer. This is because the voxels cannot be stretched in the wall normal direction to have a unidirectional grid refinement. This problem is not present in traditional CFD solvers. Thus, the best way to implement the wall function would be the proposed coarse semi-structured boundary-layer mesh and the pressure-sensitised wall functions. It is arguably possible to reduce both the cost of the meshing software (giving more options) and the computational time because of larger time-step. The downsides would be the accuracy and the need to check the accuracy of this technique for every new case.

9.2.3 Tandem Wheels as Landing-Gear Components

Various experiments and simulations of turbulent flow past landing gear were present in the literature before the beginning of the PhD project, but there were no examples of flow past two in-line wheels. A full landing gear contains a number of geometric features that can be expected to have an influence on the flow past the wheels. Thus, if considering the wheels as one of the most relevant parts of the landing gear and the aim is to understand how the flow features on the wheels change depending on some geometric parameters, the two wheels alone must be studied. To this purpose the tandem-wheel geometry with varying geometric parameters, such as inter-axis distance and installation angle, has been studied in this PhD project. It was also used as a test case to answer the two previously described questions because it was representative of the landing-gear geometry but, at the same time, simpler.

The main findings on the tandem wheels are described in the two main chapters of results (Chapter 6 and Chapter 7). They can be summarised as follows. The inter-axis distance is not particularly relevant for the mean drag coefficient, but it has effects both on the mean lift coefficients and on the RMS of both the coefficients. The effect of an increase in the installation angle is to increase the total drag, arguably because of the increased frontal projected area. Some flow features were found because of the transitional regime analysed (Reynolds range between 1.2×10^5 and 5.8×10^5): laminar separation bubbles on the wheel side, and the wheel top and bottom. The tripping devices were effective in removing the transitional features, but the repeatability of the results in the tripped configurations was low because of instabilities.

The best results comparison was between the untripped experiments and the simulations with fixed transition, because only in this way the simulations reproduce the transitional features that are so important in this case. The reason for such a high importance of the transitional features is presumably due to the smooth geometry without edges that cannot fix the flow separation, thus small differences in the boundary layer can trigger large differences in the overall force coefficients. The experiments and the simulations also allowed the identification of flow patterns in the wake by means of POD. The surface patterns visualised by the oil-flow technique and the CFD visualisations allowed the identification of the main vortical structures in the wakes of the single and the tandem wheels.

The simplest solution to overcome the Reynolds number dependency would have been to build a larger model (at least twice the size of the current model). This would modify the Reynolds number by a factor of two, with the aim of yielding a fully-turbulent flow (without tripping devices) at the higher wind-tunnel velocities. Another possible way to overcome this problem, without changing the experimental geometry, is to test the same model at higher velocities.

9.2.4 Landing-gear components interactions

The final test on the simplified four-wheel landing gear shows that the flow past the tandem wheels side by side in a configuration of four wheels is similar to the flow past the tandem wheels. The bogie beam and the axles on the wheels in tandem configuration generate a marked difference on the flow between the front and rear wheels with differences in the wake structures, and there is also a strong increase of the drag coefficients. Further adding the main leg has the effect of creating an asymmetric flow, especially on the rear wheel because of the blockage given by the long cylindrical structure of the main leg.

The next experimental tests that could follow up the tandem-wheel experiments are the three in-line wheels (in analogy to the Airbus A350-1000 landing gear), again without struts and link elements, to minimise the interactions with the flow past the wheels. In this case, it is advisable to start with a larger model in order to overcome the problems of Reynolds number dependency that was encountered here.

9.3 Summary

The proposed research questions have been answered throughout the PhD project. Unsteady aerodynamic loads were measured with a strain-gauge balance and the results validated with a vibration test, which is a novelty in aerodynamics. CFD methodologies for unsteady flow prediction were analysed and, even without generating significant improvements in the field, the indications for the future works are clearly stated. The tandem-wheel geometry appeared for the first time in the literature in the present PhD, with both experiments and simulations. Simulations of four-wheel landing gear in different configurations showed the importance of studying the tandem-wheel case and the possibility to extend all of the developed methodologies to more complex geometries.

Appendices

Appendix A

Wind-tunnel Model Drawings

In Figure A.1, a one-quarter scale drawing of the wind-tunnel model assembly is illustrated. The relevant dimensions are given in the thesis where required.

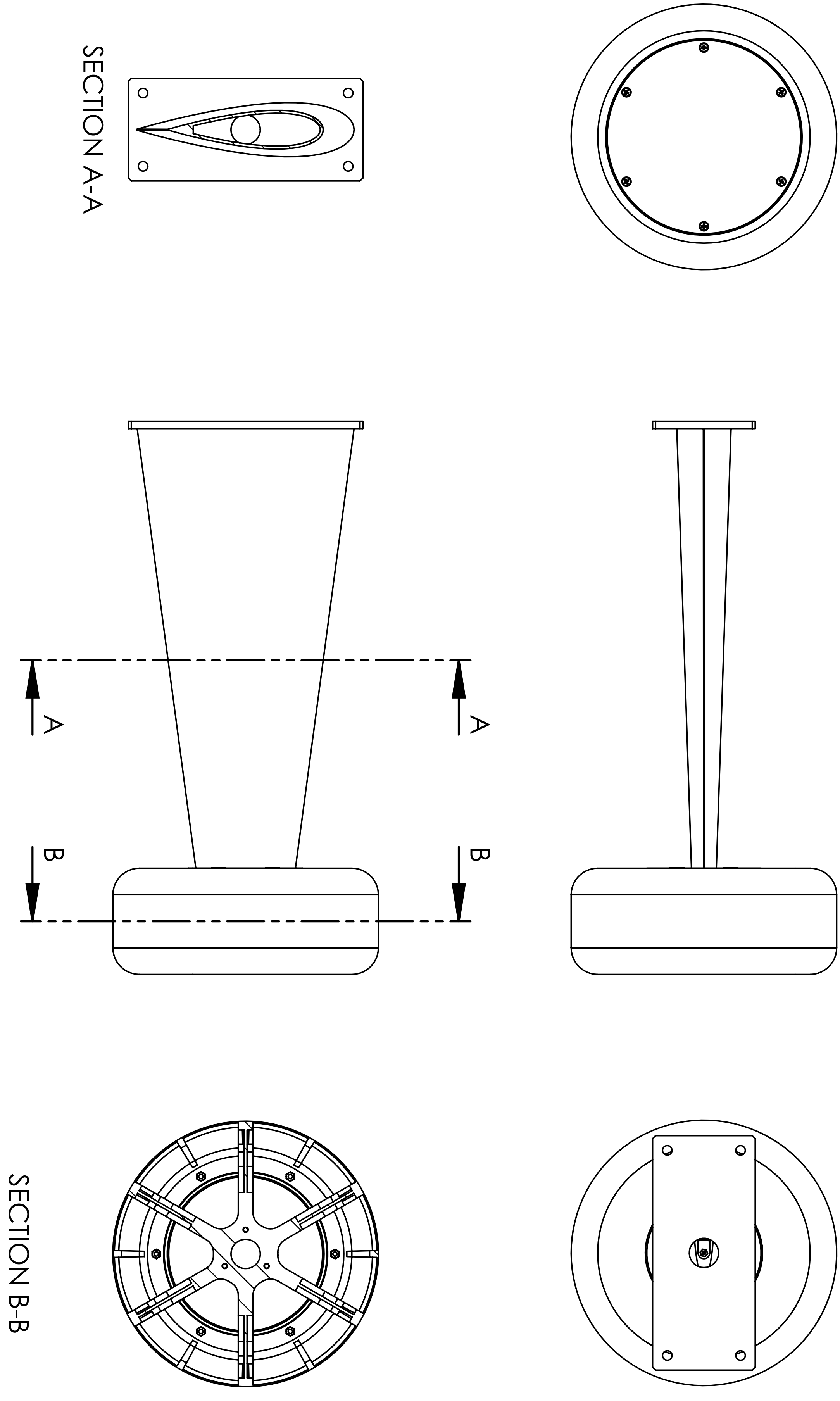

Figure A.1: Model assembly drawings, 1/4 scale.

Appendix B

Basic concepts in structure dynamics

When designing a model for unsteady loads measurement past bluff bodies, the dynamic response of the model and of the balance must be considered; in fact, the vortex shedding and the turbulent flow create pressure and friction fluctuation on the model surface that need to be transmitted as intact as possible through the model components to the balance. Nevertheless all the bodies, no matter how stiff they can appear, are *elastic* and elastic bodies behave in a very peculiar way when forced at high frequency. If their response is not controlled in some way, its effects on the collected data can be very significant if the purpose of the experiment is to get *unsteady* information.

In this chapter the basic concepts related to structure dynamics are presented, starting from the simplest case with only one degree of freedom and concluding the chapter with few notes on how we can approach realistic geometries.

A mass-spring-damper system and the role of the damping are described, then systems with more than one degree of freedom are analysed (an example with three d.o.f. is shown), and the natural frequency of a beam using is found using the beam theory. Finally the finite element method is formally introduced.

B.1 Mass-spring-damper system

In this chapter a simple linear system with only one degree of freedom is illustrated to introduce the dynamic response of a real structure.

B.1.1 Free-response

The mass-spring-damper problem can be approached starting from a case with no forcing applied. Assuming to have a mass m that is free to move along the x axis and linked to a fixed wall by means of a spring of stiffness k and a viscous damper of constant c, the following equation for Newton's second law can be written:

$$m\ddot{x} = -c\dot{x} - kx \tag{B.1}$$

where x represents the position of the mass m as shown in figure B.1.

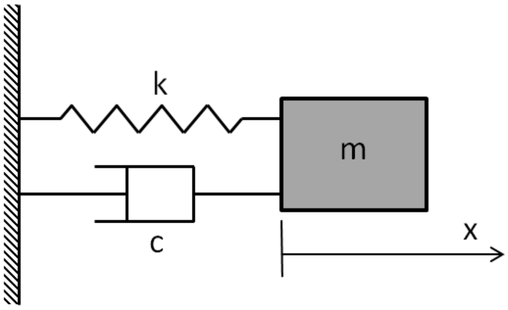

Figure B.1: Sketch of the spring-mass-damper system.

The differential equation (B.1) can be rewritten dividing by the mass m and rearranging the order of the terms:

$$\ddot{x} + 2\zeta\omega_0\dot{x} + \omega_0^2 x = 0 \tag{B.2}$$

where, accordingly to the traditional literature for this problem, $\omega_0 = \sqrt{k/m}$ is the *natural frequency* and $\zeta = c/(2\sqrt{km})$ is the *damping ratio*; ω_n and ζ are properties of the mass-spring-damper system as a whole and its dynamic behaviour is strongly dependent on these two quantities, as it is shown through this chapter. The equation (B.2) can be solved assuming a solution like the following:

$$x = e^{\lambda t}$$

and substituting, to get the characteristic equation of the differential equation:

$$\lambda^2 + 2\zeta\omega_n\lambda + \omega_n^2 = 0.$$

The two roots λ_1 and λ_2 of the equation (B.2) are:

$$\lambda_1 = -\zeta\omega_n + \omega_n\sqrt{\zeta^2 - 1}$$

$$\lambda_2 = -\zeta\omega_n - \omega_n\sqrt{\zeta^2 - 1}$$

that, depending on the value of ζ can lead to three different cases; the three cases are for $\zeta > 1$ (over-damping), $\zeta = 1$ (critical damping) and $\zeta < 1$ (under-damping).

Over-damping ($\zeta > 1$). In this case, the term under the square root in the expression of λ_i is always positive; the solution can be written as linear combination of exponential terms with negative exponent:

$$x = Ae^{\omega_n\left(-\zeta+\sqrt{\zeta^2-1}\right)t} + Be^{\omega_n\left(-\zeta-\sqrt{\zeta^2-1}\right)t} \tag{B.3}$$

with A and B real constant, that can be determined after imposing the initial conditions. Whatever is the initial condition, in this case, the mass returns to the zero position without any oscillation.

Critical damping ($\zeta > 1$). Since the two roots are real and coincident, we get a solution like the following:

$$x = (A + Bt)e^{-\omega_n\zeta t} \tag{B.4}$$

This is the case that minimises the time that the mass takes to get back to zero displacement.

Under-damping ($0 \leq \zeta < 1$). Here we can find two imaginary roots for the characteristic equation, thus we can rewrite the solution to highlight the oscillations:

$$x = e^{-\omega_n\zeta t}\left(A\cos(\omega_n\sqrt{1-\zeta^2}t) + B\sin(\omega_n\sqrt{1-\zeta^2}t)\right) \tag{B.5}$$

The mass now vibrates as consequence of a lower damping, before getting back to the zero position. The quantity $\omega_d = \omega_n\sqrt{1-\zeta^2}$ is usually called *damped natural frequency*: it is the frequency at which the mass vibrates when it start from non-zero initial condition and for small damping values it is very close to the natural frequency ω_n.

In the three cases, the solution has only a transient part, thus this problem without any time-varying force provides only information on the phase that the system take to pass from the initial conditions to the zero value; the phenomenon is always asymptotic: this means that the exact steady state is only for an infinite time. A good estimation of the transient time can be obtained by the characteristic time $\tau = 1/(\omega_n\zeta)$, that comes from the under-damped case.

B.1.2 Forced vibration

If we add an harmonic force $F = F_0\sin(\omega t)$ to the system previously studied, we can analyse the response of the system in dynamic conditions when a it is forced at constant frequency. Newton's second law for the mass becomes:

$$m\ddot{x} = -c\dot{x} - kx + F_0 \sin(\omega t) \tag{B.6}$$

that can be rewritten as follows:

$$\ddot{x} + 2\zeta\omega_n\dot{x} + \omega_n^2 x = \frac{F_0}{m}\sin(\omega t) \tag{B.7}$$

One of the different ways in which one can express the solution is:

$$x = x_0 \sin(\omega t + \phi)$$

and we can get the value of the *amplitude* x_0 after substitution and some simplifications:

$$x_0 = \frac{F_0/k}{\sqrt{(1-\omega^2/\omega_n^2)^2 + (2\zeta\omega/\omega_n)^2}}. \tag{B.8}$$

Similarly, we can get the value of the *phase* ϕ:

$$\phi = \arctan\left(\frac{2\zeta\omega/\omega_n}{1-\omega^2/\omega_n^2}\right) \tag{B.9}$$

The value of both amplitude and phase can be plotted as function of ω at different values of the damping factor ζ, as shown in figure B.2.

The amplitude value is strongly dependent on the forcing frequency ω; at low frequencies the response is flat and very close to the steady response that we can calculate form the steady form of the equation (B.6):

$$F = -kx.$$

At higher frequencies, for sufficiently low ζ ($\zeta < \sqrt{2}/2$), there is a maximum; the position of the maximum can be calculated for differentiation from equation (B.8):

$$\omega_r = \omega_n\sqrt{1-2\zeta^2} \tag{B.10}$$

that is very close to the natural frequency ω_n for low values of the damping ratio ζ; the frequency ω_r is the *displacement resonance frequency* of the system, which must not be confused neither with the natural frequency ω_n nor with the damped natural frequency ω_d, even it is generally close to both. Substituting ω_r in the equation (B.8), we get the maximum amplitude:

$$x_{0\,\max} = \frac{F_0/k}{2\zeta\sqrt{1-\zeta^2}}. \tag{B.11}$$

The maximum value depends on the damping factor, in such a way that the higher is the damping the smallest is the maximum value.

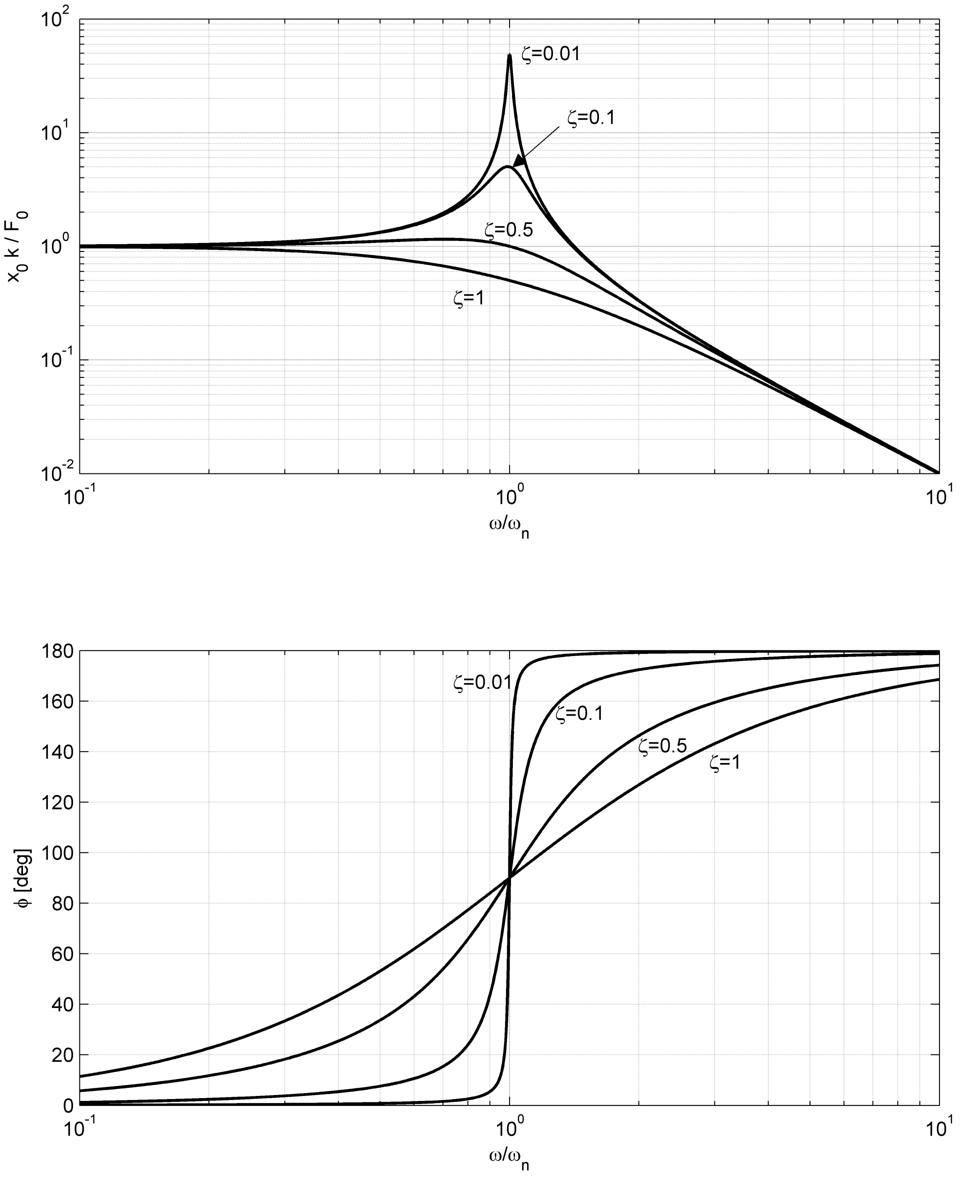

Figure B.2: Plots of amplitude and phase response for under-damped system.

For forcing frequencies much higher than the natural frequency, the amplitude decays with $1/\omega^2$.

The dynamic behaviour is consequently totally different from the static behaviour of the spring and it is dependent on a number of factors, for instance damping and vibration frequency. If we suppose to use as a balance an elastic body that behaves similarly to a spring, the output is dependent on the system dynamics.

B.2 Undamped multiple-degree-of-freedom systems

Sometimes we can find useful to approximate a structure with something that is more complex than a single mass-spring-damper system. In this case the approach is similar to the procedure reported in section B.1, but we need to remark some difference. In order to describe the procedure, the free response of a case with three degrees of freedom and no damping is taken as sample problem. The example, which is constituted by a series of three masses linked by means of three springs, is illustrated in figure B.3.

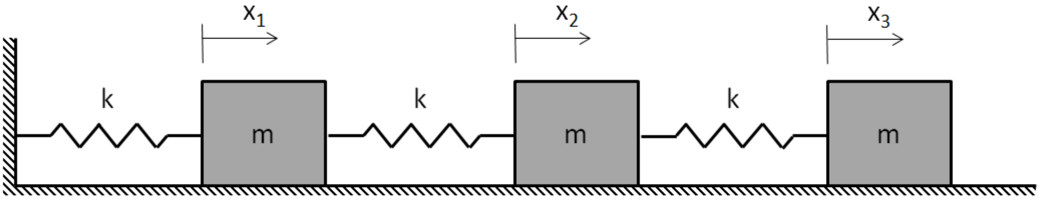

Figure B.3: Sketch of a system with 3 degrees of freedom.

The number of degrees of freedom is only three because the masses are free to move only along the x axis.

For each mass, we can write a momentum equation along the x axis:

$$m_i \ddot{x}_i = F_{xi} \tag{B.12}$$

where F_{xi} must be replaced, mass by mass, with all the forces acting on the mass. In the most general case, we can write:

$$F_{xi} = F_{\text{ext},i} - \sum_j k_{ij} x_j$$

where $F_{\text{ext},i}$ is the external force and $-\sum_j k_{ij} x_j$ is the effect of all the springs linked to the mass. In case of zero external force, we get the free-response equations:

$$m_i \ddot{x}_i + \sum_j k_{ij} x_j = 0 \tag{B.13}$$

If we assume a solution in the form:

$$x = x_{0i}\sin(\omega t)$$

as we did for the single-degree-of-freedom case, we generally get the following:

$$m_i\omega^2 D_i - \sum_j k_{ij} D_j = 0 \tag{B.14}$$

To have non-trivial solution, the determinant must be imposed equal to zero.

For this example, with $m_i = m$ and $k_i = k$, the resulting system is:

$$\begin{bmatrix} (m\omega^2 - 2k) & k & 0 \\ k & (m\omega^2 - 2k) & k \\ 0 & k & (m\omega^2 - k) \end{bmatrix} \begin{pmatrix} D_1 \\ D_2 \\ D_3 \end{pmatrix} = 0 \tag{B.15}$$

And imposing the determinant equal to zero, the resulting natural frquencies of the system are:

$$\omega_1 = 0.445\sqrt{\frac{k}{m}}, \qquad \omega_2 = 1.25\sqrt{\frac{k}{m}}, \qquad \omega_3 = 1.80\sqrt{\frac{k}{m}}.$$

After getting the natural frequencies, it is possible to have the normal modes, that are a set of values for the vector D_i that are solution of the equation (B.14).

B.3 Dynamic beam equation

The vibration problem on a real structure has an infinite number of degrees of freedom if we model it as a solid body. For instance we can start to approach a more complex situation considering a *beam*, that is a structural element with one size much longer than the other two and that is mainly designed to support transverse load without interactions between shear and twist.

If we suppose that the beam is perfectly straight before any deformation and we can get the displacement in the y direction $v(z)$ of the points along the z axis of the beam, by the Euler-Bernoulli differential equation:

$$\frac{d^2}{dz^2}\left(EI(z)\frac{d^2v}{dz^2}\right) = q(z) \tag{B.16}$$

where E is the elastic modulus of the material, $I(z)$ is the second moment of area of the beam cross-section and $q(x)$ is the distributed load applied in y direction; in detail the second moment of inertia can be calculated as follows:

$$I(z) = \iint y^2 \, dx \, dy$$

if the centroid of the section is at $x = y = 0$. To get the displacement of the bending beam, we need to know the beam geometry, the distributed load and the boundary conditions in order to find the displacement. As boundary conditions, we can usually assume $v = dv/dz = 0$ for a fixed end, $dv/dz = d^2v/dz^2 = 0$ for a hinged end and $d^2v/dz^2 = d^3v/dz^3 = 0$ for a free end.

To skip from the static equation to the dynamic equation for the beam, it is sufficient to add the inertial term on the right-hand side of the equation:

$$\frac{\partial^2}{\partial z^2}\left(EI(z)\frac{\partial^2 v}{\partial z^2}\right) = -\mu\frac{\partial^2 v}{\partial t^2} + q(z) \tag{B.17}$$

where μ is the linear density of the beam (mass per unit length). The term $\partial^2 v/\partial t^2$ represents the acceleration of the beam segment dz.

Without transverse load q and with constant $I(z) = I$, we get the following:

$$EI\frac{\partial^4 v}{\partial z^4} = -\mu\frac{\partial^2 v}{\partial t^2} \tag{B.18}$$

and we assume a solution of the form:

$$v(x,t) = \hat{v}(z)\sin(\omega t)$$

where ω is the vibration frequency. If we substitute the solution in the former equation (B.18), considering valid the equation for each frequency, we get:

$$\frac{d^4\hat{v}}{dz^4} = \frac{\mu\omega^2}{EI}\hat{v}$$

which has the following general solution:

$$\hat{v}(z) = A_1\cosh(\alpha z) + A_2\sinh(\alpha z) + A_3\cos(\alpha z) + A_4\sin(\alpha z) \tag{B.19}$$

with

$$\alpha = \left(\frac{\mu\omega^2}{EI}\right)^{1/4}. \tag{B.20}$$

Applying the boundary conditions, it is possible to determine what are the proper conditions to get the beam vibrating. For example, we can use the boundary conditions for a cantilevered beam of length L. Considering that the fixed end is at $z = 0$ and the free end is at $z = L$, the boundary conditions are:

$$\begin{aligned} \hat{v}(0) &= 0 \quad & \frac{d^2\hat{v}}{dz^2}(L) &= 0 \\ \frac{d\hat{v}}{dz}(0) &= 0 \quad & \frac{d^3\hat{v}}{dz^3}(L) &= 0 \end{aligned}$$

If we impose the boundary conditions in the general solution (B.19) and its derivatives, we get an homogeneous system of four equations in the four variables A_i:

$$\mathbb{M}\,\mathbf{a} = 0 \tag{B.21}$$

where $\mathbf{a}$ is the vector of unknowns A_i and $\mathbb{M}$ is the matrix of the coefficients of A_i. Since the system is homogeneous, the only way to get a non-trivial solution is to find when the determinant of the system is zero: $\det(\mathbb{M}) = 0$; thus we get the following non-linear equation:

$$(\alpha L)\cos(\alpha L) + 1 = 0 \tag{B.22}$$

that can be solved numerically to get the natural frequencies ω_n.

Since we found non-trivial solution only when the determinant is zero, one of the four variables A_i must remain undetermined: we can find the displacements $\hat{v}(z)$, but still with one multiplying coefficient. In fact, after substitution of A_2, A_3 and A_4 from the system (B.21) in the equation (B.19), we get the displacement for all the possible roots:

$$\hat{v} = A_1\left[\cosh(\alpha x) - \cos(\alpha x) + \frac{\cosh(\alpha L) + \cos(\alpha L)}{\sinh(\alpha L) + \sin(\alpha L)}\left(\sin(\alpha x) - \sinh(\alpha x)\right)\right] \tag{B.23}$$

The first four modes and their respective root values are shown in figure B.4.

For the *natural* frequency, every displacement is theoretically possible, but we must remark that this theory is linear and there is no damping included in the model. The real behaviour is different, but with this basic theory it is still possible to predict with reasonable accuracy what is the resonance frequency. In fact we can remind from the mass-spring-damper at one degree of freedom (see section B.1) that the position of the displacement resonance is generally close to the position of the natural frequency of the system without damping, provided that the damping is sufficiently low.

With similar analysis it is possible to define the natural frequencies of torsional beams or other simple continuous bodies, such as bending plates.

B.4 FEM modal analysis

After reviewing the most interesting cases concerning the dynamic response of simple structures, from one to infinite degrees of freedom, we can introduce now a way to

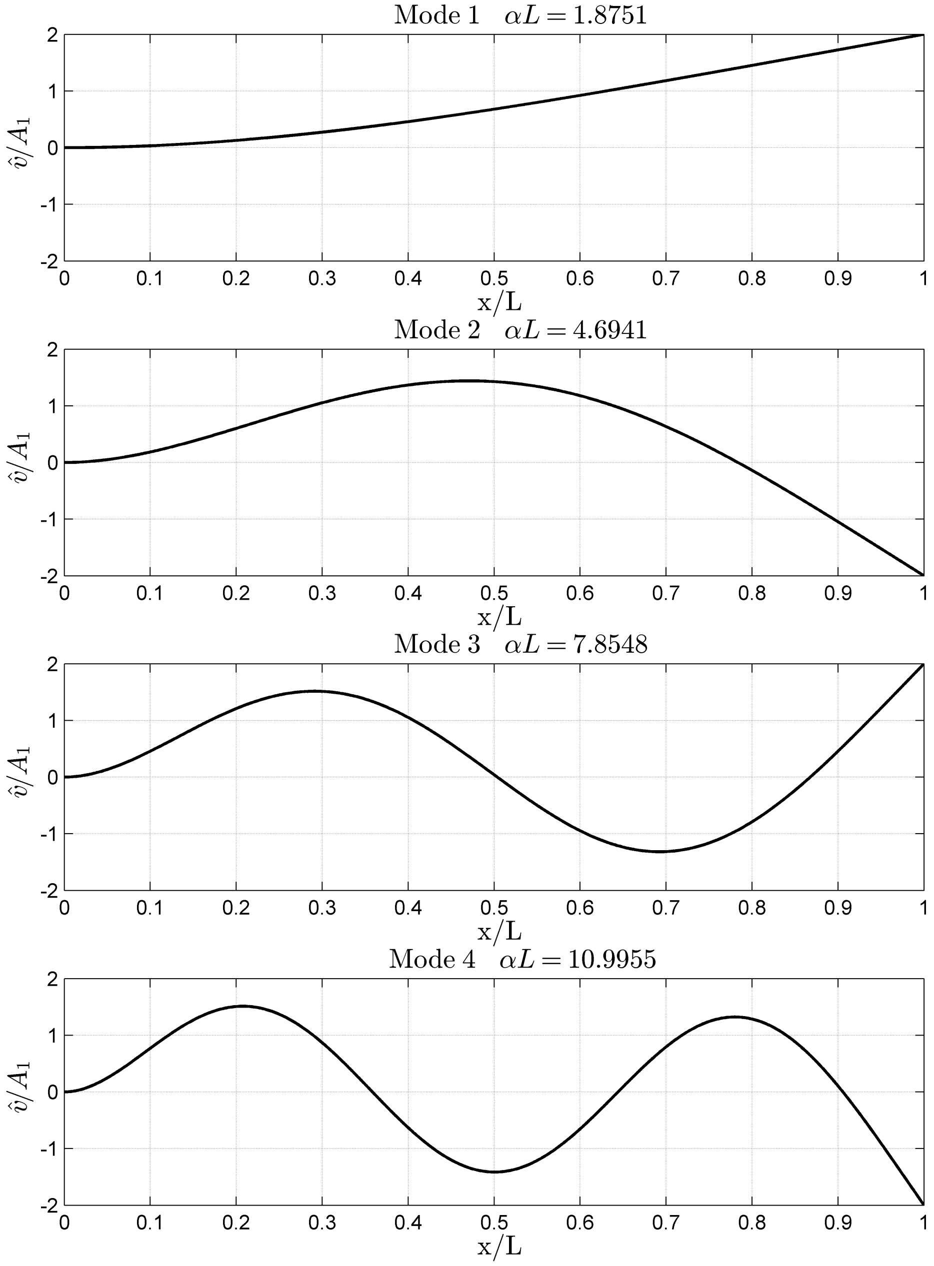

Mode 1 $\alpha L = 1.8751$

Mode 2 $\alpha L = 4.6941$

Mode 3 $\alpha L = 7.8548$

Mode 4 $\alpha L = 10.9955$

Figure B.4: First four modes of a cantilevered beam.

estimate the natural frequencies of more complex bodies. In fact, most of the bodies that we need to *dynamically* evaluate have geometries with an higher level of complexity that what we analysed in this document up to this point.

Thus, still bearing in mind the possibility to model a part of our structures in one of the ways already proposed, we feel the need to have also a more powerful tool that can deal not only with simple or simplified geometries, but also with more complex structures. The *finite element method* (FEM), that is a widely used method in many engineering fields, is helpful also for this engineering branch.

In this section there is a brief theoretical introduction to FEM modal analysis, while the followings are dedicated to the practical application of this method using the commercial software package ANSYS.

The finite element method is based on the application of minimum principles, for instance *Hamilton's principle* that is:

$$\int_{t_0}^{t_1} (\delta T - \delta U + \delta W_D + \delta W_E)\, dt = 0 \tag{B.24}$$

where T is the kinetic energy, U is the potential energy of the conservative forces, W_D is the work of the internal dissipative forces, W_E is the work of the external forces and δ represents the variational operator. The strain field ϵ is function of the displacements u as follows:

$$\epsilon = [N_{\epsilon u}]\mathbf{u}$$

and in the same way the stress σ field can be expressed as function of the displacements:

$$\sigma = [D][N_{\epsilon u}]\mathbf{u}$$

with $[D]$ that is the material elastic matrix. Using the displacements, the strains and the stresses, we can calculate the terms in the equation :

$$T = \frac{1}{2}\dot{\mathbf{u}}^T[N_u]^T[\rho][N_u]\dot{\mathbf{u}} = \dot{\mathbf{u}}^T[M]\dot{\mathbf{u}}$$

$$U = \frac{1}{2}\mathbf{u}^T[N_{\epsilon u}]^T[\rho][N_{\epsilon u}]\mathbf{u} = \mathbf{u}^T[K]\mathbf{u}$$

$$\delta W_D = \delta\mathbf{u}^T[B_D]\dot{\mathbf{u}}$$

$$\delta W_E = \delta\mathbf{u}^T[\Gamma_E]\mathbf{F_e}$$

where $[\rho]$ is the material density matrix, $[M]$ is the mass matrix, $[K]$ is the stiffness matrix. After adding the boundary conditions to the matrices, the model is complete and, after substitution we need to solve numerically an algebraic system like the following:

$$[M_{ff}]\ddot{\mathbf{u}} + [B_{ff}]\dot{\mathbf{u}} + [K_{ff}]\mathbf{u} = [\Gamma_{fe}]\mathbf{F_e} \tag{B.25}$$

The finite element theory now is mainly split in two different philosophies: the first is based on technical theories and the second relies on three-dimensional continuum theories. If we use the first approach we can simulate any combination of basic structural elements, like for example a truss can be built from boom elements or a stiffened panel can be made by shell elements. On the contrary, the second approach is more suitable to complex geometries with structures that cannot be modelled as combination of simple structures.

To perform a modal analysis, ignoring the damping, we can suppose a solution of the form:

$$\mathbf{u} = \mathbf{\Phi} \sin(\omega_n t)$$

and then substitute in the system (B.25), to get an eigenvalue problem, similarly to what we found in the other simpler cases:

$$[K]\mathbf{\Phi} - [M]\mathbf{\Phi}\omega^2 = 0.$$

From the solution of this algebraic system we can get the resonance frequencies and the natural modes of the system.

B.5 A benchmark case: FEM modal analysis of a cantilevered beam

To better understand the procedure it is worth to apply this modal analysis to a test case for which we have also analytical results. For example, we can select a beam of length L, with rectangular cross section with size $b \times t$. The beam geometry is illustrated in Figure B.5, with the sizes used in the example. The material selected for this example is the structural steel that has density $\rho = 7850\,\text{kg/m}^3$ and elastic modulus $E = 200\,000\,\text{MPa}$.

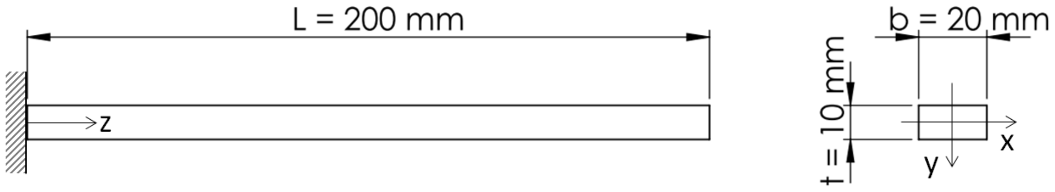

Figure B.5: Cantilevered beam geometry.

If we suppose that the first natural frequency of the beam is a flexural mode, we can estimate it with the theoretical formula from handbooks like, for example, the Harris' Shock and Vibration Handbook [58]. The second moment of area of the beam cross section with respect to the x axis is (from the formula for a rectangular cross section):

$$I_x = \frac{bt^3}{12} \approx 1.667 \times 10^{-9}\,\mathrm{m}^4 \tag{B.26}$$

and with respect to the y axis:

$$I_y = \frac{b^3 t}{12} \approx 6.667 \times 10^{-9}\,\mathrm{m}^4; \tag{B.27}$$

and the area of the cross section is:

$$A = bt = 2 \times 10^{-4}\,\mathrm{m}^2. \tag{B.28}$$

Since the second moment of area is smallest around the x axis, we expect to have the lowest natural frequency around this axis; we can estimate the frequency $\nu = \omega/(2\pi)$ from formula (7.37) in book mentioned above [58] and from the first root of the frequency equation for the cantilevered beam reported in the table of Figure 7.5 from the same book. In this document, the root of the frequency equation is αL (with L length of the beam, as usual) and the material density is μ.

$$\alpha L = \left(\frac{\mu\omega^2}{EI_x}\right)^{\frac{1}{4}} L \ \approx 1.8751 \tag{B.29}$$

where we can substitute μ with the linear density of the beam:

$$\mu = \frac{\rho A\, dz}{dz} = \rho A = 1.57\,\mathrm{kg/m}. \tag{B.30}$$

Finally we get the first natural frequency for the bending mode around x axis at the frequency:

$$\nu = \frac{\omega}{2\pi} = \frac{1.8751^2}{2\pi L^2}\sqrt{\frac{EI_x}{\mu}} \approx 204\,\mathrm{Hz}. \tag{B.31}$$

At this point, we use ANSYS to get the resonance frequencies of this beam. Our approximation would be the kind of constraint on the fixed end of the beam, for example we can choose the *fixed support* constraint.

The result of a convergence analysis test carried out on the cantilevered beam geometry is reported in Figure B.6; a visualization of the deformation for the first mode is shown in Figure B.7.

For this simple geometry there is an excellent agreement with the theoretical result, also because the beam cross-section was designed ad-hoc to get the first natural frequency for bending and not for twisting or elongation. The mesh used for this example was mapped since this geometry perfectly fits the mapped-mesh technique.

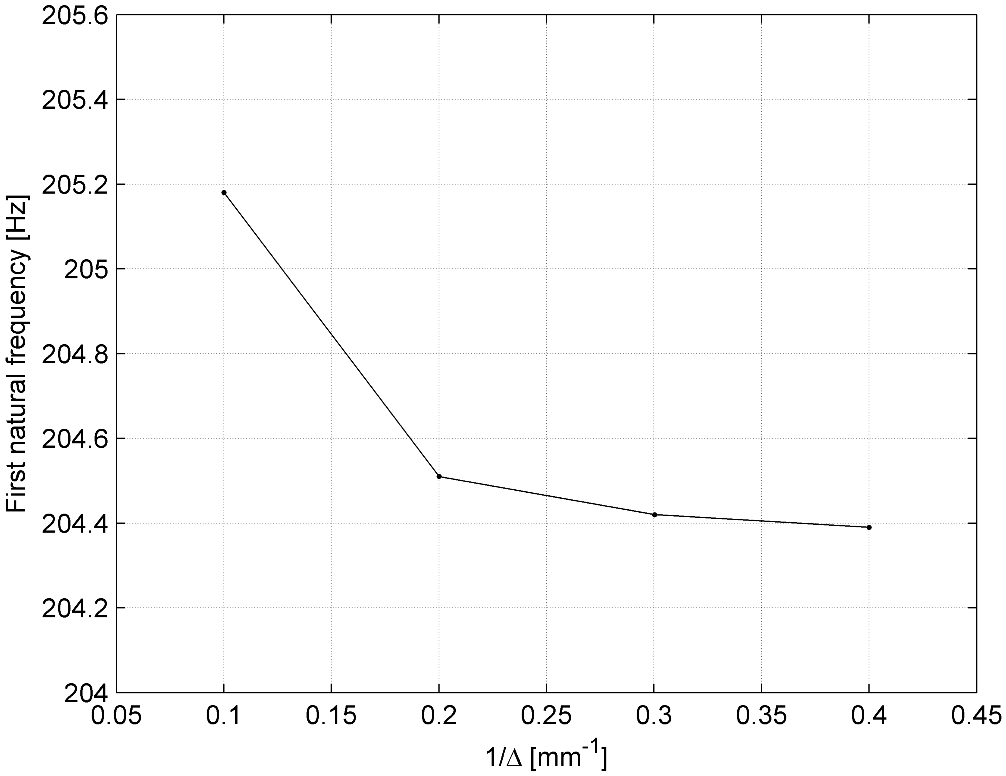

Figure B.6: Convergence plot of the natural frequency with the inverse of the element size Δ.

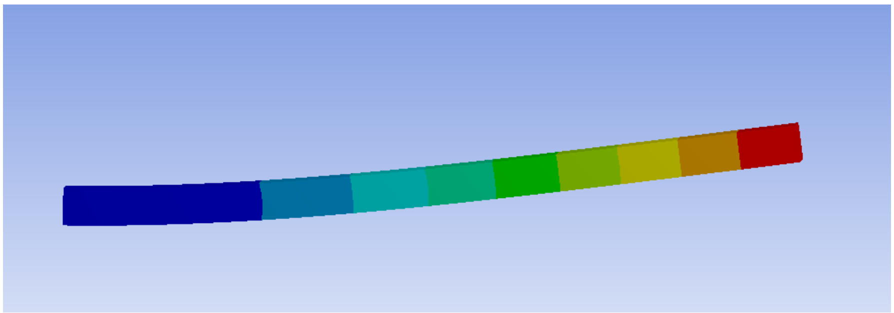

Figure B.7: Deformation of the beam for the first natural mode.

Appendix C

Experimental database

C.1 Configurations

Table C.1: List of the wind-tunnel measurements for each configuration.

Configuration			
Geometry	**Setup**	**Tripping**	**Measurements**
One Wheel	#0A (flat cover)	UT	Loads, Pressure, PIV, Oil-flow
		T zigzag	Loads, Pressure, PIV, Oil-flow
		T Grit60	Loads
	#0B (cavity only)	UT	Loads
	#0C (cavity+hub)	UT	Loads
		T zigzag	Loads
		T Grit60	Loads
Tandem Wheels	#1 ($L_w = 1.1D_w$, $\alpha = 0\,\text{deg}$)	UT	Loads, PIV
		T zigzag	PIV
	#2 ($L_w = 1.3D$, $\alpha = 0\,\text{deg}$)	UT	Loads, Pressure, PIV
		T zigzag	Loads, Pressure, PIV
	#3 ($L_w = 1.5D$, $\alpha = 0\,\text{deg}$)	UT	Loads, Pressure, PIV, Oil-flow
		T zigzag	Loads, Pressure, PIV, Oil-flow
	#18 ($L_w = 1.3D_w$, $\alpha = 20\,\text{deg}$)	UT	Loads, Pressure, PIV
		T zigzag	Loads, Pressure, PIV
	#11 ($L_w = 1.5D_w$, $\alpha = 10\,\text{deg}$)	UT	Loads, Pressure
		T zigzag	Loads, Pressure, PIV
	#19 ($L_w = 1.5D_w$, $\alpha = 20\,\text{deg}$)	UT	Loads, Pressure, Oil-flow
		T zigzag	Loads, Pressure

C.2 Forces

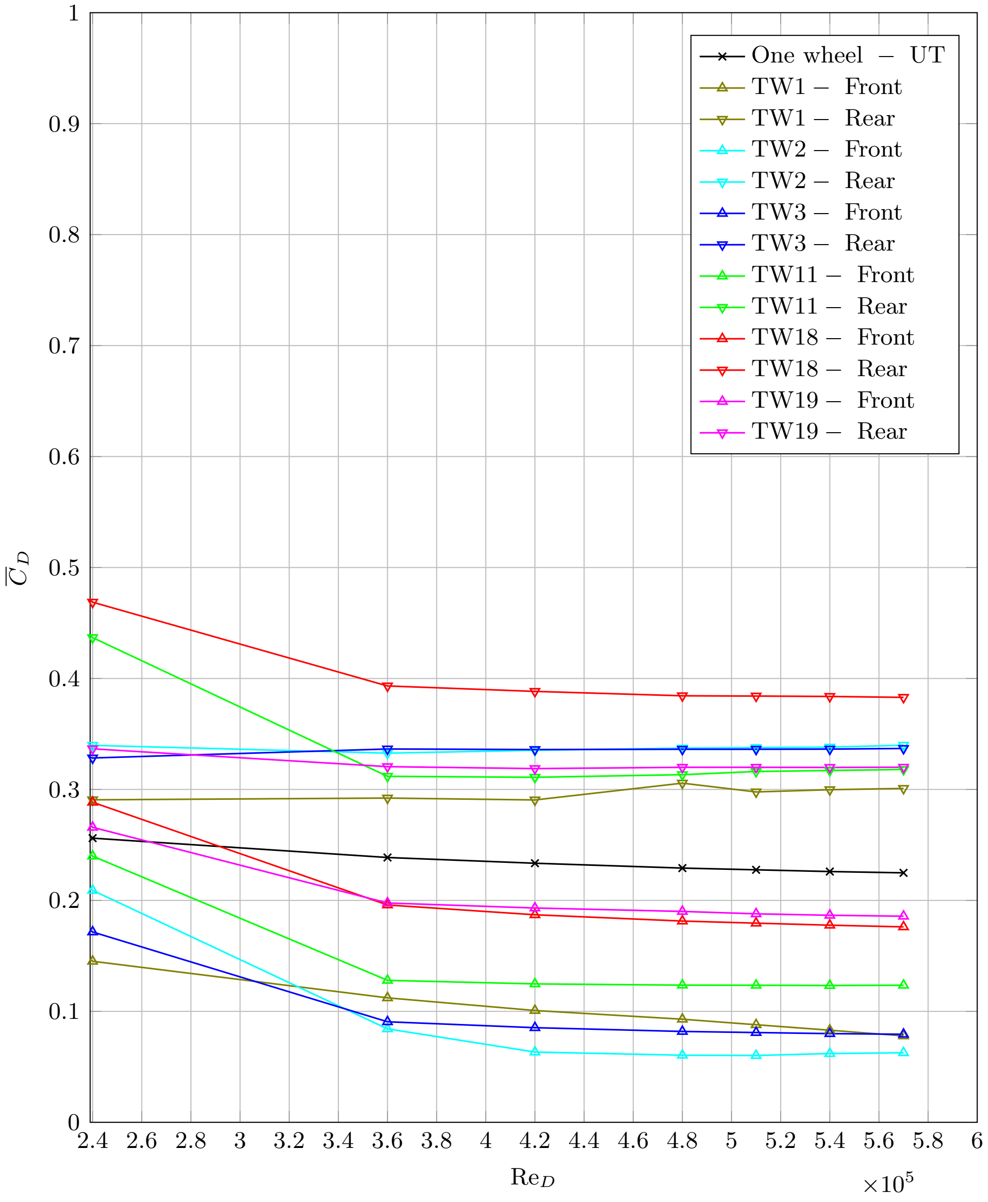

Figure C.1: Mean drag coefficient

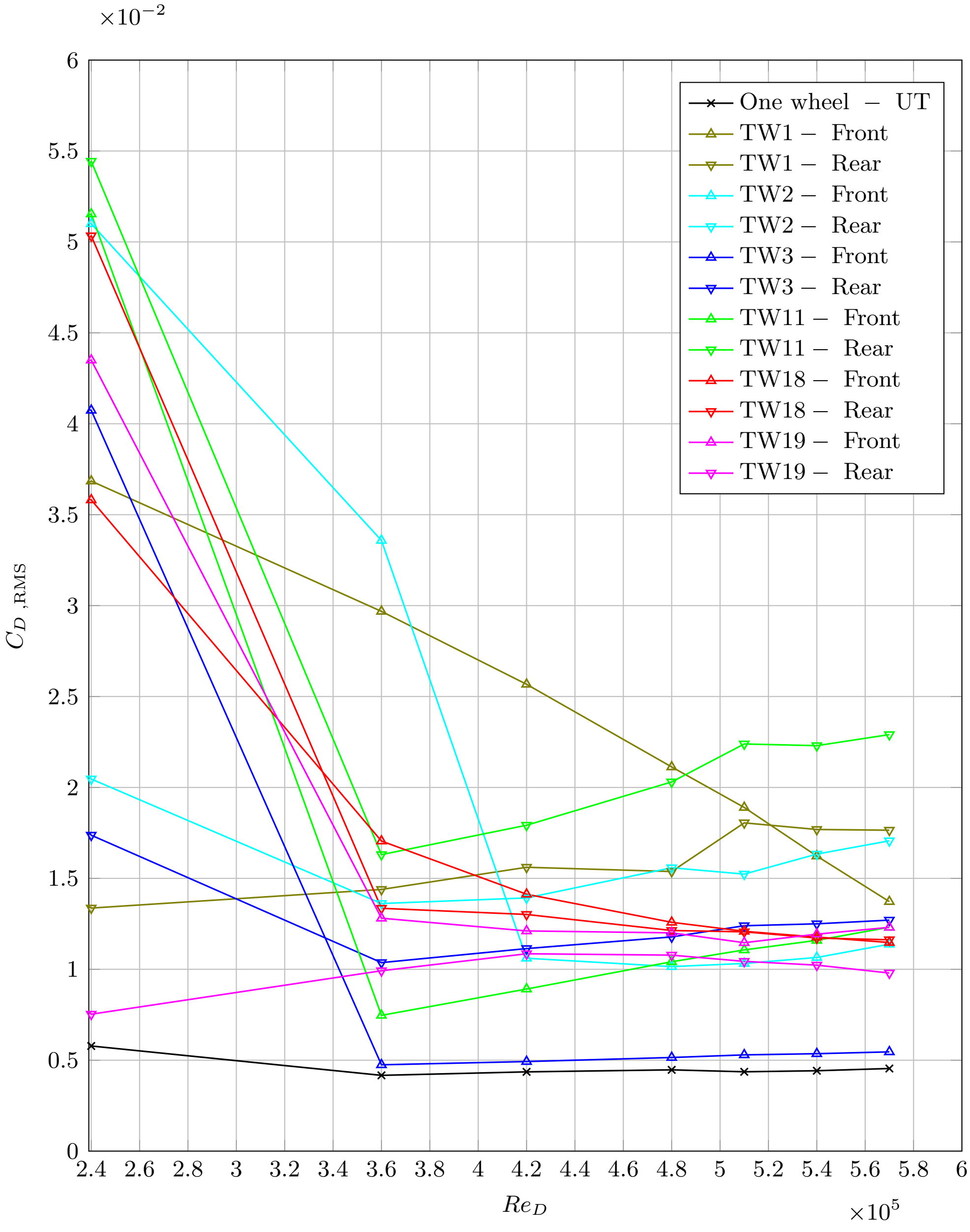

Figure C.2: Drag coefficient RMS

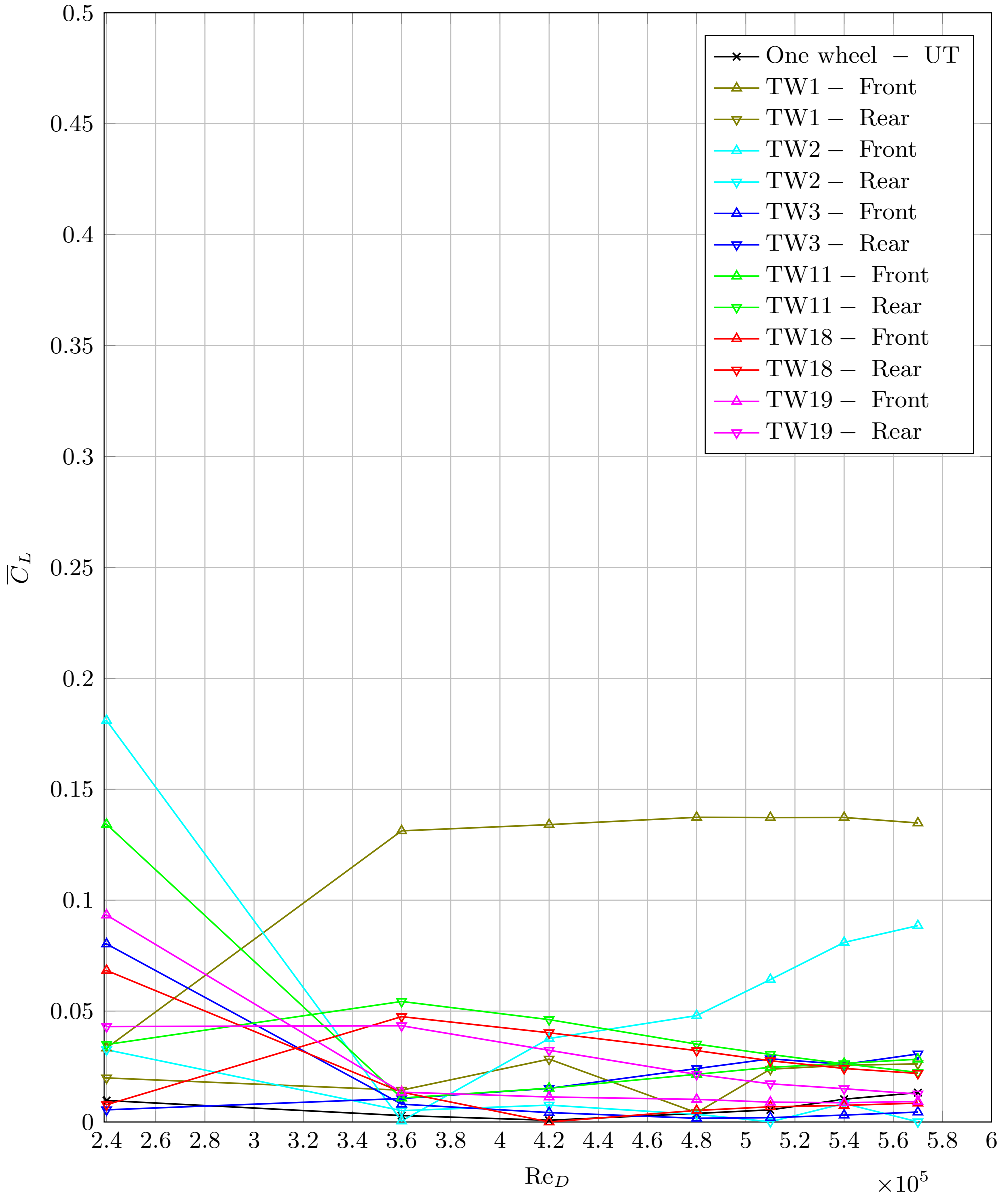

Figure C.3: Mean lift coefficient

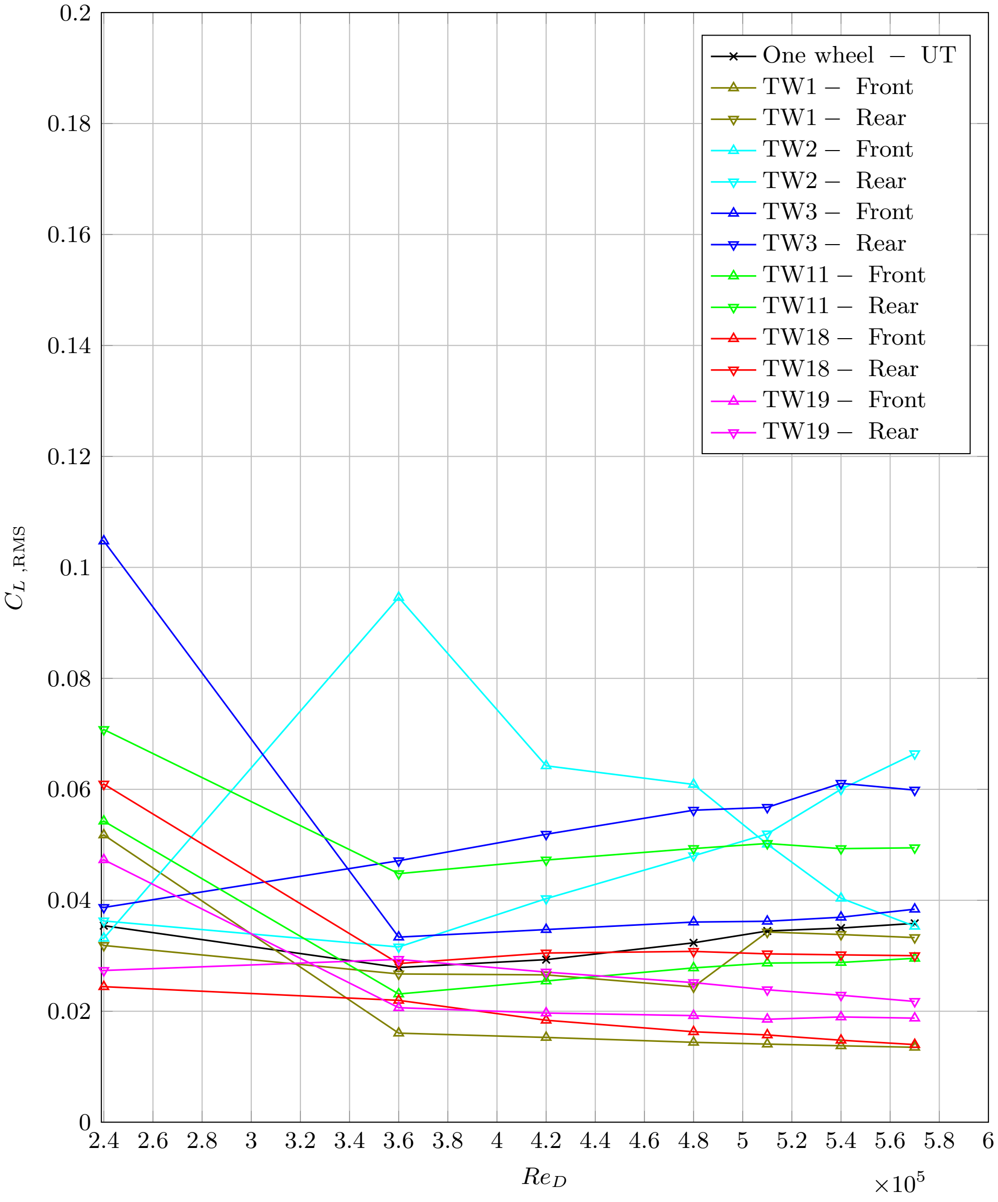

Figure C.4: Lift coefficient RMS

C.3 Pressure

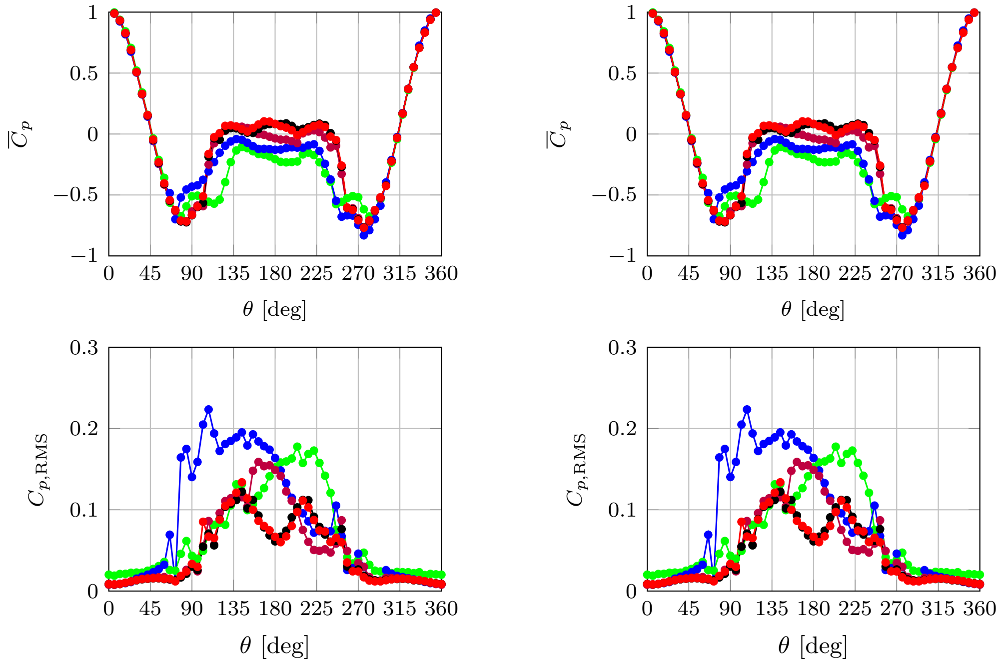

(a) Front wheel

(b) Rear wheel

Figure C.5: Configuration #2 ($L_w = 1.3D$, $\alpha = 0\,\mathrm{deg}$), mean and RMS values of the pressure coefficients C_p along the wheel centreline at various velocities: 10 m/s —●—, 20 m/s —●—, 30 m/s —●—, 40 m/s —●— and 47.5 m/s —●—.

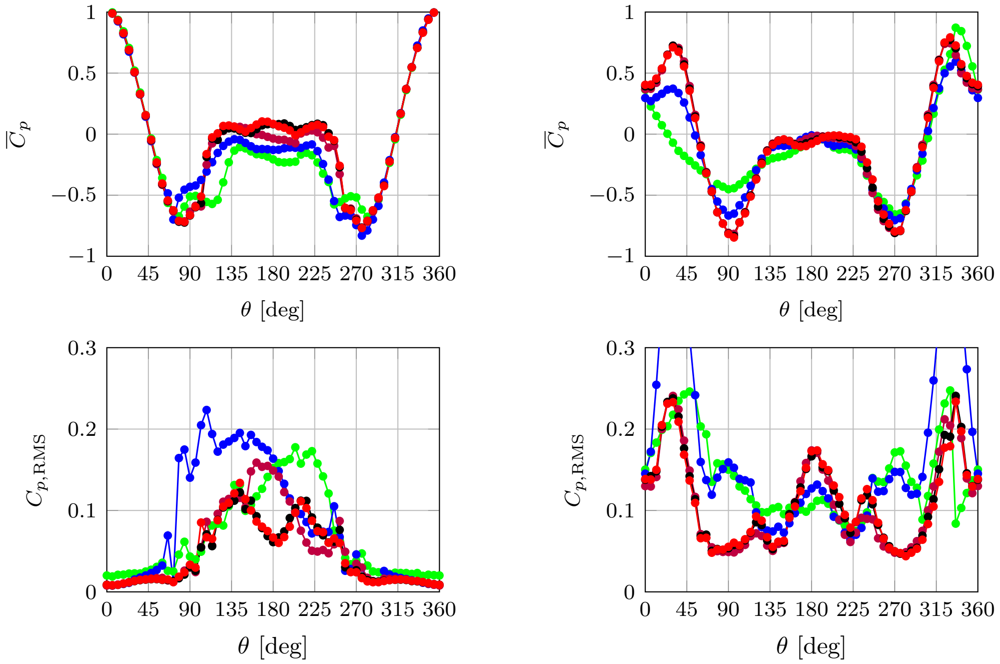

(a) Front wheel

(b) Rear wheel

Figure C.6: Configuration #3 ($L_w = 1.5D$, $\alpha = 0\,\mathrm{deg}$), mean and RMS values of the pressure coefficients C_p along the wheel centreline at various velocities: 10 m/s —●—, 20 m/s —●—, 30 m/s —●—, 40 m/s —●— and 47.5 m/s —●—.

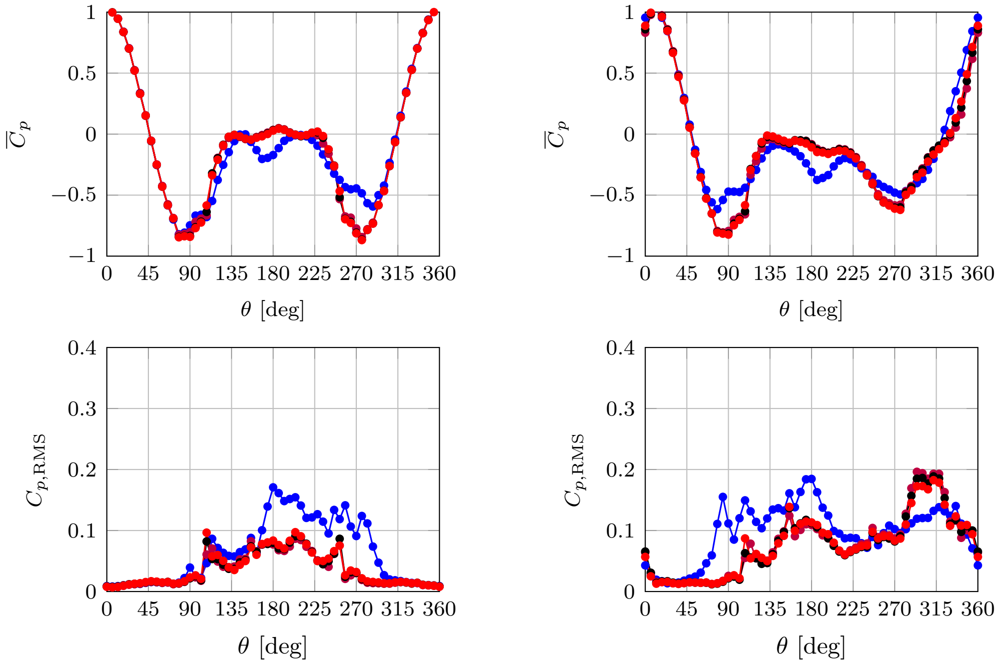

(a) Front wheel

(b) Rear wheel

Figure C.7: Configuration #11 ($L_w = 1.5D_w$, $\alpha = 10\,\mathrm{deg}$), mean and RMS values of the pressure coefficients C_p along the wheel centreline at various velocities: 10 m/s —●—, 20 m/s —●—, 30 m/s —●—, 40 m/s —●— and 47.5 m/s —●—.

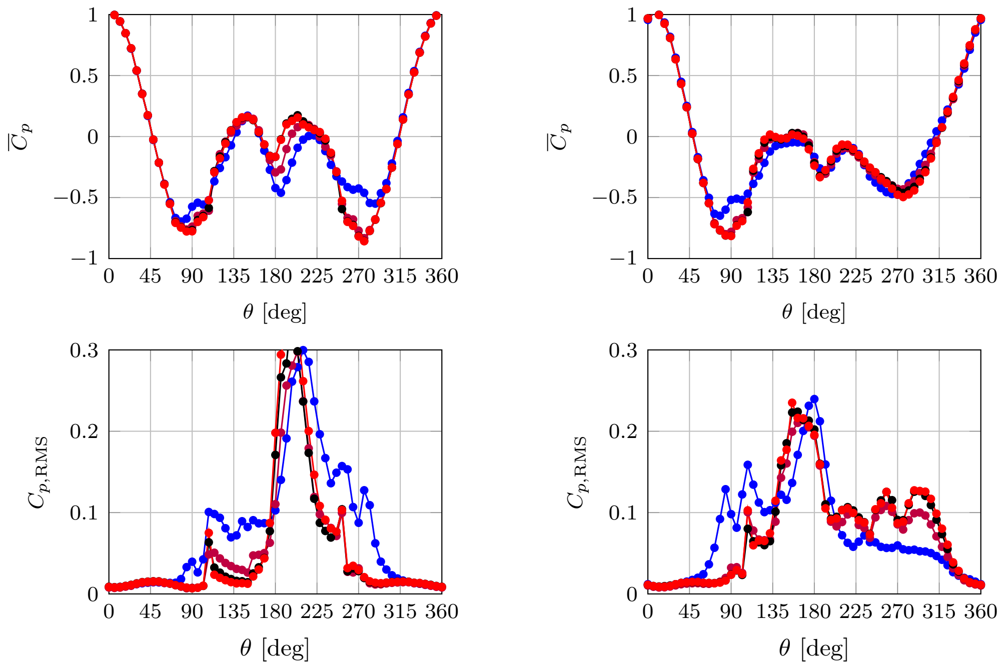

(a) Front wheel (b) Rear wheel

Figure C.8: Configuration #18 ($L_w = 1.3D_w$, $\alpha = 20\,\mathrm{deg}$), mean and RMS values of the pressure coefficients C_p along the wheel centreline at various velocities: 20 m/s —●—, 30 m/s —●—, 40 m/s —●— and 47.5 m/s —●—.

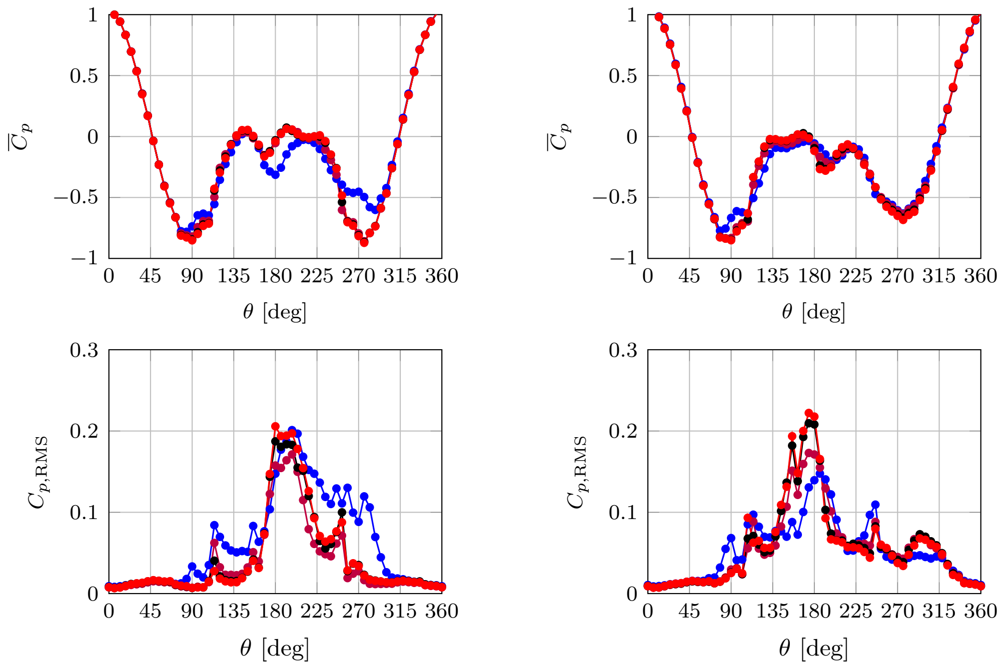

(a) Front wheel (b) Rear wheel

Figure C.9: Configuration #19 ($L_w = 1.5D_w$, $\alpha = 20\,\mathrm{deg}$), mean and RMS values of the pressure coefficients C_p along the wheel centreline at various velocities: 20 m/s —●—, 30 m/s —●—, 40 m/s —●— and 47.5 m/s —●—.

References

[1] ANSYS FLUENT theory guide. Technical report, ANSYS, 2011.

[2] Abedi, H. A simpleFoam tutorial. Technical report, Chalmers University of Technology, 2011.

[3] Ahmed, S. and Ramm, G. Some salient features of the time-averaged ground vehicle wake. *SAE-Paper*, 1984.

[4] *A340-500/-600 Aircraft characteristic airport and maintenance planning.* AIRBUS S.A.S. Customer Services, 2005.

[5] Baban, F., So, R., and Ötügen, M. Unsteady forces on circular cylinders in a cross-flow. *Experiments in Fluids*, 7:293–302, 1989.

[6] Baldwin, B. and Barth, T. *A One-Equation Turbulence Transport Model for High Reynolds Number Wall-Bounded Flows.* NASA, 1990.

[7] Berkooz, G., Holmes, P., and Lumley, J. L. The proper orthogonal decomposition in the analysis of turbulent flows. *Ann. Rev. Fluid Mech.*, 25:539–575, 1993.

[8] Bernero, S. and Fiedler, H. E. Application of particle image velocimetry and proper orthogonal decomposition to the study of a jet in a counterflow. *Experiments in Fluids*, pages S274–S281, 2000.

[9] Bohn, A. Edge noise attenuation by porous-edge extensions. *AIAA Paper*, 80, January 1976.

[10] Breuer, M., Jovičić, N., and Mazaev, K. Comparison of DES, RANS, and LES for the separated flow around a flat plate at high incidence. *International Journal for Numerical Methods in Fluids*, 41:357–388, 2003.

[11] Capece, V. and Fleeter, S. The unsteady aerodynamics of a first stage stator vane row. *Experiments in Fluids*, 4:72–78, 1986.

[12] Cebon, D. *Handbook of vehicle-road ineraction.* Taylor and Francis, 2000.

[13] Conan, B., Anthoine, J., and Planquart, P. Experimental aerodynamic study of a car-type bluff body. *Experiments in Fluids*, 50:1273–1284, 2011.

[14] Crivellini, A. and D'Alessandro, V. Spalart-allmaras model apparent transition and rans simulations of laminar separation bubbles on airfoils. *International Journal of Heat and Fluid Flow*, 47:70–83, 2014.

[15] Dahan, J. A., O'Reilly, C., and Efraimsson, G. Numerical investigation of realistic nose landing gear. AIAA Paper 2014-2077, 2014.

[16] de la Puente, F., Sanders, L., and Vuillot, F. On LAGOON nose landing gear CFD/CAA computation over unstructured mesh using a ZDES approach. AIAA Paper 2014-2763, 2014.

[17] De Lucca, N., Gordeyev, S., Jumper, E., Thordahl, J., and Wittich, D. J. The estimation of the unsteady aerodynamic force applied to a turret in flight. AIAA Paper 2013-3136, 2013.

[18] Deck, S. Zonal detached-eddy simulation of the flow around a high-lift configuration with deployed slat and flap. *AIAA J.*, 43:2372–84, 2005.

[19] Dobrzynski, W. Almost 40 years of airframe noise research: what did we achieve? *Journal of Aircraft*, 47(2):353–367, March-April 2010.

[20] EASA. *CS-36, Amendment 3*, 2013.

[21] Exa. PowerFLOW®. URL `http://www.exa.com/powerflow.html`. Visited: 24/07/2015.

[22] Ferziger, J. H. and Peric, M. *Computational Methods for Fluid Dynamics*. Springer, 3rd edition, 2001.

[23] Fink, M. R. Approximate prediction of airframe noise. *Journal of Aircraft*, 13(11), November 1976.

[24] Girimaji, S. and Abdol-Hamid, K. Partially-averaged navier stokes model for turbulence: Implementation and validation. AIAA Paper 2005-0502, 2005.

[25] Grant, I. and Owens, E. H. Confidence interval estimates in PIV measurements of turbulent flows. *Applied optics*, 29(10):1400–1402, April 1990.

[26] Haller, G. An objective definition of a vortex. *Journal of Fluid Mechanics*, 525: 1–26, 2005.

[27] Hedges, L. S., Travin, A., and Spalart, P. R. Detached-eddy simulations over a simplified landing gear. *Journal Of Fluids Engineering*, 124:413–423, June 2002.

[28] Heller, H. and Dobrzynski, W. Sound radiation from aircraft wheel-well/landing-gear configurations. *Journal of Aircraft*, 14(8), 1977.

[29] Hu, H., Yang, Z., and Sarkar, P. Dynamic wind loads and wake characteristics of a wind turbine model in an atmospheric boundary layer wind. *Experiments in Fluids*, 52:1277–1294, 2012.

[30] Humphreys, W. M. J. and Brooks, T. F. Noise spectra and directivity for a scale-model landing gear. AIAA Paper 2007-3458, 2007.

[31] ICAO. *Annex 16 - Environmental Protection, Volume I - Aircraft Noise*, 2013.

[32] Imamura, T., Hiraic, T., Amemiyad, K., Yokokawab, Y., Enomotob, S., and Yamamotob, K. Aerodynamic and aeroacoustic simulations of a two-wheel landing gear. *IUTAM Symposium on Computational Aero-Acoustics for Aircraft Noise Prediction*, 6:293–302, 2010.

[33] Keating, A., Dethioux, P., Satti, R., Noelting, S., Louis, J., Van de Ven, T., and Vieito, R. Computational aeroacoustics validation and analysis of a nose landing gear. AIAA Paper 2009-3154, 2009.

[34] Khorrami, M. R. and Mineck, R. E. Towards full aircraft airframe noise prediction: Detached Eddy simulations. AIAA Paper 2014-2480, 2014.

[35] Khorrami, M. R., Fares, E., and Casalino, D. Towards full aircraft airframe noise prediction: Lattice Boltzmann simulations. AIAA Paper 2014-2481, 2014.

[36] Khorrami, M. R., Humphreys, W. M. J., Lockard, D. P., and Ravetta, P. A. Aeroacoustic evaluation of flap and landing gear noise reduction concepts. 2014.

[37] Khorrami, M. R., Choudhari, M. M., Lockard, D., Jenkins, L. N., and McGinley, C. B. Unsteady flowfield around tandem cylinders as prototype component interaction in airframe noise. *AIAA Journal*, 45(8):1930–1941, 2007.

[38] Kurtulus, D., Scarano, F., and David, L. Unsteady aerodynamic forces estimation on square cylinder by TR-PIV. *Experiments in Fluids*, 42:185–196, 2007.

[39] Larusson, R. Aerodynamic flow simulation of a rudimentary landing gear using PANS and LES. Master's thesis, Chalmers University of Technology, 2011.

[40] Lazos, B. S. Mean flow features around the inline wheels of four-wheel landing gear. *AIAA Journal*, 40(2):193–168, 2002.

[41] Li, F., Khorrami, M. R., and Malik, M. R. Unsteady simulation of a landing-gear flow field. In *8th AIAA/CEAS Aeroacoustics Conference*, 2002.

[42] Liu, W., Kim, J., Zhang, X., Angland, D., and Caruelle, B. Landing-gear noise prediction using high-order finite difference schemes. *Journal of Sound and Vibration*, 332(14):3517–3534, July 2013.

[43] Lockard, D. P. Summary of the tandem cylinder solutions from the benchmark problems for airframe noise computations - I workshop. AIAA Paper 2011-353, 2011.

[44] Lu, F. Surface oil flow visualization. *Eur. Phys. J. Special Topics*, 182:51–63, 2010.

[45] Mangalam, A. and Davis, M. Ground/flight correlation of aerodynamic loads with structural response. AIAA Paper 2009-881, 2009.

[46] Manoha, E., Bulté, J., and Caruelle, B. LAGOON: An experimental database for the validation of CFD/CAA methods for landing gear noise prediction. AIAA Paper 2008-2816, 2008.

[47] McManus, J. and Zhang, X. A computational study of the flow around an isolated wheel in contact with the ground. *Journal of Fluids Engineering*, 128(3), 2005.

[48] Menter, F. R. and Kuntz, M. Adaptation of eddy viscosity turbulence models to unsteady separated flows behind vehicles. In McCallen, R., Browand, F., and Ross, J., editors, *The Aerodynamics of Heavy Vehicles: Trucks, Buses, and Trains.* Springer, 2004.

[49] Meyer, K. E., Cavar, D., and Pedersen, J. M. Pod as tool for comparison of piv and les data. 7th International Symposium on Particle Image Velocimetry, Rome, Italy, September 2007.

[50] NASA. The Spalart-Allmaras turbulence model, 2014. URL `http://turbmodels.larc.nasa.gov/spalart.html`. Visited: 24/07/2015.

[51] NASA. 2D zero pressure gradient flat plate validation case, 2014. URL `http://turbmodels.larc.nasa.gov/flatplate_val.html`. Visited: 24/07/2015.

[52] Nitsche, W. and Mirow, P. Piezo-electric foils as a means of sensing unsteady surface forces. *Experiments in Fluids*, 7:111–118, 1989.

[53] OpenCFD Ltd. Parallel computing, . URL `http://www.openfoam.com/features/parallel-computing.php`. Visited: 24/07/2015.

[54] OpenCFD Ltd. Standard solvers, . URL `http://www.openfoam.org/features/standard-solvers.php`. Visited: 24/07/2015.

[55] Pattenden, R. J., Bressloff, N. W., Turnock, S. R., and Zhang, X. Unsteady simulations of the flow around a short surface-mounted cylinder. *Int. J. Numer. Meth. Fluids*, 56(6):895–914, 2007.

[56] Peers, E. Numerical simulations of an isolated landing gear wheel. Project title: CADWIE, September 2010.

[57] Peers, E. Advanced landing gear - nose gear. high fiedelty CFD study, March 2011.

[58] Piersol, A. G. and Paez, T. L. *Harris' Shock and vibration handbook.* McGraw-Hill Handbooks, 6th edition, 2010.

[59] Pope, S. B. *Turbulent Flows.* Cambridge University Press, 2000.

[60] Rajaee, M., Karlsson, S., and Sirovich, L. Low-dimensional description of free-shear-flow coherent structures and their dynamical behaviour. *Journal of Fluid Mechanics*, 258:1–29, 1994.

[61] Robinson, M. and Hannemann, K. Short duration force measurements in impulse facilities. AIAA Paper 2006-3439, 2006.

[62] *ESDU 79015: Undercarriage drag prediction methods.* The Royal Aeronautic Society, September 1979.

[63] Sawanda, H. and Suda, S. Study on aerodynamic force acting on a sphere with and without boundary layer trips around the critical Reynolds number with a magnetic suspension balance system. *Experiments in Fluids*, 50:271–284, 2011.

[64] Schlichting, H. and Gersten, K. *Boundary-Layer Theory.* Springer, 8th edition, 2000.

[65] Schuster, D. M. and Byrd, J. E. Transonic unsteady aerodynamics of the F/A-18E at conditions promoting abrupt wing stall. AIAA Paper 2003-0593, 2003.

[66] Sears, W. The boundary layer of yawed cylinders. *Journal of the Aeronautical Sciences*, 15:49–52, 1948.

[67] Shur, M., Spalart, P. R., Strelets, M., and Travin, A. Detached-eddy simulation of an airfoil at high angle of attack. *Engineering turbulence modelling and experiments*, 4:669–678, 1999.

[68] Shur, M. L., Spalart, P. R., Strelets, M. K., and Travin, A. A hybrid RANS-LES model with delayed DES and wall-modeled LES capabilities. *International Journal of Heat and Fluid Flow*, 29:1638–1649, 2008.

[69] Shur, M., Spalart, P., Strelets, M., and Travin, A. Navier-stokes simulation of shedding turbulent flow past a circular cylinder and a cylinder with a backward splitter plate. In *Third ECCOMAS CFD Conference*, pages 672–682, 1996.

[70] Sirovich, L. Turbulence and the dynamics of coherent structures. Part I: coherent structures. *Quaterly of applied mathematics*, 45(3):561–571, 1987.

[71] Sørensen, N. 3d cfd computations of transitional flows using des and a correlation based transition model. Technical report, Risø DTU - National Laboratory for Sustenailbe Energy, July 2009.

[72] Soulinez, F. J., Long, L. N., Morris, P. J., and Sharma, A. Landing gear aerodynamic noise prediction using unstructured grids. *International Journal of Aeroacoustics*, 1(2):115–135, 2002.

[73] Spagnolo, S., Zhang, X., Hu, Z., and Angland, D. Numerical study of the interactions between landing-gear components. to be presented at AIAA AVIATION 2016 Forum and Exposition, 13-17 June 2016, Washington D.C., USA.

[74] Spagnolo, S., Zhang, X., Hu, Z., and Angland, D. Numerical simulations of single and tandem wheels for aerodynamic loads prediction. AIAA Paper 2015-3066, 2015.

[75] Spagnolo, S., Zhang, X., Hu, Z., Stalnov, O., and Angland, D. Unsteady force and flow features of single and tandem wheels. AIAA Paper 2015-0261, 2015.

[76] Spagnolo, S., Zhang, X., Hu, Z., Stalnov, O., and Angland, D. Unsteady force and flow features of single and tandem wheels. (journal paper submitted to Journal of Fluids and Structures), 2016.

[77] Spalart, P. R. Young-person's guide to detached-eddy simulation grids. NASA/CR-2001-211032, 2001.

[78] Spalart, P. Detached-eddy simulations. *Ann. Rev. Fluid Mech.*, 41:181–202, 2009.

[79] Spalart, P. R. and Allmaras, S. R. A one-equation turbulence model for aerodynamic flows. *Recherche Aerospatiale*, 1:5–21, 1994.

[80] Spalart, P. R., Jou, W.-H., Strelets, M., and Allmaras, S. R. Comments on the feasibility of LES for wings, and on a hybrid RANS/LES approach. *Advances in DNS/LES*, pages 137–147, 1997.

[81] Spalart, P. R., Deck, S., Shur, M. L., Squires, K. D., Strelets, M. K., and Travin, A. A new version of detached-eddy simulations, resistant to ambiguous grid densities. *Theor. Comput. Fluid Dyn.*, 20:181–195, 2006.

[82] Spalart, P. and Mejia, K. Experimental and numerical studies of the rudimentary landing gear. AIAA Paper 2011-0355, 2011.

[83] Stalnov, O., Windiate, S., Angland, D., Zhang, X., and Ashworth, R. On the contribution of individual components to landing gear loads and noise. AIAA Paper 2013-3153, 2013.

[84] Sumner, D. Two circular cylinders in cross-flow: A review. *Journal of Fluid and Structures*, 26:849–899, 2010.

[85] Tirunagari, S., Vuorinen, V., Kaario, O., and Larmi, M. Analysis of proper orthogonal decomposition and dynamic mode decomposition on LES of subsonic jets. *CSI Journal of Computing*, 1(3):2:19–2:24, 2012.

[86] Tobak, M. and Peake, D. J. Topology of three-dimensional separated flows. *Annual Review of Fluid Mechanics*, 14:61–85, 1982.

[87] Travin, A., Shur, M., Strelets, M., and Spalart, P. Detached-eddy simulation past a circular cylinder. *Flow, Turbulence and Combustion*, 63:293–313, 1999.

[88] Tropea, C., Yarin, A. L., and Foss, J. F., editors. *Springer Handbook of Experimental Fluid Mechanics.* Springer, 2003.

[89] Vatsa, V., Khorrami, M., Rhoads, J., and Lockard, D. Aeroacoustic simulations of a nose landing gear using FUN3D on Pointwise unstructured grids. AIAA Paper 2015-3255, 2015.

[90] Venkatakrishnan, L., Karthikeyan, N., and Mejia, K. Experimental studies on a rudimentary four-wheel landing gear. AIAA Paper 2011-0354, 2011.

[91] Venkatakrishnan, L., Karthikeyan, N., and Mejia, K. Experimental studies on a rudimentary four-wheel landing gear. *AIAA Journal*, 50(11):2435–2447, November 2012.

[92] Wilcox, D. C. *Turbulence Modeling for CFD.* DCW Industries Inc., 3 edition, 2006.

[93] Xiao, Z., Liu, J., Luo, K., Huang, J., and Fu, S. Investigation of flows around a rudimentary landing gear with advanced detached-eddy-simulation approaches. *AIAA Journal*, 51(1), January 2013.

[94] Xiao, Z. and Luo, K. Numerical simulations of tandem cylinders with subcritical spacing. AIAA Paper 2013-2209, May 2013.

[95] Zawodny, N. S., Liu, F., Yardibi, T., Cattafesta, L., Khorrami, M. R., Neuhart, D. H., and Van de Ven, T. A comparative study of a 1/4-scale Gulfstream G550 aircraft nose gear model. AIAA Paper 2009-3153, 2009.

[96] Zdravkovich, M. M. *Flow around circular cylinders*, volume 1. Oxford University Press, 1997.

[97] Zdravkovich, M. M., Flaherty, A. J., Pahle, M. G., and Skelhorne, I. A. Some aerodynamic aspects of coin-like cylinders. *J. Fluid Mech.*, 360:73–84, 1998.

[98] Zhang, X., Ma, Z., Smith, M., Sanderson, M., and Bissessur, P. Aerodynamic and acoustic measurements of a single landing gear wheel. AIAA Paper 2013-2160, 2013.

[99] Zhou, Y. and Yiu, M. Flow structure, momentum and heat transport in a two-tandem-cylinder wake. *Journal of Fluid Mechanics*, 548:17–48, 2006.